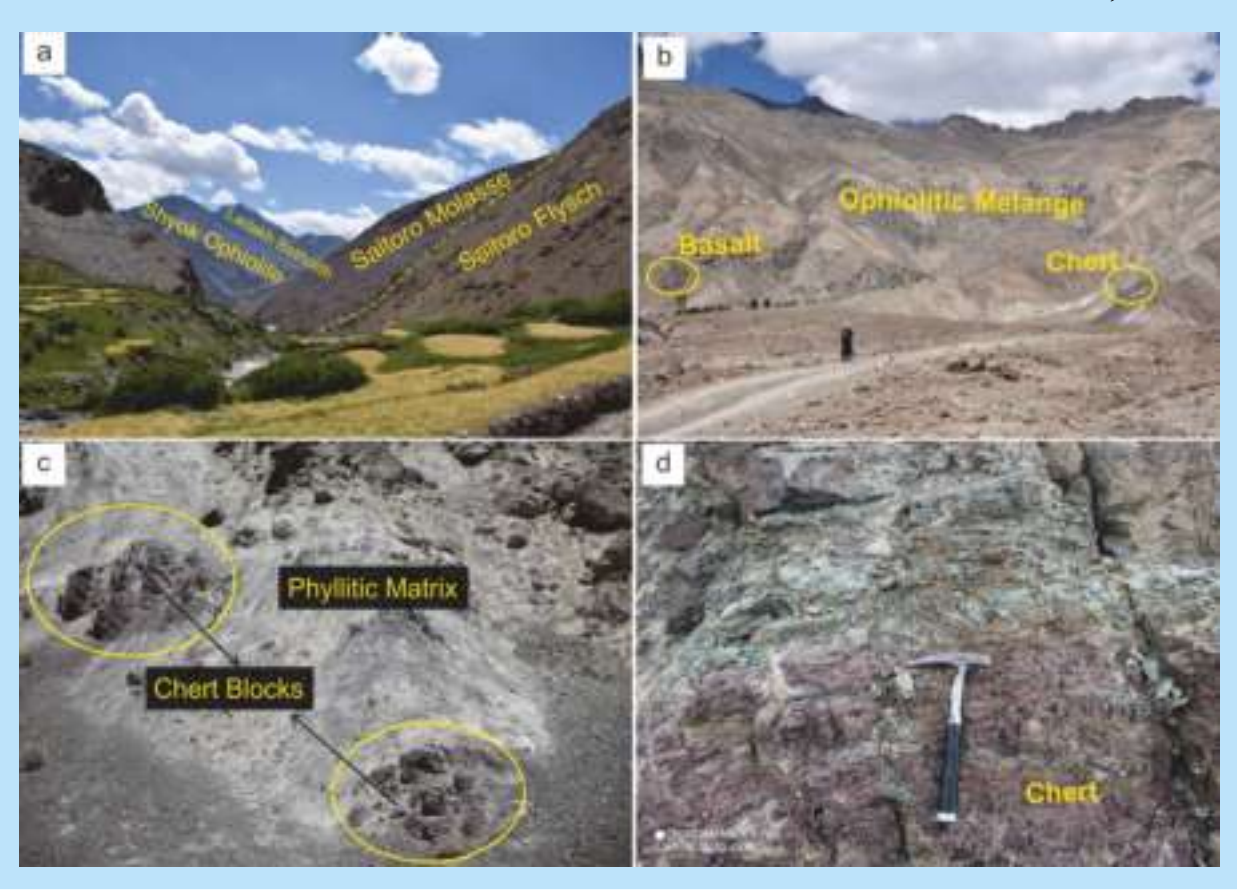
HIMALAYAN GEOLOGY

(An International Journal of Geosciences)

Vol. 46, No. 2, 2025

WADIA INSTITUTE OF HIMALAYAN GEOLOGY Dehradun 248001, India



HIMALAYAN GEOLOGY

CHIEF PATRON

Director (WIHG)

EDITORS

Editor-in-Chief

M. Jayananda

E-mail: mjayan.geol@gmail.com

Associate Editors

R. Jayangondaperumal

E-mail: ramperu.jayan@gmail.com

Jingsui Yang

E-mail: yangjsui@163.com

S.K. Parcha

E-mail: parcha 1@rediffmail.com

Naresh Kumar

E-mail: naresh.himgeol@gmail.com

Vimal Singh

E-mail: vimalgeo3213@gmail.com

D.P. Kanungo

E-mail: debi.kanungo@gmail.com

Pritam Nasipuri

E-mail: pritams@iiserb.ac.in

Rakesh Bhambri

E-mail: rakeshbhambri@gmail.com

Editorial Manager

Rambir Kaushik

E-mail: rambir.geol@gmail.com

EDITORIAL BOARD

Talat Ahmad, India R.P. Tiwari, India T.N. Singh, India Mrinal K. Sen, Austin

R.P. Singh, India Rasik Ravindra, India

G.V.R. Prasad, India

Igor M. Villa, Switzerland

J-L Mugnier, France

Lewis Owen, Raleigh

Michel Ballevre, RENNES

Robert Wasson, Australia

Simon Klemperer, Stanford

Sun-Lin Chung, Taiwan

L.S. Chamyal, India

B.P. Singh, India

D.C. Srivastava, India

Santosh Kumar, India

Chrstopher Spencer, Canada

Dhananjai Kumar Pandey, India

Di-Cheng Zhu, China

O.P. Mishra, India Peter D. Clift, USA

Prantik Mandal, India

Raymond Duraiswami, India

Richard Coffin, Corpus Christi

S.K. Ghosh, India

Umesh K. Haritashya, USA

Pradeep Srivastava, India

Satish Sangode, India

Sridevi Jade, India

Binita Phartiyal, India

Editorial Office

Publication Division

Wadia Institute of Himalayan Geology

33-General Mahadeo Singh Road, Dehradun 248001, India

Phone (Off.): +91-135-2525430; Web: http://www.himgeology.com Email: himgeol@wihg.res.in; himgeology.com@gmail.com

"Himalayan Geology" journal is published bi-annually in January and July each year. The print subscription price for 2025-26 is:

Institutional (including postage etc.)
Rs. 3000.00 (India)
US \$ 225.00 (Abroad)
Individual (including postage etc.)
Rs. 1000.00 (India)
US \$ 100.00 (Abroad)

Editorial correspondence and material submitted for publication should be addressed to the Editorial Office, "Himalayan Geology", Wadia Institute of Himalayan Geology, 33-General Mahadeo Singh Road, Dehradun - 248001, India.

Business Correspondence, including orders and remittances relating to subscriptions, advertisements should be sent to the Director, Wadia Institute of Himalayan Geology, 33-General Mahadeo Singh Road, Dehradun -248001, India.

ISSN 0971-8966

Copyright (c) by the Wadia Institute of Himalayan Geology, Dehradun 248001, India.

No material published here should be reproduced in any form without prior written permission from the publishers.

Cover Photo: Field photographs (a) Saltoro Flysch overlain by Saltoro molasse facing south from Waris Village, Shyok Ophiolite and Ladakh batholith are seen in the background; (b) Panoramic view of Shyok ophiolitic mélange facing north from Chastang near Bukdang village; (c) Ophiolitic mélange exhibiting Block-in-Matrix fabric with blocks of chert lying in matrix of phyllite at Chastang; (d) Ribbon-bedded chert at Chastang.

(Source: Rakesh Chandra & Ihsan Ullah Lone)

HIMALAYAN GEOLOGY

Vol. 46, No. 2, 2025



WADIA INSTITUTE OF HIMALAYAN GEOLOGY DEHRADUN, INDIA

Study on the numerical simulation model for quantitative evaluation on effect factors of multi-branch pinnate borehole gas extraction in high-gas thick coal seams

ZHU XIMING¹, JIA JINLONG^{1,*}, ZHANG LONGGANG^{2,#}, MA ZHENG³, QIN ZHENGYUAN¹, ZHANG HANQUAN¹, LIU ZILONG¹

¹Wuhan Institute of Technology, School of Resources and Safety Engineering, Hubei Province, Wuhan, 430205, China ²Shaanxi Coal Pubai Mining Co., Ltd, Shaanxi Province, Weinan, 715517, China ³Shaanxi Coal Industry Group Huangling Jianzhuang Mining Co., Ltd. Shaanxi Province, Yan 'an, 727307, China Email (Corresponding authors): *690201733@qq.com, *531395120@qq.com

Abstract: The multi-branch pinnate borehole gas extraction technology has the potential to address the inefficiency of traditional gas extraction methods in thick coal seam with high gas-containing. The study focuses on the 2308 working face of GJH mine and develops a continuous equation to quantitatively describe the gas drainage process of multi-branched pinnate borehole in coal seams. Utilizing numerical simulation methods, the effect of multi-branched pinnate borehole parameters on gas drainage effectiveness were systematically studied. The results indicate that the angle between the branches and the main borehole, branch length, branch hole spacing, and the number of branches are critical factors affect extraction effectiveness, and these factors are mutually influence for each other. The acute angle between the minor branches and the main borehole can rapidly decrease coal seam pressure in a short period. As a result, the length of the branches increases. The spacing between branch openings and the number of branches are considered as secondary factors. Increasing the spacing between branch openings can improve cumulative gas production per unit length of drilling, but it may lead to a reduction in drainage range. A larger branching angle can extend the drainage range, but at this point, branch spacing and quantity become the primary influencing factors. Decreasing branch spacing can improve drainage efficiency, although it may lead to an excessive number of branches; The research can offer valuable insights for the engineering of multi-lateral pinnate drilling in high-gas-content thick coal seams under similar geological conditions.

Keywords: High-gas; thick coal seam; multi-branch pinnate borehole; CBM extraction; numerical simulation

INTRODUCTION

Gas extraction in coal mining areas serves as a crucial technical method for addressing gas disasters and harnessing coalbed methane (CBM) resources. Integrating gas extraction technology into coal mine safety, ecological conservation, and enhancement of the energy structure holds considerable significance (Chen et al. 2017; Duan et al. 2012; Wang et al. 2012). Traditional gas drainage methods are not well-suited for managing gas in thick coal seams with high gas concentrations, posing problems such as high drainage expenses, substantial engineering requirements, lengthy construction timelines, low gas capture rates, limited effective drainage sections, inadequate economic returns and the creation of blind extraction zones (Fan et al. 2018; Hu et al. 2015). In contrast, the application of multi-branch borehole extraction technology utilizing directional drilling has seen widespread adoption in the CBM development within extremely thick coal seams. This approach can expand the pressure relief control zone of borehole extraction, decrease the spatial demands of drilling sites, enhance gas capture rates and productivity, prolong the lifespan of extraction boreholes, and effectively address issues related to blind extraction zones typically encountered with traditional drilling techniques (Mu et al. 2021; Duan et al. 2012; Ran et al. 2021).

Various scholars have conducted theoretical and engineering research on developing coalbed methane through multi-branch drilling from the surface, yielding diverse academic insights and engineering reference data. However, there is relatively less research on the extraction of coal seam

gas through multi-branch drilling in underground operations due to limitations between underground boreholes. Some scholars demonstrated the improvement in extraction efficiency of pinnate branch wells, even under very low permeability conditions in coal seams (Zhang et al. 2021). Other scholars, through numerical simulation studies, highlighted the substantial impact of multi-branch horizontal well structures on coal seam gas extraction efficiency (Ren et al. 2014). Key factors affecting the effectiveness of coalbed methane development include the well layout method of multi-branch horizontal wells, such as the number of main wellbore and branch wells, direction, length of the main horizontal section, number of branches, angle between branches and main branches, spacing, and length of branch wells (Huang et al. 2019; Yang et al. 2019; Zhu et al. 2019). Common multi-branch structures include configurations like a single main borehole with multiple symmetrical branches, a single main borehole with multiple asymmetrical branches, double main boreholes with multiple symmetrical branches, and multiple main boreholes with multiple symmetrical branches (Keim et al. 2011; Wang et al. 2020; Jiang et al. 2016; Yang et al. 2019). Within the same production area and similar mining environments with geological reservoirs, coal seam physical properties, and discharge management systems, various key parameters such as main borehole length, branch length, branch number, branch angle, and branch spacing in different horizontal sections will influence gas extraction efficiency and overall harvesting outcomes (Jiang et al. 2013; Shi et al. 2020). Fan et al. observed that coal seam gas pressure decreases gradually during the extraction

process, with faster pressure drops near the wellbore (He *et al.* 2023). The cumulative gas production of the coal seam is proportionate to the increase in branch length, with the choice of branch number dependent on wellbore utilization and extraction time. Moreover, a larger angle between the branch and main borehole, as identified by Ren *et al.* 2014, can expand the lateral influence range and enhance gas production; however, an excessively large branch angle may lead to reduced gas production, underscoring the importance of selecting the optimal angle (Ren *et al.* 2014). Furthermore, inadequate spacing between branch openings can also lead to decreased extraction efficiency.

Previous studies have shown that higher extraction efficiency in multi-branch drilling is associated with longer main boreholes, increased number of branches, and shorter spacing between branch openings (An et al. 2019; Fan et al. 2018; Gong et al. 2024). In the actual production process, various factors such as the physical properties of the coal reservoir, construction cost, ease of construction, and technical equipment level come into play. Setting the branch angle and spacing too small may result in an inadequate effective drainage area, which limits the utilization of the potential benefits of multilateral wells. Conversely, if the branch angle or spacing is excessively large, it could impede effective inter-well interference between adjacent wellbores, leading to prolonged drainage cycles and reduced efficiency (Fan et al. 2022; Wang et al. 2017; Zhang et al. 2020). The design requirements for multi-branch drilling technology vary depending on the coal seam conditions, indicating that a fixed multi-branch drilling structure is not universally suitable for all types of coal seams. Therefore, selecting the right multibranch drilling parameters is essential for enhancing development efficiency and maximizing economic benefits. Numerical simulation technology plays a crucial role in optimizing the selection and design parameters for coalbed methane (gas) discharge. By conducting simulations and comparative analyses, it enables the provision of a scientific decision-making basis for potential prediction, economic benefit evaluation, and the optimization selection of drainage parameters (Fan et al. 2022; Wang et al. 2017; Zhang et al. 2020). Li utilized COMSOL Multiphysics software, incorporating the elasto-plastic softening model and Darcy's flow theory, to model the evolution of coalbed methane pressure distribution over extraction time (Li 2019). By establishing a correlation between extraction time and radius, they succeeded in pre-determining the extraction radius, thus minimizing the necessity for on-site validation. Further research is needed to explore the factors influencing the discharge of underground multi-branch pinnate boreholes in extra-thick and high-gas coal seams, as well as their drainage effects.

This paper constructs a continuity equation to quantitatively describe the coal seam gas discharge process with multi-branch pinnate boreholes, drawing on the research background of high gas, thick coal seams, and gas geological conditions in the GJH well field. By utilizing numerical simulation methods, we systematically analyze the effects of

branch-to-main borehole angle, spacing between branch openings, number of branches, and branch length on coal seam gas drainage pressure, effective drainage volume, and gas production. The study also discusses the factors influencing the performance of multi-branch pinnate boreholes in draining extremely thick and high-gas coal seams. Furthermore, the optimization of their parameters is explored, providing a crucial reference for the construction of multi-branch pinnate boreholes in similar geological conditions.

COAL SEAM GAS GEOLOGICAL CONDITIONS

The GJH minefield, situated in the northern part of Linyou County, Shaanxi Province, China, primarily exploits the No. 3 coal seam of the Yan'an Formation within the Middle Jurassic System, characterized as low-metamorphic bituminous coal (Fig. 1). The thickness of the coal seam varies between 0.55 and 26.83m, with an average thickness of 10.46m, and it is buried at depths spanning 500 to 746m, with an average depth of 572m. The immediate roof of the coal seam consists of black sandy mudstone, averaging 1.00m in thickness, while the immediate floor is composed of black carbonaceous mudstone, with an average thickness of 3.5m. Specifically, the 2308 working face has been specifically engineered for the extraction of coal from the No. 3 coal seam, with a projected strike length of 1000m and an inclination length of 200m. Data obtained from the assessment of fundamental coal seam gas characteristics reveal an average coal seam gas content of 6.61m³/t at the working face, coupled with an average coal seam permeability coefficient of 0.0339m²/MPa².d (Table 1). The absolute methane outflow rate on the working surface is measured at 37.98 m³/min, while the relative outflow rate is

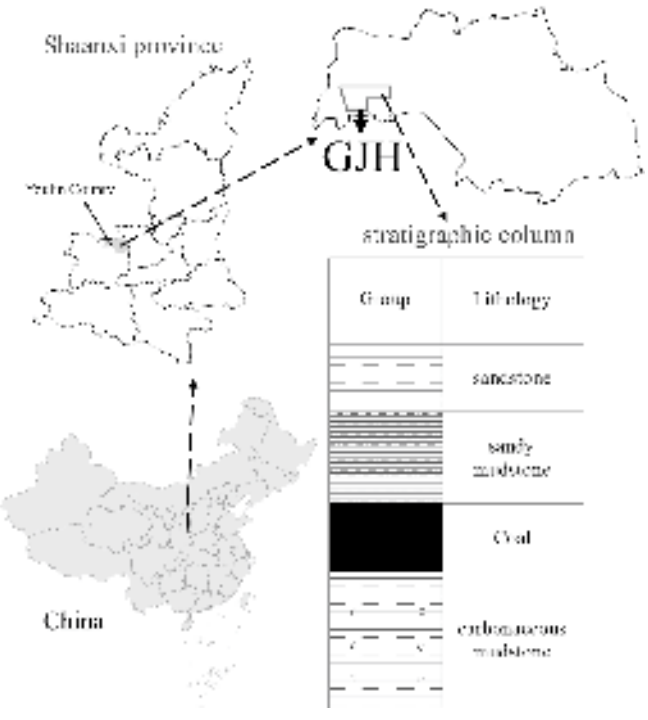


Fig. 1. Well field geographical location map and stratigraphic column chart.

 $3.52 \text{ m}^3/\text{t}$. Likewise, the absolute carbon dioxide outflow volume is $3.49 \text{ m}^3/\text{min}$, with a relative outflow volume of $0.32 \text{ m}^3/\text{t}$. It is a thick coal seam that can drain high gas content.

QUANTITATIVE ASSESSMENT AND NUMERICAL SIMULATION MODEL OF MULTI-BRANCH PINNATE BOREHOLES FOR GAS EXTRACTION FACTORS

Numerical model establishment

Basic assumptions

According to the coal seam gas occurrence and migration characteristics, before establishing a mathematical quantitative characterization model for underground multibranch borehole gas discharge, the following assumptions are made:

- 1) Coal is regarded as a poroelastic medium material composed of matrix pores and cracks.
- 2) CH₄ is approximately an ideal gas and conforms to the ideal gas equation of state.
- 3) CH₄ migrates from the matrix pore surface to the cracks and diffuses according to Fick's law. The migration of CH₄ in the fracture system conforms to Darcy's law.
- 4) The adsorption and desorption of CH₄ gas in coal can be quantitatively characterized by the Langmuir equation.
- 5) The adsorption and desorption process in coal and rock mass is a constant-temperature process, that is, the temperature change caused by gas adsorption and desorption is not considered.
- Ignore the effect of temperature on the dynamic viscosity of gases.

Coal seam gas content equation

The gas content of coal refers to the total amount of gas contained in unit volume of coal. The main component of gas is CH₄. CH₄ gas mainly exists on the matrix pore surface in an adsorbed state, a small amount exists in the crack space in a free state, and a very small amount exists in a solid solution state. The very small amount of CH₄ gas present in solid solution can be approximately ignored.

1) Adsorbed gas content in coal matrix

The volume of CH_4 gas existing in the adsorbed state in coal is often quantitatively characterized by the Langmuir equation. The equation expression is:

$$V_{s} = \frac{V_{L}P}{P_{L} + P} \tag{1}$$

Where, $V_L = \text{Langmuir volume constant in m}^3/\text{kg}$

 $P_{\rm L}$ = Langmuir pressure constant in MPa

 $P = \text{coal matrix CH}_4$ gas pressure (MPa)

According to the Langmuir equation, the adsorbed gas content in the matrix can be further expressed as:

$$m_{l} = \frac{V_{L}P_{m}}{P_{m} + P_{L}} \rho_{a}\rho_{s} \tag{2}$$

Where, m_1 = the mass of adsorbed gas existing in the coal pore system per unit volume in kg/m³

 $V_{\rm L} = \text{Langmuir volume in m}^3$

 $P_{\rm I}$ = Langmuir pressure constant in MPa

 $\rho_a =$ apparent density of coal in kg/m³

 ρ_s = standard The gas density in the state in kg/m³

 $P_{\rm m} = CH_4$ gas pressure in the coal matrix pores (MPa)

2) Free gas content in coal

According to the ideal gas equation of state, the density of gas in coal cracks under standard conditions can be expressed as:

$$\rho_{\rm f} = \frac{M_{\rm c}}{RT} P_{\rm f} \tag{3}$$

Where, $M_c = \text{molar mass of methane molecules in kg/mol}$

 $R = ideal gas constant in J/(mol \cdot K)$

T = coal seam temperature in K

 $P_f = CH_4$ gas pressure in the crack in MPa

The mass of free gas existing in cracks in unit volume of coal is:

$$m_f = \varphi_f \rho_f \tag{4}$$

Where, $m_{\rm f}$ = the mass of free gas existing in coal cracks per unit volume in kg/m³ $\varphi_{\rm f}$ = the crack rate of coal in %

Combining Eq.3 and E.4, the mass of free gas in unit volume of coal cracks can be obtained as:

$$m_f = \varphi_f \frac{M_c}{RT} P_f \tag{5}$$

It can also be obtained that the free gas content in unit volume of coal pores can be calculated by Eq.6:

$$m_2 = \varphi_m \frac{M_c}{RT} P_m \tag{6}$$

Where, m_2 = free gas mass existing in the coal pores per unit volume in kg/m³

 $\varphi_{\rm m}$ = porosity of the coal in %

 $P_{\rm m}$ = CH₄ gas pressure in the coal matrix pores in MPa.

3) Total mass of gas present in unit volume of coal

Combining Eq.2, Eq.5, and Eq.6, the total mass of gas in unit volume of coal can be obtained as:

$$m = \frac{V_{L}P_{m}}{P_{m} + P_{L}} \rho_{a} \frac{M_{c}}{V_{M}} + \varphi_{m} \frac{M_{c}}{RT} P_{m} + \varphi_{f} \frac{M_{c}}{RT} P_{f}$$
 (7)

Coal seam gas diffusion equation

Gas diffusion in coal seams is dominated by gas phase

diffusion, which can be characterized by the Fick diffusion equation. The diffusion driving force is the concentration difference between gas phase gas in the pores of the coal matrix and in the cracks, and the adsorbed gas in the coal matrix is the mass source. The mathematical representation formula of the mass exchange flux between the fracture system and the coal matrix system is:

$$(Q_{s} = D\sigma_{c} c_{m} - c_{f}) \tag{8}$$

Where, Q_s = mass exchange rate of unit volume of coal matrix and fracture system in kg/(m³·s)

 $D = \text{gas diffusion coefficient in m}^2/\text{s}$

 $\sigma_c = \text{matrix shape factor in m}^{-2}$

 $c_{\rm m}$ = Gas concentration in kg/m³

 $c_r = \text{gas concentration in the fracture system in kg/m}^3$

The mathematical representation equation of coal matrix shape factor is:

$$\sigma_{\rm c} = \frac{3\pi^2}{I^2} \tag{9}$$

Where, L = crack spacing in m.

According to the ideal gas equation of state, the calculation formula for the gas concentration in the cracks and the gas concentration in the matrix is:

$$c_{\rm f} = \frac{M}{RT} P_{\rm f} \tag{10}$$

$$c_{\rm m} = \frac{M}{RT} P_{\rm m} \tag{11}$$

The relationship between coal matrix shape factor and gas diffusion coefficient is as shown in Eq. 12:

$$\tau = \frac{1}{\sigma_{\circ} D} \tag{12}$$

Where, τ = adsorption time in s.

By combining Eq.8, Eq.10, Eq.11, and Eq.12, we can get:

$$Q_{\rm S} = \frac{M}{\tau RT} \left(P_{\rm m} - P_{\rm f} \right) \tag{13}$$

Where, M is the molar mass of methane molecules, kg/mol;

 $R = ideal gas constant in J/(mol \cdot K)$

T = coal seam temperature in K

 $P_{\rm m} = CH_4$ gas pressure in the matrix pores in MPa

 P_f = pressure in the cracks CH₄ gas pressure in MPa.

Since the adsorption and desorption of gas in coal seams is a dynamic equilibrium process, according to the law of conservation of mass, the decrease in gas in the coal matrix pores over time is equal to the increase in gas in the cracks, and it can be obtained:

$$\frac{\partial P_{\rm m}}{\partial t} = -\frac{M}{\tau RT} \left(P_{\rm m} - P_{\rm f} \right) \tag{14}$$

Combining Eq. 7 with Eq. 14 and simplifying it, the governing equation of coal matrix pore gas pressure changing with time is obtained:

$$\frac{\partial P_{\rm m}}{\partial t} = -\frac{\sigma_{\rm c} D V_{\rm m} \left(P_{\rm m} - P_{\rm f}\right) \left(P_{\rm m} + P_{\rm L}\right)^2}{V_{\rm L}^2 T P_{\rm L} \rho_{\rm c} + \varphi_{\rm m} V_{\rm m} \left(P_{\rm m} + P_{\rm L}\right)^2}$$
(15)

Coal seam gas seepage equation

Since the migration of free gas in coal seam fissures follows the law of conservation of mass, it can be obtained:

$$\frac{\partial}{\partial t} (\varphi_{\rm f} \rho_{\rm f}) = -\nabla (\rho_{\rm f} V) + Q_{\rm s} (1 - \varphi_{\rm f}) \tag{16}$$

Where, V = gas seepage velocity in the crack in m/s.

Combining Darcy's law and the ideal gas equation of state, the governing equation for the change of gas pressure in the crack with time can be obtained:

$$\varphi_{\rm f} \frac{\partial P_{\rm f}}{\partial t} + P_{\rm f} \frac{\partial \varphi_{\rm f}}{\partial t} = \nabla \left(\frac{k_{\rm e}}{\mu} P_{\rm f} \nabla P_{\rm f} \right) + \frac{1}{\tau} (1 - \varphi_{\rm f}) (P_{\rm m} - P_{\rm f})$$
(17)

Eq. 7, Eq. 15 and Eq. 17 are combined to obtain the characterization equation describing the adsorption/desorption-diffusion-seepage continuous process of multi-branch pinnate borehole extraction of coal seam gas.

Geometry establishment and boundary condition setting

According to the engineering conditions and geological conditions of the 2308 working face of No. 3 coal seam in the GJH mine field, and considering the boundary influence, a three-dimensional model of the multi-branch plume borehole was established. The overall size of the model is 1100m (length) × 200m (width) × 18m (height). The model is shown in figure 2. The model is divided into three layers from top to bottom. The first layer is the roof, with a height of 1m. The second layer is the coal seam with a height of 10m. The third layer is the base plate, with a height of 7m. The extraction coal seam area is from x=0 to x=1000. The drainage borehole slopes upward from the point (-100, 0, -7) on the floor to the point (0, 0, 0) and enters the drainage coal seam horizontally. The length of the horizontal main borehole in the drainage coal seam is 1000m. The diameter of the drainage borehole is 94mm. There is no flow around the coal seam, the initial gas pressure of the coal seam is set to 0.6MPa, and the borehole Dirichlet boundary conditions and Darcy's law pressure conditions are both set to 16KPa, which is the drainage negative pressure.

Aiming at the multi-branch pinnate borehole discharge coal seam gas adsorption/desorption-diffusion-seepage continuous process equation, multi-physics coupling

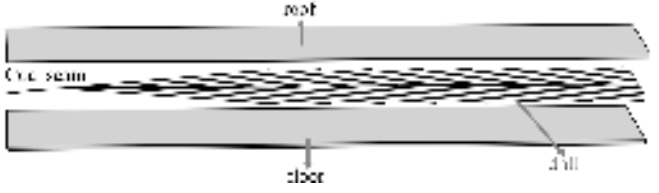


Fig. 2. Multi-branch drilling model diagram

Table 1. Measured values of basic parameters of coal seam No. 3 in the study area.

Parameter name	The measurement results	Average value
Coal seam gas	0.58~0.61	0.60
pressure (MPa)		
Coal seam gas	6.45~6.70	6.61
content (m³/t)		
Moisture M _{ad}	3.54%~4.85%	3.98%
(dimensionless)		
Ash content A _{ad}	4.06%~12.76%	9.18%
(dimensionless)		
Volatile matter V _{daf}	24.53%~35.97%	31.88%
(dimensionless)		
True Density (g/cm ³)	1.47~1.52	1.48
Apparent Density (g/cm ³)	1.37~1.41	1.38
Porosity (dimensionless)	4.32%~5.61%	4.92%
Solidity coefficient	0.59~1.10	0.95
of coal (dimensionless)		
Coal seam permeability	0.0303~0.0425	0.0365
coefficient£¤m²/MPa².d£'		
Borehole flow attenuation	n 0.3095j « 0.4136	0.3725
coefficient£¤d-1£'		

Parameter name	The measurement results	Average value
Initial crack ratio	0.012	0.012
(dimensionless)		
Initial permeability	0.12	0.12
(mD)		
Single hole diffusion	5.60×10^{-12}	5.60×10^{-12}
coefficient (m ² /s)		
CH ₄ dynamic viscosity	1.08×10^{-5}	1.08×10 ⁻⁵
(Pa·s)		
CH ₄ gas molecular mass (g/mol) 16	16
Gas state constant (J/mol/	K) 8.413510	8.413510
Langmuir pressure	2.02	2.02
constant (MPa)		
Langmuir volume constar	nt 28.8436	28.8436
(m^3/t)		
Drainage hole diameter (r	nm) 94	94
CH ₄ molar volume under	22.4	22.4
standard conditions (L/mo	ol)	
Drainage negative	16	16
pressure (kPa)		

numerical simulation calculation software is used to solve the problem, which requires fine grid division, forming a total of 177,691 units. Based on the coal and coalbed methane test parameters in the study area, the numerical simulation related parameters set are listed in table 1.

Simulation plan and evaluation reference indicators

Simulation parameter design

The length of the branches, spacing between branch openings, the angle between the branches and the main borehole, and the number of branches is key factors that influence the effectiveness of extraction. In research, it is common practice to vary only one parameter while keeping other parameters constant. However, in order to fully explore the impact of various factors, this article uses orthogonal experimental methods to quantitatively analyze the impact of each factor on the extraction effect. In order to comprehensively consider the impact of various parameters on the sampling efficiency, an orthogonal experiment was conducted with the branch-tomain borehole angle, branch length, branch number, and branch opening spacing as variable factors. Each factor had 3 levels. Based on the existing directional drilling construction technology performance indicators, the main borehole length is designed to be 1000m, with symmetrical branches on both sides of the main borehole. On this basis, an analysis was conducted to investigate the impact of branch angle with the main borehole, branch length, number of branches, and

spacing between branch openings on the effectiveness of multi-branch drilling for extraction. By adopting this design method, in which the main branch length is fixed at a constant value, analyzing the impact of branch factors on the overall outcome can effectively mitigate interference from positive and negative effects among multiple factors. The parameter design of key factors affecting multi-branch pinnate borehole extraction is shown in Table 2. According to the orthogonal table L9 (34), a total of 9 sets of different borehole parameter tests were designed.

Reference indicators for evaluation of factors affecting extraction

According to the "Interim Regulations on Coal Mine Gas Drainage Compliance Standards", when the absolute gas emission volume from the working face is greater than 30m^3 /min, the drainage rate should be greater than or equal to 20% and less than 40%. According to the "Regulations on the Prevention and Control of Coal and Gas Outbursts", the point where the residual gas pressure after pre-drainage is less than 0.74MPa is the boundary of the effective drainage radius. Zhou Shining et al., proposed the calculation formula of pre-draw rate (Zhou 1999):

$$h = 1 - \frac{\sqrt{P_1}}{\sqrt{P_0}} \tag{18}$$

Table 2. Parameter design of key factors affecting extraction of multi-branch pinnate boreholes.

Level	Test plan	Factor 1 Angle (°)	Factor 2 Branch length (m)	Factor 3 Number of branches (dimensionless)	Factor 4 Branch spacing (m)
	1-1			28	70
1	1-2	10°	500	24	80
	1-3			22	90
	2-1			28	70
2	2-2	15°	375	24	80
	2-3			22	90
	3-1			28	70
3	3-2	20°	275	24	80
	3-3			22	90

Where η is the pre-extraction rate; P_1 is the residual gas pressure, MPa; P_2 is the original gas pressure, MPa.

According to Eq.18, when the original gas pressure is 0.6MPa, in order to meet the drainage rate of 35%, the effective drainage range is that the post-drainage gas pressure is less than or equal to 0.25MPa.

SIMULATION RESULTS

Variations in gas pressure characteristics within the coal extraction area

The time-varying gas pressure cloud map of the coal seam under different multi-branch pinnate borehole gas extraction schemes is illustrated in figure 3. In this map, the effective drainage area is identified as the region where the coal seam gas pressure is less than 0.25 MPa. Furthermore, figure 3 also displays the characteristic curve depicting the variation of gas pressure over time at the top of the coal seam for various multi-branch pinnate borehole gas discharge schemes.

As the gas drainage time for the multi-branched pinnate drilling increases, there is a decreasing trend in coal seam gas pressure around both the main drilling and branch drilling, as indicated by figure 3. The analysis also reveals that the area in which the coal seam gas pressure equals or is less than 0.25 MPa is continuously expanding. The most pronounced reduction in coal seam gas pressure is observed at the point where the main borehole intersects with the branch borehole. Over time, the region with coal seam gas pressure \leq 0.25 MPa gradually extends from this intersection to the branch

borehole near the coal seam boundary, eventually forming a contiguous zone.

Based on the monitoring results of gas pressure at the top of the coal seam, all nine scenarios exhibit a rapid initial decrease in CH₄ pressure followed by a slowing rate of decline. Specifically, in schemes 1-1, 2-1, and 3-1, the coal seam top gas pressure reaches 0.25 MPa at approximately 310, 560, and 630 days, respectively, meeting the requirements for effective extraction pressure. In schemes 1-2, 2-2, and 3-2, the effective drainage pressure requirement of 0.25 MPa at the coal seam top is expected to be reached at approximately 370, 480, and 640 days, respectively. In schemes 1-3 and 2-3, the gas pressure at the top of the coal seam drops to 0.25 MPa at around 370 and 560 days, respectively, fulfilling the effective drainage pressure requirement (as illustrated in Fig.4). Conversely, in Scheme 3-3, the CH₄ pressure in the coal seam has been declining slowly and has not yet reached the required pressure.

Characteristics of variations in effective sampled volume

In figure 5, the variations in the effective extracted volume of the coal seam as extraction time increases are depicted as the coal seam pressure reaches the drainage standard. The three borehole structures, each characterized by a branching angle of 10° and a branching length of 500m, exhibit similar trends in their effective drainage volume variations. The effective drainage volume demonstrates a pattern of gradual increase followed by rapid growth, and eventual deceleration in the rate of increase, resembling an "S-shaped" curve. Notably, within

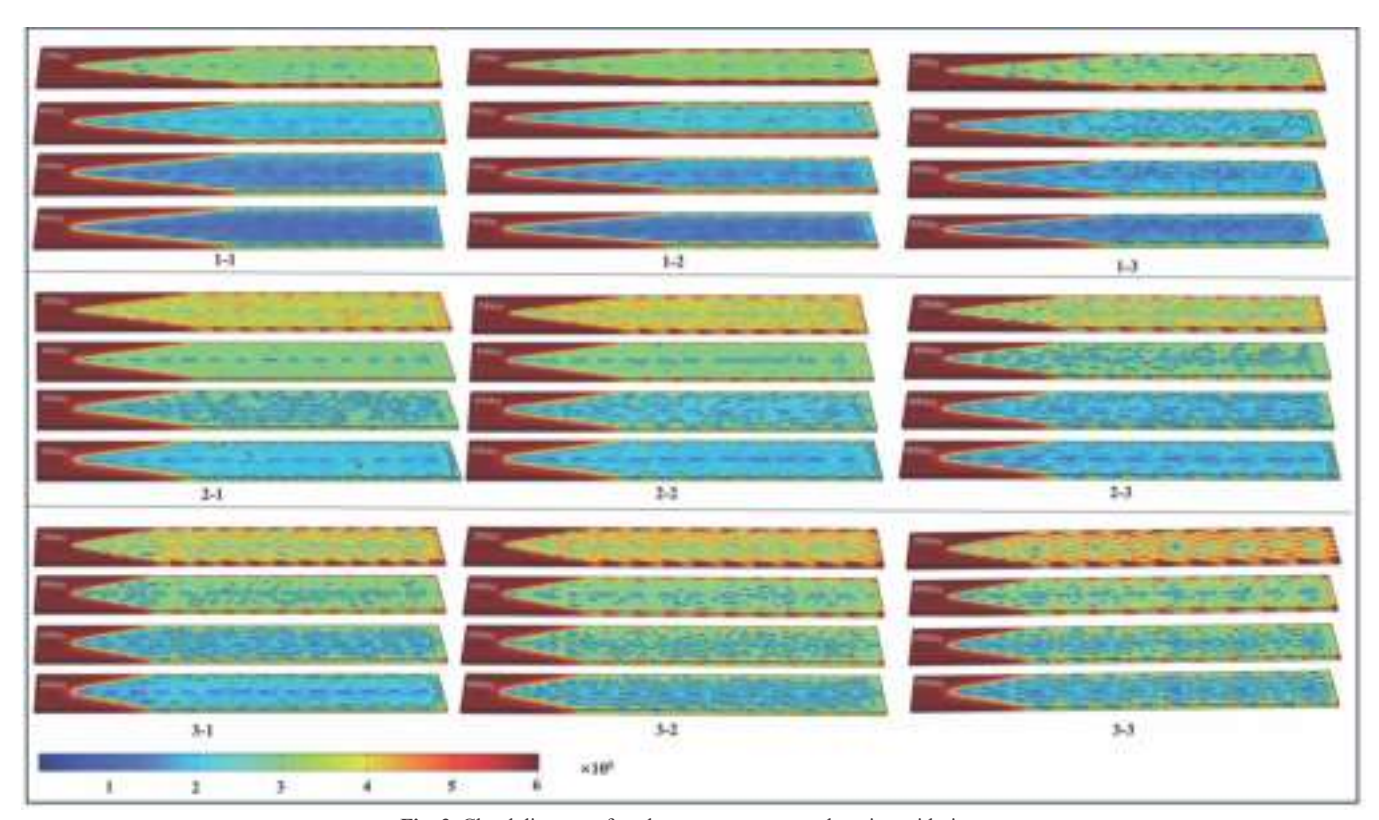


Fig. 3. Cloud diagram of coal seam gas pressure changing with time.

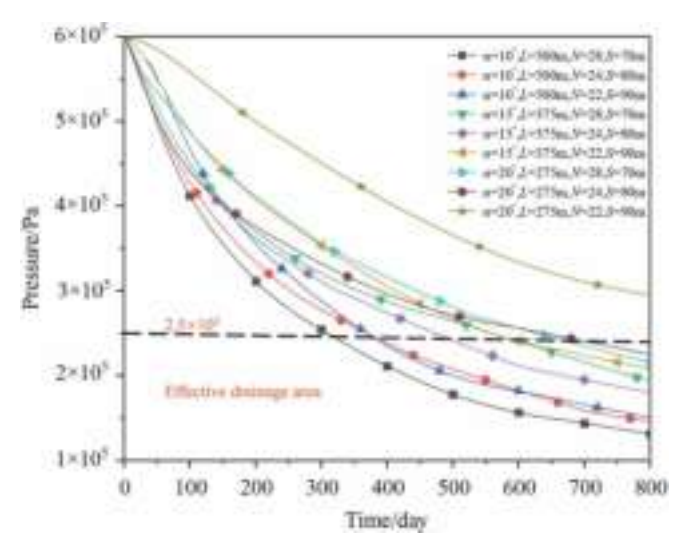


Fig. 4. Characteristic curve of gas pressure changing with time at the top of coal seam.

the first 200 days of extraction, the changes in effective extraction volume across the three structures are comparable, but diverge thereafter, with a tendency to stabilize post-400 days. Scheme 1-2 and Scheme 1-3 exhibit analogous features in the increase of effective drainage volume after 200 days of drainage; however, Scheme 1-2 experiences a slowdown in the rate of increase post-400 days, while Scheme 1-3 shows a similar deceleration after 450 days.

For the three borehole structures with a branch length of 375m and an angle of 15° between the branch and the main borehole, the effective drainage volumes all indicate a gradual increase over time, with the final effective drainage volumes converging. Conversely, the structures characterized by a branch and main hole angle of 20° and a branch length of 275m show noticeable fluctuations in effective drainage volume. Specifically, the structure featuring a branch opening

spacing of 70m and a branch number of 28 exhibits markedly higher effective drainage volume in comparison to the other two structures, demonstrating a slow but consistent growth trajectory.

Characteristics of gas extraction volume variation

After analyzing the calculation results of coal seam gas pressure and volume changes for each drainage plan, the cumulative gas production in the drainage area and the cumulative gas production per unit length of the borehole are further calculated and analyzed to optimize the optimal drainage plan. The figures depicting the cumulative gas production in the drainage area and the cumulative gas production per unit length of the borehole are shown in figure 6, respectively.

It is evident from the data presented in the figure that the cumulative gas production in the drainage area corresponds closely to variations in the effective drainage volume over time, suggesting that the effective drainage volume is a key factor influencing cumulative gas production. Figure 6 illustrates that drilling structures characterized by a branching angle of 10° and a branch length of 500m display a distinctive "S-shaped" curve pattern in cumulative gas production per unit length. This pattern indicates a gradual rise, followed by a phase of rapid growth, and ultimately a slowdown in the rate of increase. The extraction processes of Scheme 2-3 and 3-1 exhibit a similar early-stage increasing trend, with Scheme 2-3 eventually surpassing Scheme 3-1 in cumulative gas production per meter after 300 days of extraction. Both schemes then demonstrate a relatively uniform growth rate, culminating in reaching their respective maximum values sequentially. Meanwhile, the configurations of scheme 2-1 and 2-2 also follow a similar growth trajectory characterized by an initial gradual increase, a subsequent sharp surge, and a reduction in amplitude resembling a minor "S" shape. Despite having a lower curvature than the drilling structures with a

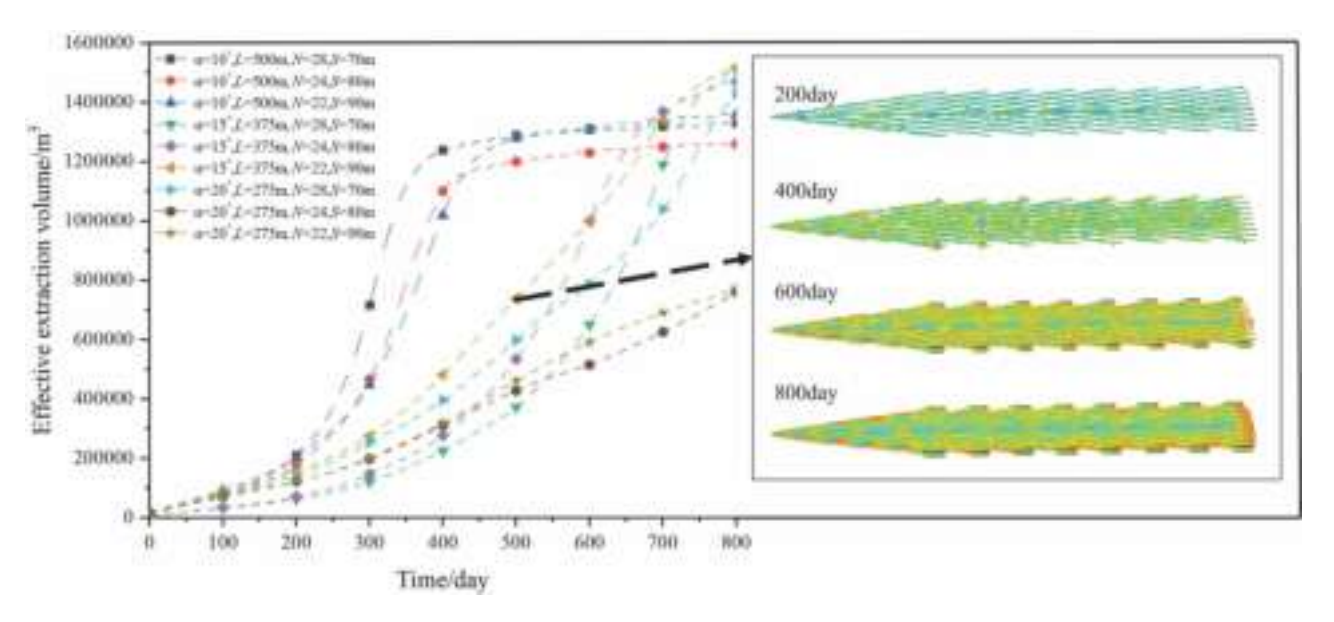


Fig. 5. Effective drainage volume change curve.

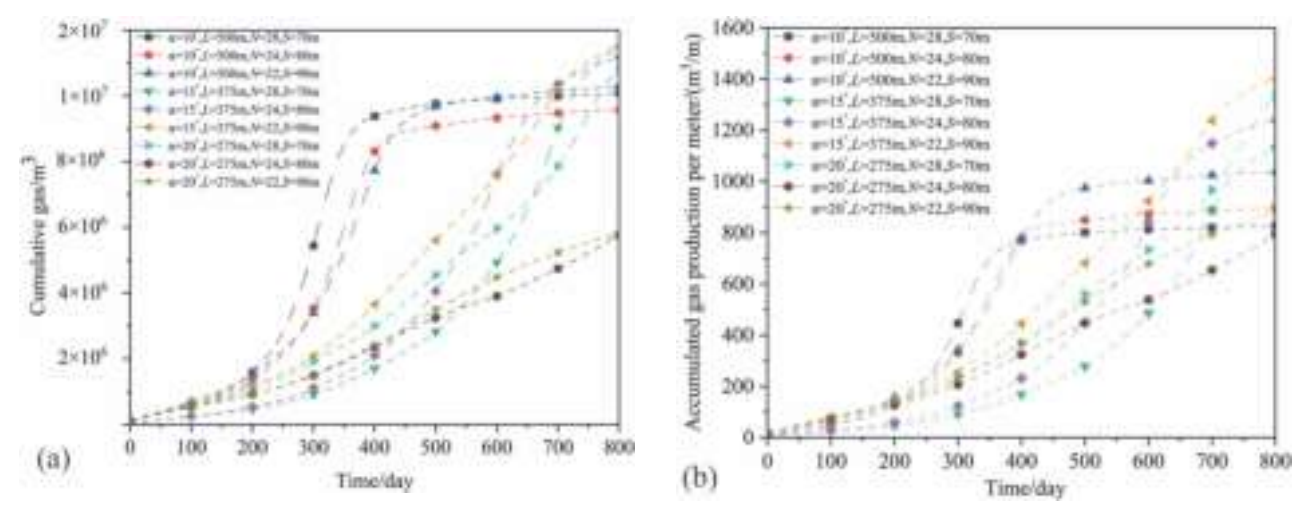


Fig. 6. Cumulative gas production in the drainage area and cumulative gas production per unit length of boreholes; (a) Cumulative gas production in the drainage area; (b) Cumulative gas production per unit length of boreholes in the drainage area.

branching angle of 10° and a branch length of 500m, the final cumulative gas production per meter of Scheme 2-1 and 2-2 surpasses that of the structures with a 10° branching angle. Conversely, for options 3-2 and 3-2, the changes in cumulative gas production per meter are similar to the changes in cumulative gas production and effective drainage volume, yielding less favorable outcomes.

DISCUSSION

The influence of branch angle and length on extraction effect

Changes in branch angles influence branch lengths, which ultimately impact the drainage effect. Branch angles and branch lengths are factors that cooperatively affect the drainage effect. According to figure 7, a spacing of 70m between branch boreholes results in higher gas production per

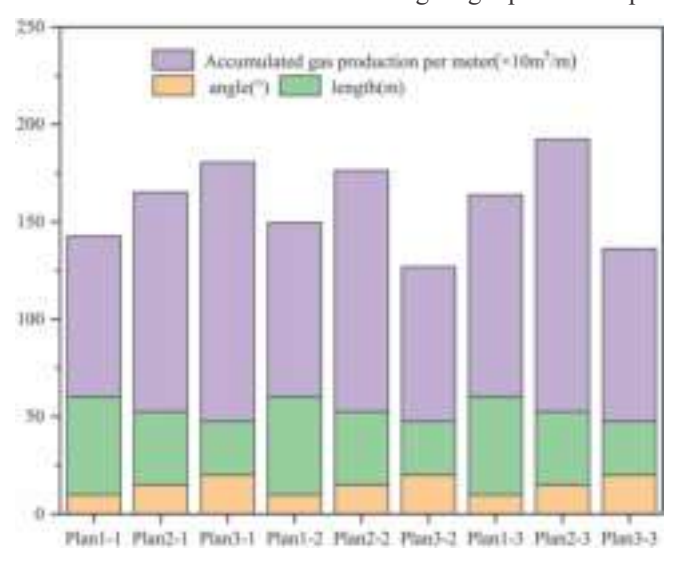


Fig. 7. Changes in cumulative gas production of three horizontal unit length boreholes when factors 3 and 4 are fixed; factor 3 is Number of branches; factor 4 is Branch spacing.

unit length of drilling with increased branching angles and decreased branch lengths. At this point, the spacing of the branch openings plays a dominant role, leading to a strong synergistic effect between them. An increase in branching angle promotes a higher gas production rate per unit length of drilling. However, limitations at coal seam boundaries result in a decrease in the length of branch drillings as the angle increases. When the branch opening distance exceeds 70m, the main influencing factors are the branch angle and branch length. The gas production per unit length of the lateral drilling increases as the branch angle increases. However, as the angle reaches a certain threshold, the cooperative interaction between adjacent lateral wells diminishes, resulting in a decline in gas production per unit length of the lateral wellbore.

When the spacing between branch openings is short, the branches are relatively close to each other. At this time, the influence of branch angle and length is lower than the impact caused by the spacing between small openings. Therefore, it may be possible to increase the branch angle further to expand the drainage area. However, this may also lead to a higher number of branches. On the other hand, when the spacing between branch openings is large, the dominant factors are the branch angle and length. Increasing the angle beyond a certain point has negative effects, causing a decline in gas production per unit length of the borehole. Thus, it is advisable to limit the increase in the branching angle and avoid excessively long branch lengths.

The impact of branch quantity and spacing on extraction efficiency

Figure 8 illustrates how alterations in branch opening spacing and the quantity of branches affect the outcome, assuming the branch angle and length remain constant. The branch angle and length are the main influencing factors when the branch angle is 15° or less, showing strong synergistic effects between branches. As the distance between branch openings widens, the number of branches decreases while the gas

production per meter increases. At this stage, the spacing between branch openings and the number of branches become secondary factors influencing the outcome. Increasing the branch angle and branch opening spacing appropriately can enhance the extraction effect, leading to reductions in branch length and branch number.

After analyzing the findings above, when the branch angle is small, the secondary influencing factors are the spacing between branch apertures and the number of branches. The spacing between branch openings has increased, leading to fewer branches and an enhanced drainage effect. However, this might lead to a constraint in the drainage area. Conversely, with a large branch angle, the primary influencing factors are the branch opening spacing and the number of branches. A wide branch opening spacing negatively impacts drainage efficiency. Therefore, decreasing the spacing between branch openings is essential for enhancing drainage effectiveness, it may lead to the issue of excessive branching.

Comprehensive impact assessment

Based on the above analysis, there exists an interactive relationship between the angle between the branch borehole and the main borehole, the length of the branch, the spacing between the branch openings, and the number of branches. When the branch boreholes have a small angle from the main borehole, they are situated closer to each other, resulting in a strong synergy between the drill holes. Consequently, a rapid decrease in a portion of the gas pressure in the coal seam to a very low level occurs in a short period, although its effective control range is limited. The spacing between branch openings and the number of branches is significant factors, albeit playing a secondary role. Increasing the spacing between branches can enhance the extraction effect while reducing the number of branches can lead to cost savings. Conversely, if the angle between the branch borehole and the main borehole is excessively large, the distance between branch openings and the number of branches becomes more influential. Failure to reduce the distance between branch openings hinders the formation of effective synergy among the drillings, resulting in limited effective control range and gas production. Consequently, for optimum pressure reduction effect, time efficiency, cost-effectiveness, effective range, and gas production, it is advisable to opt for a structure featuring a 15° angle between the branches and the main borehole, a branch length of 375m, 22 branches, and a branch opening spacing of 90m. The cumulative gas production corresponding to this configuration is displayed in figure 9. Analysis of the figure reveals a relatively gradual growth in cumulative gas production within the initial 300 days of extraction, with growth slowing down notably by the 650th day. By employing this scheme, extraction operations can be sustained until the 650th day.

CONCLUSION

According to the established mathematical representation model of gas discharge in multi-branch boreholes in ultrathick coal seams, it is concluded that:

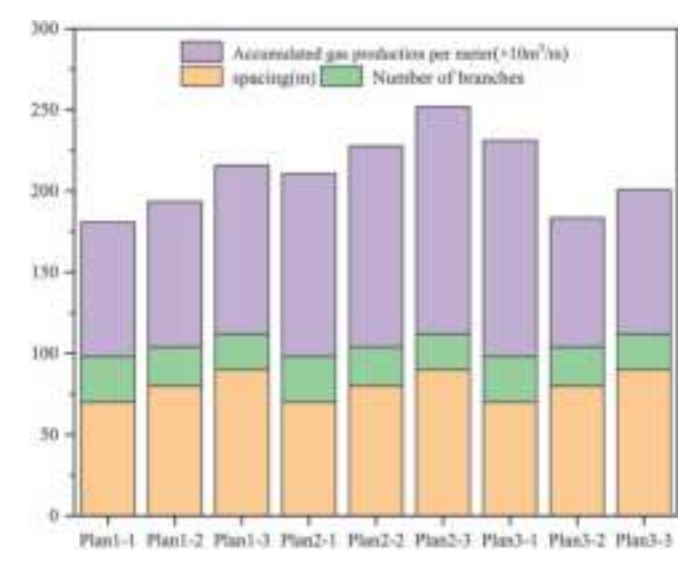


Fig. 8. Changes in cumulative gas production of three horizontal unit length boreholes when factors 1 and 2 are fixed; factor 1 is Angle; factor 2 is Branch length.

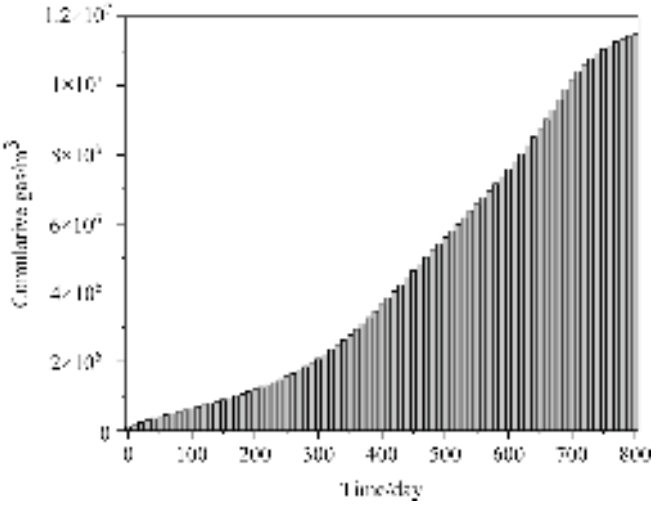


Fig. 9. Cumulative gas production change curve of the optimal scheme.

- As the drainage time increases, the coal seam gas pressure decreases nonlinearly. It will show a rapid downward trend in the early stage of drainage, and the rate of pressure decrease will also decrease as time goes by.
- 2) When the branch angle is small and both the branch angle and branch length remain constant, the opening spacing and the number of branches become secondary factors. Increasing the spacing between branch openings has the potential to enhance the cumulative gas production per unit length of boreholes and improve drainage effectiveness, although with a limited drainage range. Conversely, when the branch angle is large, the primary factors influencing outcomes are the branch opening spacing and the number of branches. A significant increase in the branch opening spacing could result in diminished drainage effectiveness. As a solution, a smaller branch opening spacing is necessary to achieve

- superior extraction results; however, this approach may lead to an issue of excessive branching.
- 3) When the number of branches and branch spacing is constant, and the branch spacing is small, the branching angle and branch length become less crucial factors in the analysis. Increasing the branching angle leads to a rise in the cumulative gas production per unit length of the drilled well, thereby enhancing extraction efficiency. Nevertheless, an issue of excessive branch numbers exists. Conversely, when the branch spacing is extensive, the main influencing factors are the branch angle and branch length. A substantial rise in the branch angle could detrimentally affect the drainage effect. Thus, it is essential to regulate the angle between the branch and the main hole to enhance the drainage effect at this juncture.
- Critical factors that influence the extraction effect include the angle between the branches and the main borehole, the length of the branches, the spacing between branch openings, and the number of branches. Among these factors, the angle and length exhibit a synergistic relationship, whereas spacing and number also demonstrate a synergistic interaction. Increasing the size of these four factors does not necessarily enhance the effectiveness of coal extraction. A small angle may lead to a narrow effective area and wasted synergistic effects between branches, while a large branch angle necessitates a smaller spacing to ensure that the branches can generate synergistic effects and achieve the objective of multibranch extraction. Accordingly, the optimal drilling plan for this model entails a 15° angle between the branch borehole and the main borehole, a branch length of 375m, a spacing between branch openings of 90m, 22 branches in total, and an extraction period of approximately 650

Nomenclature

 $V_{\rm I}$ Langmuir volume constant (m³/kg)

V_s Volume of adsorbed CH₄ in coal (m³/kg)

PCoal matrix CH₄pressure (MPa£'

P_LLangmuir pressure constant (MPa)

 m_1 The mass of adsorbed gas present in the pore system of coal per unit volume (kg/m³)

 ρ_a Apparent density of coal (kg/m³)

 ρ_s Gas density under standard conditions (kg/m³)

 P_m CH₄ gas pressure in coal matrix pores (MPa)

 $\rho_{\rm f}$ The density of gas in coal fractures under standard conditions (kg/m³)

 $m_{\rm f}$ Mass of free gas in coal fractures per unit volume (kg/m³)

 φ_f The fracture rate of coal (£¥)

M_c Molar mass of CH₄ molecule (kg/mol)

R Ideal gas constant $(J/(mol \cdot K))$

TCoal seam temperature (K)

 $P_{\rm f}$ CH₄ gas pressure in cracks (MPa)

 m_2 Mass of free gas in coal pores per unit volume (kg/m³)

 φ_{m} The porosity of coal (£¥)

 $Q_{\rm s}$ Mass exchange rate between unit volume coal matrix and

fracture system $(kg/(m^3 \cdot s))$

D Gas diffusion coefficient (m 2 /s)

 $\sigma_{\rm c}$ Coal matrix block shape factor (m⁻²)

 c_m CH₄ gas concentration in the matrix (kg/m³)

 $c_f \text{CH}_4$ gas concentration in fracture systems (kg/m³)

L Spacing between fractures (m)

 τ Adsorption time (s) VGas seepage velocity in cracks (m/s)

 $k_{\rm e}$ Effective gas permeability (m²)

u Methane viscosity (Pa·s)

Acknowledgements: This study was supported by the Knowledge Innovation Program of Wuhan-Shuguang Project (No. 2022010801020360), the Hubei Province technology innovation plan key research and development projects (No.2023BCB084), and the Graduate Education Innovation Foundation of Wuhan Institute of Technology (No. CX2023191). We are grateful to anonymous reviewers for their valuable comments on the manuscript.

References

- An, C., Wei, Z., Hua, G. 2019. Well-type optimization of naked-eye drilling multi-branch horizontal wells in coalbed methane reservoirs. *Fresenius environmental bulletin*, 28(12a), 10234-10241.
- Chen, S., Tang, D., Tao, S., Xu, H., Li, S., Zhao, J., Ren, P., Fu, H. 2017. In-situ stress measurements and stress distribution characteristics of coal reservoirs in major coalfields in China: Implication for coalbed methane (CBM) development. *International Journal of Coal Geology*, 182, 66-84.
- Duan, N., Gong, Z., Wang, H., Wang, Z., Lv, L., Huang, Q., Xu, Z. 2012. Application of Multi-Branch Horizontal Well Technology in CBM Drilling. Paper presented at the *IADC/SPE Asia Pacific Drilling Technology Conference and Exhibition*, Tianjin, China. https://doi.org/10.2118/156187-MS
- Fan, Y., Deng, C., Zhang, X., Li, F., Wang, X. 2018. Numerical study of multibranch horizontal well coalbed methane extraction. *Energy Sources, Part A: Recovery, Utilization, and Environmental Effects*, **40**(11), 1342-1350.
- Fan, N., Wang, J., Deng, C., Mu, Y., Fan, Y. 2022. Coalbed methane extraction in multibranch horizontal wells: evolutions of reservoir characteristics with different geometric parameters. *Energy Sources, Part A: Recovery, Utilization, and Environmental Effects*, **44**(1), 1375-1390.
- Gong, D., Chen, J., Cheng, C., Kou, Y. 2024. Factors influencing fracture propagation in collaborative fracturing of multiple horizontal wells. *Energy Engineering*, 121(2). https://doi.org/10.32604/ee.2023.030196
- Hu, G., Xu, J., Ren, T., Gu, C., Qin, W., Wang, Z. 2015. Adjacent seam pressure-relief gas drainage technique based on ground movement for initial mining phase of longwall face. *International Journal of Rock Mechanics and Mining Sciences*, 77, 237-245.
- Huang, D., Yang, J., Yu, H., Li, W. 2019. Study on production decline law of multilateral horizontal well in coalbed methane reservoirs. in *IOP Conference Series: Earth and Environmental Science*. 2019. IOP Publishing. https://doi.org/10.1088/1755-1315/300/2/022088
- He, J. 2023. Numerical simulation of a class I gas hydrate reservoir depressurized by a fishbone well. *Processes*, 11(3), 771. https://doi.org/10.3390/pr11030771
- Jiang, T., Yang, X., Yan, X., Ding, Y., Wang, X., Yang, H., Wang, T. 2013. Influences of branch parameters on productivity of CBM pinnate horizontal well. *Journal of China Coal Society*, 38(4), 617-623.
- Jiang, Y., Huang, L., Tang, H., Lv, D. 2016. Parameters optimization of multibranch well for low permeability gas reservoir. *Electronic Journal of Geotechnical Engineering*, 21(3).
- Keim, S.A., Luxbacher, K.D., Karmis, M. 2011. A numerical study on optimization of multilateral horizontal wellbore patterns for coalbed methane production in Southern Shanxi Province, China. *International Journal of Coal Geology*, 86(4), 306-317.
- Li, S. 2019. Research on determination method of gas drainage radius based on elastoplastic softening model. In: IOP Conference Series: Earth and Environmental Science, 384. https://doi.org/10.1088/1755-1315/384/1/012118

- Mu, Y., Fan, N., Wang, J., 2021. CBM recovery technology characterized by docking ground multi-branch horizontal wells with underground boreholes. *Energy Sources, Part A: Recovery, Utilization, and Environmental Effects*, 43(6), 645-659.
- Ren, J., Zhang, L., Ren, S., Lin, J., Meng, S., Ren, G., Gentzis, T. 2014. Multi-branched horizontal wells for coalbed methane production: Field performance and well structure analysis. *International Journal of Coal Geology*, 131, 52-64.
- Ran, X., Zhang, B., Wei, W., Yu, H., Liang, W., Wei, K. 2021. Reservoir protection and well completion technology for multi-branch horizontal wells in coalbed methane. *Arabian Journal of Geosciences*, 14(9), 802.
- Shi, J., Fang, Y., Wu, J., Sun, Z., Tang, J., Li, Q., Chen, Z., Lu, J., Ke, W., Jia, Y., Wang, Y. 2020. Productivity Evaluation of radial multi-branch horizontal well in unconventional gas reservoirs considering permeability variation: model establishment and sensitivity analyses. *In international petroleum technology conference*. https://doi.org/10.2523/JPTC-19955-MS
- Wang, H., Cheng, Y., Wang, L. 2012. Regional gas drainage techniques in Chinese coal mines. *International Journal of Mining Science and Technology*, 22(6), 873-878.
- Wang, H., Guo, J., Zhang, L. 2017. A semi-analytical model for multilateral horizontal wells in low-permeability naturally fractured reservoirs. *Journal of Petroleum Science and Engineering*, 149, 564-578.

- Wang, C., Jia, C., Peng, X., Zhu, S., Liu, F. 2020. A new well structure and methane recovery enhancement method in two coal seams. *Energy Sources, Part a: Recovery, Utilization and Environmental Effects*, 42(16), 1977-1988.
- Yang, Y., Cui, S., Ni, Y., Zhang, G., Li, L., Meng, Z. 2016. Key technology for treating slack coal blockage in CBM recovery: A case study from multilateral horizontal wells in the Qinshui Basin. *Natural Gas Industry*, B 3(1), 66-70.
- Yang, R., Huang, Z., Hong, C., Sepehrnoori, K., Wen, H. 2019. Modeling fishbones in coalbed methane reservoirs using a hybrid model formulation: Gas/water production performance in various lateral-cleatnetwork geometries. *Fuel*, 244, 592-612.
- Zhou, S. 1999. Theory of coalbed methane flow and occurrence. Beijing. *Coal Industry Press* in China.
- Zhu, Q., Yang, Y., Chen, L., Wang, Y., Chen, B., Liu, C., Zhang, C., Wang, X. 2019. Exploration and practice of methane-leading reservoir stimulation technology of high-rank coalbed methane. *In international petroleum* technology conference. https://doi.org/10.2523/IPTC-19229-MS
- Zhang, Y., Zou, Q., Guo, L. 2020. Air-leakage model and sealing technique with sealing-isolation integration for gas-drainage boreholes in coal mines. *Process Safety and Environmental Protection*, 140, 258-272.
- Zhang, P., Tian, S., Zhang, Y., Li, G., Zhang, W., Khan, W.A., Ma, L. 2021.
 Numerical simulation of gas recovery from natural gas hydrate using multi-branch wells: A three-dimensional model. *Energy*, 220, 119549.

Partial transformation of coesite to quartz in eclogitic garnets of the Tso Morari complex, Ladakh, NW Himalayas: Insights from Raman mapping

MALLIKA K. JONNALAGADDA^{1,*}, NITIN. R. KARMALKAR^{1,2}, RAYMOND A. DURAISWAMI²

¹Interdisciplinary School of Science, Savitribai Phule Pune University, Pune - 411007, India ²Department of Environmental Science, Savitribai Phule Pune University, Pune - 411007, India *Email (Corresponding author): jmallika@gmail.com; mallika.jonnalagadda@unipune.ac.in

Abstract: The coesite bearing Tso Morari eclogites are one of the only Ultra High Pressure (UHP) complexes identified in the Indian Himalayas representing the leading edge of the subducted Indian continental plate to mantle depths before being exhumed back. Raman microspectrometric analyses in mapping mode on silica inclusions within garnets were carried out to identify and record coesite-quartz transformation. Quartz inclusions in garnets are sub-rounded to elliptical and occur as single crystals as well as polycrystalline aggregates. Coesite with α -quartz (peak 464 cm⁻¹) is recognized optically and confirmed through Raman spectroscopy (peak at 521 cm⁻¹). Partial to complete transformation of coesite to α -quartz are recorded through Raman analyses in mapping mode; 95 volume% to as low as 1volume% respectively. Combination of petrographic, mineral chemistry, Raman mapping data along with prior experimental work clearly point to near complete transformation of α -quartz to coesite between temperatures 700-800 °C at 2.8 GPa pressures. Retrograde reactions of coesite to α -quartz can be envisaged between 600 – 700 °C. Experimental as well as studies carried out on natural samples clearly point to factors such as pressure vessel effect along with fast exhumation rates being instrumental in partial preservation of coesite in these eclogite samples.

Keywords: Coesite - quartz transformation, garnets, Raman mapping, Tso Morari Complex, Ladakh

INTRODUCTION

Presence of coesite (Coes 1953), the densest form of silica in metamorphic rocks, has been instrumental in changing prevailing ideas about the limits of metamorphism leading to a whole new concept of 'ultra-high pressure' metamorphic facies (e.g. Coleman & Wang 1995). Discovery of relict coesite and microdiamonds as inclusions in mineral phases like garnets and zircons are key indicators of subduction to UHP depths (>100 kms) (Chopin 1984; Smith 1984; Sobolev & Shatsky 1990; Chopin & Sobolev 1995, Burov et al. 2014). The Tso Morari crystalline complex in Ladakh, NW Himalayas, India is classic example of a continent – continent collision known to expose high pressure to ultra-high-pressure metamorphic rocks bearing coesite (Ernst & Liou 1999; Fig 1). Discovery of this high-pressure SiO₂ phase in metamorphic rocks encouraged scientists to undertake novel experiments to better constrain the thermodynamic and kinetic features of SiO₂ phase transitions and to model their natural occurrences (e.g. Chopin 1984; Gillet et al. 1984; Van Der Molen & Van Roermund 1986; Zinn et al. 1997a; Angel et al. 2001; Perrillat et al. 2003; Lathe et al. 2005; Mosenfelder et al. 2005; Guiraud & Powell 2006).

Several studies by earlier workers (e.g. Mosenfelder & Bohlen 1997; Perrillat *et al.* 2003; Mosenfelder *et al.* 2005; Guiraud & Powell 2006 and references therein) have helped understand SiO₂ phase transitions better by taking into consideration different factors such as rates of exhumation, cooling, retrograde reactions, fluid influx, deformation of the host rocks etc. Over the last two decades, several studies focussing on various parameters have been carried out on these coesite bearing eclogites and adjoining areas, adding to the wealth of information already available on UHP metamorphic and associated rocks (Berthelsen 1953; Guillot *et al.* 1997; Steck *et al.* 1998; Sachan *et al.* 1999; O'Brien &

Sachan 2000; Mukherjee et al. 2003; Sachan et al. 2004; Epard & Steck 2008; Konrad-Schmolke et al. 2008; Singh et al. 2013; St-Onge et al. 2013; Palin et al. 2014, 2017; Chatterjee & Jagoutz 2015; Wilke et al. 2015; Jonnalagadda et al. 2017 2019; Kumar et al. 2019; Sen et al. 2019; Bidgood et al. 2020; Imayama et al. 2023). Coesite inclusions in garnets from the Tso Morari eclogites were first reported by Sachan et al. (2004), redefining the minimum pressure attained by these rocks to at least 2.8 GPa. Sachan et al. (2004) presented characteristic Raman spectra of various quartz inclusions ranging from monomineralic quartz, bimineralic quartz+coesite and monomineralic coesite within garnet. Recent studies by Bidgood et al. (2020) used EBSD and misorientation analysis of matrix-scale palisade quartz in the Polokongka La granite to quantitatively define crystallographic characteristics of quartz transformation after coesite.

Given the above background information already available and studies undertaken in this area, the present study revisits the quartz/coesite inclusions in the Tso Morari eclogites providing a detailed study on seven monocrystalline silica inclusions within host garnet exhibiting characteristic quartz-coesite as well as coesite-quartz transitions. This has been identified optically and confirmed through Raman spectrometry in mapping mode. Through this contribution, we aim to highlight the efficacy of the Raman mapping technique as a robust tool to delineate and distinguish between the different silica phases and comment on patterns and extent of coesite – quartz transformation recorded during exhumation of the Indian continental crust and its subsequent implications on ultra-high-pressure metamorphism.

GEOLOGICAL SETTING AND SAMPLE DESCRIPTION

The coesite bearing eclogites form a part of the Tso Morari

Table 1. Representative Electron Probe Micro Analyses of porphyroblastic garnets in eclogites of the Tso Morari Complex.

Mineral	al Garnet				Garnet		Garnet		Garnet		
Domain	Outer Rim	Mid Rim	Inner Rim	Inner Rim	Outer Core	Core	Core	Rim	Rim	Rim	Rim
SiO ₂	39.17	38.93	38.45	38.91	38.95	38.24	38.33	39.12	38.78	38.19	38.23
TiO,	0.03	0.04	0.06	0.06	0.62	0.18	0.20	0.05	0.03	0.03	0.03
Al_2O_3	22.54	22.07	22.37	22.28	21.73	21.51	21.69	22.22	22.30	22.12	22.05
FeO	24.91	30.81	28.65	28.62	26.00	28.16	27.55	23.24	27.91	30.65	30.96
MnO	0.29	0.35	0.41	0.44	0.92	0.71	0.78	0.28	0.41	0.30	0.37
MgO	6.42	4.36	5.19	5.24	3.65	2.61	2.93	6.94	5.48	4.33	3.82
CaO	8.47	6.22	6.74	6.64	10.61	10.41	10.40	8.72	6.95	6.29	6.41
Na_2O	0.01	0.02	0.04	0.03	0.02	0.05	0.03	0.01	n.d.	0.03	0.01
K_2O	n.d.	n.d.	n.d.	n.d.	n.d.	n.d.	n.d.	n.d.	n.d.	n.d.	n.d.
Cr,O,	0.06	0.03	0.02	0.02	0.02	0.05	0.04	0.01	0.01	0.04	0.01
NiO	n.d.	0.01	n.d.	0.02	0.01	n.d.	0.03	n.d.	0.02	n.d.	n.d.
Total	101.9	102.8	101.9	102.2	102.5	101.9	101.98	100.6	101.8	101.9	101.8
Alm	51.80	65.45	60.24	60.77	55.28	59.23	57.98	49.11	58.86	64.92	66.34
Pyp	24.42	16.68	20.10	20.02	13.83	10.14	11.35	26.42	21.05	16.78	14.89
Grs	22.64	16.90	18.19	18.04	28.37	27.97	27.96	23.63	18.81	17.06	17.58
Spes	0.63	0.76	0.90	0.95	1.98	1.57	1.72	0.61	0.89	0.66	0.82

complex (TMC), situated in the Ladakh region, NW Himalayas (Fig. 1). The complex which has been studied extensively, is elongated; dome shaped and occurs as a doubly plunging anticline with a dip of 10° towards the NW with an overall thickness of less than 7 km (de Sigover et al. 2004). Detailed stratigraphic relations between the different lithostratigraphic units of the complex as well as petrographic descriptions of eclogite enclaves have been provided initially in de Sigoyer et al. (1997) and more recently by Jonnalagadda et al. (2017, 2019) and are summarized here for ready reference. Eclogites occur as boudins or lenses within the metasediments of the lower Puga and overlying Tanglang La Formations which form the core of the complex. The eclogites are marginally sheared, exhibit sharp contacts, concordant to discordant relationship with the host metasediments. The eclogites - are medium to coarse grained consisting of garnet, omphacite, phengite and amphibole, and accessories phases like epidote (mainly zoisite), quartz/coesite, rutile, zircon, sphene, magnetite and carbonates (Fig. 2A,B). Inclusions of Na-Ca amphibole, zoisite, rutile + magnetite within the garnet cores represent the pre-UHP stage resulting from metamorphism of a mafic protolith and constitute the first preserved prograde association of minerals. Garnets (0.5-1.5mm) are colorless to light pink, typically euhedral idiomorphic grains and contain numerous inclusions concentrated at the cores. Chemically, garnet porphyroblasts are almandine rich (Alm₅₇Grs+Adr₂₆Prp₁₆Sps₁) and display zoning from core to rim, with Ca and Mn rich cores and Mg rich rims indicative of garnet growth during prograde metamorphism (Table 1; Jonnalagadda et al. 2017). Matrix amphiboles and those rimming garnet boundaries are winchites whereas inclusions of bluish-green coloured amphiboles within the garnet cores are Na-Ca-amphiboles represented by ferro-kataphorite, kataphorite and taramite (Jonnalagadda et al. 2017).

Pale coloured omphacite and quartz/coesite are observed within the mantle region of the garnets, consistent to earlier reports by Sachan *et al.* (2004). Retrogressed eclogites exhibit varying degrees of amphibolite- and greenschist-facies retrogression represented by

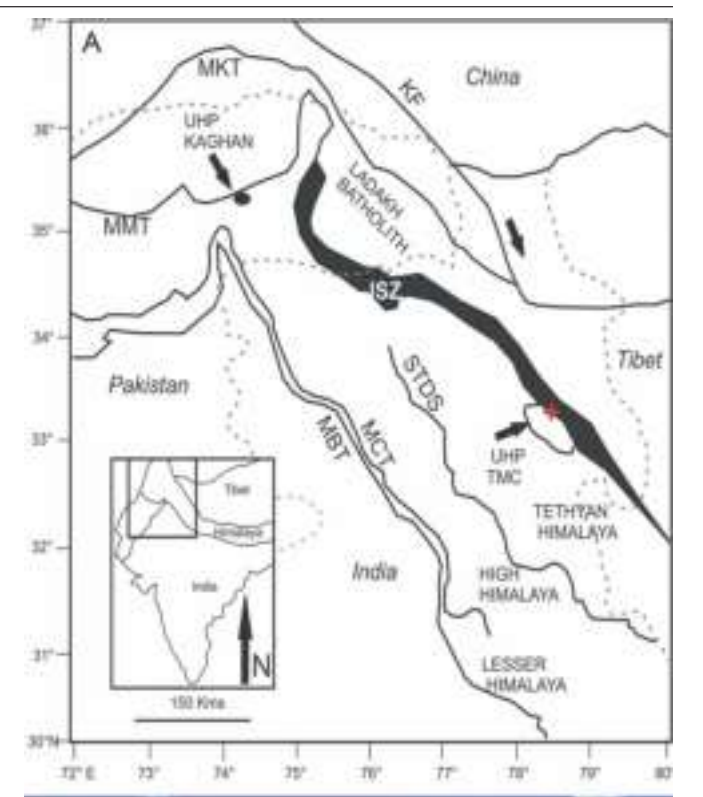




Fig. 1. A) Regional Geological map of the Himalayas showing different tectonic boundaries (after Yin 2006). The study area has been demarcated by a black box. B) Field photographs of eclogites boudins within the quartzo felspathic gneisses of the Puga Formation.

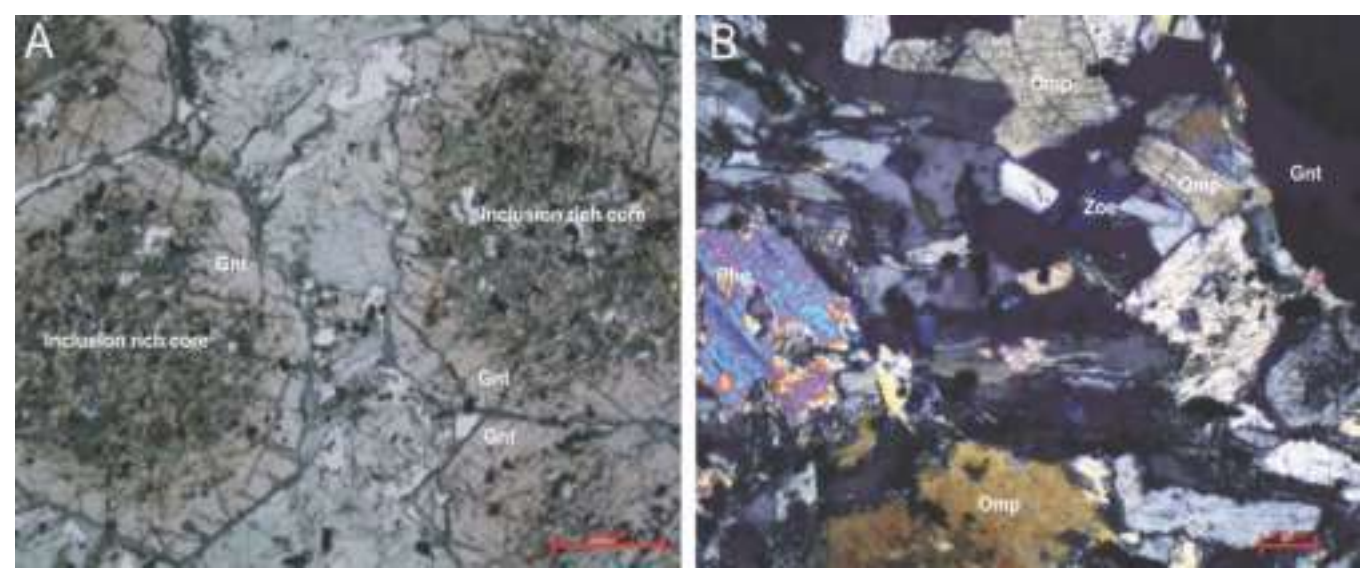


Fig. 2. A) Photomicrographs of the eclogites of the Tso Morari complex exhibiting euhedral, idiomorphic garnets along with other minerals. B) Close-up view of the eclogite sample showing presence of euhedral garnets along with omphacite, phengite and carbonate grains (BCN).

development of symplectitic association of Na poor clinopyroxene + plagioclase after omphacite, breakdown of phengite to biotite and aluminous calcic – amphiboles (e.g. pargasite) replacing the earlier, high pressure sodic- calcic or sodic amphiboles.

Quartz inclusions in garnets are sub-rounded to elliptical and occur as single crystals as well as polycrystalline aggregates. Coesite, being a high-pressure polymorph of SiO₂, can be optically recognised by characteristic features viz. 1) high refractive index, low birefringence 2) polycrystalline quartz pseudomorphs, 3) palisade quartz textures and 4) radial cracks patterns extending into the host mineral (Chopin 1984; Hirajima et al. 1990). In the present sample, coesite/quartz grains are lensied to elliptical in shape, 0.2–0.4 mm in length, transparent and display a strong anisotropic halo around them. Some grains are subhedral and display truncated boundaries. Majority of the grains contain a central core of fine-grained polycrystalline quartz with a radial rim of palisade quartz texture typical of coesite - quartz transition. Fractures radiating from the margins of the inclusions into the host garnet are commonly observed. The fractures are concentrated at the corners rather than starting from the long edges of the grains. Many of the cracks are relatively short and terminate before reaching the edge of the host garnets, whereas another set of more extensive cracks cut through the whole rock and appear independent of the cracks around the inclusions (Fig. 3A). For other mineral inclusions within garnet, fracturing of the host garnet observed is negligible. The observed textural characteristics in the quartz inclusions are indicated to be features associated with decompression, often considered a diagnostic for identification of coesite (Chopin 1984).

ANALYTICAL TECHNIQUES

Raman Spectrometry

Preliminary characterization of quartz inclusions in garnet was performed using an optical microscope and subsequently confirmed by Raman microspectrometry. Raman micro spectrometry was carried out on the area of interest firstly using point analyses of both coesite and α -quartz (Fig. 3A, B), and subsequently in mapping mode using a Confocal RAMAN imaging system Alpha 300RAS microspectrometer (WITec GmbH, Ulm, Germany). A fiber coupled diode laser of 532 nm with maximum output power after single mode fiber coupling of 50 mW was used for data acquisition. The data was collected using a multimode fiber into an ultrahigh throughput lens-based spectrometer (UHTS300) with 300 mm focal length and two gratings 600 g/mm & 1800 g/mm, both blazed at 550 nm. The UHTS300 spectrometer is connected with a peltier CCD detector cooled down to -65°C with better than 90% QE in the visible excitation. Raman imaging was done using a Zeiss 10X; 0.25 NA, Zeiss 20X;0.5NA, Zeiss 50X;0.75NA and Zeiss 100X;0.9 NA air objective. Raman signal was collected in the spectral interval with a spectral interval of 200 - 3000 cm-1 with a spectral resolution of 4 cm-1. Several 20 x 20 mappings for exposed quartz inclusions in garnet with a total of 10,000 spectra were acquired using WiTec control software and analysed with the WiTec project plus software with an integration time of 15s per spectrum.

RESULTS

Optical recognition of coesite was done for most grains and confirmed through Raman spectroscopy. Characteristic Raman peaks of α -quartz were located at 464 cm-1 (at ambient pressure), with less intense peaks at 125, 207, 269, 824 cm-1. Coesite spectra are dominated by peaks at 205, 269, and the characteristic 521 cm-1 peak (at ambient pressure; Sharma *et al.* 1981; Boyer *et al.* 1985; Hemley *et al.* 1986). At times, in addition to the coesite peak at 521 cm-1, α -quartz peaks at 465 cm-1 and 206 cm-1 are noticed in the coesite spectra. Raman spectra of all inclusions are observed to lie close to the 1st order peak of Si probably indicating that in addition to coesite, optically undetectable quartz maybe present within the inclusions. Depth profiling from the surface

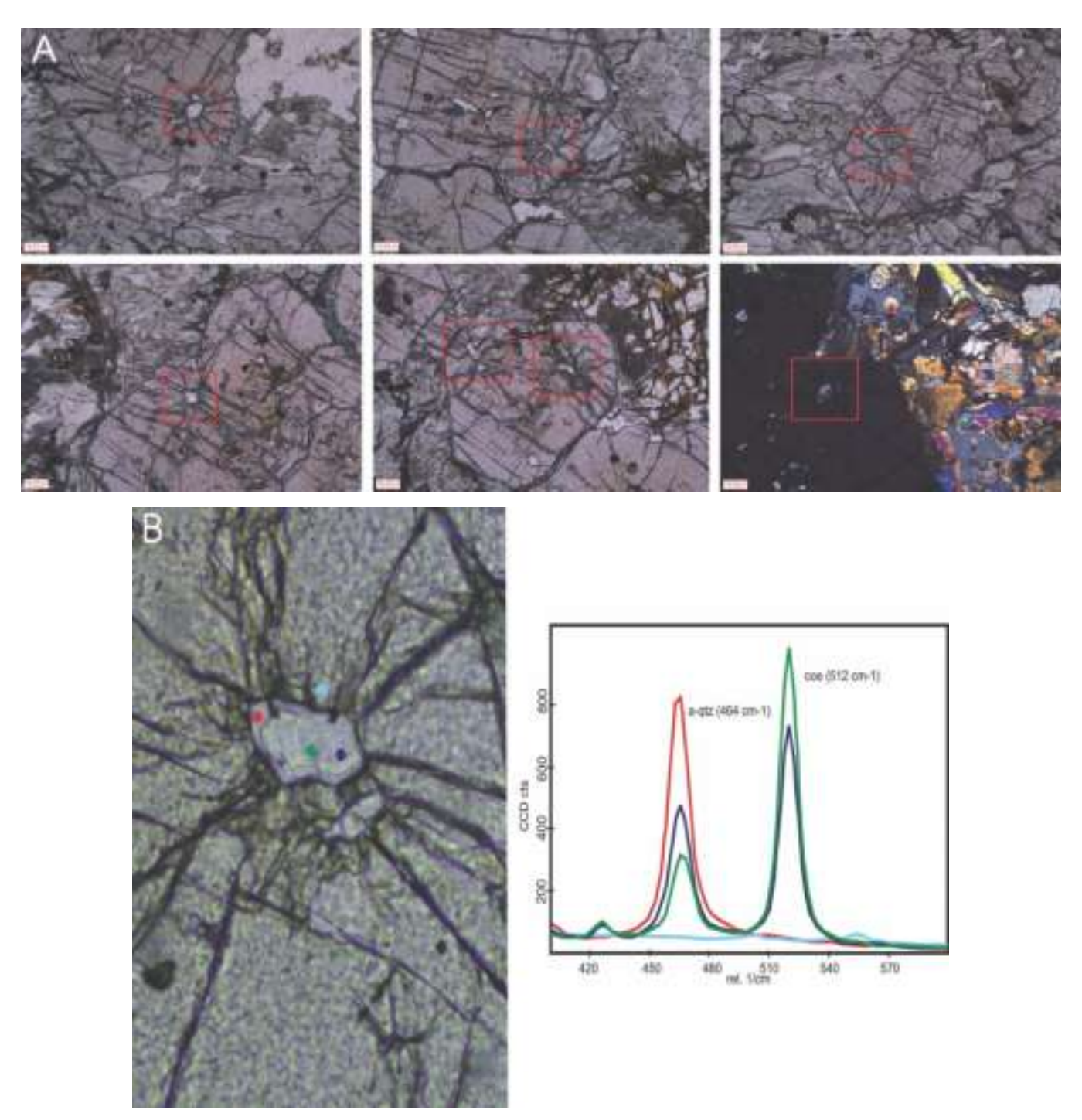


Fig. 3. A. Photomicrographs of coesite inclusions in host garnets B. Coesite inclusions exhibiting characteristic radial cracks extending into host garnets. Note the presence of thin rim of palisade quartz on the interior of the inclusion.

down through the sample could not be attempted, as the sample preserving the silica phases were prepared as a normal petrographic section glued with canada balsam, proving to be a major limitation for more detailed studies.

Raman analyses in mapping mode were carried out on 7 inclusions within the host garnet to observe silica phase distribution within the inclusions. Analysed grains display presence of both quartz phases i.e. coesite and α -quartz in

varying proportions (Fig. 4A-F). Images obtained during systematic Raman mapping across the inclusions clearly show presence of low-pressure alpha quartz occurring as rims with high-pressure coesite in the centre (Fig. 4B-F). This association of coesite being rimmed by α -quartz can be attributed to conversion of high-pressure quartz to its low-pressure phase during decompression upon exhumation. All grains are typically surrounded by a network of radial

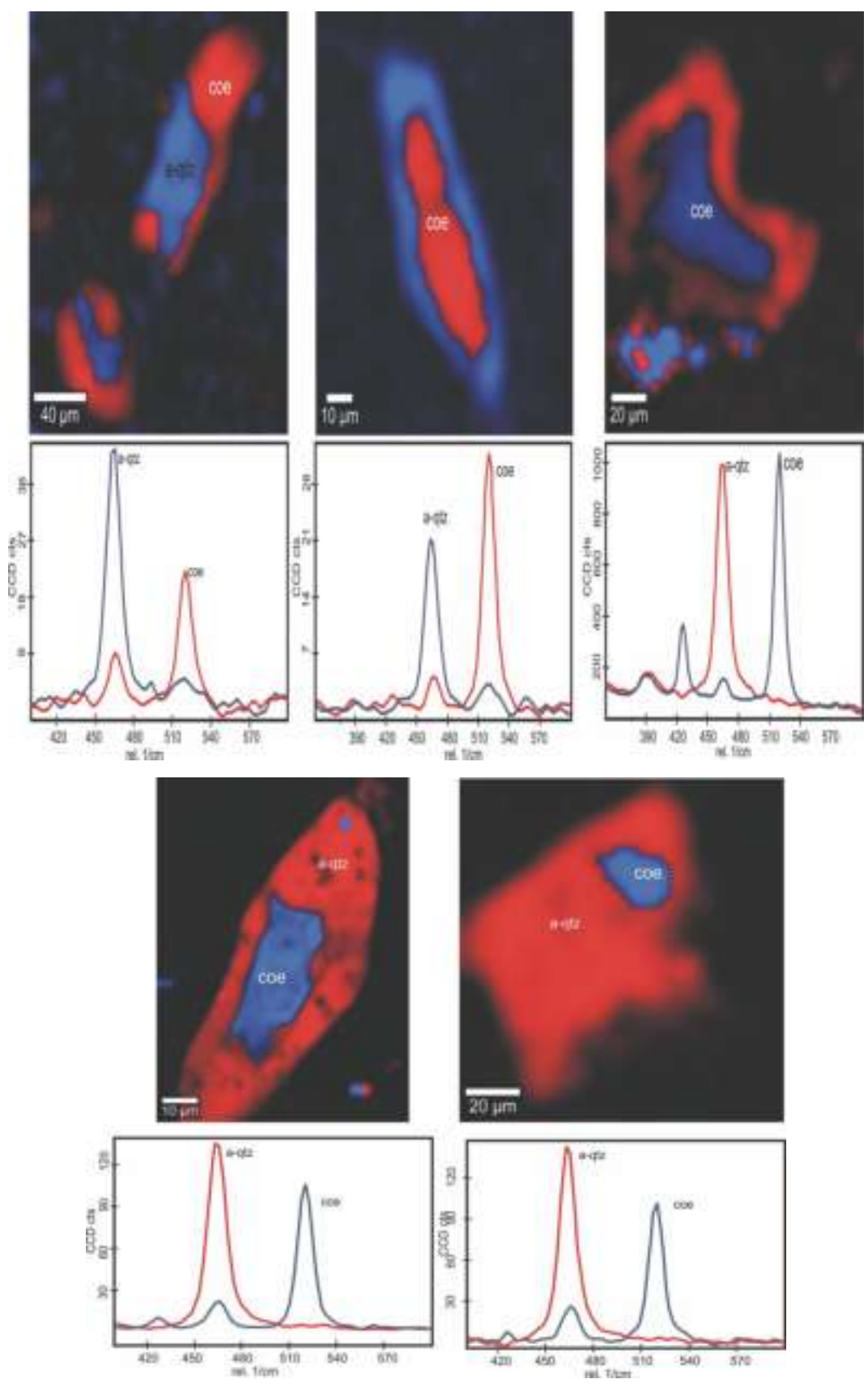


Fig. 4. Raman mapping images with characteristic Raman peaks of the silica inclusions showing the presence of coesite-quartz transformation.

fractures associated with volume expansion. Figure 4A depicts two grains, one rather rectangular in shape while the smaller one more rounded. Both these grains show the presence of coesite forming an envelope around the α -quartz. The coesite layer does not form a continuous envelope but is truncated at the boundaries allowing for α -quartz to be in direct contact with the host garnet. This peculiar situation where the α -quartz is observed in the inner part with the coesite located on the outside indicates transformation from a low pressure to high pressure commonly observed during prograde metamorphism. In order to quantify the volumetric proportions of polymorphs in the area of interest, a light statistical image processing software ImageJ 1.54f (Schneider et al. 2012) was employed. All images clearly show the varying proportions of coesite ranging from 95 volume % (Fig. 4C) to as low as 1 volume % (Fig. 4D) indicating partial to nearly complete transformation of coesite to α -quartz.

DISCUSSION

Raman spectroscopy has proved to be a robust tool providing direct information on molecular and crystal structure well suited to distinguishing polymorphs (Tuschel 2019). Identification of minute crystals in terrestrial as well as extraterrestrial materials and inclusions in optically transmissive host phases can be easily carried out by this method (e.g. Smith 1984; Wang et al. 1993; Gillet et al. 1994; Hochleitner et al. 2004; Zedgenizov et al. 2014). Although the use of Raman microspectroscopy has been instrumental in identification of coesite and /or diamond inclusions in host minerals thereby confirming evidence of Ultra high-pressure metamorphism (UHPM) (e.g. Boyer et al. 1985; Sobolev & Shatsky 1990; Tabata et al. 1998). Raman mapping is clearly a step ahead wherein not only identification of key UHP mineral phases but degree of phase transformation can be understood effectively without the need for elaborate experimental setups.

Coesite to α -Quartz transformation

Evidence of UHP metamorphism preserved in rocks sampled at or near the earth's surface yield important information about not only about peak P-T conditions but also about the possible nature of exhumation of the subducted crust from great depths. Coesite to quartz transformation can be effectively used to delineate the exhumation process that the subducted crust may have undergone. Experimental studies detailing the kinetic reactions involved in quartz - coesite phase transitions have been provided by several workers like Babich et al. (1989), Zinn et al. 1995; 1997a, 1997b; Mosenfelder & Bohlen (1997) and Perillat et al. (2003). Results of such experimental studies have helped understand the relative influence of nucleation and growth during formation of silica phases and at times can be extrapolated to natural samples, provided the temperature range investigated in both setups is uniform. Experiments carried out by Perillat et al. (2003) indicate transformation of α-quartz to coesite and vice-versa to occur at different temperatures and pressures across variable degrees. Significant observations reported are that kinetics for prograde and retrograde reactions are different with prograde α-quartz-coesite transformation occurring more or less one

order magnitude faster than coesite- α -quartz transformations. In the present study, Raman mapping data together with earlier generated geothermometric calculations carried out on coexisting stable mineral pairs (detailed in Jonnalagadda *et al.* 2019) have been compared with experimental work of Perillat *et al.* (2003) to comment on coesite-quartz transitions.

Petrographically, distinct textural features detailing progressive stages of coesite to quartz transformation have been provided by Gillet *et al.* (1984) and Wain *et al.* (2000) and are summarized here. At the beginning of re-equilibration (Stage 1), coesite is surrounded by a thin rim of polycrystalline quartz with radial extensions (palisade texture). This texture is believed to form prior to decompression and exhumation of the host rock. Stage 2 is represented by more diffused quartz, usually related to large radial fractures in host garnet on further re-equilibration. Continued recovery produces polycrystalline quartz aggregates forming a mosaic texture (Stage 3). The size of quartz grains may progressively increase forming monocrystalline inclusions (Stage 4).

Optically, the Tso Morari eclogites display micro textures similar to those described above indicating that texturally coesite to quartz transformation corresponding to all 4 stages are present in the studied samples (Fig. 3). Moreover, petrography and mineral chemistry of the whole garnets within the eclogites reveal that the garnets are compositionally heterogenous with Ca - Mn rich cores and Mg rich rims (Jonnalagadda et al. 2017 and references therein) indicating early nucleation and garnet growth during subduction. The first preserved prograde association of minerals found as inclusions in garnet cores (Na-Ca amphibole, zoisite, rutitemagnetite) are formed due to metamorphism of a mafic protolith and represent the pre-UHP stage. Inclusions of omphacite and coesite within garnet outer rims (with high Mg) defines the UHP stage. Temperatures constrained using coexisting stable mineral assemblages for the whole garnets from the Tso Morari eclogites reveal peak temperatures of 768 °C at pressures of 2.65 GPa (see Jonnalagadda et al. 2017 for details). The P-T data calculated on the present natural samples along with Raman mapping images from this study correspond well with earlier experimental data exhibiting near complete transformation of α-quartz to coesite between temperatures 700-800 °C at 2.8 GPa pressures (see Table 1 in Perillat et al. 2003).

Retrograde reactions of coesite to α-quartz transform over a range of non-uniform pressures from 2.9 GPa to 2.2 GPa and temperatures from 1010°C to 600 °C respectively with variable degrees between 90% at 700 °C to complete transformation at 600°C according to Perillat *et al.* (2003). Temperatures of 614-675 °C were constrained for garnet interiors using co-existing stable mineral assemblages of phengite+garnet rims for the present samples (Jonnalagadda *et al.* 2017). The presence of main quartz band (464cm-1) in coesite inclusions, (Boyer *et al.* 1985) can be used to conclude that a thin sub-micron envelope of quartz could be present around coesite inclusions, tracing the initial stage of coesite-quartz transformation (Korsakov *et al.* 2007). At the above

calculated temperatures, partial transformation of coesite to α -quartz is envisaged as relict coesite inclusions with well-developed radiating fractures in the garnet rims are preserved due to the volume increase during exhumation. Furthermore, Raman mapping of these studied inclusions are consistent with the above observations and show partial transformation of coesite to α -quartz. All the above observations clearly show that coesite undergoes partial transformation to α -quartz between 600 – 700 °C confirmed by textural studies and Raman mapping consistent with experimental studies carried out by previous workers (Perillat *et al.* 2003)

Implications for UHP metamorphism

Coesite, a key polymorph of silica used to identify Ultra highpressure metamorphism of the subducting crust is known to occur as inclusions in various host minerals like garnet, pyroxene, kyanite, titanite, zircon, rutile and diamond etc. with differing structural and elastic properties. Chopin (1984) identified four major factors imperative for the survival of coesite viz. pressure vessel effect, reaction kinetics, exhumation rates as well as low fluid infiltration rates during exhumation (e.g., Hacker & Peacock 1995). Inclusions in strong, rigid and robust host minerals like garnet and zircon is necessary for survival of coesite as the host mineral can exert an overpressure on the inclusion during exhumation. Raman spectroscopy and synchrotron XRD data clearly show that internal pressures as high as 3.6 GPa being exerted on coesite crystals in diamond (Parkinson & Katayama 1999; Sobolev et al. 2000). High bulk modulus for host minerals (K0 = 150 GPafor pyrope and 227 GPa for zircon) should ideally increase the pressure vessel effect allowing the inclusion to reach the coesite-quartz equilibrium at lower temperatures (Perillat et al. 2003). Most experimental studies undertaken to explain the pressure-vessel effect are carried out on coesite inclusions within pyrope garnet or zircon, however the Tso Morari eclogites have coesite inclusions within spessartinealmandine rich garnets, low in pyrope-grossular contents (Perillat et al. 2003; Mosenfelder et al. 2005). Garnet with differing compositions may result in changing rheological properties of the host mineral which may affect the extent of coesite-quartz transformation. Earlier studies by Korsakov et al. (2007) show that although rheological properties of zircon and garnet are contrasting, the values of overpressure for coesite inclusions from the same sample remain the same. In the present samples, the maximum Raman shift of the main coesite band (521 cm⁻¹ at ambient pressure) does not exceed 521 cm⁻¹, with the maximum Raman shift of the main quartz band (464 cm⁻¹ at ambient pressure) located at 465-467 cm⁻¹. Pressures calculated using calibration equations for coesite (P(GPa) = (v-521)/2.9; Hemley 1987) and quartz (P(GPa) =(v-464)/9; Schmidt and Ziemann, 2000) show a maximum of overpressure values that remain constant at 2.2-2.9 GPa (521cm⁻¹) between temperatures of 600-700 °C. It is important to note here that calculation of overpressure values may be affected by the lattice-preferred orientation of quartz subgrains within the quartz shell indicating a crystallographic control on the coesite-quartz transformations (Langenhorst & Poirier 2002). The preferred orientation may affect the Raman

shift and the calibration of [Hemley 1986 and Schmidt & Ziemann 2000] can than hardly be applied for pressure estimates. Taking into consideration the above observations:, the results derived on natural samples are consistent with experimental work of Perillat *et al.* (2003) which show that pressure vessel effect plays a critical role in coesite-quartz transformation above temperatures of 400 °C with reaction kinetics acting as the controlling factor at lower temperatures.

CONCLUSIONS

- UHP eclogites of the Tso Morari complex preserve silica inclusions that are identified optically and confirmed through Raman spectroscopy in mapping mode as coesite.
- Raman mapping clearly show presence of low-pressure α -quartz occurring as rims with high-pressure coesite in the centre. Image Analyses (Schneider *et al.* 2012) reveals that coesite is present in varying proportions ranging from 53 volume% to as low as 1volume% indicating nearly complete transformation to α -quartz.
- P-T data calculated on the Tso Morari eclogites (Jonnalagadda *et al.* 2017) along with Raman mapping from this study, show near complete transformation of α-quartz to coesite between temperatures 700-800 °C at 2.8 GPa pressures and coesite partially transforming to α-quartz between 600 700 °C. The above results derived on natural samples are consistent with experimental work carried out by previous workers (Perrillat *et al.* 2003; Mosenfelder *et al.* 2005) indicating that factors like pressure vessel effect along with high exhumation rates play a critical role in coesite-quartz transformation well above temperatures of 400 °C.

Acknowledgements: The authors acknowledge the support of the HOD, IDSS for providing the necessary facilities. This work was carried out during the tenure of the SERB POWER GRANT (SPG/2020/000453) project awarded to MKJ and MoES project (MoES/P.O. (Geo)/101(h)/2015) awarded to NRK and RAD.

References

- Angel, R. J., Mosenfelder, J. L., Shaw, C. S. J. 2001. Anomalous compression and equation of state of coesite. *Physics of the Earth and Planetary Interiors*, 124, 71–79.
- Babich, Y. V., Doroshev, A.M., Malinovsky, I.Y. 1989. Thermally activated transformation of coesite. *Geologiya I Geofizika*, **2**, 140-144.
- Berthelsen, A. 1953. On the geology of the Rupshu District, NW Himalaya: A contribution to the problem of the Central Gneisses. *Meddelelser FraDansk Geologisk Forening (Kobenhavn)*, **12**, 351–414.
- Bidgood, A., Parsons, A. J., Lloyd, G. E., Waters., D. J., Goddard, R. M. 2020. EBSD-based criteria for coesite-quartz transition. *Journal of Metamorphic Petrology*, 39, 165-180.
- Boyer, H., Smith, D., Chopin, C., Lasnier, B. 1985. Raman microprobe determination of natural and synthetic coesite. *Physics and Chemistry of Minerals*, 12, 45–48.
- Burov, E., Francois, T., Yamato, P., Wolf, S. 2014. Mechanisms of continental subduction and exhumation of HP and UHP rocks. *Gondwana Research*, 25, 464–493.
- Chatterjee, N., Jagoutz, O. 2015. Exhumation of the UHP Tso Morari eclogite as a diapir rising through the mantle wedge. *Contributions to Mineralogy and Petrology*, **169**, 3.

- Chopin, C., Sobolev, N.V. 1995. Principal mineralogic indicators of UHP in crustal rocks. *In:* Coleman, R.G., Wang X. (eds.), *Ultrahigh Pressure* metamorphism. Cambridge University Press, New York, 131p.
- Chopin, C. 1984. Coesite and pure pyrope in high–grade blueschists of the western Alps: a first record and some consequences. *Contributions to Mineralogy and Petrology*, 86, 107–118.
- Coes, L. 1953. A new dense crystalline silica. Science, 118, 131-132.
- Coleman, R. G., Wang, X. 1995. Overview of the geology and tectonics of UHPM. In: Coleman, R.G., Wang X. (eds.), Ultrahigh Pressure metamorphism. Cambridge University Press, New York, 131p.
- de Sigoyer, J., Guillot, S., Dick, P. 2004. Exhumation of the ultra-highpressure Tso Morari unit in eastern Ladakh NW Himalayas: A case study. *Tectonics*, 23, 1–18.
- de Sigoyer, J., Guillot, S., Lardeaux, J. M., Mascle, G. 1997. Glaucophane bearing eclogites in the Tso Morari dome eastern Ladakh NW Himalaya. *European Journal of Mineralogy*, **9**, 1073–1083.
- Epard, J-L., Steck, A. 2008. Structural development of the Tso Morari ultrahigh pressure nappe of the Ladakh Himalaya. *Tectonophysics*, 451, 242–264
- Ernst, W.G., Liou, J.G. 1999. Overview of UHP metamorphism and tectonics in well-studied collisional orogens. *International Geology Review*, 41, 477-493
- Gillet, Ph., Ingrin, J., Chopin, C. 1984. Coesite in subducted continental crust: P-T history deduced from an elastic model. *Earth and Planetary Science Letters*, 70, 426–436.
- Guillot, S., Sigoyer, J. D., Lardeaux, J. 1997. Eclogitic metasediments from the Tso Morari area (Ladakh, Himalaya): Evidence for continental subduction during India-Asia convergence. *Contributions to Mineralogy and Petrology*, 128(2–3), 197–212.
- Guiraud, M., Powell, R. 2006. P-V-T relationships and mineral equilibria in inclusions in minerals. *Earth and Planetary Science Letters*, 244, 683–694.
- Hacker, B.R., Peacock S.M. 1995. Creation, preservation and exhumation of UHPM rocks. In: Coleman, R.G., Wang X. (eds.), Ultrahigh Pressure metamorphism. Cambridge University Press, New York, 131p.
- Hemley, R. J., Mao, H. K., Bell, P. M., Mysen, B. O. 1986. Raman spectroscopy of SiO₂ glass at high pressure. *Physical Review Letters*, **57**, 747–750.
- Hirajima, T., Ishiwatari, A., Cong, B., Zhang, R. Y., Banno, S., Nozaka, T. 1990. Coesite from Mengzhong eclogite at Donghai county, northeastern Jangsu province, China. Mineralogical Magazine, 54, 579–583.
- Hochleitner, R., Fehr, K. T., Simon, G., Pohl, J., Schmid bauer, E. 2004. Mineralogy and Fe Mossbauer spectroscopy of opaque phases in the Neuschwanstein EL6 chondrite. *Meteoritics and Planetary Science*, 39, 1643–1648.
- Imayama, T., Dutta, D., Yi, K. 2023. The origin of the ultrahigh-pressure Tso Morari complex, NW Himalaya: implication for early Paleozoic rifting. *Geological Magazine*, 160(11),1975-1982.
- Jonnalagadda, M.K., Karmalkar, N.R., Duraiswami, R.A. 2019. Geochemistry of eclogites of the Tso Morari complex, Ladakh, NW Himalayas: insights into trace element behavior during subduction and exhumation. Geoscience Frontiers, 10, 811-826.
- Jonnalagadda, M.K., Karmalkar, N.R., Duraiswami, R.A., Harshe, S., Gain, S., Griffin, W.L. 2017. Formation of atoll garnets in the UHP eclogites of the Tso Morari Complex, Ladakh, Himalaya. *Journal of Earth System Science*, 126, 1-23.
- Konrad-Schmolke, M., O Brien, P., Capitani, C., Carswell, D. 2008. Garnet growth at high- and ultra-high pressure conditions and the effect of element fractionation on mineral modes and composition. *Lithos*, 103, 309-332.
- Korsakov, A.V., Hutsebaut, D., Theunissen, K., Vandenabeele, P., Stepanov. 2007. Raman mapping of coesite inclusions in garnet from the Kokchetav Massif (Northern Kazakhstan). Spectrochimica Acta Part A, 68, 1046-1052.
- Kumar, S., Rawat, G., Damodharan, S. 2019. Dimensionality analysis of MT impedances of Tso Morari Dome: Implication for structural interpretation. *Himalayan Geology*, 40, 190-198.

- Langenhorst, F., Poirier, J.P. 2002. Transmission electron microscopy of coesite inclusions in the Dora Maira high-pressure metamorphic pyrope-quartzite. Earth and Planetary Science Letters, 203, 793-803.
- Lathe, C., Kock-Muller, M., Wirth, R. 2005. The influence of OH in coesite on the kinetics of the coesite–quartz phase transition. *American Mineralogist*, **90**, 779–789.
- Mosenfelder, J. L., Schertl, H. P., Smyth, J. R., Liou, J. G. 2005. Factors in the preservation of coesite: the importance of fluid infiltration. *American Mineralogist*, **90**, 779–789.
- Mosenfelder, J.L., Bohlen, S.R. 1997. Kinetics of the coesite to quartz transformation. *Earth and Planetary Science Letters*, **153**, 133-147.
- Mukherjee, B. K., Sachan, H, K., Ogasawaray, Y., Muko A., Yoshioka, N. 2003. Carbonate-bearing UHPM rocks from the Tso–Morari Region Ladakh India: Petrological implications. *International Geology Review*, 45, 49–69.
- O'Brien, P. J., Sachan, H. K. 2000. Di°@sion modelling in garnet from the Tso-Morari eclogite and implications for exhumation models. 15th HKT workshop, Chengdu China.
- Palin, R. M., St-Onge, M. R., Waters, D. J., Searle, M. P., Dyck, B. 2014. Phase equilibria modelling of retrograde amphibole and clinozoisite in mafic eclogite from the Tso Morari massif, northwest India: Constraining the P-T-M (H2O) conditions of exhumation. *Journal of Metamorphic Geology*, 32(7), 675–693.
- Palin, R. M., Reuber, G. S., White, R. W., Kaus, B. J., Weller, O. M. 2017. Subduction metamorphism in the Himalayan ultrahigh-pressure Tso Morari massif: An integrated geodynamic and petrological modelling approach. *Earth and Planetary Science Letters*, 467, 108–119.
- Parkinson, C.D., Katayama, I. 1999. Present day ultrahigh pressure conditions of coesite inclusions in zircon and garnet: evidence from laser Raman microspectroscopy. *Geology*, 27, 979-982.
- Perrillat, J.P., Daniel, I., Lardeaux, J.M., Cardon, H. 2003. Kinetics of the coesite -quartz transition: Application to the exhumation of ultra-high pressure rocks. *Journal of Petrology*, 44, 773-788.
- Sachan, H. K., Bodnar, R. J., Islam, R., Law, R. D. 1999. Exhumation history of eclogites from the Tso Morari crystalline complex in eastern Ladakh: Mineralogical and '@id inclusion constraints; *Journal of Geological Society of India*, 53, 181–190.
- Sachan, H. K., Mukherjee, B. K., Ogasawara, Y., Maruyama, S., Ishida, H., Muko, A., Yoshioka, N. 2004. Discovery of coesite from Indus Suture Zone (ISZ), Ladakh, India: Evidence for deep subduction. *European Journal of Mineralogy*, 16(2), 235–240.
- Schmidt, H., Ziemann, M.A. 2000. In-situ Raman spectroscopy of quartz: A pressure sensor for hydrothermal diamond-anvil cell experiments at elevated temperatures. American Mineralogist, 82, 1725-1734.
- Schneider, C.A., Rasband, W.S., Eliceiri, K.W. 2012. NIH Image to ImageJ: 25 years of Image analysis. *Nature Methods*, **9**, 671-675.
- Sen, K., Mukherjee, B., Manas, M., Sen, K., Mukherjee, S. 2019. Two-stage exhumation of Zildat Ophiolitic Melange rocks, NW Himalaya, India. *Himalayan Geology*, **40**, 182-189.
- Sharma, S. K., Mammone, J. F., Nicol, M. F. 1981. Raman investigation of ring configurations in vitreous silica. *Nature*, 292, 140–141.
- Singh, P., Saikia, A., Pant, N.R., Verma, P.K. 2013. Insights into the P-T evolution path of Tso Morari eclogites of the north-western Himalayas: constraints on the geodynamic evolution of the region. *Earth System Science*, **122**, 677-698.
- Smith, D.C. 1984. Coesite in clinopyroxene in the Caledonides and its implications for geodynamics. *Nature*, 310, 641-644.
- Sobolev, N. V., Fursenko, B. A., Goryainov, S.V., Shu, J., Hemley, R. J., Mao, H.-K., Boyd, F. R. 2000. Fossilized high pressure from the Earth's deep interior: The coesite-in-diamond barometer. *Proceedings of National Academy of Science*, 97(22), 11,875–11,879.
- Sobolev, N.V., Shatsky, V. S. 1990. Diamond inclusions in garnets from metamorphic rocks: a new environment for diamond formation. *Nature*, 343, 742-746.
- Steck, A., Epard, J. L., Vannay, J. C., Hunziker, J., Girard, M., Morard, A., Robyr, M. 1998 Geological transect across the Tso Morari and Spiti areas: The nappe structures of the Tethys Himalaya; Swiss Journal of Geoscience, 91, 103–122.

- St-Onge, M. R., Rayner, N., Palin, R. M., Searle, M. P., Waters, D. J. 2013. Integrated pressure – temperature – time constraints for the Tso Morari dome (Northwest India): Implications for the burial and exhumation path of UHP units in the western Himalaya. *Journal of Metamorphic Geology*, 31(5), 469–504.
- Tabata, H., Yamauchi, K., Maruyama, S. 1998. Tracing the extent of a UHP metamorphic Terrane: mineral-inclusion study of zircon in gneisses from the Dabie Shan. In: Hacker, B. R., Liou, J. G. (eds), When Continents Collide: Geodynamics and Geochemistry of Ultrahigh-Pressure Rocks, pp. 261–273. Kluwer Academic Publishers, Dordrecht, Boston, London.
- Tuschel, D. 2019. Raman Spectroscopy and Polymorphism. Spectroscopy, 34, 10-21.
- Van Der Molen, I., Van Roermund, H.L.M. 1986. The pressure path of solid inclusions in minerals: the retention of coesite inclusions during uplift. *Lithos*, 19, 317-324.
- Wain, A., Waters, D., Jephcoat, A. Olijyng, H., 2000. The high-pressure to ultrahigh-pressure eclogite transition in the western Gneiss Region, Norway. European Journal of Mineralogy, 12, 667–687.
- Wang, Q., Ishiwatari, A., Zhongyan, Z., Hirajima, T., Hiramitsu, N., Enami, M., Zhai, M., Li, J., Cong, B. 1993. Coesite bearing granulite retrograde from eclogite in Weihai, Eastern China. European Journal of Mineralogy, 5, 142-152.

- Wilke, F.D.H., O'Brien, P.J., Schmidt, A., Ziemann, M.A. 2015. Subduction, peak and multi-stage exhumation metamorphism: Traces from one coesite-bearing eclogite, Tso Morari, western Himalaya. *Lithos*, 231, 77-91.
- Yin, A. 2006. Cenozoic tectonic evolution of the Himalayan orogen as constrained by along-strike variation of structural geometry, exhumation history, and foreland sedimentation. Earth Science Reviews. 76, 1-131.
- Zedgenizov, D.A., Kagi, H., Shatsky, V.S., Ragozin, A.L. 2014. Local variations of carbon isotope composition in diamonds from São-Luis (Brazil): Evidence for heterogenous carbon reservoir in sublithospheric mantle. *Chemical Geology*, 363, 114-124.
- Zinn, P., Lauterjung, J., Hinze, E. 1995. Kinetic studies of the crystallization of coesite using synchrotron radiation. *Nuclear Instruments and Methods in Physics Research B*, **97**, 89-91.
- Zinn, P., Hinze, E., Lauterjung, J., Wirth, R. 1997a. Kinetic and microstructural studies of the quartz-coesite phase transition. *Physics and Chemistry of the Earth*, **22**, 105-111.
- Zinn, P., Lauterjung, J., Hinze, E., Wirth, R. 1997b. Kinetic and microstructural studies of the crystallization of coesite from quartz at high pressure. Zeitschrift fur Kristallographie, 212, 691-698.

Comparative analysis of Himalayan rivers and Central Indian Forebulge rivers: Insights from contrasting tectonic regimes

PARV KASANA*, VIMAL SINGH, TANYA

Department of Geology, University of Delhi, Chhatra Marg, Delhi – 110007, India *Email (Corresponding author): parvgeology@gmail.com

Abstract: The morphometric analysis of a river reveals any change in the tectonic/climatic regimes experienced by the region. These morphometric parameters can be utilized to assess the geodynamics of both tectonically active regions and relatively stable regions. In this study, we compare two such contrasting regions, the Himalaya and the central Indian forebulge, to understand how tectonic forces shape the landscapes differently in these two regions. The Himalayas are continuously uplifting due to the northward movement of the Indian plate, and as a result the Indian plate has flexured due to loading of the Himalayas and given rise to the central Indian forebulge. This central Indian forebulge undergoes slow uplift and migration as the Himalayan Mountain front advances. Therefore, the rivers flowing through the Himalayan region experience high rates of uplift, whereas the forebulge rivers experience a very slow uplift rate. In this study, we measure and compare the basin morphometric parameters, such as the normalized steepness index (Ksn), precipitation-weighed normalized steepness index (KsnQ), concavity, hypsometric integral (HI), and basin gradient, with the existing erosion rates. We find that the rivers in the Himalayas show a higher steepness index, local relief, and erosion rates, suggesting a dominance of active tectonics. Conversely, the forebulge rivers show a low steepness index, erosion rates, and moderate HI values, suggesting an equilibrium between erosion and uplift. Comparisons reveal that the primary control on the evolution of rivers in both regions is tectonics, with climate playing a secondary role.

Keywords: Himalaya, central Indian forebulge, Normalized steepness index (Ksn), Concavity, Himalayan rivers

INTRODUCTION

The collision of Indian and Eurasian plates has resulted in the formation of one of the highest and most tectonically active mountain belts in the world, the Himalayas. The subduction of the Indian plate beneath the Eurasian plate also resulted in the flexural uplift of Indian plate, parallel to the Himalayan orogeny; this uplifted area has been termed as the central indian forebulge (CIF), and the topographic expression of it is manifested in the form of the central Indian plateau (Bilham *et al.* 2003; Bilham 2004). The subduction of the Indian plate also led to the development of a foredeep region that is filled by the sediments deposited by the rivers originating both from the Himalayas and the central Indian forebulge. This provides a unique setting of the rivers originating in rapidly uplifting areas (i.e., the Himalayas) and slowly uplifting areas.

The longitudinal profile of a river is its life story, written on its slopes. It reveals information about the erosion, sediment transport, and depositional processes. It is influenced by the tectonic and climatic processes (Gilbert 1877; Kirby & Whipple 2001; Whipple 2004; Wobus *et al.* 2006; Whittaker 2012; Adams et al. 2020). It is for this reason they have remained one of the most studied topics in fluvial geomorphology (e.g., Gilbert 1877; Hack 1973; Merritts et al. 1994; Keller & Pinter 1996; Sklar & Dietrich 1998; Leopold et al. 2020; Goren et al. 2022; Khan et al. 2021). Several morphometric indices, such as Ksn, concavity, chi, Stream-Length gradient index, etc., have been developed based on the longitudinal profile of a river. The longitudinal profiles of the Himalayan rivers have always remained an important topic of research because they reveal significant insights into how tectonics and climatic processes influence these rivers (e.g., Seeber & Gornitz 1983; Sonam & Jain 2018). In contrast, the longitudinal profiles of rivers in the central and peninsular India are less investigated. However, it has been established

that in a slow/quiescent tectonic setting (such as the cratons and their interiors), the topographic metrics (viz., slope, relief, normalized steepness index, and river profile) can indicate the bedrock erodibility, climate variability, and isostatic adjustments (Jansen *et al.* 2010; Gallen 2018; Peifer *et al.* 2021; Zondervan *et al.* 2020).

The Himalayas and central Indian forebulge regions are two contrasting regions that experience different types of geodynamic and geomorphic processes (Fig. 1). The Himalayas are characterized by compressional tectonics, with active thrust faulting resulting in the formation of high-relief topography, steep gradients, deep valleys, and high-altitude terrain (Thakur 1987; Yin 2006; Owen 2014); in contrast, the CIF experiences extensional tectonics, related to the flexural uplift of the Indian plate resulting in the formation of extensional faults (Agarwal et al. 2002; DeCelles & DeCelles 2001; DeCelles 2011). In general, the forebulge regions experience slow uplift rates and have geomorphic features like escarpments, canyons, and low-relief plateau regions (Flemings & Jordan 1989,1990; Catuneanu 2019). In the Himalayas, higher river slopes result in a higher stream power, which leads to a higher bedrock erosion rate. The Himalayas also experiences frequent landslides (Gerrard 1994), glaciation, flash floods (Kumar et al. 2018; Sarkar & Singh 2022) and intense monsoonal precipitation, leading to a dynamic geomorphic system. On the other hand, CIF is affected by slower tectonic movements, slow river incision, and low erosion rates (e.g., Lupker et al. 2012), which are guided by the thrust formation and southward migration of the Himalayan mountain front. The regions of the Himalayas and CIF are influenced by the subsurface basement ridges present on the Indian plate (Valdiya 1976; Gahalaut & Kundu 2012; Godin & Harris 2014; Divyadarshini & Tandon 2022; Kandregula et al. 2024; Manglik et al. 2025). The basement structure affects the flexural response of the Indian plate to the

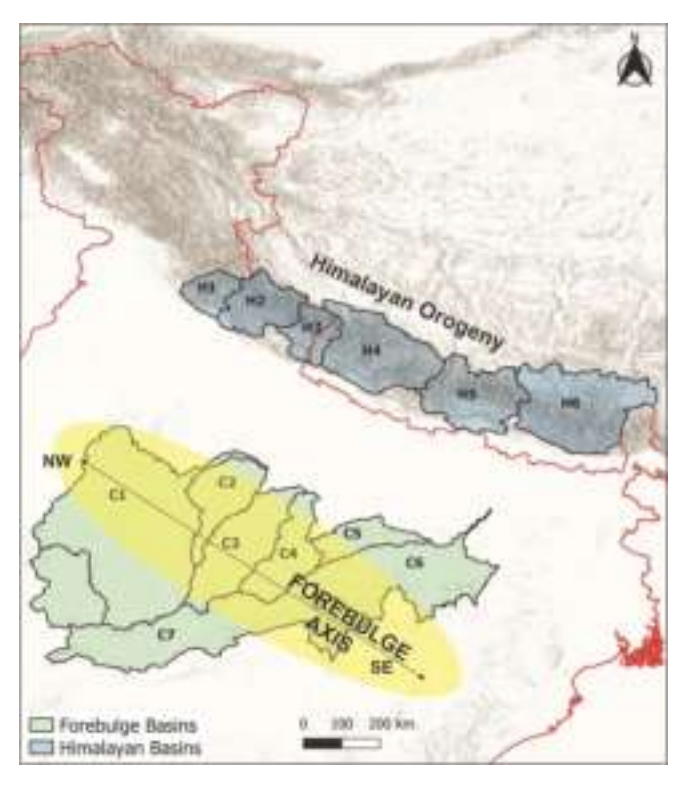


Fig. 1. Map showing the basins analysed in this study. The blue shaded basins are central Himalayan basins and are named as H1= Yamuna, H2 = Ganga, H3 = Sharda, H4 = Karnali, H5 = Narayani, H6 = Kosi. The green shaded basins are central Indian forebulge basins and named as C1= Chambal, C2 = Sindh, C3 = Betwa, C4 = Ken, C5 = Tamas (Tons), C6 = Sone, C7 = Narmada. The yellow shaded region is a subtle structural/morphological feature present in the Indian plate known as the forebulge.

loading of the Himalayas, influencing both uplift and subsidence patterns (Godin *et al.* 2023). By using geomorphic indices, such as hypsometric integral (HI), steepness index (SL), and others, we can decipher the effects of these tectonic forces and surface processes.

Geomorphic indices like hypsometric integral (HI) and steepness index (Ksn) help analyze these tectonic processes and surface dynamics, offering new perspectives on the geodynamic and geomorphic evolution of both regions. In this study, we compare the morphometric indices in the Himalayas and the central Indian forebulge region (Fig. 1) with the objective of identifying differences in the role of tectonic and climatic forces in landscape development and adjustment of river profiles in two contrasting regions. In addition, slow tectonics in the forebulge region would mean dominance of climatic forces, but do we observe the same pattern in the central Indian forebulge? Therefore, in order to seek answers to these questions, we analysed the river basins flowing in the central parts of the Himalayas (west to east - Yamuna, Ganga, Sharda, Karnali, Narayani, Kosi) and the forebulge (west to east - Chambal, Sindh, Betwa, Ken, Tamas or Tons, and Sone). We conducted morphometric analysis such as the normalized steepness index (Ksn), precipitation weighed steepness index (KsnQ), hypsometric integral, and concavity for these basins.

STUDY AREA

The river basins analysed in this study drain two major geological regions of India:1) the Himalayan catchments which drains the central Himalayas (spanning between Uttarakhand to Nepal), and 2) catchments, which drain the central India plateau or the central Indian forebulge region. We analysed six major basins of the central Himalayan region (CH basins) and the six basins of the central Indian forebulge (CIF basins). The following sections explain the geology of the CH and CIF basins.

The geological features of the Himalayan region and the Central Indian Forebulge (CIF) are different (Fig. 2) due to tectonic forces, but both are influenced by the convergence of Indian-Eurasian plates. The average rate of convergence is ~40 mm/yr, increasing from 35 mm/yr to 50 mm/yr eastwards (Bilham *et al.* 1997; Freymueller *et al.* 1996; Jade *et al.* 2017). Similarly, the uplift rates along the Himalayan front also vary, in the northwest, uplift rates range from 4–6 mm/yr (Kumar *et al.* 2006; Wesnousky *et al.* 1999); in central regions (Nepal), the front is uplifting at the rate of around 10 mm/yr (Lavé & Avouac 2001), followed by similar rates of 10–15 mm/yr in the Eastern Himalaya (Burgess *et al.* 2012; Berthet *et al.* 2014; Bouscary *et al.* 2024).

This orogenic system is a result of complex deformation over geological time, with distinct lithologies separated by continental-scale thrust faults. These include the South-Tibetan Detachment System (STDS), Main Central Thrust (MCT), Main Boundary Thrust (MBT), and Main Frontal Thrust (MFT), which separate the area into different lithotectonic units: Tethys Himalaya, Higher Himalaya, Lesser Himalaya, and Sub-Himalaya (Fig. 3a; Heim & Gansser 1939; Gansser 1964; LeFort 1975, 1996; Thakur 1987). The Indus-Tsangpo Suture Zone (ITSZ) marks the collision boundary between the two plates, which is characterized by ophiolites and high-pressure metamorphic rocks such as blueschist and eclogites (Corfield et al. 1999; 2001). The Tethys Himalaya consists of fossiliferous marine sedimentary rocks deposited from the Neoproterozoic to the Eocene (Heim & Gansser 1939; Garzanti et al. 1986, 1987; Gaetani & Garzanti 1991). The Higher Himalaya is marked by high-grade metamorphic assemblages, with altitudes ranging from 3000 to 8848 m (Hodges et al. 1992, 1996; Godin et al. 2001; Hubbard & Harrison 1989; Coleman 1998). It is separated from the Lesser Himalaya, which is composed of low to medium-grade greenschist metamorphic rocks, ranging in age from the Paleoproterozoic to Lower Paleozoic (LeFort 1975; Valdiya 1980). The Sub-Himalaya features Cenozoic deposits, including the Siwalik Supergroup (Kumar et al. 2003; Sangode et al. 2003; Raiverman 2007), which are thrust over the Indo-Ganga plains along the MFT, the most active thrust and extends for approximately 2400 km (Lavé & Avouac 2000; Nakata 1972; Gansser 1964; Yeats & Lillie 1991). The MFT ruptured around 2 million years ago and remains as an immature thrust system in the eastern Himalayas (Wesnousky et al. 1999; Mukul 2000; Thakur et al. 2014; Dev et al. 2022).



Fig. 2. Photographs showing the Himalayan (a and b), and the central Indian forebulge (c and d) landscapes.

In contrast, the Central Indian Forebulge is a low-relief region bounded by the Indo-Gangetic plains in the north, the Central Indian Tectonic Zone in the south (comprising Son-Narmada-Tapti fault systems), the Aravalli ranges in the west, and the Rajmahal traps/Garo Gap in the east (Fig. 3b). The region contains the Meso-Neoproterozoic Vindhyan Supergroup rocks, Cretaceous basaltic rocks from the Deccan volcanism, and surrounding tectonic units, including the Archean Bundelkhand Granitic Complex and the Gondwana Group (Ramakrishnan & Vaidyanathan 2008; GSI 2018). The major geological structures include the Great Boundary Fault, a NE-striking reverse fault marking the western limit of the study area, and the Son-Narmada fault system (SNF), which divides the Indian shield into northern and southern cratonic blocks (Valdiya 2016). The SNF is an E-W striking fault system located south of the study area and mainly comprises deep grabens, with the Narmada River flowing through one of them (Yellur 1968; Murty et al. 2004). The Central Indian Forebulge region has not been extensively studied in terms of uplift rates, and therefore, data regarding the uplift/ exhumation rates of this region are currently unavailable.

So, the Himalayas have complex, tall mountain ranges and thrust faults because of the ongoing collision of continents, whereas the CIF has a low-relief area influenced by the loading of the Himalayas and older tectonic structures like the Great Boundary Fault and SNF.

METHODS

To compare the role of tectonics and climate in controlling the channel morphometry in the Central Indian Forebulge and Central Himalayas, we have calculated various morphometric parameters using the SRTM digital elevation model having a spatial resolution of 90 m. We have used the Topographic Analysis Kit, or TAK tool (Forte & Whipple 2019), which is a MATLAB-based tool that utilises and combines the algorithms of TopoToolbox (Schwanghart & Scherler 2014) for advanced geomorphometric analysis. TAK enables the users to calculate the intricate channel and basin morphometric parameters such as the normalized steepness index (Ksn), concavity, gradient, Chi coordinate values, hypsometric integral etc. These parameters have been widely used to assess the impact of tectonics on fluvial systems (Keller & Pinter 2002; Kirby & Whipple 2012; Clementucci *et al.* 2022, etc.).

Ksn and KsnQ

The Ksn, or Normalized Steepness Index gives valuable information on local erosion rate in river reaches (Cyr et al. 2010). DiBiase et al. (2010) have shown a positive correlation of erosion rate with Ksn, similar to the predictions of Gilbert (1877). Previous studies (Kirby & Whipple 2001; Snyder et al. 2003; Wobus et al. 2006; DiBiase et al. 2010) have suggested that an ideal channel profile can be constrained to a single Ksn value under uniform boundary conditions, whereas deviations point towards differential uplift rates, lithologic contrasts, and precipitation rates (Allen et al. 2013; Gallen 2018; Zondervan et al. 2020; Adams et al. 2020; Peifer et al. 2021). Therefore, we investigate the variation in the steepness index to constrain these parameters along Central Himalayan catchments and Central Indian Forebulge catchments.

We used the SRTM Digital Elevation Model (DEM) with a 90-meter spatial resolution to derive the Ksn values for the

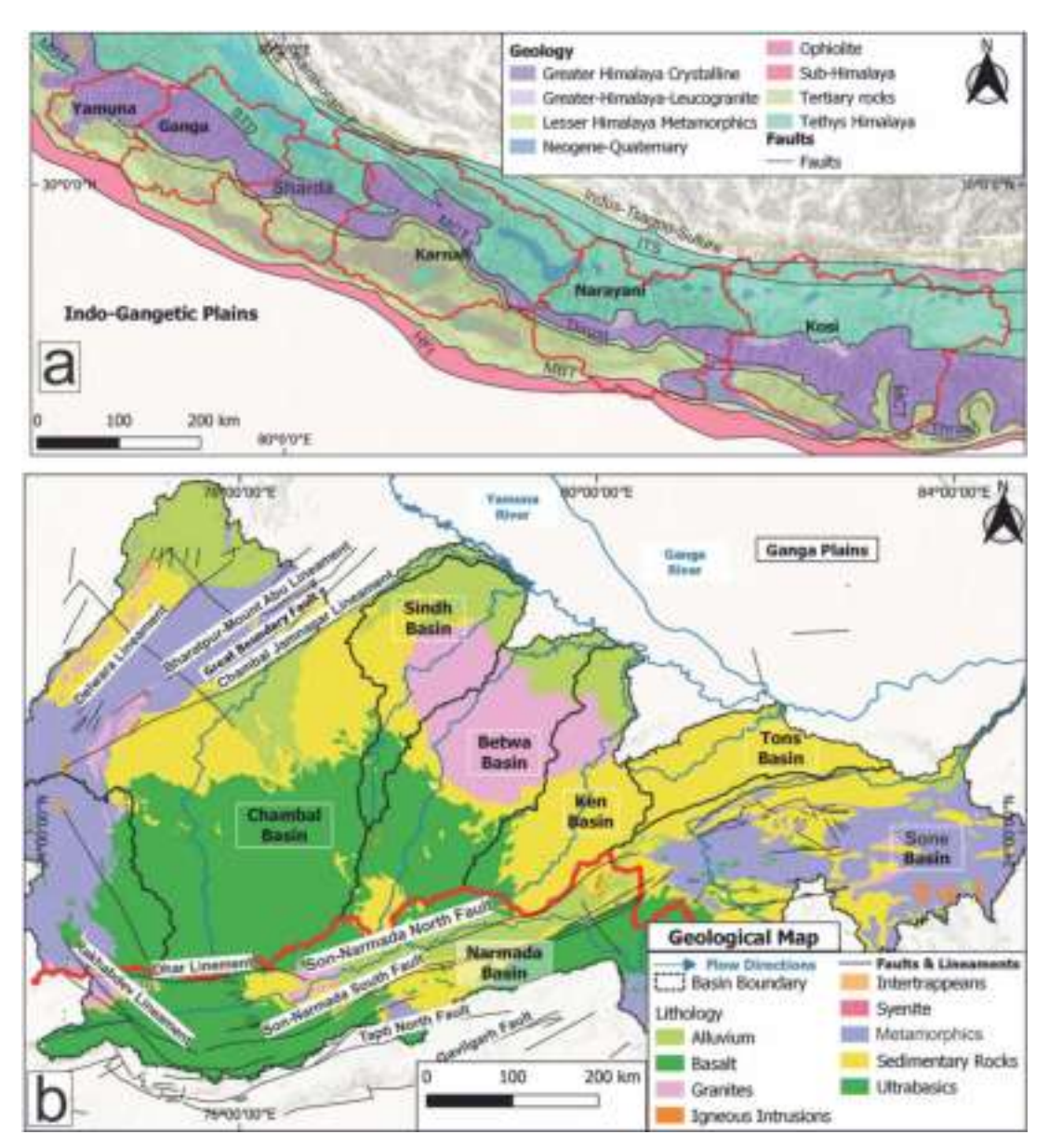


Fig. 3. Geological map of the (a) central Indian Himalayas and (b) central Indian forebulge, showing various lithological units and faults observed in the region. In figure (a), HFT = Himalayan Frontal Thrust, MBT = Main Boundary Thrust, MCT = Main Central Thrust, ITS = Indus-Tsangpo Suture and basin boundaries are shown as red. In figure (b) red line marks the drainage divide between the Ganga and the Narmada River tributaries.

watersheds that drain the study area. Within the tool TAK, we used a commonly accepted theta value (concavity index) of 0.45 to calculate the Ksn metrics.

Additionally, it has been established that incorporating the variability of precipitation in the calculation of the steepness index can help in near accurate prediction of erosion rates and rock uplift rates (Leonard *et al.* 2023). Since KsnQ is sensitive to changes in rainfall, it can be used to isolate the impact of climate in river channels where uplift rates and lithological variability are homogeneous. For example, if a catchment with homogeneous lithology is experiencing a steady uplift rate and higher precipitation, then it will grow less steep and show low Ksn values (Adams *et al.* 2020).

To compute the rainfall sensitive topographic metrics KsnQ, we utilized the SRTM DEM of 90 m spatial resolution. We extracted the daily precipitation grids of the CHIRPS datasets, which are provided by the ClimateSERV server (https://climateserv.servirglobal.net/map), and calculated the mean annual rainfall (in meters/year) for the study area. Then we input the DEM and precipitation datasets in TAK to calculate the stream networks and precipitation weighed Ksn or KsnQ (Forte & Whipple 2019; Adams *et al.* 2020; Leonard *et al.* 2023).

Concavity

The concavity of a river simply suggests how quickly a channel loses its gradient flowing downstream. Concavity of river channels can give useful insights about the role of tectonics/climate on the fluvial morphology. Concavity is positive for a concave-up channel, negative for a convex-up channel, and zero for a channel with a constant slope. Tectonic activity significantly influences the concavity of river profiles. For instance, in the Siwalik Hills, variations in uplift rates correlate with changes in channel concavity, suggesting that uplift drives erosion patterns (Kirby & Whipple 2001).

Whipple (2004) characterized concavity (h) into four types: (i) low concavities (<0.4), associated with either short, steep drainage influenced by debris flow or with a downstream increase in incision rate or rock strength, commonly related to knickpoints; (ii) moderate concavities (0.4–0.7), associated with actively uplifting bedrock channels in homogeneous substrates experiencing uniform (or near-uniform) rock uplift; (iii) high concavities (0.7–1.0), associated with a downstream decrease in rock uplift rate or rock strength; and (iv) extreme concavities (negative or >1), associated with abrupt knickpoints due to either pronounced along-stream changes in substrate properties or spatial/temporal differences in rock uplift rate, including transitions from incisive to depositional conditions (Lee & Tsai 2010).

Hypsometric Integral

We also calculated the Hypsometric Integral (HI) of the CH and CIF basins. This geomorphic index is used to analyse the distribution of elevation within a catchment area (Strahler 1952; Keller & Pinter 2002). The values can lie between 0 and 1, where the values greater than 0.5 indicate the majority of the catchment area has high elevation, and lower values indicate

the catchment with the majority region in lower elevation values. Given uniform lithology and precipitation, the hypsometric integral can act as a proxy for the dominance of either tectonic uplift (high value) or climatic erosion (lower value) in the catchment (Keller & Pinter 2002). Later studies (Hurtrez *et al.* 1999) stressed the importance of the catchment size. They argued that HI as a proxy for uplift or erosion dominance works well for the smaller catchments; however its efficiency as a proxy is affected by the high erosion rates in the larger catchments.

RESULTS

The results of various morphometric parameters (Ksn, KsnQ, concavity, hypsometric integral, mean channel gradient, local relief, and rainfall gradients; Table 1) are explained below.

Ksn and KsnQ

The steepness index values for the CH catchments (H-1 to H-6) vary between 0 and 14930 (Fig. 4a), whereas for the CIF catchments the values are observed to be between 0 and 2267 (Fig. 4b). Within the CH catchments, there is an increase in the Ksn values from south-to-north. This particular south to north increase in steepness index values is observed in all of the CH catchments (H-1 to H-6). But interestingly, in the H-6 catchment (Kosi River catchment), the Ksn values first increase south to north but sharply decrease further towards the north. We observed that the regions north of the Main Boundary Thrust primarily exhibit higher Ksn values. In the CH catchments, the basin-averaged Ksn values don't show any east-to-west variation (Fig. 6e). The basin H-4 (428.31) shows

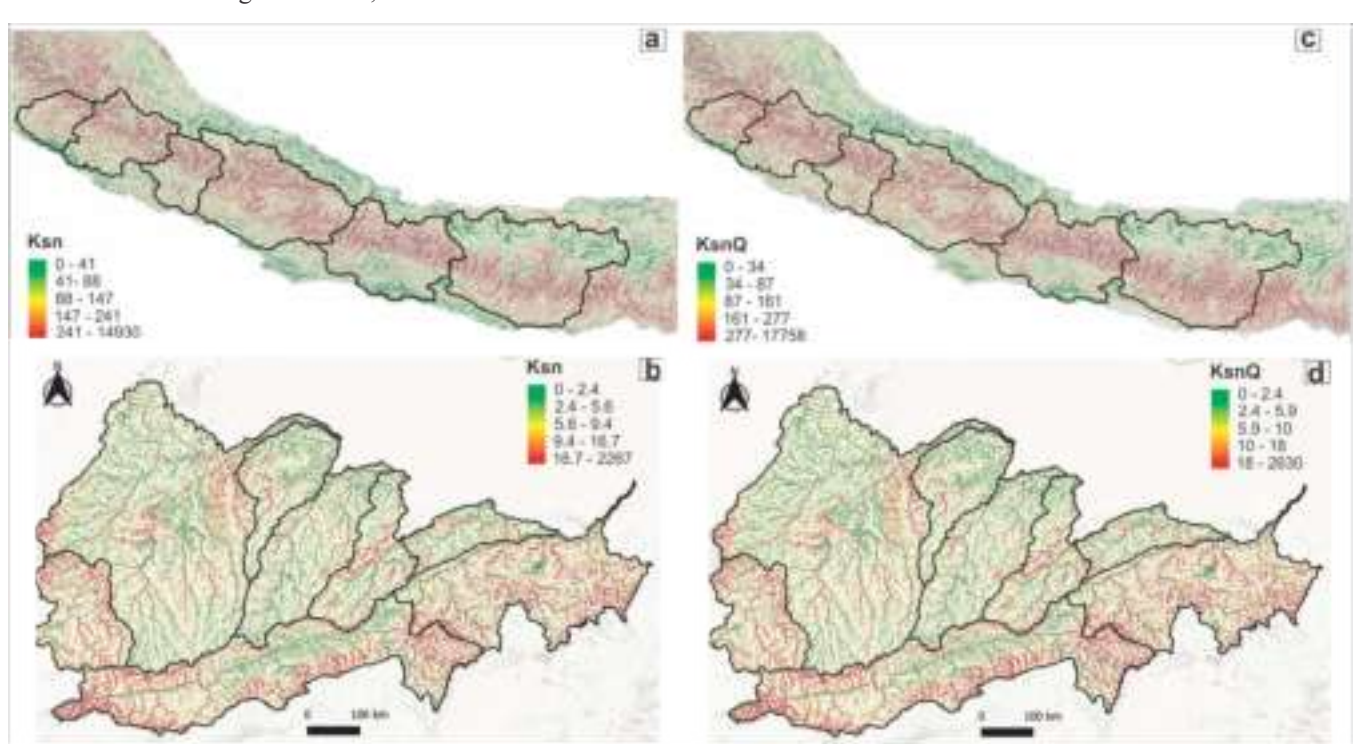


Fig. 4. The Ksn calculated for CH basins and CIF basins are shown in figure (a) and (b) respectively. The KsnQ calculated for CH and CIF basins is shown in (c) and (d) respectively. Note that the difference between Ksn and KsnQ values for CIF and CH basins are large (a-b and c-d), but the difference between the Ksn and KsnQ values of the same basins is not very significant.

the highest basin mean Ksn value, while the adjacent basins (H2-419.44, H3-394.4, and H5-394.89) located in the central part of the CH basins shows similar values. Interestingly, the mean basin Ksn values are lowest for the H1-330.70 (westernmost) and H6-327.92 (easternmost) basins.

In the CIF basins, the Ksn values are mostly observed in the range of 0-30, but extremely high values are also visible along certain channel segments. Basin mean Ksn values increase from basin C1 (westernmost) to C6 (easternmost). The basin mean Ksn of C1 is 16.2, higher than adjacent basins C2-C3, but lower than the central basins C4 (20.1), C5 (22), and easternmost C6 (31.5).

The precipitation weighed steepness index, or KsnQ values, are comparatively higher than Ksn values for both CH and CIF basins (Fig. 4c and d). In the regions where Ksn values are high, the KsnQ values are also high, i.e., the dispersion of Ksn and KsnQ values are similar within the channel segments. KsnQ values for CH basins vary in the range of 0-17758, and for the CIF basins, they vary between 0 and 2630. Interestingly, the KsnQ values for both CIF and CH basins are slightly higher but do not show any correlation with the extreme precipitation gradient observed along the Himalayas or the low precipitation gradient in the central Indian forebulge (Fig. 5).

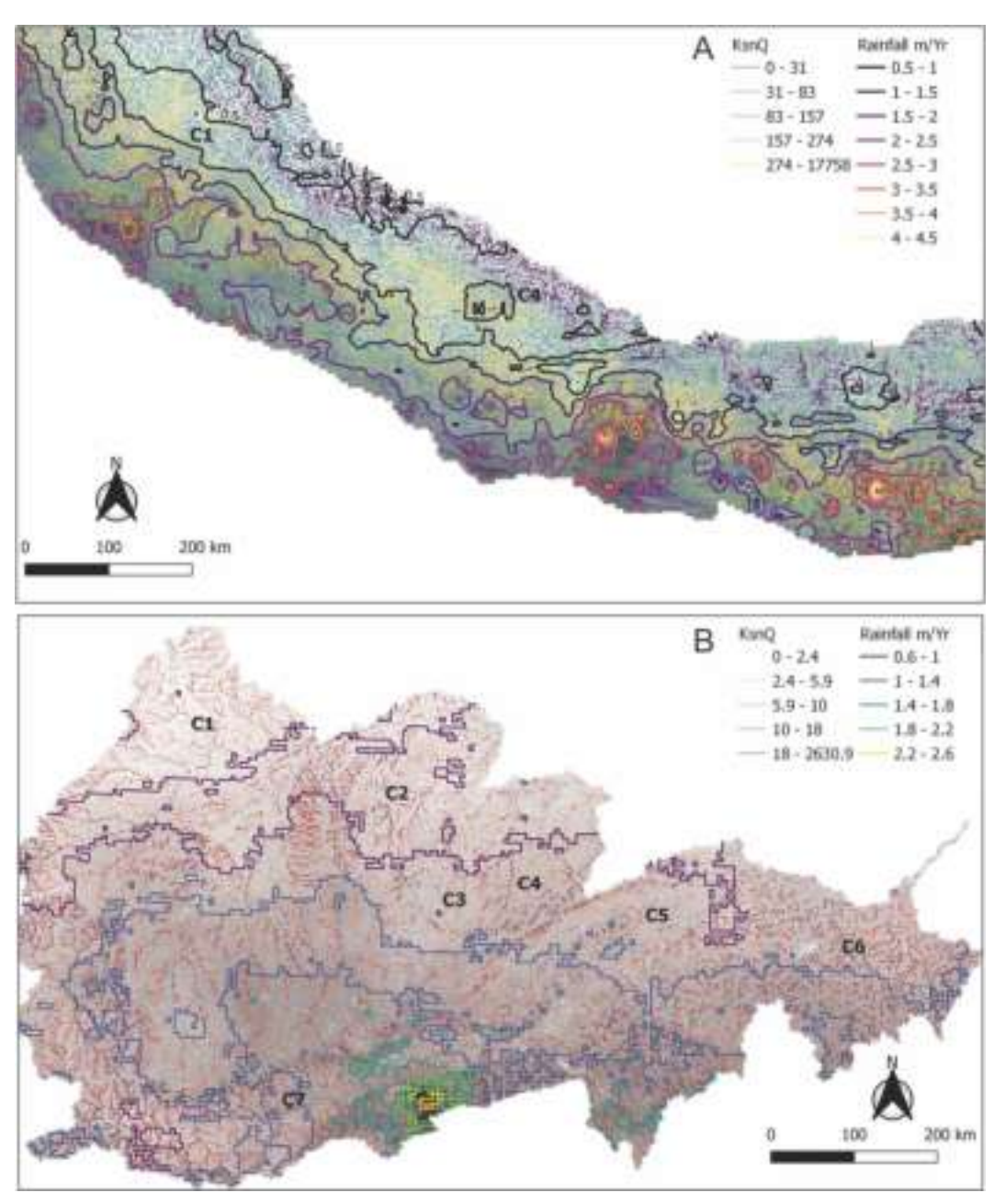


Fig. 5. Map showing the KsnQ plotted with the rainfall contours for (a) CH basins and (b) CIF basins. Note that in both the cases higher KsnQ values are not related to areas with high precipitation rates.

Concavity

Concavity index values for CH basins decrease from H1 to H6. Basin H1 showed concavity of 0.642, and H6 shows a value of 0.19 (Fig. 6d). The concavity values for CIF basins vary between 0.509 (C1) in the west and 0.455 (C6) in the east (Fig. 6d). The concavity values for basins lying between C1 and C6 are lower than 0.455.

Hypsometric Integral (HI)

The values of the hypsometric integral for CH basins vary between 0.29 and 0.44 (Fig. 6a). The variations in CH basins show an increase from H1 (westernmost) to H6 (easternmost). The HI for the H1 basin is 0.34, which increases to 0.38 (H2), 0.34 (H3), 0.42 (H4), and 0.33 (H5) and reaches up to 0.44 for

the H6 basin. The results of Himalayan catchment are counterintuitive as they show most of the basins are erosion dominated implying material added to the catchment due to uplift is less than the material removed from the catchment. The CIF basins, on the other hand don't show any east-west variations for HI values. The HI value for basin C3 is the highest, i.e., 0.45, which lies in the central part of the CIF. The HI values for basins C2 (0.41) and C4 (0.4) are also relatively high. In general, it shows that the uplift and erosion are in balance.

Mean Channel Gradient

The mean channel gradient for CH basins varies between 0.39 and 0.53 (Fig. 6b). The westernmost basins, H1-H4, show higher gradient, whereas H5 (0.48) and H6 (0.39) show a

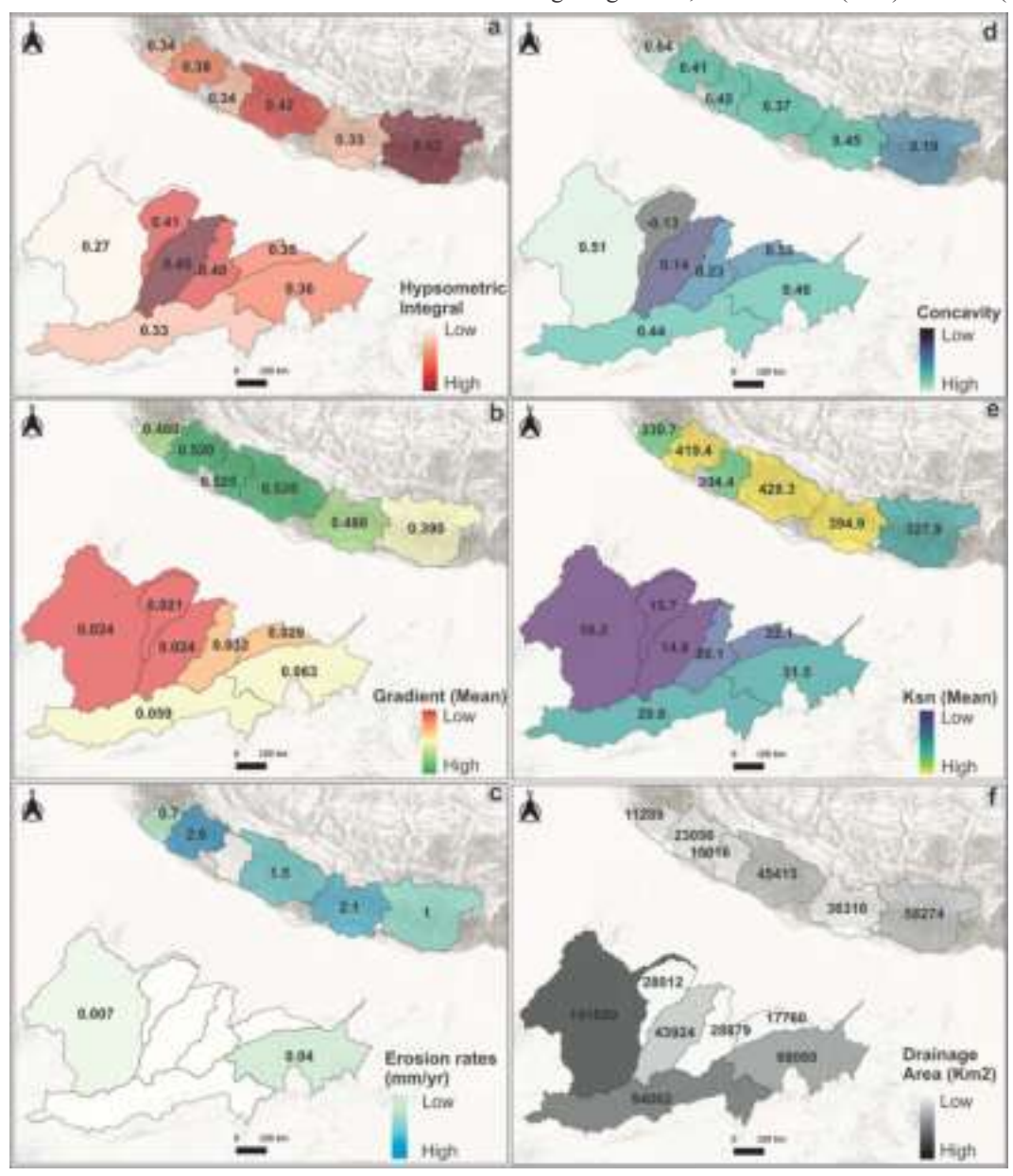


Fig. 6. Maps showing the calculated morphometric parameters of CH and CIF basins (a) hypsometric integral, (b) mean basin gradient (given in m/m), (c) erosion rates, (d) concavity, (e) basin mean Ksn, and (f) drainage area.

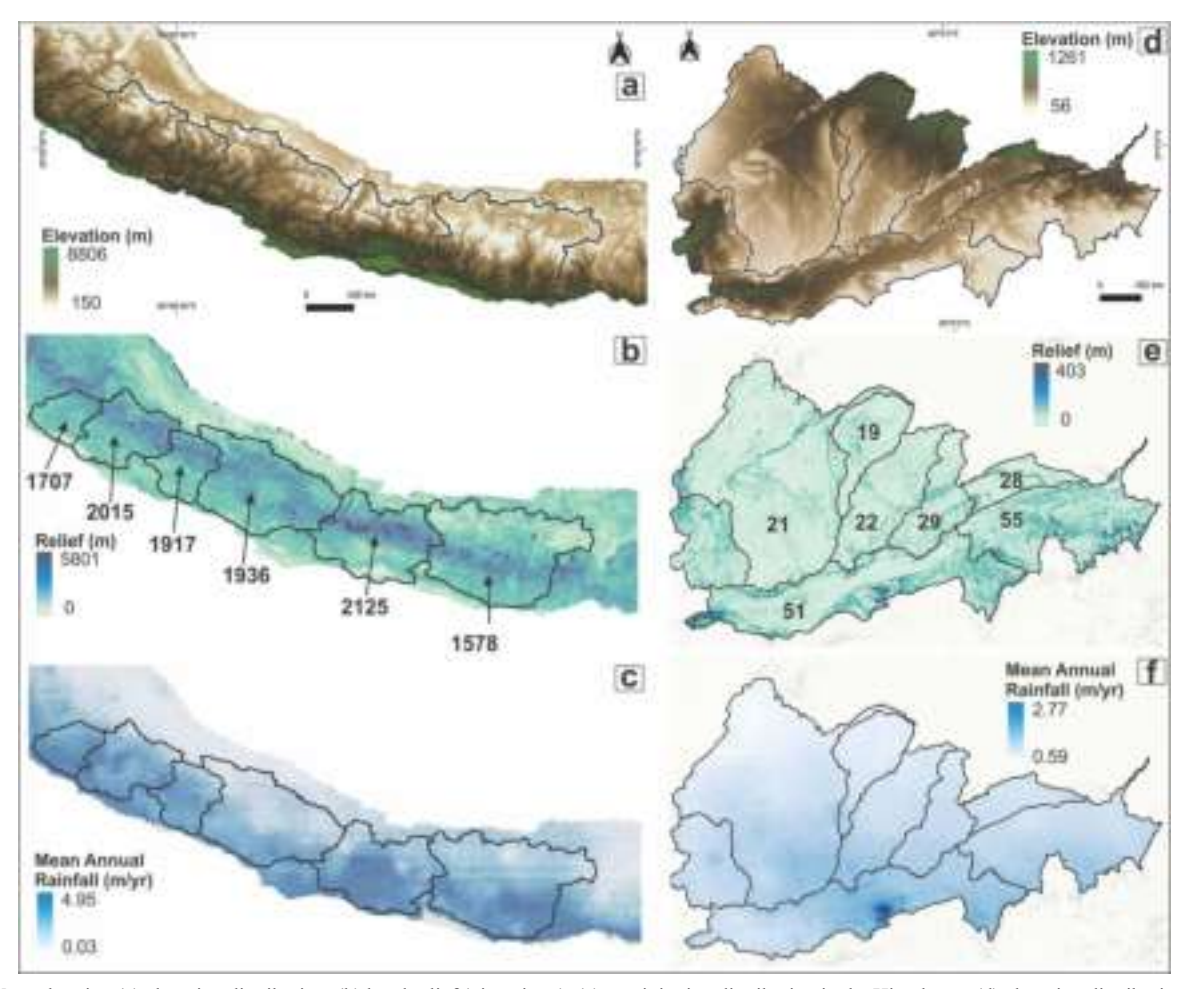


Fig. 7. Maps showing (a) elevation distribution, (b) local relief (given in m), (c) precipitation distribution in the Himalayas; (d) elevation distribution, (e) local relief (given in m), and (f) precipitation distribution in the forebulge region.

relatively lower gradient. In basins H1 to H4 we observe gradient values of 0.46, 0.52, 0.525, and 0.53, respectively. It can be inferred that there exists a west-to-east decrease in mean basin gradient values. On the contrary, we find that the CIF basins show a very low, mean channel gradient varying between 0.02 and 0.06. The westernmost C1-C2 basins have a gradient of 0.024 and 0.021, respectively. Whereas, for basin C4 we observed a gradient of 0.032 and basin C6 (easternmost) displayed the highest mean gradient value of 0.063. We find that there exists west-to-east increase in the mean basin gradient values for the CIF basins.

Local Relief

As expected, the local relief for the CH basins is significantly higher than the CIF basins. The local relief for CH basins is 10–5801 m (Fig. 7b), and for CIF basins it lies between 4 and 403 m (Fig. 7e). The local relief values for CH basins are highest in the central part of their respective basins, and they reach a maximum average value for the H5 basin (2125 m, Fig. 7b). On the other hand, CIF basins, because of a flatter topography, show low values (Fig. 7e). The basins show higher local relief and slope along the escarpments and canyons, which are ubiquitous in CIF.

Rainfall Variations

The mean annual rainfall for CIF and CH shows extreme variations. In CH basins, the mean annual rainfall varies between 0.02 and 4.9 m/year (Fig. 7c), which is almost double that of the CIF basins, which receive rainfall in the range of 0.59-2.77 m/year (Fig. 7f). A north-to-south rainfall variation across the CH basins shows an overall increase, while a similar increasing trend is also observed from west to east along the CH basins. On the other hand, CIF basins do not show any significant rainfall pattern.

DISCUSSION

It has been established that river systems are efficient recorders of tectonic and climatic perturbations. The changes in slopes (tectonic influence) or discharge (climatic influence) of river systems generally result in the changes in steepness and gradient of the river profiles (Kirby & Whipple 2001; Whipple 2004; Wobus *et al.* 2006; Whittaker 2012; Adams *et al.* 2020; Seybold *et al.* 2021). The impacts of such changes are transmitted to the entire landscape as the tributary systems and hillslopes react to the base level fall/increase in the main river (e.g., Seagren & Schoenbohm 2019; Gailleton *et al.*

Table 1. Morphometric parameters and erosion rates for the Himalayan and central Indian forebulge basins.

Region	Basin Name	Hypsometric Integral	Drainage area (Km²)	Ksn mean	Gradient mean	Concavity	Erosion rates (mm/yr)
craton	Betwa	0.447	43924	14.78	0.024	0.136	NA
craton	Tamas	0.348	17759.914	22.09	0.029	0.325	NA
craton	Sindh	0.411	28012.14	15.7	0.021	-0.128	NA
craton	Ken	0.396	28878.905	20.13	0.032	0.234	NA
craton	Sone	0.365	68059.95	31.53	0.063	0.455	0.04
craton	Chambal	0.272	141880.25	16.2	0.024	0.509	0.007
craton	Narmada	0.325	94062.25	29.56	0.059	0.442	NA
Himalayas	Ganga	0.379	23055.82	419.44	0.52	0.407	2.6
Himalayas	Karnali	0.418	45415.42	428.31	0.526	0.373	1.5
Himalayas	Kosi	0.435	58274.01	327.92	0.39	0.19	1
Himalayas	Narayani	0.326	36316.35	394.898	0.48	0.453	2.1
Himalayas	Sharda	0.339	15016.158	394.4	0.525	0.454	NA
Himalayas	Yamuna	0.34	11288.634	330.704	0.46	0.642	0.7

2021). The process ultimately results in the changes in the topography and morphometric parameters of the river basin. Therefore, by analysing the morphometric parameters of a basin, useful inferences can be made. We analyze the results of morphometric parameters (Table 1) calculated to infer the dominant processes in shaping the two contrasting regions in the subsequent discussion. However, before discussing the tectonic and climatic influence on the river systems, we assess the correlation between the morphometric parameters.

In both the Himalavan and cratonic catchments, there is a strong positive correlation between the Ksn, basin mean gradient, and average relief (Fig. 8a and b). This outcome aligns with expectations, given that these parameters are dependent on the elevation variations present in the area. On the other hand, there is a significant inverse correlation between concavity and the hypsometric integral in both the Himalayas ($r^2 = -0.93$) and cratonic catchments ($r^2 = -0.75$) (Fig. 8a and b). The expectation aligns with the understanding that increased concavity correlates with enhanced erosion. In cratonic catchments, concavity exhibits moderate positive correlations with basin mean Ksn and relief, with r² values ranging from 0.50 to 0.51. Catchment erosion rates exhibit weak correlations with the majority of variables in the CH catchment, where a moderate correlation with average relief is observed ($r^2 = 0.54$). The analysis shows that the hypsometric integral has either weak or no correlation with most morphometric parameters in both Himalayan and cratonic catchments, suggesting that it does not depend on other morphometric factors.

Response of River profiles to Tectonic and Climatic Variability

Effects of Climatic Variability

The Himalayan catchments receive more precipitation than the basins that drain the forebulge, resulting in higher discharge and higher stream power, which brings the channel gradient to equilibrium (Fig. 7c and f).

To assess the influence of climate, we calculated KsnQ (the product of river steepness and precipitation). Although this calculation is based on present-day precipitation values, we surmise that past precipitation patterns were similar to current distributions. This would mean that regions

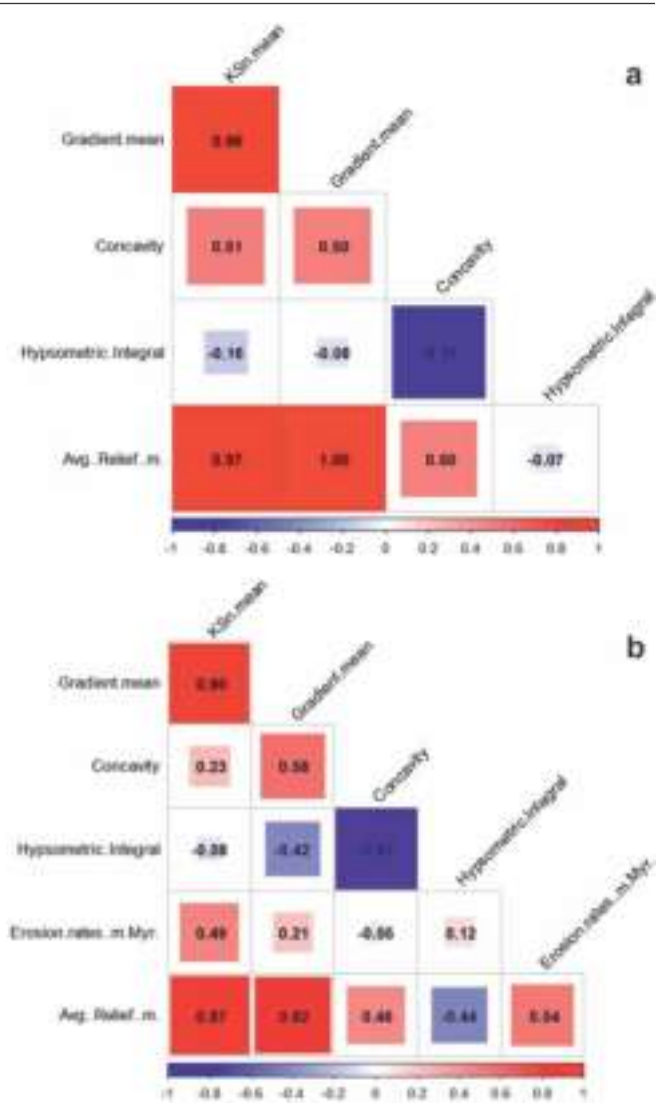


Fig. 8. Correlation matrix showing correlation coefficient values for various morphometric parameters and erosion rates for, a) CIF catchments, b) CH catchments.

experiencing higher precipitation today likely exhibited similar conditions in the past. We find that the difference between the KsnQ and Ksn values within CH and CIF basins is minimal (Fig. 4 a-d). Our finding implies that there is limited

influence of climate on river steepness; this was also observed when we plotted precipitation contours over KsnQ values in the CIF and CH basins (Fig. 5). These observations suggest limited climatic influence on the morphometric parameters of the river systems of CIF and CH.

Effects of Regional Tectonics

Rivers in the regions of slow tectonic uplift generally exhibit gradual adjustments in their longitudinal profiles and sediment transport mechanisms. In contrast, rivers subjected to active tectonics respond more dynamically and often exhibit features indicative of rapid adjustment (Schumm 1986; Kirby & Whipple 2012; Whittaker 2012). The tectonic uplift often results in the formation of knickpoints—sharp changes in river gradient that can cause imbalance in sediment transport and create local erosion features (Whipple & Tucker 1999). Kirby & Whipple (2012) suggested that because of tectonic forcing, rivers may experience a feedback loop where increased uplift leads to intense channel bed incision that further modifies the river's morphology.

Uplift rates along the Himalayan front show a systematic increase from the northwestern part to the eastern part (Table 2). In the northwest, the uplift rate ranges from 4 to 6 mm/yr (Kumar *et al.* 2006; Wesnousky *et al.* 1999), while in Nepal, the front is uplifting at the rate of around 10 mm/yr (Lavé & Avouac 2001), followed by similar rates of 10–15 mm/yr in the Eastern Himalaya (Burgess *et al.* 2012; Berthet *et al.* 2014; Bouscary *et al.* 2024). The eastward increase in the uplift rate well aligns with the erosion rates, which range from 1 to 2.6 mm/yr. In contrast, the erosion rates in the central Indian forebulge region vary between 0.04 and 0.007 mm/yr (Lupker *et al.* 2012; Rahaman *et al.* 2017), indicating extremely low uplift rates.

Despite this, various geophysical studies have questioned the tectonic stability of the CIF region (Bilham *et al.* 2003; Bilham 2004; John & Rajendran 2008; Godin *et al.* 2023). The sedimentological, geochemical, geophysical, and structural works in this region have argued that this region shows indications of neotectonics, possibly related to the Quaternary period (Agarwal *et al.* 2002; Srivastava *et al.* 2003; Bilham 2004; Gibling *et al.* 2005; Sinha *et al.* 2009; Ghosh *et al.* 2019, 2021; Godin *et al.* 2023). In general, it is challenging to detect the imprint of tectonics/neotectonics on a forebulge because the uplift is very slow and their tectonic signals get eroded with time.

Morphometric Indicators

Our results highlight that the rivers flowing in CIF show comparatively lower values for steepness index, precipitationaveraged steepness index, and gradient when compared with the CH rivers, as anticipated. However, the values for concavity and hypsometric integral are similar to the CH catchments. The concavity and hypsometric integral are considered as good indicators to identify the dominance of either tectonics or climate in a region, with higher values suggesting the dominance of tectonics in the region (Chen et al. 2003; Seybold et al. 2021). We observe that most of the basins in both regions show values between 0.3 and 0.45, indicating that the catchments are either in equilibrium or they are dominated by erosional processes. Interestingly, some of the basins of CIF also show HI values ranging from 0.4 to 0.5, suggesting that the catchments are in equilibrium. The relatively higher HI values suggest that this region is uplifting at a rate that is either faster than the rate at which the sediments are eroded in the catchments or equal to the uplift rate. However, another factor that influences HI is lithology. It has been suggested that the lithology can potentially produce the false signals of tectonics in a stable region (Lifton & Chase 1992; El Hamdouni et al. 2008). The CIF rivers flow over sandstones, orthoquartzites, granites, limestones, basalt, etc. which have higher rock strength; as a result, they are harder to erode. Therefore, we surmise that both tectonics and lithology play an important role in the region.

On the other hand, the Himalayan rivers flow over lithologies such as phyllites, quartzites, gneisses, schists, limestones, etc., and the region is rapidly uplifting. Still, the HI values are mostly low, indicating that erosion dominates over uplift. It could be due to the fact that various physiographic units of different elevations are considered together in this analysis. For example, the Higher Himalayas have an elevation between 3000 and 8848 m whereas the Lesser Himalayas generally have an elevation between 1500 and 3000 m, and the Sub-Himalayas have an elevation between 350 and 1500 m (Yin 2006). When we consider all these physiographic units together in a catchment, the value is derived assuming that all the units were at higher elevation in the beginning and a large volume is removed from the Sub-Himalaya and the Lesser Himalaya;, thus we get low values. Therefore, the HI results from CIF and CH may not be suitable for direct comparison.

The concavity values of the CIF rivers are relatively lower than the CH rivers, pointing towards a dominant tectonic influence in the Himalayan basins. Interestingly, tectonics and climate cannot explain the very high concavity values observed in the CIF basins C1 and C6. This could be due to the presence of large river dam and reservoir systems (namely the Jawahar Sagar, Rana Pratap Sagar, and Gandhi Sagar Dams), as well as the lithological variation from softer Quaternary

Table 2. *Uplift rates for the Himalayan region.*

Region	Uplift Rate	Derived From	References
NW Himalaya	4-6 mm/yr > 6.9 +/- 1.8 mm/yr	Strath Terrace (Ghaggar, Markanda, Shahjahanpur, and Kosi River) Piedmont Rivers Khajnawara and Shahjahanpur Rao (Between Yamuna and Ganga)	Kumar <i>et al.</i> 2006 Wesnousky <i>et al.</i> 1999
Central Himalaya NE Himalaya	10 - 15 mm/yr 8.4 - 14.6 mm/yr	Terrace (Baghmati, Bakeya, Narayani, Ratu) Terraces across Bhalukpong thrust (NE Himalayas)	Lavé & Avouac 2001 Burgess et al. 2012

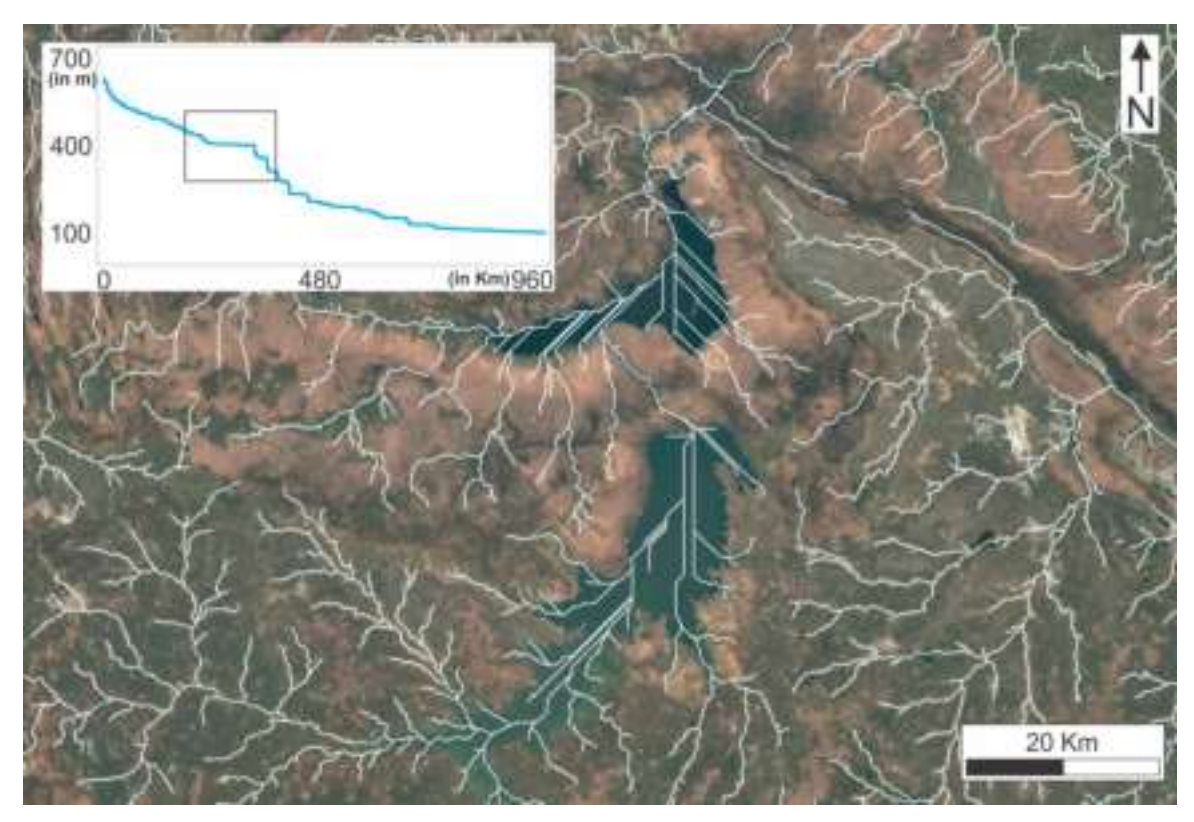


Fig. 9. Diagram showing location of the knick point observed on the longitudinal profile on the Google Earth Image. Inset image shows the longitudinal profile of the Chambal River showing a flatter low gradient region in the same stretch where these dams are present. Two major reservoirs can be observed on the Google Earth image. White lines show the drainage network and on the reservoir it shows flow trajectory.

alluvium to harder Proterozoic sedimentary rocks in these basins. This observation suggests that lithology and anthropogenic activities, such as dams, have influenced the concavity of the CIF channels (Fig. 9). This is in agreement with several other studies where such controls have been highlighted (e.g., Duvall *et al.* 2004; Lima & Flores 2017; Mudd *et al.* 2014, 2018; VanLanigham *et al.* 2006; Zhou *et al.* 2021).

The Himalayan rivers exhibit up to 10 times higher steepness indices (Ksn) than the CIF basins. We attribute this difference to the lithological contrasts and varying uplift rates of the two regions. We noticed that the northern and central regions of all of the CH basins showed higher Ksn values. This region comprises of Higher Himalayan crystallines and Lesser Himalayan meta-sedimentary sequences. The lithologies in these sequences exhibit higher strength and lesser erodibility. The Ksn values for the CIF basins also correlate with the lower uplift and erosion rates observed in this region. There are regions like escarpments, canyons, and waterfalls related to high Ksn values in the CIF. We surmise that the lithological variability in this region explains these higher Ksn values related to escarpments and canyons.

The results of the morphometric indices highlight the complex interplay of tectonics, climate, lithology, and anthropogenic activities in shaping their river profiles and geomorphic parameters.

Role of Subsurface Ridges

The subducting Indian lithosphere consists of multiple NE-SW oriented subsurface ridge systems and associated faults (Gahalaut & Kundu 2012; Godin & Harris 2014; Godin et al. 2019; Divyadarshini & Tandon 2022; Fig. 10). The Delhi-Sargodha ridge lies in the west, the Faizabad ridge is observed in the central part, and the Munger-Saharsa ridge is found in the east (Fig. 10). Associated with these ridge systems are many NE-SW oriented (unnamed) subsurface faults, which are linked with the seismicity in the Indo-Ganga plains, cratonic interiors, and the dynamics of the Himalayas (Bilham 2004; Gahalaut & Kundu 2012; Godin & Harris 2014; Duvall et al. 2021; Kandregula et al. 2024; Manglik et al. 2025). A study based on the morphometric analysis of the Ken basin (C4 basin in this study) of central India suggested the link between the reactivation of the subsurface Faizabad ridge fault system, landscape development in central India, and the Himalayan orogeny (Godin et al. 2023). This study highlighted the role of activation of the Pokhara subsurface fault system (SE of Faizabad ridge) during Plio-Quaternary period and its impact on the upliftment of the Vindhyan suite of rocks. We observed that the river systems flowing west of the subsurface Faizabad ridge are generally incised in their alluvium, whereas the river systems on the east are aggrading and avulsive in their respective floodplains (Fig. 10). Interestingly, the mean Ksn, gradient, and hypsometric

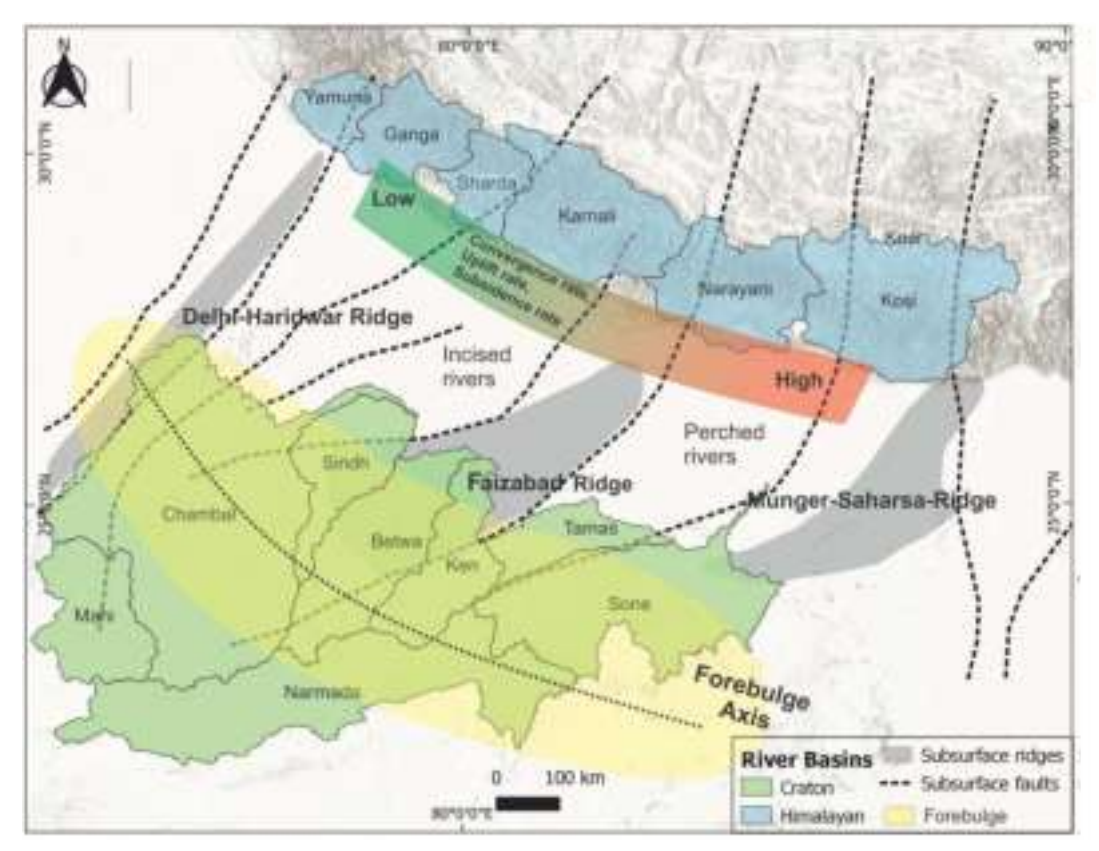


Fig. 10. Map showing the relationship between the basins investigated in this study and the basement structures (Godin & Harris 2014). Subsurface ridges, such as the Delhi-Haridwar Ridge (DHR), Faizabad Ridge (FR), and Munger-Saharsa Ridge (MSR), are overlain by the Ganga sediments. Note that the convergence rate and uplift rate, in the Himalaya and subsidence velocity along the Himalayan front increases towards east (Dingle *et al.* 2016; Lavé & Avouac 2000; Kumar *et al.* 2010; Burgess *et al.* 2012).

integral are high for the CIF (C3, C4) and CH (H4, H5) basins present over this ridge (Figs. 6, 10). Whereas the contrast between the lower erosion rates, relief, and high basin mean Ksn of the H4 basin suggests a strong tectonic influence. Therefore, we suggest that the Faizabad ridge, which is connected to both the Himalayan and forebulge river systems can also act as a prominent link controlling the forebulge and Himalayan tectonics, affecting the drainage on either side (C3, C4 and H4, H5). This observation leads us to conclude that the interconnectedness between forebulge dynamics and Himalayan tectonics guides the geomorphic process in these regions.

CONCLUSIONS

River systems record the tectonic and climatic shifts in the form of their gradient, steepness, concavity, and discharge. In this study, we investigated rivers in the rapidly uplifting Himalayas and the rivers on the very slowly uplifting central Indian forebulge. Comparison of the data from two contrasting regions suggests the following:

• The high values of the normalized steepness index and local relief, and the low values of the hypsometric integral in the Himalayan rivers highlight the dominance of tectonic uplift in shaping their profile.

- The HI values and low Normalized Steepness Index in CIF basins suggest a near-equilibrium state between uplift and erosion.
- High Ksn values (like H6) and patterns of channel gradients show that local lithology and structures affect the CH basins.
- The steepness indices and rainfall gradients do not show any correlation, suggesting tectonics as the primary driver of landscape evolution in both regions.

Acknowledgements: PK would like to thank CSIR for providing a fellowship (file number: 09/045(1509)/2017-EMR-I) for this research. PK, Tanya, and VS would like to thank the Department of Geology and University of Delhi for providing the basic infrastructure for conducting this study. Tanya would like to thank UGC for providing fellowship for this research.

Declaration of competing interest: The authors declare that they have no known competing financial interests or personal relationships that could have appeared to influence the work reported in this paper.

References

Adams, B.A., Whipple, K.X., Forte, A.M., Heimsath, A.M., Hodges, K.V. 2020. Climate controls on erosion in tectonically active landscapes. *Science Advances*, **6**(42), eaaz3166.

- Agarwal, K., Singh, I., Sharma, M., Sharma, S., Rajagopalan, G. 2002. Extensional tectonic activity in the cratonward parts (peripheral bulge) of the Ganga Plain foreland basin, India. *International Journal of Earth Sciences*, 91(5), 897-905.
- Allen, G.H., Barnes, J.B., Pavelsky, T.M., Kirby, E. 2013. Lithologic and tectonic controls on bedrock channel form at the northwest Himalayan front. *Journal of Geophysical Research: Earth Surface*, 118(3), 1806-1825.
- Berthet, T., Ritz, J.F., Ferry, M., Pelgay, P., Cattin, R., Drukpa, D., Régis, B., Hetényi, G. 2014. Active tectonics of the eastern Himalaya: New constraints from the first tectonic geomorphology study in southern Bhutan. *Geology*, 42(5), 427-430.
- Bilham, R., Larson, K., Freymueller, J. 1997. GPS measurements of present-day convergence across the Nepal Himalaya. *Nature*, **386**(6620), 61-64.
- Bilham, R., Bendick, R., Wallace, K. 2003. Flexure of the Indian plate and intraplate earthquakes. *Journal of Earth System Science*, **112**(3), 315-329.
- Bilham, R. 2004. Earthquakes in India and the Himalaya: Tectonics, Geodesy and History. *Annals of Geophysics*, **47**, 839-858.
- Bouscary, C., King, G.E., Grujic, D., Lavé, J., Almeida, R., Hetényi, G., Herman, F. 2024. Sustained deformation across the Sub-Himalayas since 200 ka. *Geology*, **52**(1), 72-76.
- Burgess, W.P., Yin, A., Dubey, C.S., Shen, Z.K., Kelty, T.K. 2012. Holocene shortening across the Main Frontal Thrust zone in the eastern Himalaya. *Earth and Planetary Science Letters*, **357**, 152-167.
- Catuneanu, O. 2019. First-order foreland cycles: Interplay of flexural tectonics, dynamic loading, and sedimentation. *Journal of Geodynamics*, 129, 290-298.
- Chen, Y.C., Sung, Q., Cheng, K.Y. 2003. Along-strike variations of morphotectonic features in the Western Foothills of Taiwan: tectonic implications based on stream-gradient and hypsometric analysis. *Geomorphology*, 56(1-2), 109-137.
- Clementucci, R., Ballato, P., Siame, L.L., Faccenna, C., Yaaqoub, A., Essaifi, A., Leanni, L., Guillou, V. 2022. Lithological control on topographic relief evolution in a slow tectonic setting (Anti-Atlas, Morocco). *Earth and Planetary Science Letters*, 596.
- Coleman, M.E. 1998. U-Pb constraints on Oligocene-Miocene deformation and anatexis within the central Himalaya, Marsyandi Valley, Nepal. American Journal of Science, 298(7), 553-571.
- Corfield, R.I., Searle, M.P., Green, O.R. 1999. Photang thrust sheet: an accretionary complex structurally below the Spontang ophiolite constraining timing and tectonic environment of ophiolite obduction, Ladakh Himalaya, NW India. *Journal of the Geological Society*, 156(5), 1031-1044
- Corfield, R.I., Searle, M.P., Pedersen, R.B. 2001. Tectonic setting, origin, and obduction history of the Spontang Ophiolite, Ladakh Himalaya, NW India. *The Journal of Geology*, **109**(6), 715-736.
- Cyr, A.J., Granger, D.E., Olivetti, V., Molin, P. 2010. Quantifying rock uplift rates using channel steepness and cosmogenic nuclide–determined erosion rates: Examples from northern and southern Italy. *Lithosphere*, 2(3), 188-198.
- DeCelles, P.G., DeCelles, P.C. 2001. Rates of shortening, propagation, underthrusting, and flexural wave migration in continental orogenic systems. *Geology*, **29**(2), 135-138.
- DeCelles, P.G. 2011. Foreland Basin Systems Revisited: Variations in Response to Tectonic Settings. In: Busby C., Azor, A. (eds.), Tectonics of Sedimentary Basins. Wiley-Blackwell. 672p. https://doi.org/10.1002/ 9781444347166.ch20
- Dey, S., Thiede, R.C., Chauhan, N., Nath, D., Schaaf, N.W., Jain, V. 2022. Pleistocene–Holocene out-of-sequence faulting along the Medlicott-Wadia Thrust in the NW Himalaya. *Terra Nova*, **34**(4), 278-289.
- DiBiase, R.A., Whipple, K.X., Heimsath, A.M., Ouimet, W.B. 2010. Landscape form and millennial erosion rates in the San Gabriel Mountains, CA. Earth and Planetary Science Letters, 289(1-2), 134-144.
- Dingle, E.H., Sinclair, H.D., Attal, M., Milodowski D.T., Singh, V. 2016. Subsidence Control on River Morphology and Grain Size in the Ganga Plain. *American Journal of Science*, **316**, 611-635.

- Divyadarshini, A., Tandon, S.K. 2022. Transverse tectonic features of the Himalaya and sub-surface basement structures of the foreland basin: implications for organic segmentation and seismicity distribution. Himalayan Geology, 43(1 B), 180-200.
- Duvall, M.J., Waldron, J.W., Godin, L., Najman, Y., Copley, A. 2021. Indian plate structural inheritance in the Himalayan foreland basin, Nepal. *Basin Research*, 33(5), 2792-2816.
- Duvall, A., Kirby, E., Burbank, D. 2004. Tectonic and lithologic controls on bedrock channel profiles and processes in coastal California. *Journal of Geophysical Research: Earth Surface*, 109.
- El Hamdouni, R., Irigaray, C., Fernández, T., Chacón, J., Keller, E. A. 2008. Assessment of relative active tectonics, southwest border of the Sierra Nevada (southern Spain). *Geomorphology*, **96**(1-2), 150-173.
- Flemings, P.B., Jordan, T.E. 1989. A Synthetic Stratigraphic Model of Foreland Basin Development. *Journal of Geophysical Research*, 94, 3851-3866.
- Flemings, P.B., Jordan, T.E. 1990. Stratigraphic modeling of foreland basins: interpreting thrust deformation and lithosphere rheology. *Geology*, **18**(5), 430-434.
- Forte, A.M., Whipple, K. X. 2019. The topographic analysis kit (TAK) for TopoToolbox. *Earth Surface Dynamics*, **7**(1), 87-95.
- Freymueller, J., Bilham, R., Bürgmann, R., Larson, K.M., Paul, J., Jade, S., Gaur, V. 1996. Global positioning system measurements of Indian plate motion and convergence across the Lesser Himalaya. *Geophysical Research Letters*, 23(22), 3107-3110.
- Gaetani, M., Garzanti, E. 1991. Multicyclic history of the Northern India continental margin (Northwestern Himalaya). AAPG bulletin, 75(9), 1427-1446.
- Gahalaut, V.K., Kundu, B. 2012. Possible influence of subducting ridges on the Himalayan arc and on the ruptures of great and major Himalayan earthquakes. *Gondwana Research*, **21**(4), 1080-1088.
- Gallen, S.F. 2018. Lithologic controls on landscape dynamics and aquatic species evolution in post-orogenic mountains. Earth and Planetary Science Letters, 493, 150-160.
- Gailleton, B., Mudd, S. M., Clubb, F.J., Grieve, S.W., Hurst, M.D. 2021. Impact of changing concavity indices on channel steepness and divide migration metrics. *Journal of Geophysical Research: Earth Surface*, 126(10), e2020JF006060.
- Gansser, A. 1964. The Geology of the Himalayas. Wiley Interscience, New York, 289p.
- Garzanti, E., Baud, A., Mascle, G. 1987. Sedimentary record of the northward flight of India and its collision with Eurasia (Ladakh Himalaya, India). *Geodinamica Acta*, 1(4-5), 297-312.
- Garzanti, E., Casnedi, R., Jadoul, F. 1986. Sedimentary evidence of a Cambro-Ordovician orogenic event in the northwestern Himalaya. Sedimentary Geology, 48(3-4), 237-265.
- GSI (Geological Survey of India) 2018. Geomorphology and Landforms database for India. Available at: https://bhukosh.gsi.gov.in/Bhukosh/MapViewer.aspx (accessed June 2019).
- Gerrard, J. 1994. The landslide hazard in the Himalayas: geological control and human action. *In: Geomorphology and natural hazards*. 221-230.
- Ghosh, R., Srivastava, P., Shukla, U.K., Sehgal, R.K., Singh, I.B. 2019. 100 kyr sedimentary record of Marginal Gangetic Plain: Implications for forebulge tectonics. *Palaeogeography, Palaeoclimatology, Palaeoecology*, 520, 78-95.
- Ghosh, R., Shukla, U.K., Srivastava, P., Sharma, A. 2021. Constraints of lithostratigraphy on the landscape evolution in response of erosion, climate and tectonics in the Marginal Ganga Plain, India. *Journal of Asian Earth Sciences*, 219, 104892.
- Gibling, M.R., Tandon, S.K., Sinha, R., Jain, M. 2005. Discontinuity-bounded alluvial sequences of the southern Gangetic Plains, India: aggradation and degradation in response to monsoonal strength. *Journal of Sedimentary Research*, 75(3), 369-385.
- Gilbert, G.K. 1877. Geology of the Henry Mountains. United States Geological Survey, 1-160.

- Godin, L., Harris, L.B. 2014. Tracking basement cross-strike discontinuities in the Indian crust beneath the Himalayan orogen using gravity data-relationship to upper crustal faults. *Geophysical Journal International*, 198(1), 198-215.
- Godin, L., Crilly, B., Schoenbohm, L.M., Wolpert, J. 2023. Recent basement fault reactivation and fluvial drainage modification in an intraplate setting, eastern Bundelkhand Craton, Madhya Pradesh, India. Geomorphology, 436, 108781.
- Godin, L., Parrish, R.R., Brown, R.L., Hodges, K.V. 2001. Crustal thickening leading to exhumation of the Himalayan metamorphic core of central Nepal: Insight from U-Pb geochronology and 40Ar/39Ar thermochronology. *Tectonics*, 20(5), 729-747.
- Godin, L., Soucy La Roche, R., Waffle, L., Harris, L. B. 2019. Influence of inherited Indian basement faults on the evolution of the Himalayan Orogen. Geological Society, London, Special Publications, 481(1), 251-276.
- Goren, L., Fox, M., Willett, S.D. 2022. Linear inversion of fluvial long profiles to infer tectonic uplift histories. *In:* Shroder J.F. (eds.), *Treatise* on *Geomorphology (Second Edition)*, 10, 7464p.
- Hack, J.T. 1973. Stream-profile analysis and stream-gradient index. *Journal of Research of the U.S. Geological Survey*, 1, 421–429.
- Heim, A., Gansser, A. 1939. Central Himalaya: Geological observations of the Swiss Expedition 1936. Hindustan Publishing Corporation, 245p.
- Hodges, K. V., Parrish, R.R., Housh, TB., Lux, D. R., Burchfiel, B.C., Royden, L.H., Chen, Z. 1992. Simultaneous Miocene extension and shortening in the Himalayan orogen. *Science*, 258(5087), 1466-1470.
- Hodges, K.V., Parrish, R.R., Searle, M.P. 1996. Tectonic evolution of the central Annapurna range, Nepalese Himalayas. *Tectonics*, 15(6), 1264-1291.
- Hubbard, M. S., Harrison, T. M. 1989. ⁴⁰Ar/³⁹Ar age constraints on deformation and metamorphism in the Main Central Thrust zone and Tibetan Slab, eastern Nepal Himalaya. *Tectonics*, 8(4), 865-880.
- Hurtrez, J.E., Sol, C., Lucazeau, F. 1999. Effect of drainage area on hypsometry from an analysis of small-scale drainage basins in the Siwalik Hills (Central Nepal). Earth Surface Processes and Landforms: The Journal of the British Geomorphological Research Group, 24(9), 799-808.
- Jade, S., Shrungeshwara, T.S., Kumar, K., Choudhury, P., Dumka, R.K., Bhu, H. 2017. India plate angular velocity and contemporary deformation rates from continuous GPS measurements from 1996 to 2015. Scientific Reports, 7(1), 11439.
- Jansen, J.D., Codilean, A.T., Bishop, P., Hoey, T.B. 2010. Scale dependence of lithological control on topography: Bedrock channel geometry and catchment morphometry in western Scotland. *The Journal of Geology*, 118(3), 223-246.
- John, B., Rajendran, C.P. 2008. Geomorphic indicators of neotectonism from the Precambrian terrain of peninsular India: a study from the Bharathapuzha Basin, Kerala. *Journal-Geological Society of India*, 71(6), 827.
- Kandregula, R.S., Pavankumar, G., Manglik, A. 2024. Indian plate segmentation along the Himalayan arc: A multi-proxy approach. *Quaternary Science Advances*, 13, p.100153.
- Keller, E.A., Pinter, N. 1996. Active tectonics: Earthquakes, uplift, and landscape. Prentice Hall. Upper Saddle River, New Jersey, USA, 338p.
- Keller, E.A., Pinter, N. 2002. Active Tectonics, Earthquakes, Uplift and Landscape. 2nd Edition, Prentice Hall, Upper Saddle River, 362p.
- Khan, S., Fryirs, K.A., Ralph, T.J. 2021. Geomorphic controls on the diversity and patterns of fluvial forms along longitudinal profiles. *Catena*, 203, 105329.
- Kirby, E., Whipple, K. 2001. Quantifying differential rock-uplift rates via stream profile analysis. *Geology*, 29(5), 415-418.
- Kirby, E., Whipple, K.X. 2012. Quantifying differential rock uplift rates in the southern Sierra Nevada, California, using a spatially explicit model of river incision. *Geological Society of America Bulletin*, 124(7-8), 1144-1164.
- Kumar, R., Ghosh, S.K., Sangode, S.J. 2003. Mio-Pliocene sedimentation history in the northwestern part of the Himalayan foreland basin, India. *Current Science*, 1006-1013.

- Kumar, S., Wesnousky, S.G., Rockwell, T.K., Briggs, R.W., Thakur, VC., Jayangondaperumal, R. 2006. Paleoseismic evidence of great surface rupture earthquakes along the Indian Himalaya. *Journal of Geophysical Research: Solid Earth*, 111(B3). https://doi.org/10.1029/ 2004JB003309
- Kumar, A., Gupta, A.K., Bhambri, R., Verma, A., Tiwari, S.K., Asthana, A.K.L. 2018. Assessment and review of hydrometeorological aspects for cloudburst and flash flood events in the third pole region (Indian Himalaya). *Polar Science*, 18, 5-20.
- Lavé, J., Avouac, J. P. 2000. Active folding of fluvial terraces across the Siwaliks Hills, Himalayas of central Nepal. *Journal of Geophysical Research: Solid Earth*, 105(B3), 5735-5770.
- Lavé, J., Avouac, J. P. 2001. Fluvial incision and tectonic uplift across the Himalayas of central Nepal. *Journal of Geophysical Research: Solid Earth*, 106(B11), 26561-26591.
- Lee, C. S., Tsai, L.L. 2010. A quantitative analysis for geomorphic indices of longitudinal river profile: a case study of the Choushui River, Central Taiwan. *Environmental Earth Sciences*, 59(7), 1549-1558.
- LeFort, P. 1975. Himalayas—collided range—present knowledge of continental arc. *American Journal of Science*, **275**(A), 1–44.
- Lefort, P. 1996. Evolution of the Himalaya. *In:* Yin, A., Harrison, T.M. (eds.), *The Tectonics of Asia*. Cambridge University Press, New York, 666p.
- Leonard, J.S., Whipple, K.X., Heimsath, A.M. 2023. Isolating climatic, tectonic, and lithologic controls on mountain landscape evolution. *Science Advances*, 9(3), eadd8915.
- Leopold, L.B., Wolman, M.G., Miller, J.P., Wohl, E.E. 2020. Fluvial processes in geomorphology. Courier Dover Publications. PLACE 522p.
- Lifton, N.A., Chase, C.G. 1992. Tectonic, climatic and lithologic influences on landscape fractal dimension and hypsometry: implications for landscape evolution in the San Gabriel Mountains, California. *Geomorphology*, **5**(1-2), 77-114.
- Lima, A.G., Flores, D.M. 2017. River slopes on basalts: Slope-area trends and lithologic control. *Journal of South American Earth Sciences*, 76, 375-388.
- Lupker, M., Blard, P.H., Lavé, J., France-Lanord, C., Leanni, L., Puchol, N., Bourlès, D. 2012. 10Be-derived Himalayan denudation rates and sediment budgets in the Ganga basin. Earth and Planetary Science Letters, 333, 146-156.
- Manglik, A., Thiagarajan, S., Suresh, M., Chakravarthi, N.N., Demudu Babu, M., Pavankumar, G., Adilakshmi, L. 2025. Shallow subsurface geoelectric structure of the central Ganga Basin by magnetotellurics: A proxy for basin-scale changes in the sedimentary environment. Near Surface Geophysics.
- Merritts, D.J., Vincent, K.R., Wohl, E. E. 1994. Long river profiles, tectonism, and eustasy: A guide to interpreting fluvial terraces. *Journal of Geophysical Research: Solid Earth*, **99**(B7), 14031-14050.
- Mudd, S.M., Attal, M., Milodowski, D.T., Grieve, S.W., Valters, D.A. 2014. A statistical framework to quantify spatial variation in channel gradients using the integral method of channel profile analysis. *Journal of Geophysical Research: Earth Surface*, 119(2), 138-152.
- Mudd, S.M., Clubb, F.J., Gailleton, B., Hurst, M.D. 2018. How concave are river channels? *Earth Surface Dynamics*, **6**(2), 505-523.
- Mukul, M. 2000. The geometry and kinematics of the Main Boundary Thrust and related neotectonics in the Darjiling Himalayan fold-and-thrust belt, West Bengal, India. *Journal of Structural Geology*, **22**(9), 1261-1283.
- Murty, A. S. N., Tewari, H. C., Reddy, P. R. 2004. 2-D Crustal velocity structure along Hirapur-Mandla profile in Central India: an update. *Pure and Applied Geophysics*, **161**(1), 165-184.
- Nakata, T. 1972. Geomorphic History and Crustal Movement of the Foothills of the Himalaya. Vol. 22. Japan, 7th series (Geography), pp. 39-177.
- Owen, L.A. 2014. Himalayan landscapes of India. *Landscapes and landforms of India*, 41-52.
- Peifer, D., Persano, C., Hurst, M.D., Bishop, P., Fabel, D. 2021. Growing topography due to contrasting rock types in a tectonically dead landscape. *Earth Surface Dynamics*, 9(2), 167-181.

- Rahaman, W., Wittmann, H., von Blanckenburg, F. 2017. Denudation rates and the degree of chemical weathering in the Ganga River basin from ratios of meteoric cosmogenic 10Be to stable 9Be. Earth and Planetary Science Letters, 469, 156-169.
- Raiverman, V. 2007. Geothermic revolution, mountain elevation, tectonic pulsation and foreland sedimentation in the Himalayan System. *Himalayan Geology*, 28(2), 33-44.
- Ramakrishnan, M., Vaidyanadhan, R. 2008. *Geology of India*. Bangalore: Geological Society of India, Vol. 1, pp. 261-333.
- Sarkar, A., Singh, V. 2022. Characterisation and assessment of a flash flood in the Himalaya: understanding the significance of high magnitude events in sediment mobilisation. *Journal of the Geological Society of India*, 98(5), 678-686.
- Sangode, S.J., Kumar, R., Ghosh, S.K. 2003. Magnetic polarity stratigraphy of the Late Miocene Siwalik group sediments from Kangra re-entrant, HP, India. *Himalayan Geology*, **24**(1), 47-61.
- Schumm, S.A. 1986. Alluvial river response to active tectonics. *In:* National Research Council, Division on Engineering, Physical Sciences et al. (eds), *Active Tectonics: Impact on Society*. National Academies Press, 280p.
- Schwanghart, W., Scherler, D. 2014. TopoToolbox 2–MATLAB-based software for topographic analysis and modeling in Earth surface sciences. Earth Surface Dynamics, 2(1), 1-7.
- Seagren, E.G., Schoenbohm, L. M. 2019. Base level and lithologic control of drainage reorganization in the Sierra de las Planchadas, NW Argentina. *Journal of Geophysical Research: Earth Surface*, 124(6), 1516-1539.
- Seeber, L., Gornitz, V. 1983. River profiles along the Himalayan arc as indicators of active tectonics. *Tectonophysics*, *92*(4), 335-367.
- Seybold, H., Berghuijs, W.R., Prancevic, J.P., Kirchner, J.W. 2021. Global dominance of tectonics over climate in shaping river longitudinal profiles. *Nature Geoscience*, 14(7), 503-507.
- Sinha, R., Kettanah, Y., Gibling, M.R., Tandon, S.K., Jain, M., Bhattacharjee, P.S., Ghazanfari, P. 2009. Craton-derived alluvium as a major sediment source in the Himalayan Foreland Basin of India. *Geological Society of America Bulletin*, 121(11-12), 1596-1610.
- Sklar, L., Dietrich, W.E. 1998. River longitudinal profiles and bedrock incision models: Stream power and the influence of sediment supply. Geophysical Monograph-American Geophysical Union, 107, 237-260.
- Snyder, N.P., Whipple, K.X., Tucker, G.E., Merritts, D.J. 2003. Importance of a stochastic distribution of floods and erosion thresholds in the bedrock river incision problem. *Journal of Geophysical Research: Solid Earth*, 108(B2).
- Sonam, Jain, V. 2018. Geomorphic effectiveness of a long profile shape and the role of inherent geological controls in the Himalayan hinterland area of the Ganga River basin, India. *Geomorphology*, **304**, 15-29.
- Srivastava, P., Singh, I.B., Sharma, S., Shukla, U.K., Singhvi, A.K. 2003. Late Pleistocene–Holocene hydrologic changes in the interfluve areas of the central Ganga Plain, India. *Geomorphology*, **54**(3-4), 279-292.
- Strahler, A.N. 1952. Hypsometric (area-altitude) analysis of erosional topography. *Geological society of America bulletin*, **63**(11), 1117-1142.

- Thakur, V.C. 1987. Plate tectonic interpretation of the western Himalaya. *Tectonophysics*, **134**(1-3), 91-102.
- Thakur, V.C., Joshi, M., Sahoo, D., Suresh, N., Jayangondapermal, R., Singh, A. 2014. Partitioning of convergence in Northwest Sub-Himalaya: estimation of late Quaternary uplift and convergence rates across the Kangra reentrant, North India. *International Journal of Earth Sciences*, 103, 1037-1056.
- Valdiya, K.S. 1976. Himalayan transverse faults and folds and their parallelism with subsurface structures of North Indian plains. *Tectonophysics*, 32 (3–4), 353-386.
- Valdiya, K.S. 2016. The Evolving Indian Continent. *In: The Making of India:* Geodynamic Evolution, 889-924.
- Valdiya, K.S. 1980. Geology of the Kumaon Lesser Himalaya. Wadia Institute of Himalaya, Dehra Dun, India, 291p.
- Van Laningham, S., Meigs, A., Goldfinger, C. 2006. The effects of rock uplift and rock resistance on river morphology in a subduction zone forearc, Oregon, USA. Earth Surface Processes and Landforms: The Journal of the British Geomorphological Research Group, 31(10), 1257-1279.
- Wesnousky, S.G., Kumar, S., Mohindra, R., Thakur, V.C. 1999. Uplift and convergence along the Himalayan Frontal Thrust of India. *Tectonics*, 18(6), 967-976.
- Whipple, K. X., Tucker, G. E. 1999. Dynamics of the stream-power river incision model: Implications for height limits of mountain ranges, landscape response timescales, and research needs. *Journal of Geophysical Research: Solid Earth*, 104(B8), 17661-17674.
- Whipple, K.X. 2004. Bedrock rivers and the geomorphology of active orogens. Annual Review of Earth and Planetary Sciences, 32(1), 151-185.
- Whittaker, A.C. 2012. How do landscapes record tectonics and climate?. *Lithosphere*, 4(2), 160-164.
- Wobus, C., Whipple, K.X., Kirby, E., Snyder, N., Johnson, J., Spyropolou, K., Crosby, B., Sheehan, D. 2006. Tectonics from topography: Procedures, promise, and pitfalls, In: Special Paper 398: Tectonics, Climate, and Landscape Evolution. *Geological Society of America*, 55–74.
- Yeats, R.S., Lillie, R.J. 1991. Contemporary tectonics of the Himalayan frontal fault system: folds, blind thrusts and the 1905 Kangra earthquake. *Journal of Structural Geology*, **13**(2), 215-225.
- Yellur, D.D. 1968. Carbonatite complexes as related to the structure of Narmada valley. *Geological Society of India*, 9(2), 118-123.
- Yin, A. 2006. Cenozoic tectonic evolution of the Himalayan orogen as constrained by along-strike variation of structural geometry, exhumation history, and foreland sedimentation. *Earth-Science Reviews*, 76(1-2), 1-131.
- Zhou L., Liu W., Chen X., Wang H., Hu X., Li X., Schwanghart W. 2021. Relationship between Dams, Knickpoints and the Longitudinal Profile of the Upper Indus River. *Frontiers in Earth Science*, **9**, 1-13.
- Zondervan, J.R., Stokes, M., Boulton, S.J., Telfer, M.W., Mather, A.E. 2020. Rock strength and structural controls on fluvial erodibility: Implications for drainage divide mobility in a collisional mountain belt. *Earth and Planetary Science Letters*, **538**, 116221.

Mapping intensity distribution of Mw~6.1 Dhekiajuli earthquake in the context of tectonic settings

HIMANTA BORGOHAIN^{1,*}, SOWRAV SAIKIA², SUMER CHOPRA², RAJIB BISWAS³, SANTANU BARUAH⁴, VICKEY SHARMA³, BIBHUTI GOGOI⁵

¹Department of Petroleum Technology, Dibrugarh University, Dibrugarh-786004, Assam, India ²Institute of Seismological Research, Gandhinagar-382009, Gujarat, India ³Department of Physics, Tezpur University, Tezpur-784028, Assam, India ⁴Geosciences & Technology Division, CSIR-NEIST, Jorhat-785006, Assam, India ⁵Department of Geology, Cotton University, Guwahati-781001, Assam, India *Email (Corresponding author): himantaborgohain@ymail.com

Abstract: On the early morning of 28th April, 2021, a large earthquake of magnitude M_w~6.1, origin time 07 h 51 min 25.0 s of IST (Indian Standard Time), jolted the Dhekiajuli sub-division, Sonitpur district, Assam, India. This event, occurred in the central part of the Brahmaputra river basin, not only shook the basin, but was also widely felt in the entire Northeast India region (NER). The epicenter is within the Kopili fault zone at 26.781°N, 92.457° E, with a focal depth of 40 km as per Global Centroid Moment Tensor (GCMT) solution. This earthquake is the largest event in NER after the 3rd January 2016, Mw~6.7 Tamenglong (Manipur) earthquake (Gahalaut et al. 2016). As per the media reports and macroseismic survey, this earthquake can be assigned a maximum intensity of VIII in the meizoseismal area. The damage distribution shows an asymmetric and heterogeneous pattern. The isoseismal map pertinent to this event shows an E-W trend intensity distribution with an elongation towards the WSW direction along the Brahmaputra basin. This earthquake caused significant damage to poorly built buildings and old framed structures up to 150 km from the epicenter zone. We summarize the damage reports of macroseismic field surveys, media reports and graphically represent the damage in the form of isoseismal map for the earthquake. The seismic intensity decreased sharply with distance from the epicenter. The egg-shaped isoseismal pattern might have been controlled by local geological conditions, focal mechanism and different seismic moment-rate releases along the propagating rupture. As the epicentral region is located in the foredeep of the great Himalayan thrust belt region, as well as along with fast-growing urbanization on the alluvial plain of the Brahmaputra basin, as such the risk of severe seismic hazard is of high concern, and warrants further scientific and policy involvement.

Keywords: Intensity, Kopili fault zone, isoseismals, Seismic hazard

INTRODUCTION

The Kopili fault zone (KFZ) is a transverse structure that cuts across the Himalayan thrust system that slips dextrally at the rate of 2-3mm/year, and cuts MBT on its northern edge, while reaches the Naga Schuppen belt to its southern margin (Fig. 1) (Nandy 2001; Dasgupta & Nandy 1982; Nandy & Dasgupta 1986, Biswas et al. 2007; Barman et al. 2014; Vernant et al. 2014). The 28th April, 2021 Mw 6.1 earthquake that occurred in the Dhekiajuli region (henceforth referred as Dhekiajuli earthquake) is within 20 km periphery of KFZ and around 30 km away from Main Boundary thrust (MBT). Since the epicentral region is located in a sparsely populated area with sporadic building structures, the effects of this earthquake on built environ is relatively less. The shaking was very intense. and the vibrations were felt on the whole of the NER (Biswas 2021; Bhadran et al. 2022; Dey et al. 2022; Joshi et al. 2023). Apart from all major cities in NER, the earthquake was also felt and reported in many distant cities like Kolkata, Patna, Siliguri, Thimphu (Bhutan), Chittagong (Bangladesh), Sylhet (Bangladesh), and Mandalay (Myanmar) (Table 1). In the Dhekiajuli region, people stayed out-door for almost 2 days in the fear of the possibility of the occurrence of similar large aftershocks. The liquefaction and ground fissures were observed at many localities (Figs. 2, 3). The landslides have been observed at few locations around the outer Himalayan terrain (Suppl. Fig. S1). The United States Geological Survey (USGS) assigned the Dhekiajuli earthquake a maximum intensity of VII. Two persons lost their lives with ten persons

severely injured during this earthquake (The Indian Express, 28th April, https://en.wikipedia.org/wiki/2021_Assam_earthquake). This multi-hazardous 28th April, 2021 earthquake was also described by various authors (Halder *et al.* 2021; Sitharam 2021; Joshi *et al.* 2023).

This earthquake was followed by 18 aftershocks (M>2.5) within 24 hours; with M 4.3 being the largest aftershock (https://riseq.seismo.gov.in/riseq/earthquake; Biswas 2021). Plenty of tremors were also felt by local people in the epicentral region, which continued for the next 7 months. The aftershock sequence with 79 events of M>2.5 was recorded by the National Center for Seismology, Govt. of India (Fig. 1). Although, no aftershock has M>5.0, still people were alerted for several weeks. In the present work, we will discuss the damage pattern, intensity distributions of the Dhekiajuli earthquake, and probable rupture propagation of this earthquake.

THE GEOTECTONIC SETTING AND SEISMICITY OF KFZ

The NER (North Eastern Region) of India is squeezed between the Indo-Myanmar subduction zone and the Eastern Himalayan counterpart to the north, making it highly susceptible to frequent earthquake occurrences. This region comprises of complex tectonics like; subducted regions, collision zone associated with elongated flood plains, plateaus, fold belts that merge with many active faults and lineaments. Some of the active faults in the NER are Main

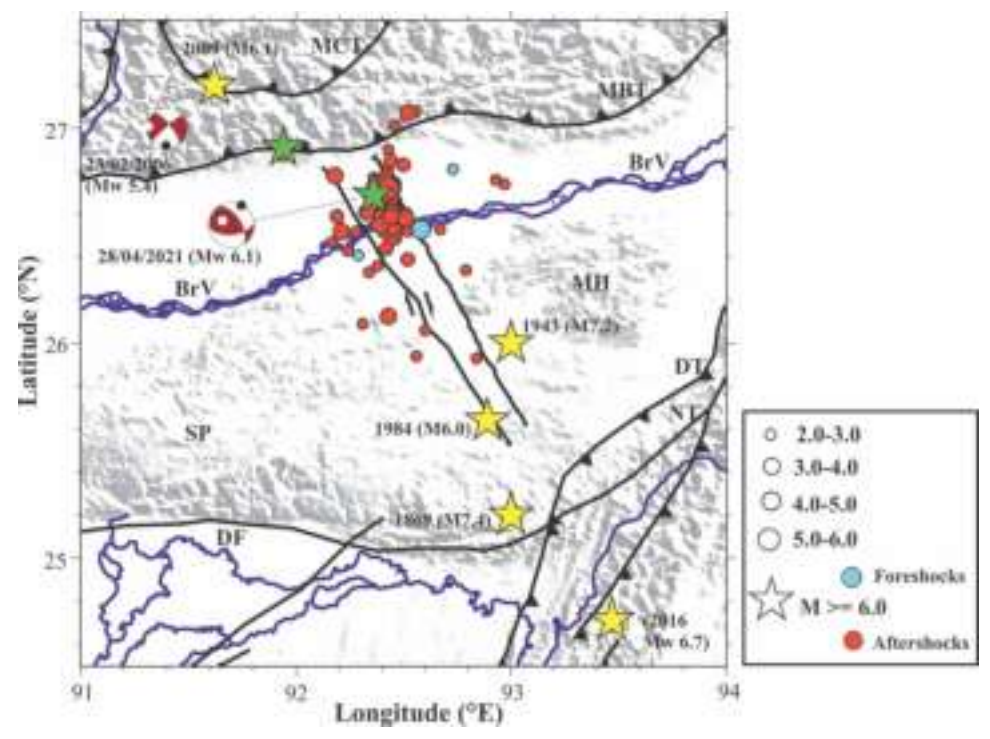


Fig. 1. Seismotectonic map of KFZand its neighboring tectonics with major faults. Significant historical earthquakes and seismic activity in the year 2021 (source: NCS [MoES, Govt. Of India]). Here, MCT: Main Central Thrust, MBT: Main Boundary thrust, KFZ: Kopili Fault Zone, BrV: Brahmaputra Valley, SP: Shillong plateau, DT: Disang Thrust, NT: Naga Thrust: DF: Dauki fault abbreviated in the map.

Central Thrust (MCT), Main Boundary Thrust (MBT), Dauki fault (DF), Lohit Thrust, Churachandpur Mao fault and KFZ (Kopili Fault Zone), DT (Disang Thrust), NT (Naga Thrust) which can produce large earthquakes (Fig. 1). Due to such complex tectonics and frequent earthquakes, NER is considered to have the highest seismic hazard and have been assigned zone V in the seismic zoning map of India (BIS 2002). The NER have experienced two great (M_s 8.7 in 1897 and M_s 8.6 in 1950) and 17 large (M_s ; 7.0) earthquakes in the last century (Kayal 2008). The Brahmaputra valley basin, in the heart of NER, with thick sedimentary layer on its top, has the potential of amplifying the ground motions during a large earthquake. Furthermore, many cities with rapid urbanization and dense populations are notably situated in this stretched basin, which altogether increases the seismic risk in this region.

The KFZ is constituted by Neogene-Quaternary sediments that were directly deposited over the Archean to Proterozoic basement gneisses (Nandy 2001). The KFZ, which bisects the Brahmaputra basin, is an approximately 300 km long and 50 km wide NNW-SSE trending zone, a transverse tectonic feature to the Himalayan arc (Dasgupta & Nandy 1982; Kayal 2008). This zone is flanked by two tributary rivers of the Brahmaputra, namely the Kopili and the Kalang, that cause broad topographic depression in the area. It has thick layer of sediments with thickness up to 1.0-1.5 km that decreases to ~700 m in the southern parts of the Kopili depression towards the Naga Schuppen belt (Singh *et al.* 2005; Saikia *et al.* 2017; Saikia 2019). The KFZ is characterized by 10 to 15 km broad

topographic depression that separates two Precambrian massifs, namely the Mikir Hills (MH) Massif and the Shillong Plateau, which are located on each side of this fault and divide the whole Brahmaputra basin into two blocks; Shillong block and Assam block, which rotates clockwise relative to Indian plate (Barman et al. 2014; Vernant et al. 2014). Despite a topographic depression, there is no surficial signature of KFZ that has been documented till now. Based on the seismotectonic analysis, the epicentral map of the KFZ shows the highest activity in the northern part as compared to the southern part (Sharma et al. 2018). Kayal et al. 2012 inferred that the earthquakes in the southern KFZ at Mikir hill (MH) region are caused by long and deep-rooted Kopili fault explicitly transverse to the Himalayan trend (Fig. 1). Historically, this highly active zone has experienced 2 large earthquakes (Mw 7.4, 1869 Cachar Earthquake and Mw 7.2, 1943 Mikir hill earthquake) and innumerable sizeable (M > 4.0) earthquakes since catastrophic Cachar earthquake (Ambraseys & Douglas 2004; Kayal 2008). There have been some other significant earthquakes in the KFZ, including a 1941 Ms 6.5 earthquake in the Tezpur region, which caused significant damage to the Brahmaputra valley (Kayal 2008). Another large earthquake, Mw 6.1, 2009 Bhutan earthquake occurred near MBT in the northern edge of KFZ (Kayal et al. 2010). From the study of fault slip rate, moment rate, and seismic activity; the KFZ can produce an earthquake with a maximum magnitude of 7.6 Mw in the near future (Sharma & Baruah 2017).

MEDIA REPORTS AND MACROSEISMIC INVESTIGATIONS

The field observations was observed from 6th May to 8th May, 2021 covered only certain localities of the Dhekiajuli subdivision due to COVID-19 pandemic restrictions. We have taken care to azimuthally cover the maximum number of localities to present a reasonably good picture of the impact of the main shock. The survey started with severely affected places; afterwards some low-intensity regions of the nearby township were covered. Accordingly, the survey comprised of 19 field survey locations; some 14-information obtained from personal communication with local residents and covered some other 46 sites through print media (Table 1). Additionally, this earthquake was felt in many cities of

neighboring countries, like Bhutan, Bangladesh, and Myanmar within 700 km periphery. As per preliminary investigation from macro- seismic field data, the isoseismal map depicts the maximum intensity 8 on the basis of EMS98 intensity scale in the Dhekiajuli subdivision (Fig. 4). From the field survey, it is found that the northern and the southern sides of the epicentral zone suffered much less damage compared to the regions at similar distances towards the eastern and western sides. All the field felt reports are mostly within ~150 km radial distance from the epicenter, can be seen in epicentral track intensity map; while all other intensities distribution of distant places within NER, obtaining from mainly print media are also plotted in regional distributions of intensity map.

Table1: *Earthquake felt reports of various places:*

A) Media based reports on 28th April, 2021 Mw 6.1 Dhekiajuli Earthquake

Sl. No.	Location	Coordinates	Report	EMS-98 scale	Source
1.	Bhairabkunda	26.8900°N, 92.1150°E	Strong tremor, ground cracks observed, duration is about a minute, some part of Bhairabkunda hill was collapse and occurred massive landslide (Fig. 3)	VI	The Arunachal Times, PTI
2.	Tezpur	26.6739° N, 92.8577° E	Cracks in the middle of the road developed, building and boundary walls were damaged (Photo 2, 3)	VII	Asomiya Pratidin, Aamar Ashom, The Telegraph, The Indian Express, Khabar
3.	Nagaon	24.7936° N, 88.9318° E	Building tilted and cracks developed (Photo 4), 1 persons injured, 1 person died due to heart attack which could be indirectly related to the earthquake	VII	Asomiya Pratidin, Aamar Ashom, The Telegraph, Khaba
4.	Guwahati	26.1445° N, 91.7362° E	Governments offices, Hospital, Apartments, Shopping Malls damages. Hotel Vivanta also reported damages in glass panels and cracks developed in the walls (Photo 5), 1 person died due to heart attack which could be indirectly related to the earthquake	VI	Asomiya Pratidin, Aamar Ashom, The Telegraph, Dainik Janambhumi, PTI, Niyomia Batra, Khabar, The Indian Express
5.	Morigaon	26.2600° N, 92.2630° E	Shaking for 20 sec. cracks developed in cultivation field, cracks in concrete wall and som mud houses damages	VI	Asomiya Pratidin, Niyomia Batra, DD Northeast
5.	Narayanpur	26.9518° N, 93.8592° E	Major cracks developed in different parts of the region and liquefaction observed in the cultivated lands (Photo 6)	VI	AsomiyaPratidin, Niyomia Batra, DD Northeast
6.	Shillong	25.5788° N, 91.8933° E	People felt a moderate tremor for about 20-30 sec. but not visible damages at the ground	e V	The Shillong Times, Asomiya Pratidin, The Telegraph
7.	Papum pare, Arunachal Pradesh	27.0844° N, 93.6053° E	Strong tremor accompanied by cracks developed in some buildings in Itanagar and Kameng Dist.	IV	The Arunachal Times
8.	West Bengal (Jalpaiguri, Siliguri, Coochbehar etc.)	26.5215° N, 88.7196° E	People felt strong tremors in Jalpaiguri, Alipurduar, Coochbehar and Darjeeling district but no damage was reported	III	PTI, Aajkal, Anand Bazar Patrika
9.	Bihar (Patna)	25.5941° N, 85.1376° E	People felt moderate tremors in some parts but no damage was reported	III	Bihar Samachar, Dainik Bhaskar, PTI
10.	Bangladesh (Sylhet)	24.8949° N, 91.8687° E	Moderate tremor felt along its northern margin, no observable damages	III	The daily Prothom Alok, PTI
11.	Darrang	26.4523° N, 92.0273° E	Strong felt for 30 sec, cracks developed in the walls, 6 persons injured, mud houses damaged.	VII	Asomiya Pratidin, The telegraph, Khabar
12.	Lumding	25.7516° N, 93.1729° E	Moderate shaking for 10 sec., no damages	IV	AsomiyaPratidin, Karbi Anglong Today
13.	Jorhat	26.7509° N, 94.2037° E	Moderate shaking for about 30 sec. felt by all. Visible cracks in old and mud houses well visible, Tiles of old and poor construction falls down. (Fig. 4)	V	Dainik Janambhumi, Asomiya Pratidin, Agradoot, Khabar
14.	Thimphu (Bhutan)	27.4712° N, 89.6339° E	Weak shaking for about 10 sec. No damages	IV	Bhutan Times, Bhutan Today, PTI
15.	Dimapur	25.9091° N, 93.7266° E	Moderate vibration for approx. 15 sec.	IV	The Nagaland Post, PTI
16.	Imphal	24.8170° N, 93.9368° E	Moderate shaking for 15-20 sec., no damages	IV	Manipur Daily, Door Darshan Northeast
17.	Agartala	23.8315° N, 91.2868° E	Weak shaking for only a few sec.	IV	Tripura Today, PTI

18.	Tinsukia	27.4886° N, 95.3558° E	Moderate shaking for 10-15 sec.	IV	Asomiya Pratidin, Khabar, Dainik Janambhumi, Aajir
19.	Dibrugarh	27.4728° N, 94.9120° E	Moderate shaking for 10-15 sec.	V	Ashom Asomiya Pratidin, Khabar, Dainik Janambhumi, The
20	Golaghat	26.5240°N, 93.9631°E	Strong shaking for 30 sec, felt by all. Cracks visible in old concrete pakka construction, some old houses substantial	VI	Telegraph, PTI Asomiya Pratidin, Khabar, The Telegraph, Dainik Janambhumi
			damaged		PTI
21.	Kohima	25.6751° N,	weak shaking for 10-15 sec, felt by many.	IV	The Negeland Post DTI
22.	Karimganj	94.1086° E 24.8649° N,	Moderate shaking, no damages, , felt by many.	IV	The Nagaland Post, PTI Asomiya Pratidin, PTI
22.	Kurinigunj	92.3592° E	wioderate shaking, no damages, , lot by many.	1 4	7130iiiiya 11atidiii, 111
23.	Diphu	25.8465° N,	Moderate shaking for about 15 sec. felt by all, cracks in old	V	The Hill Times, Karbi Anglong
	-	93.4299° E	concrete houses		Today, Asomiya Pratidin
24.	Hooghly	22.9012° N,	Light shaking, no damages	III	PTI, Aajkal, Anand Bazar
2.5	77 1	88.3899° E	W 1 1 1 1 C 1 C	***	Patrika
25.	Kalimpong	27.0594° N,	Weak shaking for only a few sec.	III	Kalimpong Times, PTI,
26.	Baksa	88.4695° E 26.6935° N,	Himalayan Times Moderate shaking for 15 sec. felt by all, cracks in some	V	Asomiya Pratidin, Khabar
20.	Daksa	91.5984° E	concrete houses, visible cracks in mud houses.	v	Asomiya i fatidili, Kilabai
27.	Jowai	25.4509° N,	Light shaking for about 10-15 sec, felt by all	V	Asomiya Pratidin, The Shillong
		92.2089° E			Times
28.	Katihar	25.5541° N,	Very weak shaking only for a few sec.	III	Dainik Bhaskar
		87.5591° E			
29.	Hailakandi	24.6811° N,	Shaking for 20 sec, felt by all. Visible cracks on weak and	V	Asomiya Pratidin, The
20	D	92.5638° E	old constructions	* 7	Telegraph
30.	Barpeta	26.3216° N,	Moderate shaking for about 20 sec, felt by all.	V	Asomiya Pratidin, Khabar
31.	Numaligarh	90.9821° E 26.5885° N,	Moderate shaking for about 20 sec, visible cracks on old	VI	Asomiya Pratidin, Khabar,
51.	rumangam	93.7486° E	concrete and mud houses	V 1	Dainik Janambhumi
32.	Kishanganj	26.0982° N, 87.9450°	ELight shaking for 10 sec, felt by a few persons	III	Dainik Bhaskar
33.	Malda	25.0108° N, 88.1411° E	Very light shaking for only a few sec.	III	Dainik Bhaskar
34.	Majuli	27.0016° N,	Moderate shaking, no damages, some cracks in mud		
	J	94.2243° E	houses, felt by all	V	Asomiya Pratidin, Khabar, Dainik Janambhumi
35.	Rangpo	27.1761° N, 88.5287° E	Light shaking for about 10 sec.	IV	Sikkim Express, PTI, Himalayan Times
36.	Kolkata	22.5726° N, 88.3639° E	Very light shaking for less than 5 sec.	III	The Telegraph, Anand Bazar Patrika, The Statesman
37.	Tura	25.5141° N, 90.2032° E	Shaking for 10-15 sec, felt by some	IV	The Shillong Times, PTI
38.	Bagdogra	26.6986° N, 88.3117° E	Light shaking for few seconds	III	Anand Bazar Patrika, PTI
39.	Biratnagar (Nepal)	26.4525° N, 87.2718° E	Very light shaking only for a few sec.	II	PTI, Kathmandu Post
40.	Chittagong	22.3569° N,	Weak shaking for 10-15 sec, felt by some	IV	Bangladesh Pratidin, PTI
	(Bangladesh)	91.7832° E	· · ·		,
41	Lhasa (Tibet)	29.6524°N, 91.1721°E	Very light shaking, felt by a few peoples	III	PTI
42	Sikkim	27.3799N, 88.5857E	Weak shaking for 10 sec, felt by a few peoples	III	Sikkim Express, PTI, Himalayan Times
43	Durgapur	24.4843N,	Weak shaking for 10 sec, felt by a few peoples	III	PTI, Aajkal, Anand Bazar
11	(West Bengal)	88.7448E	Shaking for 10-15 sec, felt by some peoples, ceiling fans	IV	Patrika The Telegraph, The Arunachal
44	Tawang	27.3909N, 91.8597E	and other hanging objects oscillates	1 V	Times
45	Haflong	25.1643N,	and other nanging objects oscillates		111103
	114110115	93.0124E	Moderate shaking for about 15 sec, felt by all.	V	Asomiya Pratidin, Khabar
		75.012TL			

B) Survey based reports

Sl. No.	Location	Coordinates	Report	EMS-98 scale
47	LOKD college, Dhekiajuli	26.7050°N, 92.498°E	Gov. structure, jolting for 40 sec, hard to stand stable, cracks in houses, visible rupture in paddy fields	VIII
48	Natun Chirajuli	26.6872°N, 92.4836°E	People heard explosion sound before jolting, breaking of glass objects, cracks in grounds as well as private buildings, hard to stand stable.	VIII
49	NumBagari	26.6752°N, 92.4955°E	People heard explosion sound before jolting, mud house collapsed, hard to stand still, well developed cracks in roads and paddy fields.	VIII

50	Dhekiajuli Bagan	26.7188°N, 92.4755°E	People heard explosion sound before jolting	VIII
51	Thelamara	26.7069°N, 92. 4272°E	Jolting about 40 sec. hard to stand stable.	VIII
52	Tiulip Bagan	26.6972°N, 92.4469°E	People heard explosion sound before jolting, 3 person injured due to tinsheet roof falling	VIII
53	Surjyapur	26.7297°N, 92.4677°E	Strong shaking for a minute, visible cracks and mud houses damaged.	VIII
54	Bagaribari Gaon	26.6766°N, 92.5002°E	Jolting about 40 sec. hard to stand stable, visible cracks in paddy fields,	VIII
	•		hard to stand stable	
55	Thelamara	92.5555°N, 26.6927°E	Jolting about 40 sec., 2 people injured, hard to stand stable.	VIII
56	Palash PatherGoan	92.4647°N, 26.7130°E	Jolting about 40 sec. Hard to stand stable.	VIII
57	Turipum Gaon	26.6304N, 92.4180E	Strong shaking for a minute, well devolped cracks in concrete houses	VIII
58	BhoiraGuri Gaon	26.6926N, 92.3703E	Strong shaking, walls fallen down of old and weak houses	VIII
59	Mazbat	26.8128N, 92.2667E	Jolting about 40 sec. Hard to stand stable.	VIII
60	ChapaiRoumari Gaor	1 26.8502N, 92.3703E	Jolting about 40 sec. Hard to stand stable.	VIII
61	Maidangpur	26.8564N, 92.4657E	Jolting about 40 sec. Hard to stand stable.	VIII
62	Mainapur	26.9434N, 92.6149E	Jolting about 40 sec. Hard to stand stable.	VIII
63	Tiulip Bagan	26.6978N, 92.4469E	Jolting about 40 sec. Hard to stand stable.	VIII
64	Joynagar Gaon	26.7047N, 92.4597E	Jolting about 40 sec. Hard to stand stable.	VIII
65	Dhekiajuli Bagan	26.7197N, 92.4775E	Jolting about 40 sec. Hard to stand stable.	VIII

C) Personal communication based reports

Sl. No.	Location	Coordinates	Report	EMS-98 scale
66	Morigaon	26.8900°N 92.1150°E	Ground cracks are visible in many localities, shaking continue for nearly 20s	VII
67	Rowta	26.6739° N, 92.8577° E	Peoples felt the shock outdoor and indoor. Plasters fell down in some houses	VI
68	Rangapara,	24.7936° N, 88.9318° E	Peoples felt the shock outdoor and indoor, shaking ground for 20 sec	VI
69	Baihata,	26.1445° N, 91.7362° E	Hanging objects moves, ground shake for nearly 20 sec	V
70	Udalguri	26.9518° N, 93.8592° E	Ground vibrates intensly for 20 sec. Glass windows cracks, hanging objects oscillates significantly	VII
71	Jakhalabondha	25.5788° N, 91.8933° E	People felt the shock indoor as well outdoor, shaking continues for more than 10 sec\	
72	Jagiroad	27.0844° N, 93.6053° E	Everyone felt the shock, ground vibrates	V
73	Bokakhat	26.5215° N, 88.7196° E	Vibration felt everywhere for 10 sec.	IV
74	Rupa	25.5941° N, 85.1376° E	Vibration felt everywhere for 10 sec.	IV
75	Bomdila	24.8949° N, 91.8687° E	Mild vibration felt people inside home	III
76	Silchar	24.8333°N, 92.7789°E	Vibration felt everywhere for 10 sec	IV
77	Tinsukia	24.4886°N, 95.3558° E	Vibration felt everywhere for 10 sec	IV
78	Kohima	25.6751°N, 94.1086° E	Mild vibration felt people inside home	III
79	Aizwal	23.7307°N, 92.7173° E	Mild vibration felt people inside home	III

Isoseist VIII

The isoseist VIII covered almost 800 square km in the Dhekialjuli sub-division. Some old houses in Dhekialjuli completely turned into rubbles. The glass windows and clay objects of many residential buildings were completely broken. The earthquake caused widespread surficial deformation; as many mud houses and old construction suffered considerable damages. The ground deformation, with ground fissures, cracks, sand-blow fountain formation, and soil liquefaction were observed everywhere in this region (Fig. 3). Long cracks in highways were visible at many places with a maximum slip

of around 12 cm in the area near to the epicenter (Fig. 2). The cracks are visible in many concrete buildings (Suppl. Fig. S2). Many sand-dykes were seen in paddy fields. Many individuals found it difficult to remain upright during the intense shaking. In newly constructed houses, plasters fell, water pipes were damaged and roads in the region have cracks. One senior citizen panicked and fell unconscious during the earthquake and did not survive. Although, there is no causality of livestock, as the earthquake was in the morning time, all were freed in the open field.





Fig. 2. Example of fractures and cracks occurring in many places around the Dhekiajuli region. The falling of bricks walls in the Dhekiajuli is shown in image B, collecting from Press Trust of India (PTI, 29 April, 2021).

Isoseist VII

The isoseist VII has more or less irregular shape and covers an area of about 8,000 km² and the major axis of the isoseist is aligned in the ENE-WSW direction. The Tezpur and Nagaon cities, which are ~30 km and ~45 km distant from the epicenter, and many towns, like Morigaon, Darrang, and Udalguri fall on VII isoseist. Considerable damage to mud houses, long cracks in concrete walls and joints, cracks in national highways, and tilting of multistory buildings were observed (Suppl. Fig. S2). The spillage of water from buckets and water tanks was also seen during the earthquake. In Tezpur, people felt intense shaking that lasted for 20 s -25 s, and it was hard to stand still. Some parts of wall plaster, bricks, and roof tiles fell, windows were broken, a few small and weakly built walls collapsed, pipes were damaged, and objects fell off from their position.

Isoseist VI

The isoseists VI covers major cities, Guwahati, Itanagar, and towns like, Rowta, Rangapara, Baihata, Jakhalabondha, Jagiroad that suffered moderate damages. More than 10 towns and 2000 villages felt shaking equivalent to intensity VI. The maximum damages were seen in the capital city of Guwahati, Assam state. Many high-rise buildings, like multistory hotels, and residential apartments suffered considerable damages, like long cracks, falling tiles, destroyed roofs, tilting of the building, etc. Long visible cracks were seen in Government, as well as private buildings in many localities, although no injuries happened due to these damages. At few places, weak and old-constructed churches, Temples, Hospitals, and RCC residential buildings suffered considerable damage. Swinging of fans, breaking of windows glass, and tiles falling from walls were reported from many places.

Isoseist V

The isoseist-V covered cities like Jorhat, Dibrugarh, Itanagar, Silchar, Shillong, and many small towns like Bokakhat, Rupa, Bomdila, etc. Some landslides were also seen in Bhairabkunda and Rupa (Suppl. Fig. S1). The indoor people felt shaking, hanging objects swing considerably, and glass windows rattled. Domestic livestock got uneasy and frightened. The older and poorly built structures suffered some damage (Suppl. Fig. S1). The ground-shaking lasted for around 15 sec and all were alerted by the sudden shock.

Isoseist IV

The isoseist IV area follows a similar pattern to isoseist V. The region pertaining to isoseist IV felt vibrations for 10-15 sec, but apparently, no damages occurred in this region. The damages were only seen because of diverse types of residential houses, but also due to the presence of buildings on different types of outcropping like heterogeneous rocks and Quaternary sediments. Mild shakings was felt at some places like Diphu, Haflong, Dimapur, Tinsukia (Assam), Kohima, Imphal, Aizwal, Thimphu, (Bhutan), Sylhet (Bangladesh), etc. Although Diphu (~110 km from epicenter) and Haflong town (~148 km) are located at a shorter distance from Dhekiajuli than Guwahati and Jorhat city, no damages were

reported and the ground shaking was also less, which can be attributed to the rocky outcrops at many places.

As per MSK-98 scale, the damage expected from the intensity scale is ascribed on Table 1 and we correlate the degree of observed damage with the MSK scale. On mapping the isoseists, it became evident that they are not circular or even elliptical, but are egg-shaped with the narrow end pointing approximately WSW indicating that the intensity of the shock was greater at the ENE-WSW end of this line than at the NNW-SSE end. This implies that a slip might occur in the northern edge of KFZ, in ENE-WSW along the Brahmaputra valley, in which the highest intensity was observed within the neighborhood of Dhekiajuli region.

The 28th April, 2021 Dhekiajuli earthquake left imprints of damage in different parts of Assam with massive liquefaction in and around Dhekiajuli. The earthquakeaffected regions were examined for ground failure effects like liquefaction, lateral spreading, water level changes, and development of wide fissures in open paddy fields and along the roads. Certain embankment failure was observed at several places. A good number of sandblasting and watering like phenomena is observed in different parts near the epicentral region (Fig. 3). Some fissures were up to a meter wide and tens of centimeters deep were seen, exposing liquified soil. Bhadran et al. 2022 reported 15 cm offset around the epicentral track. There were also substantial number of small fissures and ground cracks were observed in a100 sq. km area around the epicentral region. In the present earthquake, lateral displacement causing building collapses were less, since very few masonry buildings, and constructions were observed in the Dhekiajuli region. Recent study by Joshi et al. 2023 described the site amplification and liquefaction models of 28th April, 2021 earthquake in detail as well as showed spatial schematic model of the source zone within the Brahmaputra valley.

DISCUSSION AND CONCLUSION

The earthquakes along the KFZ follow NW-SE structural trend and it is found that the entire crust is seismogenic in nature (Bhattacharya *et al.* 2008). From the hypocentral distribution of events along the KFZ, it is observed that seismicity extends to 45 km depth, reaching the uppermost mantle, with 40 km average crustal thickness of the Brahmaputra basin (De & Kayal 1990; Bhattacharya *et al.* 2008; Kayal & Zhao 1998; Saikia *et al.* 2022). As the Dhekiajuli earthquake occurred at lower crust (~40 km), there was relatively less destruction. The damage distribution is very heterogeneous and isolated, which favors the deeper depth of the KFZ.

The KFZ with steep dip, nearly 75° towards NE, is very active owing to its transverse tectonics is the causative fault of the Dhekiajuli earthquake and has a prolonged history of many big to large earthquakes (Kayal 2001; Kayal 2008, Kayal *et al.* 2012; Bhattacharya *et al.* 2008; Dey *et al.* 2022). Focal mechanism solutions for well-constrained events in this fault zone yielded strike-slip solutions with high angle dip



Fig. 3. Photographs of soil liquefaction in the form of sand dykes and sand boils along with ground cracks occurred aftermath of the 28th April 2021 Dhekiajuli earthquake. The open ground crack image is collected from PTI, 28th April, 2021.

(Dasgupta et al. 1987; Kayal et al. 2012; Sharma et al. 2018). The fault plane solutions obtained from Dey et al. 2022 shows the Dhekiajuli earthquake is of reverse strike-slip nature having nodal planes, NP-1 (strike 335°, dip 69° and slip 134°) and NP-2 (strike 85°, dip 47° and slip 28°) and can be correlated to the source properties of KFZ earthquakes, wherein the 28th April, 2021 earthquake was triggered along a high angle dipping thrust plane trending NW-SE. The hypocentral location of the mainshock is obtained from NCS, New Delhi, where 14 stations from NER used to derive the location along with more than 10 stations outside NER (riseq.seismo.gov.in/riseq/earthquake/archive). The four sizeable aftershocks of the Dhekiajuli earthquake also show a strike-slip mechanism having nodal plane striking in the NW-SE direction (GCMT solution, Dev et al. 2022). It is also seen that the region had several moderate earthquakes showing reverse strike-slip mechanisms with nodal plane striking in NW-SE directions.

We observed that the Dhekiajuli earthquake caused more seismic damage more towards the Western and Eastern of the KFZ along the Brahmaputra valley plain, which is obvious due to the thick sedimentary layer of the Brahmaputra basin that also generated ground liquefaction along the valley (Fig. 4). Recent ground motion prediction study of Choudhury *et al.* 2021 inferred that observed ground accelerations are relatively high in the Brahmaputra basin due to the thick sedimentary cover, which is accountable for amplified ground

motion. This earthquake is well recorded at TZR broadband seismograph station, which is located at around 45 km distance from the epicenter. From the derived empirical scaling equations of the ground motion prediction study of Choudhury et al. 2022 we observed peak ground acceleration 0.0149 g in the TZR broadband seismic station. It is observed that relatively less damages are observed towards the north due to Himalayan thrust faults and south by the Naga-Disang Thrust, Naga hill range. The damage pattern of the 1950 Great Assam earthquake is also towards Brahmaputra valley and lesser damage towards the East, North, or South due to the presence of a continuous Himalayan orogeny belt (Mathur 1953, Poddar 1950). One of the major reasons for the relatively less damage during this earthquake is the fact that the earthquake is a deep-focus earthquake, so the impact of the shock got reduced though it is widely felt. Also, the epicentral region is sparsely populated, and all the life stocks and peoples are outdoors in the early hours of morning time.

METHODOLOGICAL LIMITATIONS AND SCOPE

The mapping methodology that we adopted during the course of the study yields effective insights into the intensity distribution and damage patterns associated with the Mw~6.1 Dhekiajuli earthquake. Notwithstanding, we must acknowledge certain limitations to enhance the comprehensive understanding of the findings and their potential applicability to similar seismic events.

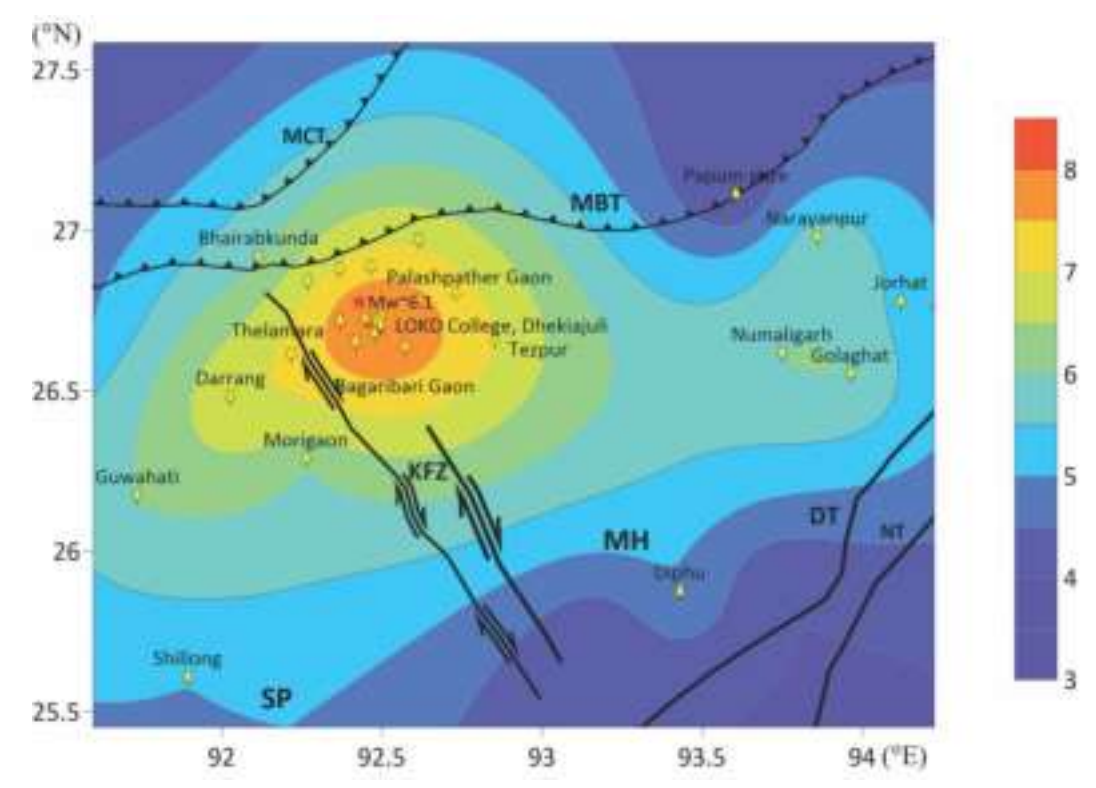


Fig. 4. The Regional Intensity distribution of the Dhekiajuli earthquake according to EMS-98 scale.

Mapping Constraints: The approach of intensity mapping largely depends on the availability and accuracy of ground-truth data from field surveys and media reports. Because of COVID-19 restrictions, we had limited access to potential damaged areas which hampered the resolution of our intensity map. Consequently, this constraint may affect the representation of the intensity distribution, especially in sparsely populated or remote regions where fewer field data points were available.

Sensitivity to Tectonic Settings: It is well established that the Kopili Fault Zone (KFZ) and surrounding areas, because of their diverse tectonic settings, influence the propagation of seismic waves and the resulting intensity distribution. Apart from this, differences in subsurface structures, such as sediment thickness and fault geometries, can lead to localized amplification or attenuation that may not be fully captured in a generalized mapping model. Since the Brahmaputra valley is recognized as a highly heterogeneous tectonic zone encompassing these traits, our methodology may have limited sensitivity to these variations.

Limitations in Attenuation Modeling: Although our mapping provides an empirical view of intensity attenuation across the region, modeling attenuation in such a complex tectonic setting remains challenging. The non-uniform attenuation patterns, potentially driven by variations in lithology and fault dynamics, are not fully accounted for in this study. Future work incorporating more refined attenuation models with site-specific amplification factors would improve the robustness of these findings.

Considering these methodological limitations, future studies could benefit from integrating high-resolution geophysical data and near-field strong-motion records to refine the spatial intensity patterns and attenuation characteristics. Despite these constraints, the present study provides a valuable foundation for understanding the seismic hazard in the KFZ and underscores the need for further research to enhance predictive models for similar tectonic environments.

CONCLUSION

The macro-seismic study carried out after the Dhekiajuli earthquake led us to present the following specific points:

- The intensity of the mainshock can help us to well demarcate the regions with different intensities, like VIII, VII, VI, V, and IV so on. The maximum intensity is VIII in the epicentral region, which covers an area of ~800 square km.
- There were numerable aftershocks clustering around the main shock for a week, including two aftershocks of M 3.9 and M 3.7, suggesting the triggering of multi-sources in the region for the release of seismic energy.
- Intensity attenuation in the seismic zone demonstrates asymmetry in the intensity distribution concerning the distance from epicenter location. The regions located on soft sediments of Brahmaputra Valley basin experienced higher shaking compared to hilly outcrop regions.
- By studying and evaluating the damage pattern, it is hard to find the rupture propagation, as whether it is along the KFZ or transverse to KFZ or along the hidden

Brahmaputra fault or any other hidden tectonics. The near-field strong motion data can provide clear image of rupture dynamics, require for extensive study of the Dhekiajuli earthquake and KFZ.

Acknowledgements: The authors acknowledge individual agencies that maintain earthquake catalogs, and publish them freely on GCMT and NCS (MoES) website. Figures are prepared in GMT (version 5.4) and Grapher5.1 software.

Author's contribution: HB and SS designed the research. HB visited the earthquake-affected sites and prepared the report, RB gives some valuable inputs of the work; SS, SB and BG drafted the paper, VS drew some figures. SC thoroughly checked the draft and discussed all the important findings of the work. Overall SS did the science planning and drafting of the manuscript by collecting all the inputs from all co-authors.

References

- Ambraseys, N.N., Douglas, J. 2004. Magnitude calibration of north Indian earthquakes. *Geophysics Journal International*, **159**, 165-206.
- Barman, P., Ray J.D., Kumar, A., Chowdhury, J.D., Mahanta, K. 2014. Estimation of present-day inter-seismic deformation in Kopili fault zone of north-east India using GPS measurements. *Geomatics, Natural Hazards and Risk*, doi: 10.1080/19475705.2014.983187.
- Bhattacharya, P.M., Mukhopadhyay, S., Majumdar, R.K., Kayal, J.R. 2008. 3-D seismic structure of the Northeast India and its implication for local and regional tectonics. *Journal of Asian Earth Sciences*, **33**, 25-41. doi: 10.1016/j.jseaes.2007.10.020
- Bhadran, A., Sreejith, K.M., Girishbai, D., Duarah, B.P., Agrawal, R., Gopinath, G. 2022. An appraisal of ground failure and hydro-geological changes associated with the April 28, 2021 M_w 6 Sonitpur earthquake, Assam, India, using field evidences and InSAR measurements. *Bulletin of Seismological Society of America*, 93, 1440-1451.
- BIS 2002. Indian standard criteria for earthquake resistant design of structures, Part 1: general provisions and buildings. *Bureau of Indian Standards*. *New Delhi*.
- Biswas, R. 2021. A brief review of the recent Assam Earthquake. *Physics Astronomical International Journal*, **5**(3), 90-91. DOI: 10.15406/paij.2021.05.00239
- Biswas, S., Coutand, I, Grujic, D., Hager, C. Stöckli, D., Grasemann, B. 2007. Exhumation and uplift of the Shillong plateau and its influence on the eastern Himalayas: New constraints from apatite and zircon (U-Th-[Sm])/He and apatite fission track analyses. *Tectonics*, 26, TC6013.
- doi: 10.1029/2007TC002125.
- Choudhury, P., Roy, K.S., Kamra, C., Chopra, S. 2022. Development of empirical relationship between the observed and the estimated ground acceleration values of small to moderate earthquakes in northwest (Gujarat) and northeast (NE) regions of India. *Geomatics, Natural Hazards and Risk*, 13 (1), 364-389.
- Dasgupta, S., Nandy, D.R. 1982. Seismicity and tectonics of Meghalaya Plateau, northeastern India. *Proc. VII symposium, Earthquake engineering, University of Roorkee*, 1, 19-24.
- Dasgupta, S., Mukhopadhyay, M., Nandy, D. R. 1987. Active transverse features in the central position of the Himalaya. *Tectonophysics*, 136, 255-264.
- De, Reena, Kayal, J.R. 1990. Crustal P-wave velocity and velocity-ratio study in northeast India by a microearthquake survey. Pure and Applied Geophysics, 134, 93-108.
- Dey, C., Baruah, S., Abdelwahed, M.F., Saikia, S., Kayal, J.R. et al. 2022. The April 28, 2021 Kopili Fault earthquake (M_w 6.1) in Assam Valley of Northeast India: Seismotectonic Appraisal, *Pure and Applied Geophysics*, 179(6), 2167-2182
- Gahalaut, V., Martin, S., Srinagesh, D., Kapil, S.L., Suresh, G., Saikia S., Kumar, V., Dadhich, H., Patel A., Prajapati, S., Shukla, H.P., Gautam J.L., Baidya, P.R., Mandal, S., Jain, A. 2016. Seismological, geodetic, macroseismic and historical context of the 2016 M_w 6.7 Tamenglong (Manipur) India earthquake. *Tectonophysics*, 688, 36-48. doi: 10.1016/j.tecto.2016.09.017

- Halder, L., Dutta, S.C., Sharma, R. P., Bhattacharya, S. 2021. Lessons learnt from post-earthquake damage study of Northeast India and Nepal during last ten years: 2021 Assam earthquake, 2020 Mizoram earthquake, 2017 Ambasa earthquake, 2016 Manipur earthquake, 2015 Nepal earthquake, and 2011 Sikkim earthquake. Soil Dynamics and Earthquake Engineering, 151, 106990.
- Joshi, M., Naik, S.P., Mohanty, A. et al. 2023. First hand observations from the April 28, 2021 Sonitpur (M_w 6.4) earthquake, Assam, India: possible mechanism involved in the occurrence of widespread ground effects. Geoscience Journal, 27, 225-239. https://doi.org/10.1007/s12303-022-0032-z
- Kayal, J.R., Zhao, D. 1998. Three-Dimensional Seismic Structure beneath Shillong Plateau and Assam Valley, Northeast India. Bulletin of Seismological Society of America, 88, 667-676.
- Kayal, J.R. 2001. Microearthquake activity in some parts of the Himalaya and the tectonic model. *Tectonophysics*, 339, 331-351.
- Kayal, J.R. 2008. Microearthquake Seismology and Seismotectonics of South Asia. Heidelberg, Germany: Springer.
- Kayal, J.R., Are° ev, S., Baruah, S., Tatevossian, R., Gogoi, N., Sanoujam, M., Gautam, J.L., Hazarika, D., Bora, D. 2010. The 2009 Bhutan & Assam felt earthquakes (Mw 6.3 and 5.1) at the Kopili fault in the northeast Himalaya region. *Geomatics, Natural Hazards & Risk,* 1, 273-281.
- Kayal, J.R, Arefiev, S.S., Baruah, S., Hazarika, D., Gogoi, N., Gautam, J.L., Baruah, S., Dorbath, C., Tatevossian, R. 2012. Large and great earthquakes in the Shillong plateau, Assam valley area of northeast India region: popup and transverse tectonics. *Tectonophysics*, 532-535,186-192.
- Mathur, L.P. 1953. Assam earthquake of 15th Aug., 1950 A short note on factual observations. *The Central Board of Geophysics*, **1**, 56-60.
- Nandy, D.R. 2001. Geodynamics of Northeastern India and the Adjoining Region. ACB publications, Calcutta, 209p.
- Nandy, D., Dasgupta, S. 1986. Application of remote sensing in regional geological studies-a case study in northeastern part of India. In Proceedings of the International Seminar on Photogrammetry and Remote Sensing for Developing Countries, Survey of India, New Delhi, pp. T.4-P./6.1-T.4-P./6.4.
- Poddar, M.C. 1950. The Assam earthquake of 15th August 1950. *Indian Mineralogy*, **4**(4), 167-176.
- Saikia, A. 2019. The unquiet river: A biography of the Brahmaputra. Oxford University Press, New Delhi, 583, ISBN-13: 9780199468119.
- Saikia, S., Chopra, S., Baruah, S., Singh, U.K. 2017. Sedimentary structure of the Brahmaputra basin from Receiver function analysis. *Pure and Applied Geophysics*, 174 (229), doi: 10.1007/s0002401613713.
- Saikia, S., Chopra, S., Gogoi, B., Sharma, A., Gautam, J.L., Borgohain, H., Singh, U. K. 2022. Variation in Moho topography and Poisson's ratio in the Eastern Himalayan arc. *Physics and Chemistry of the Earth*, Parts A/B/C, 103134.
- Singh, S.K., Srin, M.M., France-Lanord, C. 2005 Chemical erosion in the eastern Himalaya: major iron composition of the Brahmaputra and δ^{13} C of dissolved inorganic carbon. *Geochim. Cosmochim. Acta* **69**, 3573-3588.
- Sitharam, T.G. 2021. Earthquake: Seismic Risk at present situation in Assam very high. Press Note: Northeast Now, https://www.iitg.ac.in/cdmr/dir-msg.html.
- Sharma, S., Baruah, S. 2017. Modelling of the Kopili Fault based on slip rate, moment rate and seismic activity in Mikir Hills Plateau of Northeastern India. *Geomatics, Natural Hazards and Risk*, **8**(2), 1157-1172. doi: 10.1080/19475705.2017.1300609
- Sharma, V., Bora, D. K., Biswas, R. 2022. Spatio-temporal analysis of b-value prior to 28 April 2021 Assam Earthquake and implications thereof. *Annals of Geophysics*, 65(5): SE534.
- Sharma, S., Sarma, J. N., Baruah, S. 2018. Dynamics of Mikir hills plateau and its vicinity: Inferences on Kopili and Bomdila Faults in north-eastern India through seismotectonics, gravity and magneticanomalies. *Annals of Geophysics*, **61**(3), doi: 10.4402/ag-7516.
- Vernant, P., Bilham, R., Szeliga, W., Drupka, D., Kalita, S., Bhattacharyya, A.K., Gaur, V.K., Pelgay, P., Cattin, R., Berthet, T. 2014. Clockwise rotation of the Brahmaputra Valley relative to India: Tectonic convergence in the eastern Himalaya, Naga Hills, and Shillong Plateau. *Journal of Geophysical Research: Solid Earth*, 119, 6558-6571. doi: 10.1002/2014JB011196

Appendix: Supplementary Figures



Suppl. Fig. S1. A landslide occurred at Bhairabkund, near to MBT as a post-earthquake effect of the Dhekiajuli earthquake. The bottom penal shows the fallen of walls of old construction in rural locality of Jorhat, around 200 km away from the epicenter



Suppl. Fig. S2. Damage scenario in residential constructions at Tezpur town, nearly 30 km away from epicenter of the mainshock.

Petrogenesis of Granite and Granite gneiss of Lansdowne Klippe, Garhwal Lesser Himalaya, Uttarakhand, India

DEEPA ARYA^{1,*}, GUNJAN ARYA^{1,2}

¹Department of Geology, Kumaun University, Nainital-263002, India ²Department of Geology, B.D. Govt. P.G. College Jaiharikhal, Pauri Garhwal-24619, India *Email (Corresponding author): arya.earth11@gmail.com

Abstract: Granite emplaced into Lansdowne klippe of Garwal Lesser Himalaya occur as small, isolated body that rests over the Krol Formation of the Garhwal nappe. Field investigation and petrography show that Lansdowne Granite (LG) and Lansdowne Granite Gneiss (LGGn) are medium to coarse-grained rocks, composed of plagioclase+K-feldspar+quartz+biotite+muscovites+tremolite+sphene+apatite and zircon, exhibiting porphyritic and perthitic texture. Dynamic recrystallization in quartz and feldspar phenocrysts caused grain size reduction and asymmetric strain softening. The geochemical composition shows an affinity to high-K calcic-alkali to shoshonite series. Its peraluminous characteristics reflect a syn-collisional to post-orogenic tectonic setting and S-type nature. The LG and LGGn are enriched in LREE and relatively depleted in HREE, with prominent negative Eu anomalies with high Th-U, Y, and Pb contents, and low Ba, Sr, Ti, and Nb contents. The Rb/Sr versus Rb/Ba ratios indicate an origin from clay-poor, plagioclase-rich greywacke..

Keywords: Lansdowne Granite, Lansdowne Granite Gneiss, Petrography, Geochemistry, Peraluminous granite, S-type granite

INTRODUCTION

The Himalaya is subdivided, above the basal Indo-Gangetic plain, into the Sub-Himalaya, Lesser Himalaya, Greater Himalaya, Tethys Himalaya, and Trans-Himalaya. The Lesser Himalaya is separated from the Higher Himalaya by a tectonic lineament, the Main Central Thrust (MCT; Fig. 1A). There are several klippen in the Kumaun-Garhwal region of the Greater Himalayan crystallines overlying the thrust sheets i.e., Tons, Ramgarh and Berinag thrust. These klippen are situated above the low angle fault correlated with MCT (Celerier et al. 2009; Valdiya 1980b). One of them is the Lansdowne klippe situated in the Garhwal Himalaya (Fig. 1B). The Himalayan granites are categorized into Proterozoic (2200-1800 Ma; 1400-1200 Ma), Early Palaeozoic (600-500 Ma), Trans Himalayan plutonic complex (103-40 Ma), and collision-related Tertiary leucogranites (30-12 Ma) based on their age and tectonic setting (Islam 2005). The Lesser Himalayan belt, predominantly situated in south, forms a discontinuous mass composed of both gneissic and non-gneissic granite (Le Fort et al. 1986).

The study area lies in the district of Pauri Garhwal, Lesser Himalava, Uttarakhand, It lies between Latitude N29°40'0" to N29°51'30" and Longitude E 78°39'30" to E 78°41'30" in Geological Survey of India toposheet no. 53K/9. An isolated and small LG and LGGn body occurs around Lansdowne town. It rests over the Krol Formation of the Garhwal nappe. The LGGn forms a sheet thrust over Lansdowne metamorphites and is preserved as a synclinal outlier (Gupta 1976a, b). The previous work on the Lansdowne region has been done by Auden (1937) who suggested that the LG intruded into the underlying metamorphites before the formation of Garhwal thrust (pre-Miocene). Vishnoi (1971) elaborated about the geology of the area. Shanker and Ganesan (1973) considered LG an intrusive into underlying metmorphites (chandpurs / chails) (Fig. 2A&B). Rupke (1974) showed a sharp and rootless contact of gneiss with the

metamorphites. Both rock types have been grouped into a tectonic unit called Amri unit. Gupta (1976a) revealed that the LGGn is thrusted over the underlying metamorphites and called the tectonic contact the Lansdowne thrust. Shah & Patel (1978) forwarded a contrasting view and suggested a metasomatic origin for these gneisses based on their chemical analysis with metamorphites. Elsdon & Gupta (1981), based on petrochemical studies of the LGGn, indicate an initial magmatic origin with pronounced gneissosity due to later deformation.

Recently, Mishra *et al.* (2021), distinguished three different age groups of Chail granites, Lesser Himalaya crystalline sequence in Garhwal region. Paleoarchean (3.5 Ga), Neoarchean (2.78 Ga and 2.62 Ga), and Paleoproterozoic (2.1 Ga) depicting their magmatic origin based on geochemical characteristics. In the present study we aim to conduct petrographic studies and geochemical analyses of the LG and LGGn to understand their origin, tectonic settings, and magmatic evolution.

GEOLOGY AND FIELD RELATIONSHIP

The Lansdowne Formation comprises low-grade metasediments recognized within the Garhwal Nappe, and the formation can be divided into two distinct members: the lower Bijni and the upper Amri, which correspond to the Bijni quartzite and Amri phyllite, respectively (Auden 1937; Fuchs & Sinha 1978). In the Garhwal nappe the Bijni member is the lowest litho-unit, which lies above the sedimentary rocks of the Krol nappe and comprises quartzites, phyllites and schists (Auden 1937). The Amri phyllite is correlated with the Chandpur phyllite of the Chail nappe (Saklani 1993). Tectonically, the overlying Amri member is the Lansdowne Formation, marked by the Amri thrust (Valdiya 1980a). This region has been identified as Lansdowne metamorphic (Gupta 1976a, b) and Lansdowne crystalline (Valdiya 1980a). The Garhwal nappe includes deformed phyllite and schist, topped by a small exposure of LGGn. Furthermore, there is an

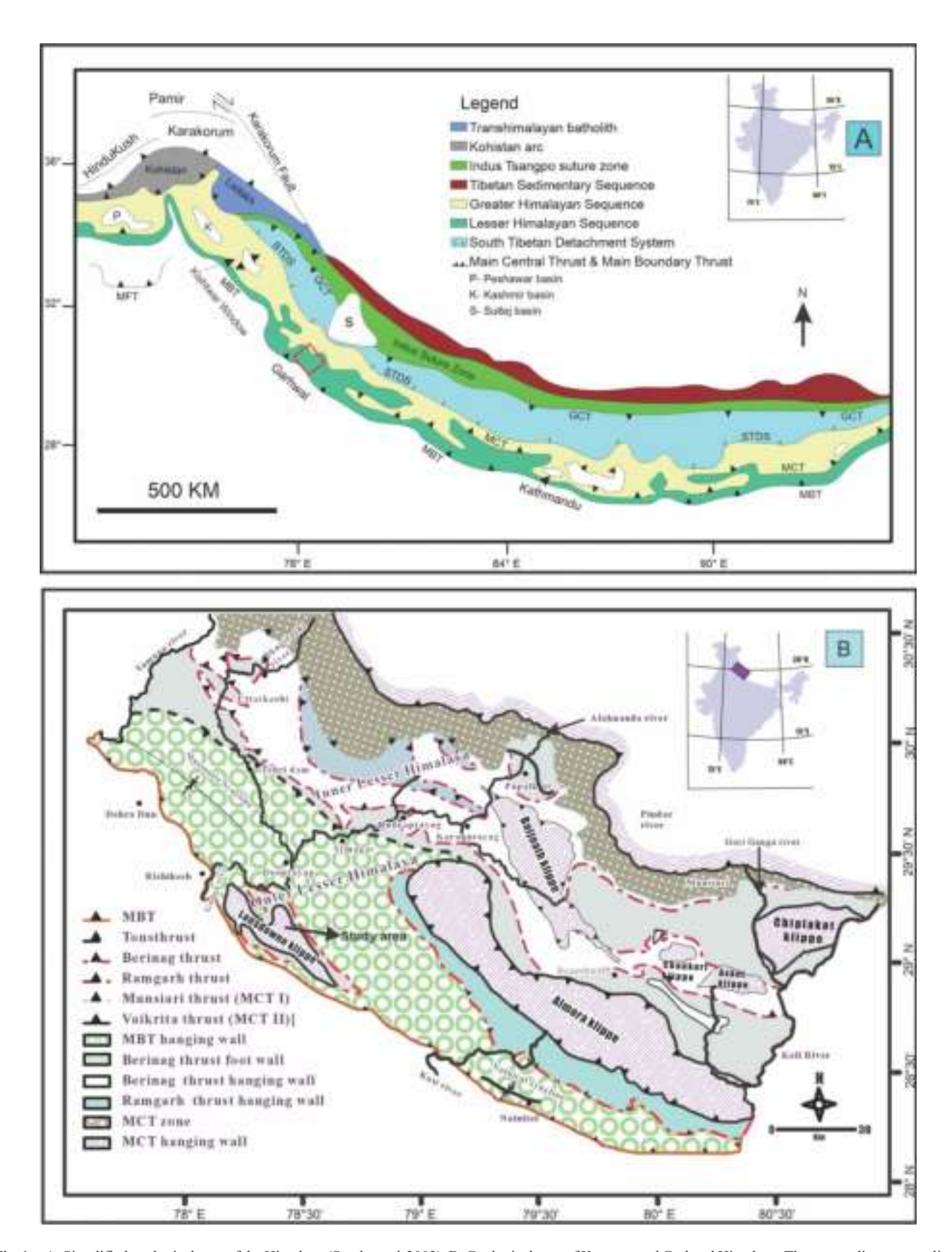
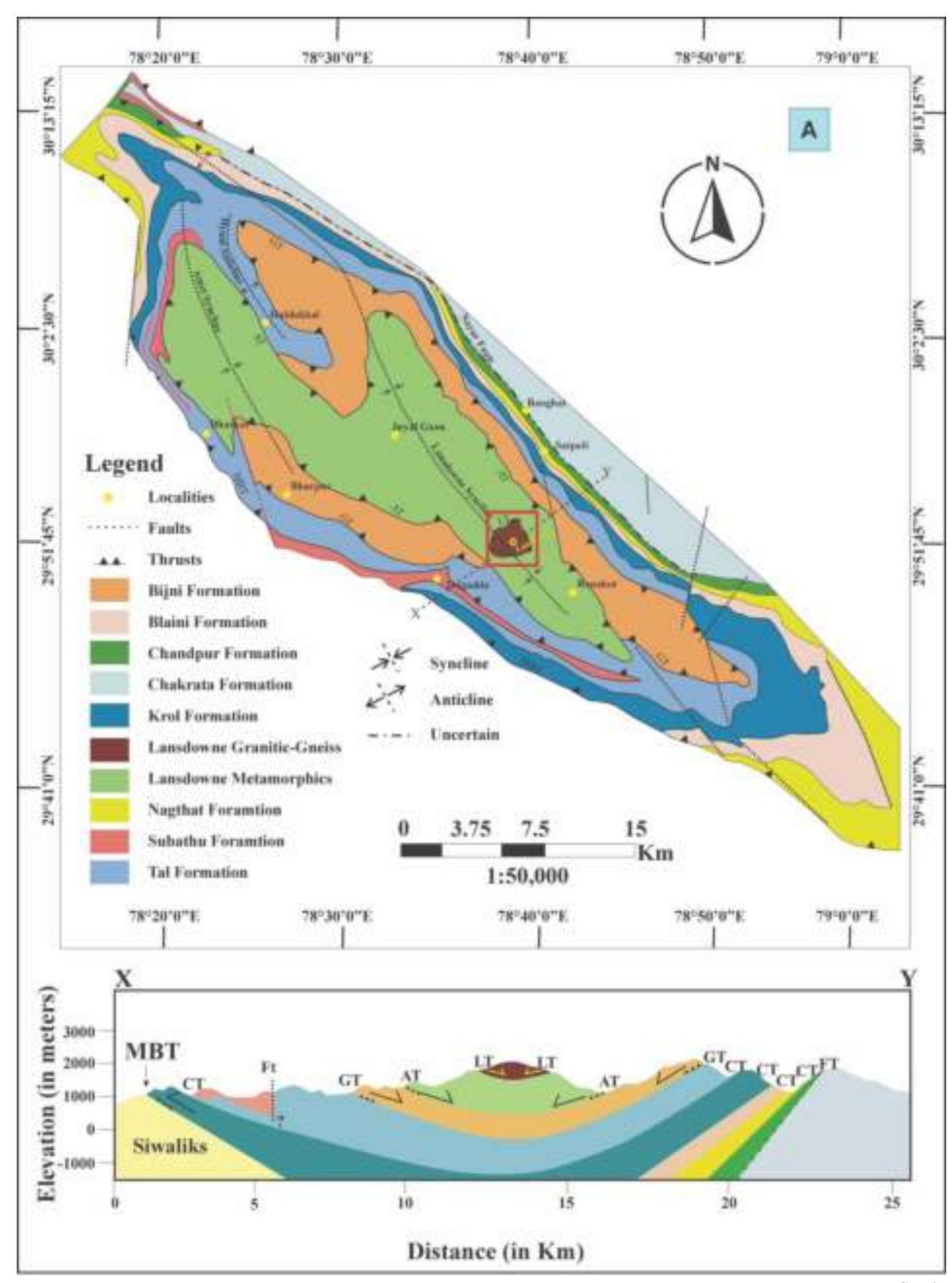


Fig. 1. A. Simplified geological map of the Himalaya (Searle *et al.* 2003). B. Geological map of Kumaun and Garhwal Himalaya. The metasediments overlie in several klippen on the MCT hanging wall (Valdiya 1980b).



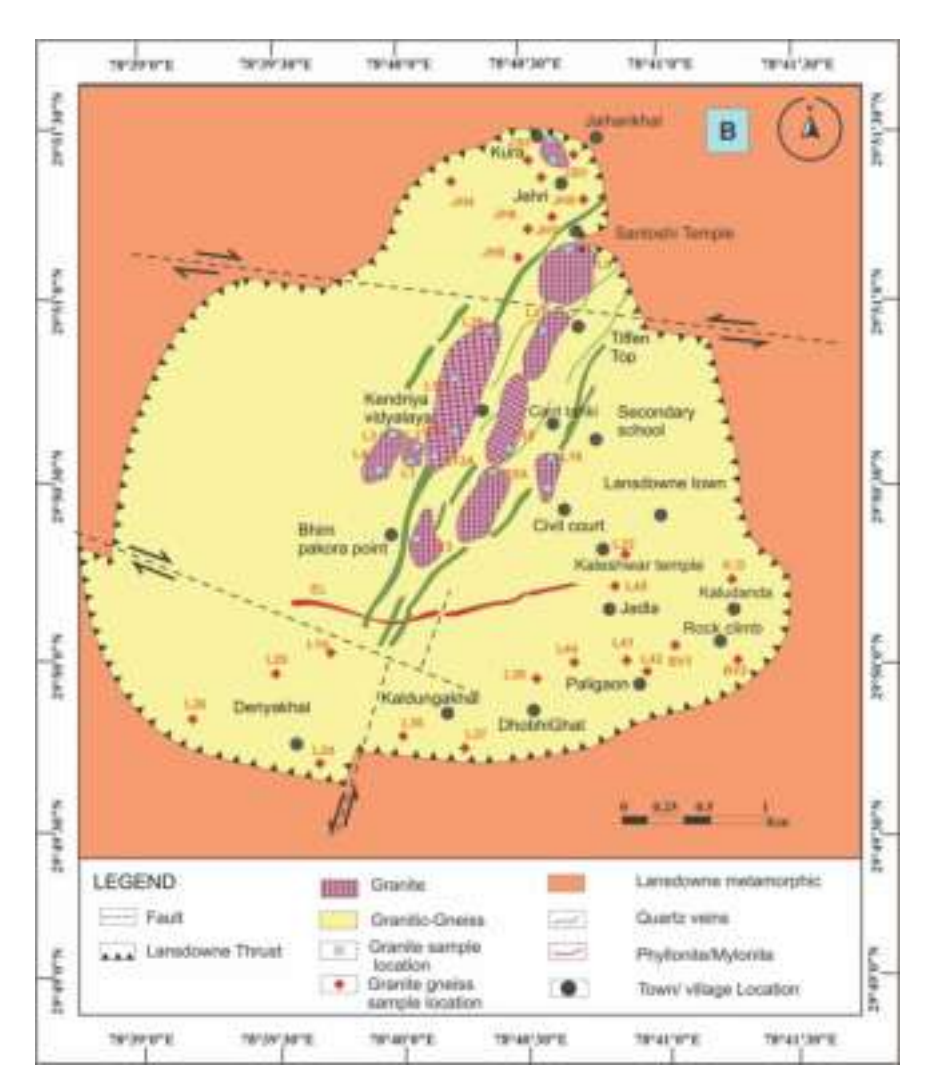


Fig. 2. A. Geological map with major lithology and tectonic units (after Fuchs & Sinha 1978: Valdiya 1980a) and B. Geological map of the study area.

evidence of granite intrusion in metasediments in Lansdowne area (Kumar & Daundhiyal 1980). A prominent tectonic contact is present between the LGGn and Lansdowne metasedimentary rocks, where the LG has metamorphosed into LGGn, leading to further deformation into augen gneiss and mylonite (Gupta 1976a, b).

The LG is an isolated and small pluton located around Lansdowne town (Fig. 3A). It is medium to coarse-grained, primarily composed of K-feldspar, plagioclase, quartz, muscovite, biotite, and tourmaline. Euhedral to subhedral feldspar and quartz phenocrysts, varying in size up to 1-2 inches in length, exhibits porphyritic texture (Fig. 3B). In certain areas, the LG shows greisen alteration due to chemical weathering, imparting a dark appearance (Fig. 3C). LGGn displays porphyroblasts of segregated feldspar, quartz and mica minerals, exhibiting augen structure (Fig. 3D). Its contact with phyllite depicts the close proximity to the Lansdowne thrust (Fig. 3E). It was intruded by thick quartz veins, extending up to 10-12 meters oriented in northeast-southwest direction (Fig. 3F).

ANALYTICAL METHOD

Petrography is carried out using a polarized light microscope (LEICA DM4 P) at the Department of Geology, Kumaun University Nainital. Thin section preparation and whole rock major oxides were analysed by X-Ray fluorescence (XRF) spectrometry at Wadia Institute of Himalayan Geology, Dehradun, Uttarakhand. Whole-rock major and trace element analysis was conducted with Wave Dispersive-X-ray Fluorescence (WD-XRF) using the Bruker-Tiger S8 instrument. Bulk analysis of rock samples was performed using homogenized fine powder and pressed powdered pellets made using polyvinyl alcohol. All were transferred into the die of the pellets preparation machine and pressed using a hydraulic pressure of 2000 kg/cm². The procedure uses the software SPECRAplus program QUANT to assist in editing quantitative analytical programs to evaluate and optimizing calibration.

PETROGRAPHY

The LG plagioclase crystals are medium to coarse-grained



Fig. 3. A. Outcrop of granite pluton LG, B. Leucocratic medium to coarse grained LG showing porphyritic texture. C. LG, rock showing dark appearance on the exposed surface. D. Porphyroblasts of segregated feldspar and quartz with mica creating foliation plane in LGGn. E. Contact of LGGn and phyllite determining the Lansdowne thrust. F. Thick quartz vein intrusions extend several meters in the LGGn.

exhibiting porphyritic and perthitic texture. In Section LG6 plagioclase phenocryst enclosed with subhedral to anhedral quartz intense sericitization occurred in the core of the crystal (Fig. 4A). The K-feldspar crystals are characterized by carlsbad and cross-hatched twinning with inclusions of zircon and apatite (Fig. 4B). Section L-13 exhibits coarse-grained interstitial micro perthite enclosing fine to medium-grained subhedral and highly sericitized plagioclase. In section L-6 quartz crystals are subhedral to anhedral, medium to coarse grained, colourless and highly fractured. They often exhibit interstitial space and show wavy extinction. Quartz contains inclusions of titanite (sphene), zircons, muscovite, and epidotes (Fig. 4C). Biotite in section JH-1 is associated with plagioclase, orthoclase, quartz, muscovite, and titanite. It appears segregated into interstitial spaces (Fig. 4D).

In LGGn, section L-39 exhibits alternate bands of quartz and muscovite (Fig. 4E). Section L-22 shows K-feldspar porphyroblasts showing dextral shear sense in LGGn. Fractures in the K-feldspar are filled by secondary quartz (Fig. 4F), depicting its transformation to megacrysts during postmagmatic deformation (Vernon 2004).

In section JH4, tourmaline is an accessory phase found as clusters of zoned, fractured, and coarse to medium-grained crystals (Fig. 4G). In section L-39 both muscovite and biotite define the foliation and the resulting gneissosity (Fig. 4H). Plagioclase crystals are normally zoned and shows albitic twinning (Fig. 4I).

WHOLE ROCK GEOCHEMISTRY

The whole rock geochemical data (major, trace, and REE elements) of LG (N=6) and LGGn (N=18) is given in

supplementary data table 1. The LG shows homogeneous SiO_2 (69.47-70.72 wt.%), and moderate variation in Al_2O_3 (16.76-17.18 wt.%), Na_2O (3.75-4.32 wt.%) and K_2O (4-93-5.38 wt.%). The values for Fe₂O3, CaO, MgO, P2O5, MnO, and TiO_2 are 0.99-1.27 wt.%, 0.55-0.69 wt.%, 0.14-0.21 wt.%, 0.28-0.33 wt.%, 0.03 wt.% and 0.10-0.14 wt.%, respectively. The variations for Ba, Rb, Cr are 147-193 ppm, 364-395 ppm and 60-135 ppm, respectively. There are moderate variations in Sr (54-69 ppm), Zr (38-57 ppm), Pb (38-59 ppm), Zn (42-60 ppm), Ni (13-16 ppm), Ga (20-24 ppm), Y (34-37 ppm) and Nb (10-16 ppm) and considerably low contents of Co, Sc, V, Th, U and Cu contents (3-5 ppm, 1-3 ppm, 7-10 ppm, 4-7 ppm, 2.0- 2.6 ppm and 8-12 ppm), respectively.

For LGGn the values of SiO₂ are 68.30-72.71 wt.%, moderate variation in Al₂O₃ (16.19-17.77 wt.%), low Na₂O (3.59-4.47 wt.%) and K₂O (4.04-5.42 wt.%). The contents of Fe₂O₃, CaO, MgO, P₂O₅ MnO, and TiO₂ are 0.86-1.14 wt.%, 0.50-0.77 wt.%, 0.14-0.25 wt.%, 0.28-0.42 wt.%, 0.03-0.05 wt.% and 0.09-0.16 wt.%, respectively (Table 2). They exhibit high variations in Ba (79-222 ppm), Rb (301-488 ppm), and Cr (21-188 ppm), moderate in Sr, Zr, Pb, Zn, Ni, Ga, Y, and Nb (25-70 ppm, 38-59 ppm, 31-62 ppm, 32-74 ppm, 10-24 ppm, 20-28 ppm, 31-46 ppm and 11-22 ppm) and considerably low amounts of Co (3-8 ppm), Sc (1-4 ppm), V (5-14 ppm), Th (4-9 ppm), U (2.0-2.8 ppm) and Cu (4-13 ppm).

Geochemical data shows that the LG and LGGn plot are within the granite field in Na₂O+ K₂O versus SiO₂ diagram (Fig. 5A). In the normative parameters of Q'-ANOR (Streckeisen & Le Maitre 1979) diagram, they fall into the

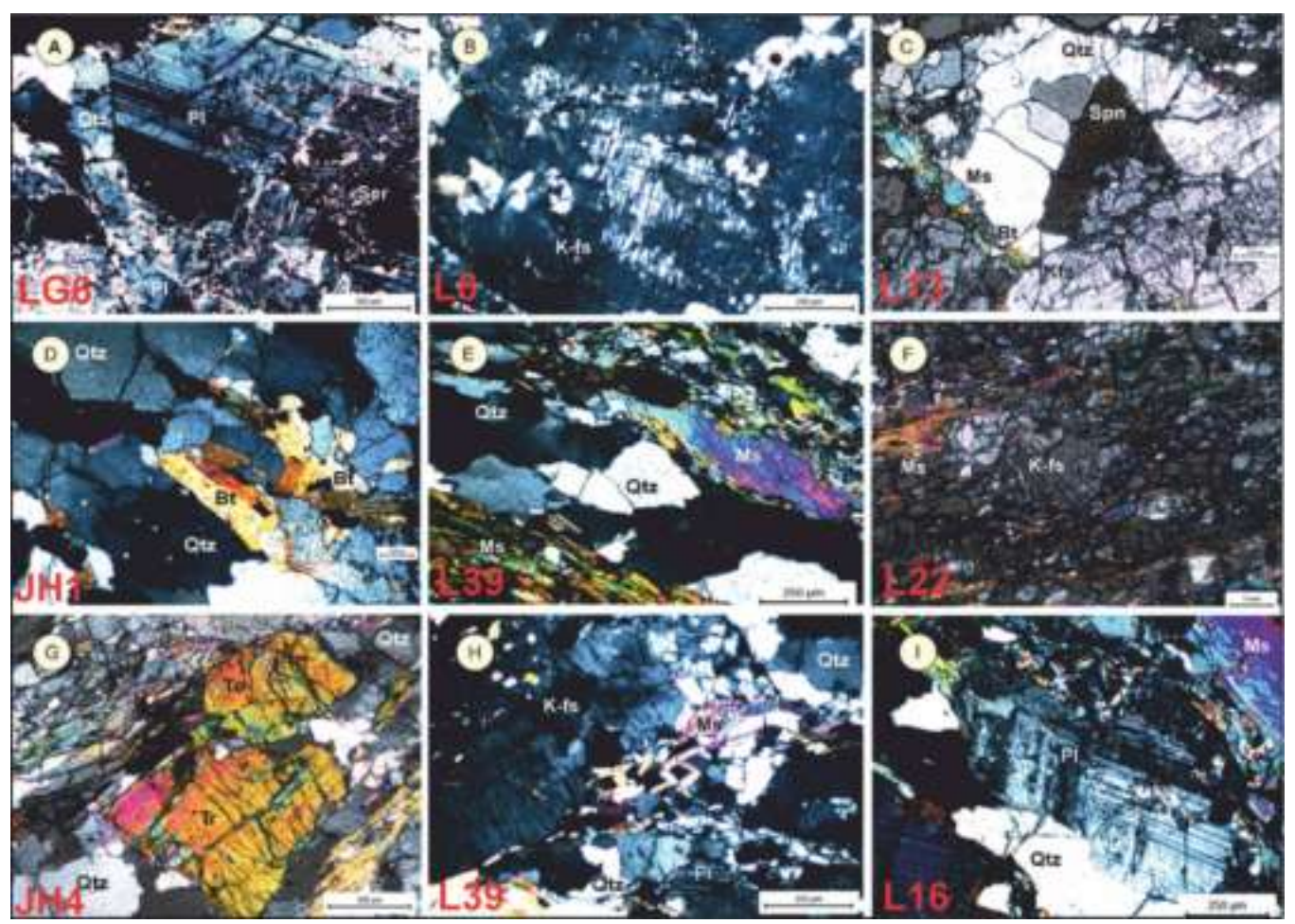


Fig. 4. A. Coarse-grained plagioclase phenocryst enclosed within subhedral to anhedral quartz in LG. Sericitization is intense in the core of the crystals. B. The Kfs crystals are characterized by carlsbad and polysynthetic (cross-hatched and carlsbad) twinning with tiny inclusions of zircon and apatite. C. Highly fractured subhedral to anhedral quartz crystals contain inclusions of titanite (sphene). D. Biotite crystals appear as mafic segregate and occupy interstitial spaces. E. LGGn showing alternate bands of quartz and muscovite. F. K-feldspar porphyroblasts showing dextral shear sense G. A high-relief tourmaline found as clusters of zoned and fractured. H. Muscovite and biotite defined foliation. I. Normal zoning in plagioclase reveal sodic nature and exhibits albitic twinning.

alkali feldspar granite field (Fig. 5B). They exhibit distinct ferroan trends (Fig. 6A). Most of the samples show alkalic composition while, a few fitting in the alkalic-calcic field (Fig. 6B), and depicting a peraluminous nature (Fig. 6C). The K₂O versus SiO₂ binary plot, defines them in the high K calcalkaline to shoshonite magma series (Fig. 7A). In the AFM plot all the samples fall in the calc-alkaline field towards the alkaline corner (Fig. 7B). The chondrite-normalized (Anders & Grevesse 1989) REE patterns show moderate LREE enrichment (La/Sm)_N=2.66-3.12) with highly depleted HREE (Gd/Yb)_N=4.63-5.11) resulting in a significant fractionated pattern ((La/Yb)_N=16.94-20.35) (Fig. 8A), with moderate to high negative Eu anomalies (Eu_N/Eu*=0.29-0.92). In primitive mantle normalized (McDonough and Sun, 1995) multi-elemental variation diagrams (Fig. 8B), LG show prominent negative anomalies for Ba, Sr, Ti, and Nb, a slightly negative anomaly for Yb, positive anomaly for Th-U and Y, a very prominent positive anomaly for Pb. The chondrite normalized REE patterns indicates a very high degree of LREE to HREE fractionation (La_N/Yb_N=14.63-21.48),

prominent negative Eu anomalies ($Eu_N/Eu_N^*=0.24-0.73$), and almost inclined HREE patterns ($Gd_N/Yb_N=3.46-5.40$) in LGGn. In the primitive mantle-normalized spider diagrams (McDonough and Sun, 1995), LGGn show prominent negative anomalies for Ba, Sr, Ti, and Nb, a slightly negative anomaly for Y, a positive anomaly for Th-U, and a very prominent positive anomaly for Pb.

DISCUSSION

The mineral assemblage of the LG and LGGn, including K-feldspar, plagioclase, quartz, muscovite, biotite, tourmaline, sphene, zircon, and apatite corresponds to S-type granite (Chappell & White 1974, 1992; Mishra *et al.* 2021). Perthitic texture from exsolution between two intergrowth feldspars suggest sub-solvus conditions. Slow cooling and late crystallization of magma give rise to the porphyritic texture of the rock. Carlsbad and albite twinning in plagioclase and perthite in K- feldspar suggest slow magma cooling and changing chemical compositions during fractional crystallization (Winter 2014).

 Table 1. Whole-rock (wt. %), trace element (ppm) and REE (ppm) analysis of LG from Lansdown klippe.

		41 /	41 /			1.1	
S.N.	1.00	2.00	3.00	4.00	5.00	6.00	7.00
Sample No.	L13	L15	L16	L19	L21	L45	JH2
SiO ₂	69.50	70.72	70.19	69.47	70.15	69.79	69.35
TiO ₂	0.12	0.12	0.10	0.13	0.14	0.12	0.09
Al_2O_3	17.18	16.83	16.98	16.98	16.76	16.96	17.00
Fe_2O_3	1.27	1.29	0.99	1.38	1.48	1.31	1.16
MnO	0.03	0.03	0.03	0.03	0.03	0.03	0.05
MgO	0.19	0.18	0.14	0.20	0.21	0.18	0.15
CaO Na,O	0.69 4.17	0.55 3.75	0.63 4.32	0.65 3.81	0.63 3.82	0.63 4.28	0.53 4.14
K ₂ O	5.15	5.15	5.38	5.02	5.18	4.93	4.75
P_2O_5	0.33	0.30	0.28	0.33	0.33	0.32	0.42
LOI	1.48	1.81	1.46	1.60	1.65	1.35	.50
TOTAL	98.63	98.92	99.04	98.00	98.73	98.55	97.64
A/CNK	0.27	1.34	1.21	1.32	1.31	1.26	1.32
A/NK	1.38	1.43	1.31	1.45	1.41	1.37	1.42
Mg#	95.83	94.83	95.45	95.59	95.45	95.45	91.38
$Fe_2O_3/(Fe_2O_3+MgO)$	0.87	0.88	0.88	0.87	0.88	0.88	0.89
Norm	24.54	20.71	22.51	25.24	27.20	25.22	26.71
qtz	24.71	28.61	23.71	27.34	27.38	25.32	26.74
crn	4.28 30.43	4.81 30.44	3.58 31.79	4.89 29.67	4.51 30.61	4.20 29.14	5.05 28.07
or ab	35.28	31.73	36.56	32.24	32.32	36.22	35.03
an	1.27	0.77	1.30	1.07	0.97	1.04	0.00
hy	0.47	0.45	0.35	0.50	0.52	0.45	0.37
ilm	0.06	0.06	0.06	0.06	0.06	0.06	0.11
hm	1.27	1.29	0.99	1.38	1.48	1.31	1.16
ru	0.09	0.09	0.07	0.10	0.11	0.09	0.03
ap	0.78	0.71	0.66	0.78	0.78	0.76	0.95
TRACE							
ELEMENTS (PPM)	1.67.00	102.00	171.00	170.00	102.00	1.47.00	70.00
Ba Rb	167.00 365.00	193.00 366.00	171.00 364.00	178.00 368.00	183.00 377.00	147.00 395.00	79.00 438.00
Sr	69.00	63.00	68.00	61.00	63.00	54.00	34.00
Y	35.00	35.00	34.00	35.00	36.00	37.00	46.00
Zr	50.00	57.00	38.00	51.00	54.00	49.00	41.00
Nb	14.00	13.00	10.00	15.00	16.00	16.00	20.00
Cr	135.00	104.00	59.00	89.00	94.00	60.00	25.00
Ni	13.00	13.00	16.00	14.00	15.00	16.00	24.00
Co	5.00	3.00	3.00	5.00	3.00	4.00	4.00
Sc	2.00	2.00	2.00	3.00	1.00	2.00	0.90
V Cu	9.00 8.00	9.00 9.00	7.00 12.00	8.00 9.00	10.00 8.00	7.00 8.00	5.00 7.00
Pb	48.00	49.00	59.00	42.00	42.00	38.00	35.00
Zn	52.00	51.00	42.00	57.00	61.00	60.00	67.00
Ga	23.00	21.00	20.00	22.00	22.00	24.00	26.00
Th	6.00	6.00	4.00	7.00	7.00	6.00	5.00
U	2.30	2.40	2.00	2.30	2.60	2.50	2.20
RATIO	5.0 0	5 0			7 .00	7.31	10.00
Rb/Sr	5.29	5.8	5.35	6.03	5.98	7.31	12.88
Rb/Ba	2.19	1.9	2.13	2.07	2.06	2.69	5.54
CaO/Na ₂ O Mol. A/CNK	0.17 0.27	0.15 1.34	0.15 1.21	0.17 1.32	0.16 1.31	0.15 1.26	0.13 1.32
RARE EARTH ELEN		1.34	1.21	1.52	1.31	1.20	1.32
La	13.72	16.15	7.58	9.69	13.72	11.32	9.31
Ce	27.53	36.92	16.13	22.40	30.06	24.82	20.96
Pr	3.18	3.84	1.71	2.26	3.24	2.71	2.23
Nd	10.49	13.57	5.87	7.85	10.81	9.21	7.83
Sm	2.98	3.62	1.52	2.19	3.15	2.60	2.19
Eu	0.56	0.63	0.46	0.38	0.47	0.33	0.20
Gd Tb	2.84 0.49	3.63 0.63	1.50 0.25	2.22 0.40	3.19 0.55	2.48	2.15
Dy	2.43	3.07	1.27	1.93	2.60	0.41 1.93	0.39 1.82
Но	0.30	0.37	0.16	0.24	0.31	0.25	0.22
Er	0.70	0.85	0.35	0.58	0.71	0.53	0.50
Tm	0.08	0.10	0.04	0.07	0.08	0.07	0.06
Yb	0.50	0.60	0.26	0.40	0.52	0.42	0.35
Lu		0.08	0.04	0.05	0.07	0.05	0.05
	0.07						
∑REE	65.88	84.05	37.13	50.65	69.47	57.14	48.26
∑REE LaN/SmN	65.88 2.89	2.80	3.12	2.77	2.73	2.72	2.66
∑REE LaN/SmN Gd/Yb	65.88 2.89 4.66	2.80 5.00	3.12 4.80	2.77 4.63	2.73 5.11	2.72 4.88	2.66 5.03
∑REE LaN/SmN	65.88 2.89	2.80	3.12	2.77	2.73	2.72	2.66

 Table 2. Whole-rock (wt. %), trace element (ppm) and REE (ppm) analysis of LGGn from Lansdown klippe.

S.N. Sample No.	1 BV1	2 EL	3 JH1	4 JH4	5 JH6	6 KG	7 L4	8 L6	9 L22
SiO,	69.47	68.38	70.04	71.46	71.56	68.58	69.71	69.00	68.30
TiO ₂	0.13	0.15	0.11	0.14	0.10	0.14	0.10	0.12	0.15
Al_2O_3	17.07	17.42	16.92	16.24	16.35	17.77	17.04	17.34	17.64
Fe_2O_3	1.41	1.66	1.21	1.65	1.14	1.51	1.03	1.32	1.52
MnO	0.03	0.03	0.03	0.04	0.04	0.03	0.03	0.03	0.03
MgO	0.21	0.31	0.16	0.21	0.14	0.22	0.15	0.18	0.22
CaO	0.64	0.77	0.61	0.58	0.50	0.50	0.58	0.61	0.63
Na ₂ O K ₂ O	3.94 4.96	3.79 4.79	4.47 4.71	3.86 4.18	4.12 4.60	3.59 4.65	4.10 5.36	3.99 4.94	3.72 5.01
P_2O_5	0.32	0.32	0.38	0.33	0.37	0.32	0.28	0.34	0.36
LOI	1.65	1.75	1.49	1.64	1.66	2.29	1.84	1.92	2.14
TOTAL	98.18	97.62	98.64	98.69	98.92	97.31	98.38	97.87	97.58
A/CNK	1.32	1.36	1.25	1.37	1.30	1.51	1.25	1.34	1.39
A/NK	1.44	1.53	1.36	1.49	1.39	1.62	1.36	1.46	1.53
Mg#	12.96	15.74	11.68	11.29	10.94	12.72	12.71	12.00	12.64
$Fe_2O_3/(Fe_2O_3+MgO)$ Norm	0.87	0.84	0.88	0.89	0.89	0.87	0.87	0.88	0.87
qtz	26.80	26.80	25.55	32.39	29.76	29.41	24.68	26.28	26.83
crn	4.82	5.37	4.27	5.10	4.57	6.69	4.11	5.13	5.81
or	29.31	28.31	27.35	24.70	27.19	27.48	31.68	29.19	29.61
ab	33.34 1.08	32.07 1.73	37.82 0.54	32.66 0.72	34.86 0.06	30.38 0.39	34.69 1.05	33.76 0.81	31.48 0.77
an hy	0.52	0.77	0.54	0.72	0.35	0.55	0.37	0.81	0.77
ilm	0.06	0.06	0.06	0.32	0.09	0.06	0.06	0.45	0.06
hm	1.41	1.66	1.21	1.65	1.14	1.51	1.03	1.32	1.52
ru	0.10	0.12	0.08	0.10	0.06	0.11	0.07	0.09	0.12
ap TRACE ELEMENTS (0.76 PPM)	0.76	0.90	0.78	0.88	0.76	0.66	0.81	0.85
Ba	160.00	222.00	109.00	91.00	110.00	167.00	191.00	159.00	167.00
Rb	388.00	301.00	463.00	409.00	488.00	372.00	386.00	401.00	377.00
Sr	59.00	70.00	46.00	34.00	44.00	47.00	62.00	55.00	59.00
Y	37.00	31.00	41.00	39.00	42.00	36.00	36.00	38.00	36.00
Zr Nb	51.00 16.00	59.00 13.00	44.00 17.00	55.00 22.00	38.00 16.00	55.00 18.00	45.00 11.00	51.00 17.00	54.00 17.00
Cr	21.00	66.00	26.00	60.00	31.00	46.00	78.00	23.00	21.00
Ni	16.00	10.00	17.00	18.00	17.00	15.00	15.00	16.00	15.00
Co	3.00	8.00	6.00	3.00	6.00	4.00	8.00	3.00	8.00
Sc	1.40	2.60	2.30	1.40	1.60	2.10	2.60	1.20	1.20
V	9.00	14.00	7.00	8.00	6.00	9.00	6.00	8.00	10.00
Cu	10.00	7.00	4.00	12.00	6.00	11.00	9.00	9.00	9.00
Pb	44.00	42.00	36.00	31.00	43.00	61.00	48.00	41.00	38.00
Zn	61.00	55.00	59.00	74.00	59.00	64.00	43.00	58.00	63.00
Ga Th	26.00 7.00	21.00 8.00	27.00 6.00	28.00 9.00	20.00 4.00	25.00 9.00	22.00 6.00	26.00 7.00	22.00 8.00
U	2.00	2.70	2.50	2.80	2.20	2.00	2.50	2.40	2.80
RATIO	2.00	2.70	2.00	2.00	2.20	2.00	2.00	2	2.00
Rb/Sr	6.58	4.3	10.06	12.03	11.09	7.91	6.22	7.29	6.39
Rb/Ba	2.43	1.36	4.25	4.5	4.44	2.23	2.02	2.52	2.26
CaO/Na2O	0.15	0.2	0.14	0.15	0.12	0.14	0.14	0.15	0.17
Mol. A/CNK RARE EARTH ELEM		1.36	1.25	1.37	1.30	1.51	1.25	1.34	1.39
La	13.91	13.44	9.33	14.24	5.99	16.38	11.30	17.27	9.38
Ce	31.43	28.33	16.98	31.99	6.71	33.39	25.40	36.71	18.59
Pr Nd	3.31 11.50	3.07 10.50	2.26 7.11	3.44 11.85	1.59 4.08	3.83 12.77	2.74 9.35	4.05 13.60	2.21 7.34
Sm	3.21	2.73	2.25	3.32	1.56	3.52	2.52	3.80	2.22
Eu	0.44	0.58	0.28	0.26	0.20	0.44	0.52	0.52	0.35
Gd	3.08	2.64	2.11	3.29	1.50	3.45	2.45	3.61	2.26
Tb	0.53	0.47	0.38	0.55	0.27	0.57	0.41	0.61	0.40
Dy	2.56	2.39	1.82	2.63	1.25	2.60	2.03	3.02	2.00
Но	0.31	0.32	0.22	0.32	0.16	0.32	0.25	0.36	0.26
Er	0.73	0.80	0.50	0.79	0.34	0.77	0.58	0.83	0.59
Tm Yb	0.08 0.52	0.10 0.63	0.07 0.38	0.10 0.56	0.05 0.26	0.10 0.53	0.07 0.43	0.10 0.57	0.07 0.44
Lu	0.32	0.03	0.38	0.36	0.26	0.33	0.43	0.37	0.44
and the second s									
Σ REE	71.69	66.08	43.72	73.44	23.99	78.73	58.12	85.16	46.17

Table 2. *Continue table 2*...

S.N. Sample No.	10 L23	11 L25	12 L30	13 L31	14 L33	15 L35	16 L37	17 L42
SiO ₂	69.28	72.71	70.58	70.67	70.27	68.99	70.22	70.20
TiO ₂	0.12	0.11	0.13	0.12	0.12	0.12	0.16	0.11
Al_2O_3	17.45	16.19	16.76	16.68	16.95	17.22	16.62	16.76
Fe_2O_3	1.28	0.86	1.44	1.28	1.31	1.33	1.78	1.14
MnO	0.03	0.05	0.04	0.03	0.03	0.04	0.04	0.03
MgO	0.18	0.19	0.19	0.18	0.19	0.19	0.25	0.16
CaO	0.57	0.56	0.64	0.63	0.59	0.61	0.66	0.60
Na ₂ O	3.96	4.34	4.09	3.94	4.09	4.12	3.65	3.94
K ₂ O	5.42	4.04	5.02	4.88	4.91	4.80	4.47	5.18
P_2O_5	0.29	0.38	0.36	0.32	0.32	0.34	0.35	0.35
LOI	2.05	1.74	1.53	1.39	1.40	1.66	1.56	1.41
TOTAL	98.58	99.43	99.25	98.73	98.78	97.76	98.20	98.47
A/CNK A/NK	1.30 1.41	1.30 1.41	1.27 1.38	1.28 1.42	1.29 1.41	1.33 1.44	1.39 1.53	1.28 1.39
Mg#	12.33	18.10	11.66	12.33	12.67	12.50	12.32	12.31
Fe ₂ O ₃ /(Fe ₂ O ₃ +MgO)	0.88	0.82	0.88	0.88	0.87	0.88	0.88	0.88
Norm	0.00	0.62	0.00	0.00	0.67	0.00	0.00	0.00
qtz	24.84	31.60	26.95	28.37	27.05	26.03	31.09	26.93
crn	4.73	4.57	4.30	7.54	4.60	4.95	5.42	4.42
or	32.03	23.88	29.67	28.84	29.02	28.37	26.42	30.61
ab	33.51	36.72	34.61	33.34	34.61	34.86	30.89	33.34
an	0.93	0.30	0.82	1.04	6.84	0.81	0.99	0.69
hy	0.45	0.47	0.47	0.45	0.47	0.47	0.62	0.40
ilm	0.06	0.11	0.09	0.06	0.06	0.09	0.09	0.06
hm	1.28	0.86	1.44	1.28	1.31	1.33	1.78	1.14
ru	0.09	0.05	0.09	0.09	0.09	0.08	0.12	0.08
ap	0.69	0.90	0.85	0.76	0.76	0.81	0.83	0.83
TRACE ELEMENTS (P)		00.00	146.00	155.00	152.00	1.40.00	124.00	160.00
Ba Rb	205.00 379.00	80.00 411.00	146.00 408.00	155.00 362.00	153.00 397.00	140.00 393.00	134.00 386.00	160.00 399.00
Sr	67.00	25.00	59.00	59.00	56.00	50.00	49.00	59.00
Y	35.00	39.00	38.00	35.00	37.00	37.00	36.00	38.00
Zr	46.00	44.00	53.00	48.00	50.00	48.00	58.00	46.00
Nb	14.00	18.00	17.00	14.00	16.00	16.00	20.00	15.00
Cr	158.00	280.00	188.00	25.00	61.00	55.00	68.00	44.00
Ni	15.00	13.00	18.00	15.00	19.00	19.00	13.00	15.00
Co	7.00	6.00	7.00	8.00	8.00	7.00	5.00	6.00
Sc	3.00	3.50	2.60	1.70	2.00	2.70	1.80	2.00
V	4.00	6.00	7.00	8.00	7.00	8.00	10.00	6.00
Cu	10.00	4.00	9.00	11.00	13.00	13.00	8.00	7.00
Pb	53.00	11.00	59.00	55.00	41.00	36.00	34.00	62.00
Zn	54.00	32.00	62.00	54.00	59.00	59.00	70.00	51.00
Ga	24.00	22.00	26.00	23.00	25.00	25.00	24.00	21.00
Th U	5.00 2.30	6.00 2.40	7.00 2.00	5.00 2.00	5.00 2.00	5.00 2.10	8.00 2.70	6.00 2.50
RATIO	2.30	2.40	2.00	2.00	2.00	2.10	2.70	2.50
Rb/Sr	5.66	16.44	6.92	6.14	7.09	7.86	7.88	6.76
Rb/Ba	1.85	5.14	2.8	2.34	2.6	2.81	2.88	2.5
CaO/Na ₂ O	0.14	0.13	0.16	0.16	0.14	0.15	0.18	0.15
Mol. A/CNK	1.30	1.30	1.27	1.28	1.29	1.33	1.39	1.28
RARE EARTH ELEMEN	NTS PPM							
La	8.00	9.32	11.26	9.64	11.32	12.22	10.69	11.54
Ce	15.35	18.65	24.94	21.20	25.11	27.61	23.97	24.99
Pr	1.85	2.20	2.72	2.28	2.75	2.97	2.58	2.75
Nd	5.97	7.06	9.14	7.73	9.43	10.02	8.77	9.46
Sm	1.67	1.99	2.57	2.12	2.60	2.74	2.41	2.62
Eu	0.40	0.19	0.38	0.40	0.33	0.39	0.31	0.44
Gd Tb	1.62 0.29	2.00 0.32	2.57 0.46	2.16 0.38	2.57 0.43	2.72 0.47	2.42 0.43	2.59 0.46
Dy	1.45	1.57	2.26	1.86	2.17	2.28	2.06	2.24
Но	0.18	0.19	0.28	0.24	0.26	0.28	0.26	0.27
Er	0.46	0.46	0.66	0.53	0.61	0.64	0.58	0.61
Tm	0.05	0.05	0.08	0.07	0.08	0.08	0.07	0.01
Yb	0.32	0.35	0.46	0.39	0.44	0.50	0.41	0.44
Lu	0.04	0.05	0.06	0.05	0.06	0.07	0.05	0.06
∑REE	37.64	44.39	57.85	49.04	58.16	62.98	55.01	58.53
Eu/Eu*	0.73	0.28	0.45	0.57	0.39	0.43	0.38	0.52
LaN/YbN	17.41	18.55	17.10	17.11	17.66	16.99	17.88	18.24
				2.85		2.80	2.78	2.76
LaN/SmN	3.01 4.20	2.94 4.75	2.74 4.65	4.58	2.73 4.78	4.52	4.84	4.87

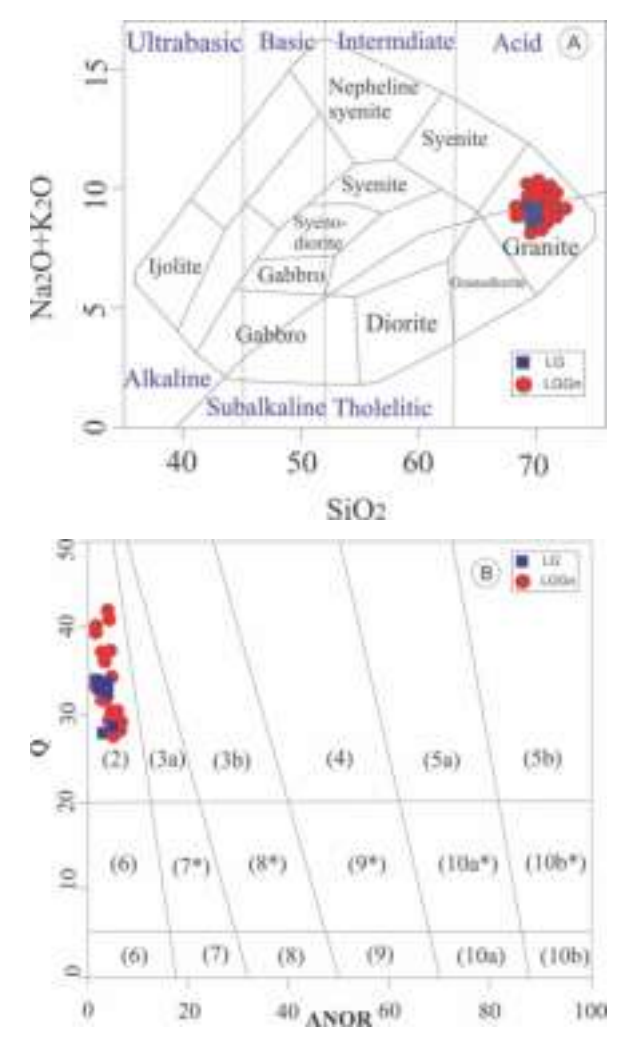


Fig. 5. A. TAS (Total alkali-silica) diagram after (Cox et al. 1979) determines granite field. B. Normative Q' vs ANOR plot of the LG and LGGn samples falls in the K-feldspar granite field. Description of fields are (2) K- feldspar granite, (3a) Monzosyenite, (3b) Monzogranite, (4) Granodiorite, (5a) Tonalite, (5b) Ca-tonalite, (6*) K- feldspar quartz syenite, (7*) Quartz syenite, (8*) Quartz Monzonite, (9*) Quartz monzodiorite, (10a*) Quartz diorite, (10b*) Quartz gabbro, (6) K-feldspar syenite, (7) Syenite, (8) Monzonite, (9) Monzodiorite, (10a) Diorite, (10b) Gabbro after (Streckeisen & LeMaitre 1979).

Geochemical analysis indicates that Lansdowne magma originated from substantial fractional crystallization, as supported by Elsdon & Gupta (1981).

In the Rb vs. (Y + Nb) tectonic discrimination diagram the data fit in the syn-collision granite fields, while the Y vs. Nb discrimination diagram determines post-collision granite fields (Fig. 9 A & B), resulting from crustal anataxis in the collisional zone. Similarly, R1-R2 [R1=4Si4+-11(Na++K+) 2(Fe3++Ti4+), molar; R2=6Ca2++2Mg2++Al3+ molar] tectonic discrimination diagram indicates a syn-collision tectonic setting. In the ACF [Al2O3-CaO-(FeO+MgO)] diagram the LG and LGGn falls into S-type granite field (Fig. 10A&B). The homogeneous nature of S-type granite suggests that the melt rises through the crust or involves contaminating its source, incorporating sediments from the subduction zone, resulting in the peraluminous character for calc-alkaline granites (Rao & Sharma 2009). Geochemical evidence suggests that a subduction-related magmatism occurred in the Garhwal Himalaya during the Paleoproterozoic, as suggested by Mishra et al. (2021).

S-type peraluminous melts originating from clay-rich sources, deficient in plagioclase, typically exhibit a low CaO/Na2O ratio (<0.3). Conversely, melts derived from clay-poor sources, rich in plagioclase, display a high CaO/Na2O ratio (>0.3) (Sylvester 1998). The present study determines low CaO/Na2O ratios (0.12-0.18) corresponding (except few) to psammites (meta-greywacke) domain of Lachlan fold belt (Fig. 11A). S-type, granites originating from crustal melt are untainted by any influence from the mantle (Castro *et al.* 1999, Ghani *et al.* 2013, El-bialy & Omar 2015). Molar A/CNK value of LG and LGGn felsic rock with high (ASI>1) illustrate S-type granite formed from metasedimentary sources (Chappell & White 1974).

Additionally, the Rb/Sr and Rb/Ba higher ratio with increasing trend determines a clay-rich source, and the Rb/Sr and Rb/Ba lower ratio with decreasing trend determines a clay-poor source (Condie 1993). Most samples originate from immature psammitic sources, such as meta-greywackes, indicating the anatexis of crustal blocks accreted within collisional zones and prevalent in the convergent plate

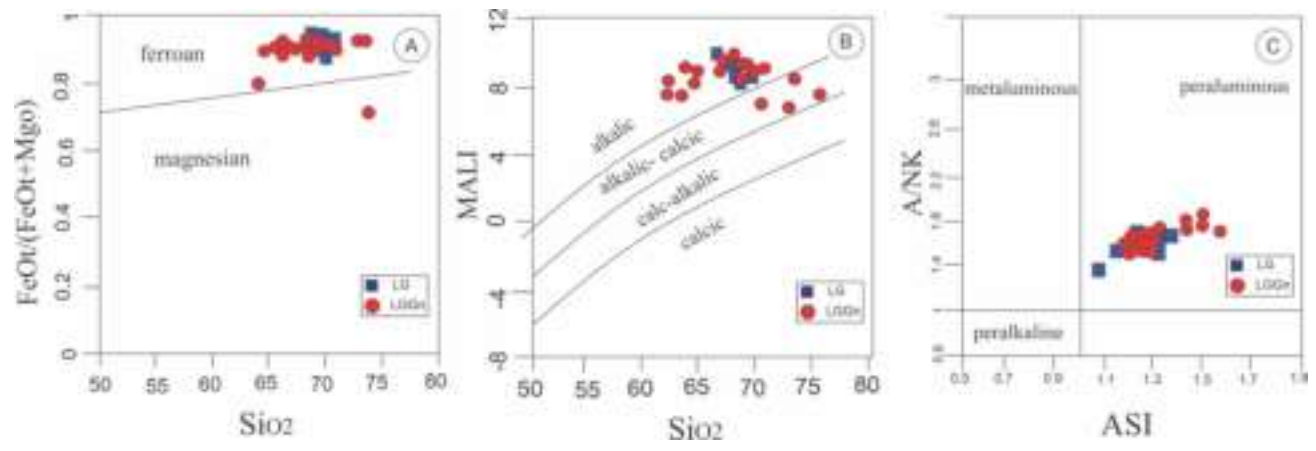


Fig. 6. A. FeO₂/FeO₂+MgO vs SiO₂, B. Modified alkali lime index (MALI) vs SiO₂ and C. Alumina saturation index (ASI) vs SiO₂ of the LG and LGGn samples (Frost *et al.* 2001).

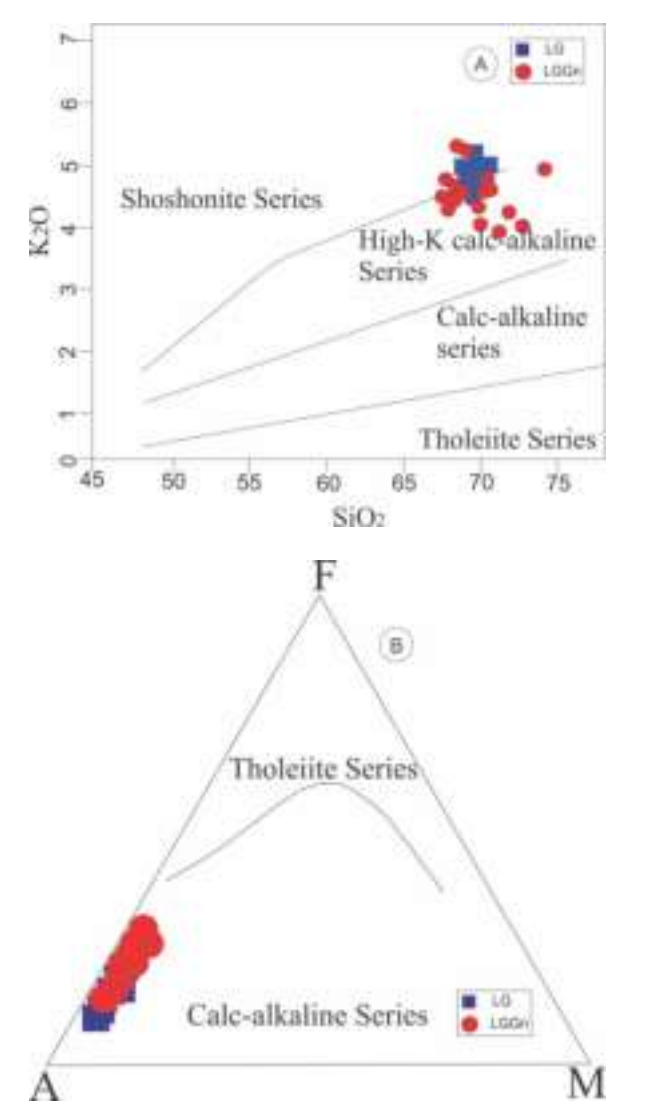
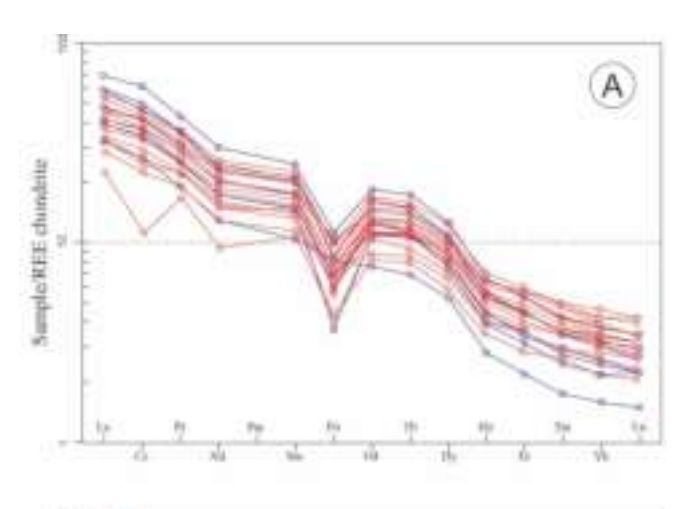


Fig. 7. A. Binary plot (K₂O versus SiO₂) LG and LGGn belong to the high K calc-alkaline to Shoshonite magma series (Le Maitre *et al.* 1989 and Peccerillo & Taylor 1976). B. Data shown in the AFM ternary diagram demarcate the line between tholeite and calc-alkaline series samples plots towards alkaline (Irvine & Baragar 1971).



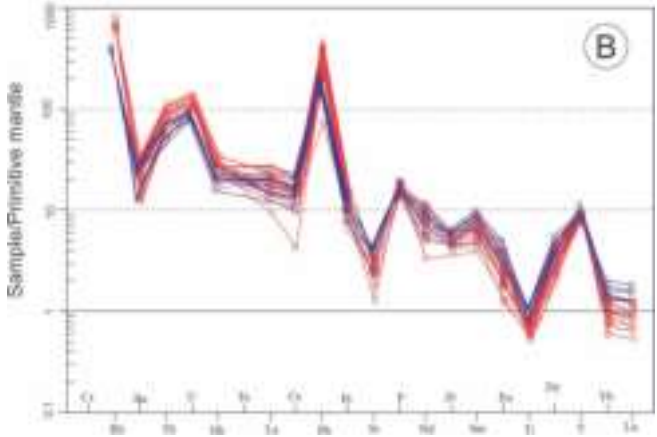


Fig. 8. A. Chondrite-normalized REE plots for the LG and LGGn (Anders & Grevesse 1989) and B. Primitive mantle-normalized multi elemental variation diagram (McDonough & Sun 1995).

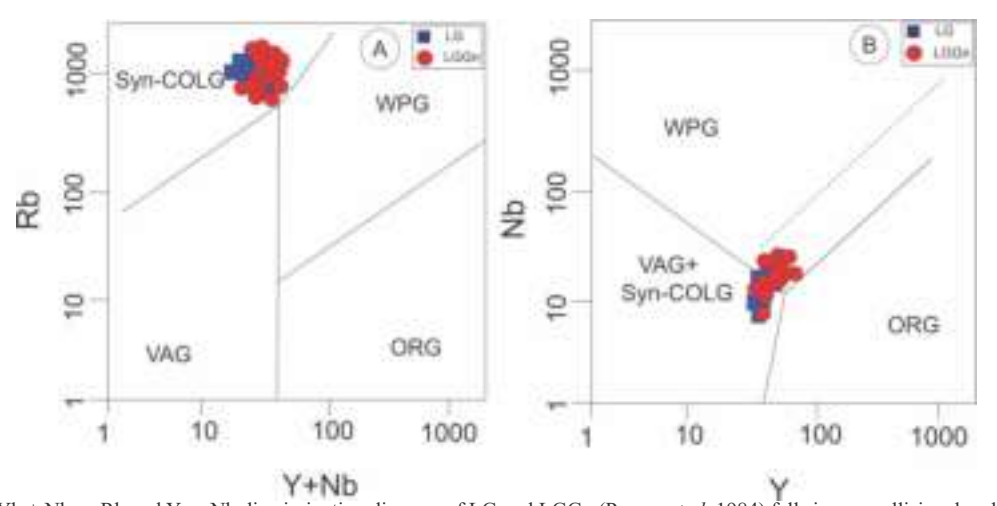
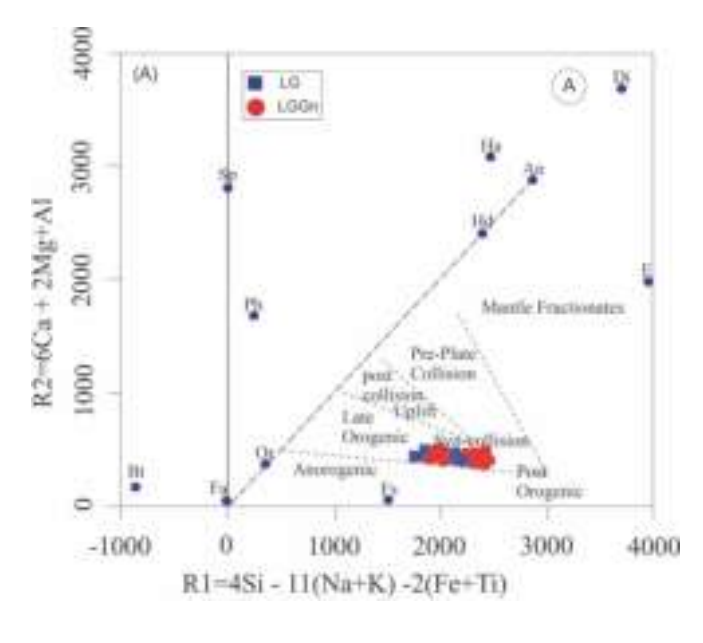


Fig. 9. A & B. The Yb + Nb vs Rb and Y vs Nb discrimination diagram of LG and LGGn (Pearce et al. 1984) falls in syn-collisional and post orogeny field.



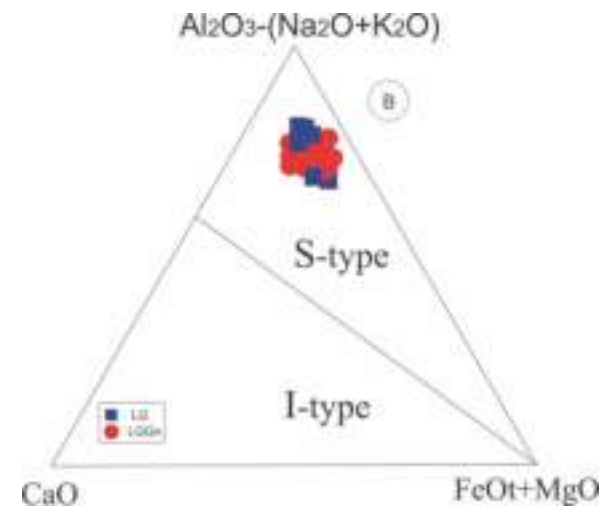
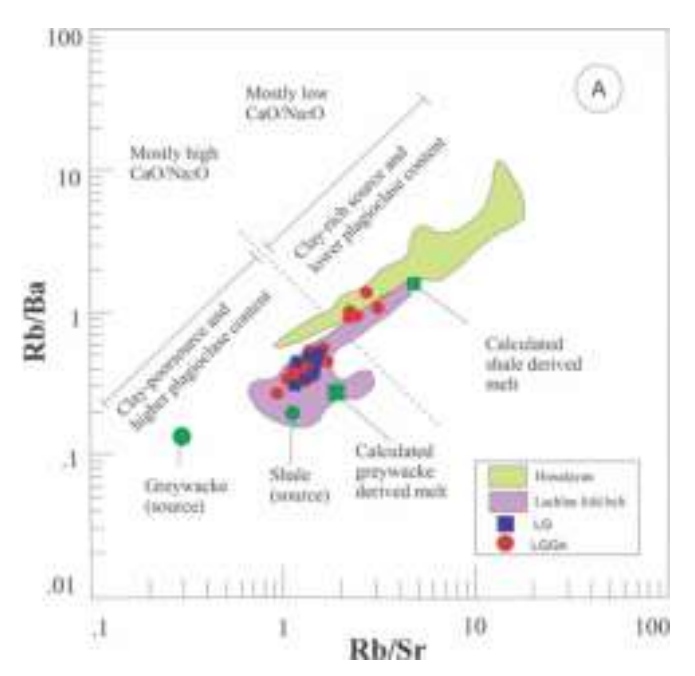


Fig.10. A. The R1 - R2 [R1 = 4Si4+-11(Na++K+) 2(Fe3++Ti4+), molar; R2 = 6Ca2++2Mg2++Al3+, molar] (Batchelor & Bowden 1985) tectonic discrimination diagram shows syn-collision type of tectonic setting. B. The ACF diagram determines S-type granite field (Chappell & White 1992).

margins of the Himalaya (Vielzeuf & Montel 1994 and Sylvester 1998).

The LG and LGGn are strongly differentiated granites, and Rb, Ba, and Sr trace elements (Fig. 11 B), suggest that they are highly differentiated granites (Ahrens *et al.* 1952; Taylor *et al.* 1956). Strongly differentiated granites explain the increasing ratio of the Rb/Sr and the rapidly decreasing ratio of the Ba/Rb in a linear trend (Bouseily & Sokkary 1975).

Both LG and LGGn are in erosional remnants of the thrust sheet that overlies the Chail Nappe of the Garhwal Himalaya. The geochemical data determines that they have an affinity to S-type granite, showing syn-collision to post-orogeny tectonic settings, and its evolution is related to partial



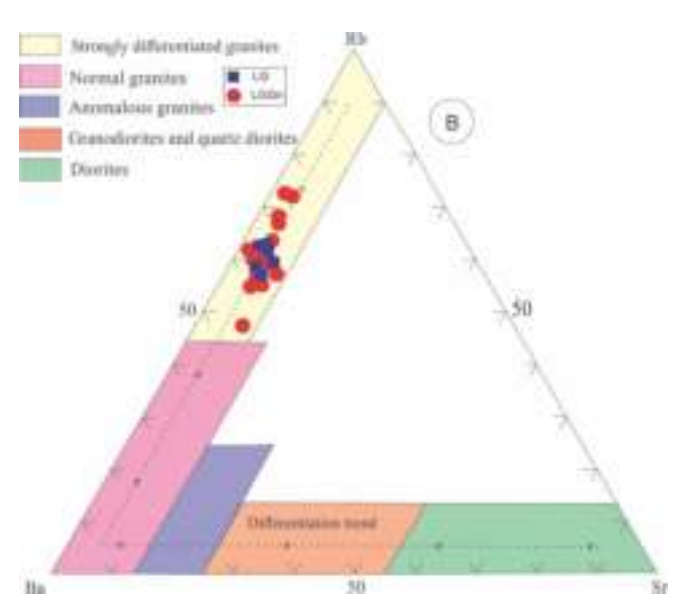


Fig.11. A. Rb/Sr vs Rb/Ba ratio diagram for the LG and LGGn, S-type granites determine clay poor sources (Sylvester 1998) B. Ternary diagram of Rb, Ba and Sr of numerous granite group showing strongly differentiated granite field of the given data (Bouseily & Sokkary 1975).

melting of continental crust derived from metasedimentary source. These findings are similar to those reported by Mishra *et al.* (2021) for the Chail Group in the Garhwal Himalaya.

CONCLUSION

- Field observations and petrography reveal that the LG and LGGn are leucocratic and porphyritic rocks with similar composition and texture.
- Geochemical data of the LG and LGGn show rocks of calc-alkali to shoshonitic and ferroan composition.

- Peraluminous characteristics depict a syn-collisional to post-orogeny tectonic setting.
- The partial melting of recycled crustal material determines its felsic composition.
- The Lansdowne klippe may be an erosional remnant of a large, sub-horizontal thrust sheet. This thrust sheet is associated with the Main Central Thrust (MCT) hanging wall, as described by Heim & Gansser (1939).

Acknowledgements: The authors are highly grateful to the Department of Geology, Kumaun University, Nainital for providing basic facilities. We acknowledge Director Wadia Institute of Himalayan Geology, Dehradun for rendering Lab facilities. Special thanks to Prof. Fernando Corfu Sir who made constant painstaking efforts to improve the previous manuscript and for his valuable advice and encouragement to publish this paper. We are also thankful to all the anonymous reviewers who further improved this paper. We acknowledge the help and support of M. Anas in compilation. The paper benefited from the comments and suggestions of the Editor and Editorial Manager.

References

- Ahrens, I. H., Pinson, W.H., Kearns, M.M. 1952. Association of rubidium and potassium and their abundance in common igneous rocks and meteorites. *Geochimica et Cosmochimica Acta*, **2**, 229-242.
- Anders, E., Grevesse, N.1989. Abundance of the elements: Meteoritic and solar. *Geochemica et Cosmochimica Acta*, 53, 197-214. https://doi.org/10.1016/0016-7037(89)90286-X.
- Auden, J.B. 1937. Structure of the Himalaya in Garhwal. *Records, Geological Survey of India*, **71**, 407–433.
- Batchelor, R.A., Bowden. P. 1985. Petrogenetic interpretation of granitoid rock series using multi cationic parameters. *Chemical Geology*, **48**, 43-55.
- Bouseily, A.M. El., Sokkary, A. A. El. 1975. The relation between Rb, Ba AND Sr in granitic rocks. *Chemical Geology*, **16**, 207-219.
- Castro, A., Patino Douce, A.E., Corretg, L. G., De La Rosa, J. D., El-Biad, M., El-Hmidi, H. 1999. Origin of peraluminous granites and granodiorites, Iberian massif, Spain: An experimental test of granite petrogenesis; Contribution Mineral Petrology, 135, 255–276.
- Celerier, J., Harrison, T.M., Yin, A., Webb, A.A.G. 2009. The Kumaun and Garhwal Lesser Himalaya, India: Part 1. Structure and Stratigraphy. *Geological society of America Bulletin*, **121** (9/10), 1262-1280.
- Chappell, B.W., White, A.J.R. 1974. Two contrasting granite types. *Pacific Geology*, **8**, 173–174.
- Chappell, B.W., White, A.J.R. 1992. I- and S-type granites in the Lachlan Fold Belt. *Transactions of the Royal Society of Edinburgh. Earth Sciences*, 83,1–26.
- Condie, K.C. 1993. Chemical composition and evolution of the upper continental crust: contrasting results from surface samples and shales. *Chemical Geology*, **104**, 1-37.
- Cox, K.G., Bell, J.D., Pankhurst, R.J. 1979. The Interpretation of Igneous Rocks, 1st ed. *Springer science and business Media*. https://doi.org/10.1007/978-94-017-3373-1.
- El-Bialy, M. Z., Omar, M.M. 2015. Spatial association of Neoproterozoic continental arc- type and post-collision A-type granitoids in the Arabian-Nubian Shield: The Wadi Al- Baroud older and younger granites, Northeastern Desert, Egypt. *Journal of African Earth Science*, 103, 1–29.
- Elsdon. R., Gupta. L.N.1981. Petrochemical studies of the Lansdowne Granite Gneiss, Lesser Himalaya, India. *Journal Geological Society of India*, 22, 503-516.
- Frost, B.R., Barnes, C.G., Collins, W.J., Arculus, R.J., Ellis, D.J., Frost, C.D. 2001. Geochemical Classification for Granitic Rocks. *Journal of Petrology*, 42, 2033–2048. https://doi.org/10.1093/petrology/42.11.2033.

- Fuchs, G., Sinha, A.K. 1978. The Tectonics of the Garhwal-Kumaun Lesser Himalaya. *Jahrb. Geol. Bundesanst*, 121, 219-241.
- Ghani, A. A., Searle, M., Robb, L., Chung, S. L. 2013. Transitional I-S type characteristic in the Main Range Granite, Peninsular Malaysia; *Journal* of Asian Earth Science, 76, 225–240.
- Gupta, L. N. 1976a. A contribution to the geology of the Lansdowne area, Garhwal Himalayas, India; *Journal Geological Society of India*, 17, 449–460.
- Gupta, L. N. 1976b. Abnormal tectonics of the allochthonous LG and the tectonic history of Garhwal nappe; *Indian Mineral*, 17,73–85.
- Heim. A., Gansser. A. 1939. Central Himalaya, Geological observations of Swiss expedition 1936. Memoires de la Société Helvetica Sciences Naturelles, 73, 1-245.
- Islam, R., Ahmad, T., & Khanna, P.P. 2005. An overview on the granitoids of the NW
- Himalaya. Himalayan Geology, 26 (1), 49-60.
- Irvine, T.N., Baragar, W.R.A., 1971. A guide to the chemical classification of the common volcanic rocks. *Canadian Journal of Earth Sciences*, 8, 523-548
- Kumar, G., Dahundhiyal, J.N. 1980. On the stratigraphic position of the Tal formation, Garhwal synform, Garhwal, and Tehri Garhwal districts, Uttar Pradesh.
- Le Fort, P. 1986. In collisional tectonics (ed. M. P. Coward & A. C. Ries) Geological society of London, special publications, 19, 159-172.
- Le Maitre, R.W., Bateman, P., Dudek, A., Keller, J., Lameyre, J. 1989. A Classification of Igneous Rocks and Glossary of Terms: Recommendations of the International Union of Geological Sciences Sub-Commission on the Systematics of Igneous Rocks. New York: Cambridge University Press.
- McDonough, W. F., Sun, S.S. 1995. The composition of the Earth. *Chemical Geology*, **120**(3-4), 223-253. https://doi.org/10.1016/0009-2541(94) 00140-4.
- Mishra, S., Nainwal, H.C., Singh, V.K., Slabunov, A.I. 2021. Geochemistry of Granites from Chail Group of Garhwal Region, Lesser Himalaya, NW India. *Journal of Mountain Research*, **16**(3), 23-30.
- Pearce, J. A., Harris, N. B. W., Tindal, A. G. 1984. Trace element discrimination diagrams for the tectonic interpretation of granitic rocks; *Journal of Petrology*, 25, 956–983. https://doi.org/10.1093/petrology/ 25.4.956.
- Peccerillo, A., Taylor, S.R. 1976. Geochemistry of Eocene calc-alkaline volcanic rocks from the Kastamona area, northern Turkey. *Contributions to Mineralogy and Petrology*, **58**, 63-81.
- Rao, D.R., Sharma, R. 2009. Petrogenesis of the Granitoid rocks from Askot crystallines, Kumaun Himalaya. *Journal of Geological Society of India*, 74, 363-374.
- Rupke, J. 1974. Stratigraphic and structural evolution of the Kumaun Lesser Himalaya. Sedimentary Geology, 2, 81-265.
- Saklani, P.S. 1993. *Geology of the Lower Himalaya (Garhwal)*. International Books and Periodicals Supply Service, New Delhi, 246p.
- Searle, M.P., Simpson, R.L., Law, R.D., Parrish, R.P., Waters, D. J. 2003. The structural geometery, metamorphic and magmatic evolution of the Everest massif, High Himalya of Nepal -South Tibet. *Journal of the Geological Society of London*, **160**, 345-366.
- Shah, A.N., Patel, P.P. 1978. Granitic gneisses of Lansdowne (District Pauri-Garhwal, U.P). *Journal of the Geological Society of India*, 19, 368-372.
- Shanker, R., Ganeshan, T.M. 1973. A note on the Garhwal nappe. *Himalayan Geology*, **3**, 72-82.
- Streckeisen, A., Le Maitre, R.W. 1979. A chemical approximation to the modal QAPF classification of the igneous rocks. *Neues Jahrb. fur Mineral*. Abh., 136, 169–206.
- Sylvester, P. J. 1998. Post-collisional strongly peraluminous granites. *Lithos*, **45**, 29–44.
- Taylor, S.R., Emeleus, C.H., Exley, C.S. 1956. Some anomalous K/Rb ratio in igneous rocks and their petrological significance. *Geochimica et Cosmochimica*. *Acta*, **10**, 224-229.

- Winter, J.D. 2014. Principles of Igneous and Metamorphic Petrology: Pearson New International Edition. *Pearson Education Limited, Harlow, UK*.
- Valdiya, K. S. 1980a. *Geology of Kumaun Lesser Himalaya*. Wadia Institute of Himalayan Geology, Dehradun, 291p.
- Valdiya, K.S. 1980b. The two intracrustal boundary thrusts of the Himalaya, *Tectonophysics*, **66**, 323-348.
- Vernon, R.H. 2004. A Practical Guide to Rock Microstructure. Cambridge University Press, Cambridge. http://dx.doi.org/10.1017/CBO9780511807206
- Vielzeuf, D., Montel, J.M. 1994. Partial melting of metagreywackes. Part I. Fluid-absent experiments and phase relationships. *Contributions to Mineralogy and Petrology*, 117, 375-393.
- Vishnoi, R.K. 1971. Geology of the Area Around Lansdowne (District Pauri, U.P.) with Special reference to the Study of Granite Gneiss. Masters' Theses (Earth Science) Indian Institute of Technology Rorkee, 87p.

Stress pattern analysis and its tectonic implications in the Eastern Himalayan Syntaxis: A special emphasis to the Siang Valley, Arunachal Pradesh, Northeast India

ASHISH PAL^{1,2}, DILIP KUMAR YADAV^{1,*}, DEBONIL BARUAH¹, ABHISHEK KUMAR GUPTA¹, H.C. NAINWAL², PARAKH SAHU¹

¹Wadia Institute of Himalayan Geology, Dehradun-248001, India ²Hemvati Nandan Bahuguna Garhwal University, Srinagar Garhwal-246174, India *Email (Corresponding author): dilipky@yahoo.com

Abstract: The Siang Valley of northeast Himalaya is one of the most seismotectonically active area that lies within the Eastern Himalayan Syntaxis (EHS). In this study the Focal Mechanism Solutions (FMSs) are determined and estimated FMSs are used to understand the existing stress field in the region. The depth distribution of seismicity ranges up to a focal depth of 60 kilometers, with a higher concentration in the upper crustal part. We estimated 18 FMSs using P-wave first motion for the events having a magnitude (M_1) ranging from 3.5 to 5.4, showing normal, thrust and a combination of strike-slip mechanism which follows the major tectonic feature/faults in the region. From the analysis of stress inversion, it is observed that the direction of the highest compression (P) axis is SSE, indicating the presence of a radial compressional stress regime in the western part of Siang Valley. In the eastern part of Siang Valley, a predominant transtension stress regime is observed and P axis is oriented in the SSW direction. The Siang Valley and adjoining region, the estimated maximum principal stress (σ 1) shows a trend towards the SSW direction. The stress regime index (R') indicates a strike slip with reverse faulting occurring in this region. The FMSs and stress tensor outlined in our study provide valuable insights for developing a more comprehensive understanding of the seismotectonic implications in this area. This information is beneficial for evaluating seismic hazards and related geodynamic activities.

Keywords: Focal mechanism solutions, Stress tensor, Siang Valley, Eastern Himalayan Syntaxis

INTRODUCTION

The Eastern Himalayan Syntaxis (EHS) of Arunachal Pradesh, NE India, is one of the most seismotectonically dynamic region. In Northeast India, a convergence was observed among three significant tectonic plates, namely Indian, Eurasian, and Burmese. This phenomenon encompasses the presence of two primary mountain ranges; in the north are the Himalayas, and in the southeast are the Indo-Burmese Ranges, accompanied by a significant intraplate area in Northeast India. There is an agreement on the presence of north-south compression triggered by the collision of plates between India and Eurasia. The specifics regarding the directional variations in compression and the nature of alignments of seismotectonic stress patterns, still need to be more adequately understood. The absence of clarity is notably evident in the Assam syntaxis region, where the meeting point of the two primary mountain ranges occurs near the coordinates 28°N and 96°E. Previous studies have emphasized the importance of continental collision in this scenario (Molnar & Tapponnier 1975; Mitchell 1981; Curray et al. 1982; Tapponnier et al. 1982, 1986). The Himalayan range represents the largest orogenic belt globally, where one continental crust subducts beneath another continental crust. This geological phenomenon has been extensively studied (Le Fort 1975; Nandy 2001; Zhao et al. 1993; Mitra et al. 2005). The amalgamating structures constituting a complex geotectonic framework (Curray et al. 1982) exert pressure on the northeastern sector of the Indian plate, resulting in deformation (Chen and Molnar 1990; Kayal 1991; Bilham & England 2001). From a broader perspective, the Arunachal Himalaya encompasses the furthest eastern section of the Himalaya, situated between longitudes 91°30 E and 96°E, encompassing the EHS. The Indian plate is gently dipping to the north beneath the Himalayas (Zhao et al. 1993; Mitra et al.

2005). The northeastern syntaxis of the Himalaya delineates the region in which the Himalayan arc undergoes a significant southward trend, situated proximate to the eastern boundary shared by India and China. Seismic activity is notably influenced by the intraplate deformation within northeastern India and the eastern Himalayan syntaxis caused by the collision of India with Eurasia and the subduction of India beneath Burma. Earlier studies (Bilham 2006; Thingbaijam et al. 2008; Kayal et al. 2006) have documented that Namche Barwa massif (NB), a prominent dome-shaped formation marking the termination of the Himalayan Arc in the east, exhibits substantial seismicity (Khattri et al. 1983). This region is seismically active (Das Gupta & Nandy 1982; Gupta et al. 1984; Kayal & De Reena 1991; Baruah et al. 1997; Kayal 1998; Rajendran et al. 2004; Bilham 2006; Kayal et al. 2006; Thingbaijam et al. 2008), with the remarkable exception of the Assam Gap (Khattri et al. 1983).

EHS and its surrounding area have encountered two big seismic events namely, 1947 Ms 7.7 Lang earthquake and 1950 Ms 8.6 Zayu earthquake along with several minor tremors, predominantly clustered in the northeastern region which were mainly concentrated in the north eastern part of the EHS. In contrast, fewer earthquakes have occurred in the western part of the EHS and in the Namche Barwa (NB) area (Yang et al. 2018). The spatial distribution and characteristics of the shallow and intermediate earthquakes suggest subduction and collision of the crust in the upper part of the Himalayan arcuate range (Priestley et al. 2008). Therefore, studying of these earthquake will provide more insights of seismicity around EHS. Seismicity is usually concentrated in a narrow zone of about 50-70 kilometers wide, traversing along the Main Central Thrust (MCT) in EHS, which is one of the major fault systems in the Himalayas. The other two are the Main Boundary Thrust (MBT) and the Himalayan Frontal

Thrust (HFT) in this region (Ni & Barazangi 1984). The geometry and friction of the Main Himalayan Thrust (MHT) play a significant role in controlling seismic ruptures and stress interactions. The seismic activity in the Siang Valley is notable, with earthquakes manifesting in various zones at depths ranging from 5 to 45 km (Rai et al. 2024). The determination of seismotectonic stress regimes within a region is performed through the analysis of FMSs of earthquakes. This analysis provides new perspectives on the active tectonics of the region and facilitates the evaluation of geodynamic implications. Typically, the focal mechanism solution pertains to the fault orientation, the seismic slip with respect to the plate motion and stress release patterns. Rastogi et al. (1973) ascertained 11 FMSs for earthquakes that occurred in the Assam-Myanmar region by utilizing P-wave first-motion direction data. Their findings indicated that the primary modes of deformation observed in the region are associated with thrust faulting. Chandra (1978) calculated a total of eighteen FMSs for the seismic events in the Himalayan region by employing P-wave first motion data. The findings revealed a predominant thrust faulting pattern in the northeast region of India. Pal et al. (2024a) studied the source parameter and seismotectonic analysis in the Siang Valley region of northeastern Himalaya. The investigation into the focal mechanism solution by Hazarika et al. (2022) and the stress inversion study by Kamra et al. (2023) was executed in the northeastern sector of the eastern Himalayan Syntaxis.

In our present study, using the recently acquired seismic data, i.e. more data compared with previous studies, evaluation of FMSs using P- wave first polarity method with the depth section across the Siang window and stress tensor inversion has been applied using focal mechanisms of events that occurred in the Siang Valley, NE Himalayas. We focused on investigating the trend of the primary stress axes to comprehend the local-regional stress field in the region which are divided into two sub-region.

GEOLOGY AND TECTONICS

Siang Valley is located in the eastern part of the Himalayas, where the Himalayan arc bends sharply southward. The tectonic setting of Siang Valley is complex and involves different tectonic units and fault systems. A large antiform structure called the Siang antiform, dominates the Siang Valley, which exposes the Lesser Himalayan Crystalline Sequence (LHCS) (Fig. 1) The LHCS is a representation of a metamorphic belt consisting of gneisses, schists, quartzites and marbles, situated within the eastern flank of the Siang antiform (Gururajan & Choudhuri 2003; Misra 2009); the LHCS's boundaries are delineated by Trans-Himalayan tectonic units, specifically the Tidding suture zone and the Lohit plutonic complex (LPC). The centre of the Siang antiform is characterized by sedimentary rocks of the Mesozoic era (Singh 1993). In the Siyom Valley, which is a tributary of the Siang River, the LHCS is structurally detached from the Lesser Himalayan Sequence (LHS) by the Main Central Thrust-I (MCT-I) at a lower structural level; nevertheless, it is in juxtaposition with the Higher Himalayan Crystalline Sequence (HHCS) along Main Central Thrust-II (MCT-II) at a higher structural level. MCT-I and MCT-II are prominent thrust faults responsible for accommodating crustal shortening and thickening in the Himalayan region. The MCT and MBT depict the primary tectonic characteristics observed in the Eastern Himalayan region. The Main Central Thrust (MCT) has been identified as a significant intracontinental ductile shear zone, which is linked to an inverted metamorphic zone that is thought to have formed since the mid-Tertiary period, shows minor recent movements as well (Valdiya 1980). Acting as a demarcation line, the MCT divides two distinctive geological terrains - the Lesser Himalaya situated to the south and in the north higher Himalayan Crystallines. The primary geological division differentiates the lesser and sub-Himalayan areas by the Main Boundary Thrust (MBT), acknowledged for its continuous high seismic activity leading to devastating earthquakes. This prominent thrust belt emerged during the Pliocene epoch and remained dynamic throughout the Pleistocene era (Valdiya 1980). The Assam syntaxis zone is situated within the easternmost part of the Himalayas, representing a significant tectonic region where the convergence of the Himalayan arc, Burmese arc, and Mishmi block occurs, featuring thrust trends in the NW-SE direction as evidenced by the Lohit and Mishmi thrusts (Fig. 1). It is worth noting that this particular zone was the focal point of the major earthquake of 1950 as documented (Poddar 1950).

METHODOLOGY

Seismic Network and Data

The Wadia Institute of Himalayan Geology (WIHG) Dehradun has installed a network comprising 8 broad-band Seismic (BBS) stations in the Siang Valley, Northeast India, with the primary objective of investigating the Seismotectonic attributes of the region. The initiation of the seismic stations' operations occurred in December 2018, as documented by Yadav et al. (2021). Positioned on top of Granitoids rocks, the Gelling (GLNG) seismic station is the most northerly station, while the Jengging (JNGG) station is located on the gneissic rocks of the Lesser Himalayas. The Mariyang (MRNG) and Yingkiong (YINK) seismic stations are positioned on the Yingkiong formation (Acharyya & Saha 2013). The Along (ALON) station is located on the sequences of the Lesser Himalayas, whereas the Padu (PADU) and Boleng (BLNG) stations are found on the Miri Quartzite. The Pasighat (PASI) seismic station, the station furthest to the south, is situated on the alluvial sediments of the Brahmaputra River Basin. The BBS stations are furnished with a three-component Trillium Compact-120 sensor and Centaur digitizer. The instrument is configured with a compact flash memory card intended for the continuous recording of data of 100 samples per second (SPS). A sensitivity of 1500 V/m/s is demonstrated by the digitizer. These seismic stations operate independently and are furnished with GPS receivers to ensure accurate time synchronization.

The SEISAN analysis software by Havskov & Ottemoller (1999) was utilized to examine and distinguish the P and Sphases for the purpose of determining the hypocentral

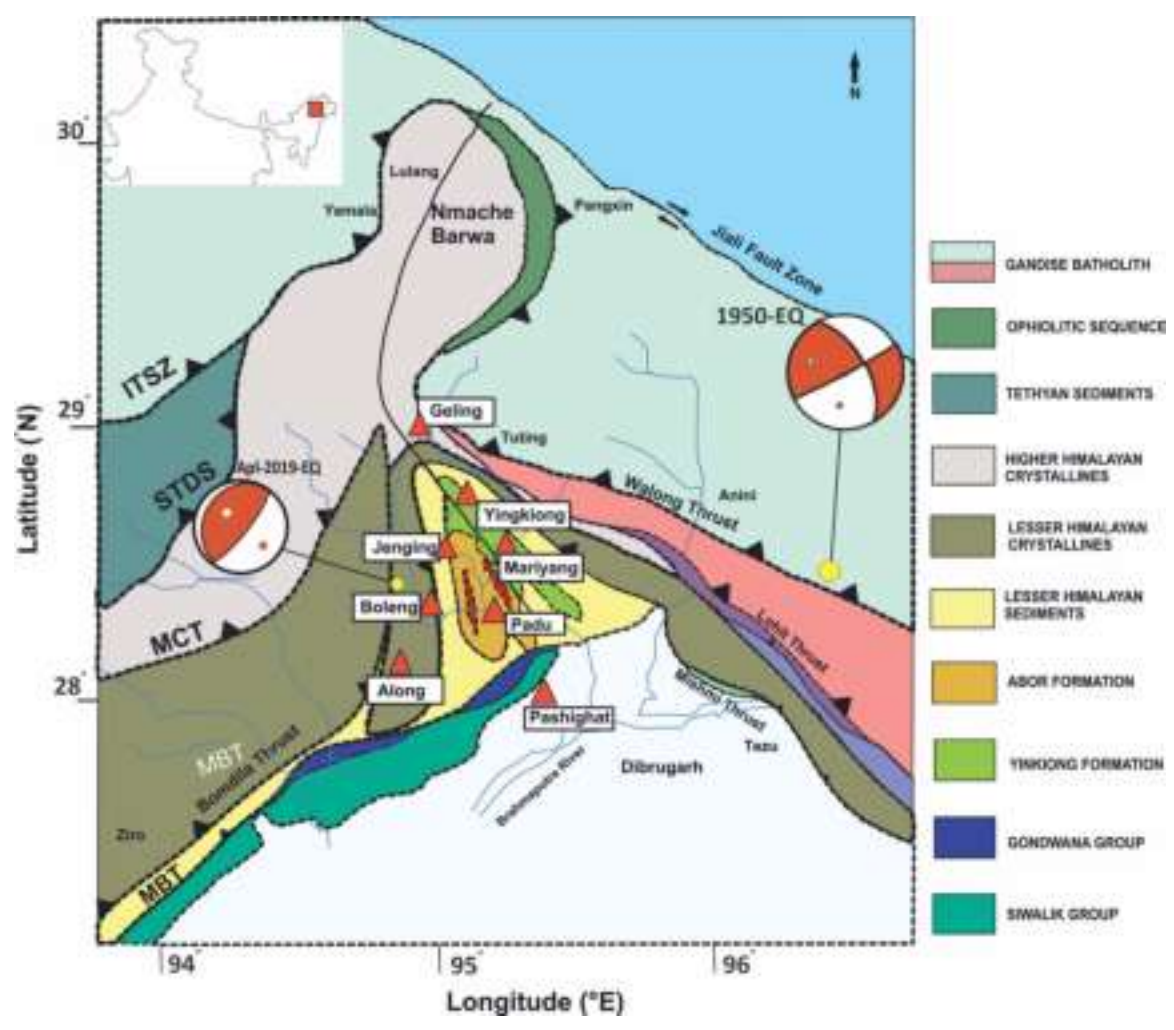


Fig. 1. Geology and Tectonic map of the Siang Valley in the Eastern Himalayan Syntaxis of the northeast Himalaya (modified after Yadav *et al.* 2021). The installation of broad band Seismic stations by WIHG is denoted by red triangles on the map. Various significant tectonic features such as the MBT, MCT, STDS, ITSZ, Lohit Thrust, Walong Thrust, and Mishmi Thrust can be identified in the region. The rivers in the area are represented by blue lines.

parameters of the earthquake. The hypocentral parameters are computed using the HYPO71 software, which was created by Lee & Lahr (1975). For the computational studies of seismic events, a five-layer velocity model (Table 1) introduced by Raoof *et al.* (2017) with Vp/Vs ratio of 1.74 is employed. The seismic events are identified, processed, and relocated to produce a Seismological catalogue of Siang Valley within the geographical coordinates of 27.75°- 29.25°N Latitude and 94.5°-96°E Longitude (Fig. 2). The uncertainties in epicenter locations range approximately ±5 km, with the Root Mean Square (RMS) value varying from 0.2 to 0.5 seconds.

Focal Mechanism Solution

FMSs are determined from the P wave first motion polarity using the FOCMEC application, as elaborated by Snoke *et al.* (1984). The package contains programs for determining and displaying double-couple earthquake focal mechanism. Input data are polarities (P, SV, SH) and/or amplitude ratios (SV/P, SH/P, SV/SH). The application performs an efficient, systematic search of the focal sphere. Application have been made to finding best constrained fault plane solutions for suits

of earthquakes recorded at local to regional distances and using recorded polarities and relative amplitudes to produce waveforms synthetics (Snoke 2003). Employing the lower hemisphere equal area projection, the P and T axes correspondingly represent the directions of compression and tension. Within this framework, the compressional quadrant is illustrated by the shaded region on the focal sphere, while the dilatational quadrant remains unshaded. The determination of fault geometry by employing P-wave first motion data using FMS presents a direct approach, hinging on the polarity

Table 1. 1D velocity model of northeast India used for the present study (Raoof et al. 2017).

Depth to the bottom layer	Vp(km/s)	Vs(km/s)
0	5.57	3.18
5	5.65	3.22
10	5.78	3.30
20	6.25	3.57
30	6.89	3.93
40	7.91	4.52
50	8.30	4.74

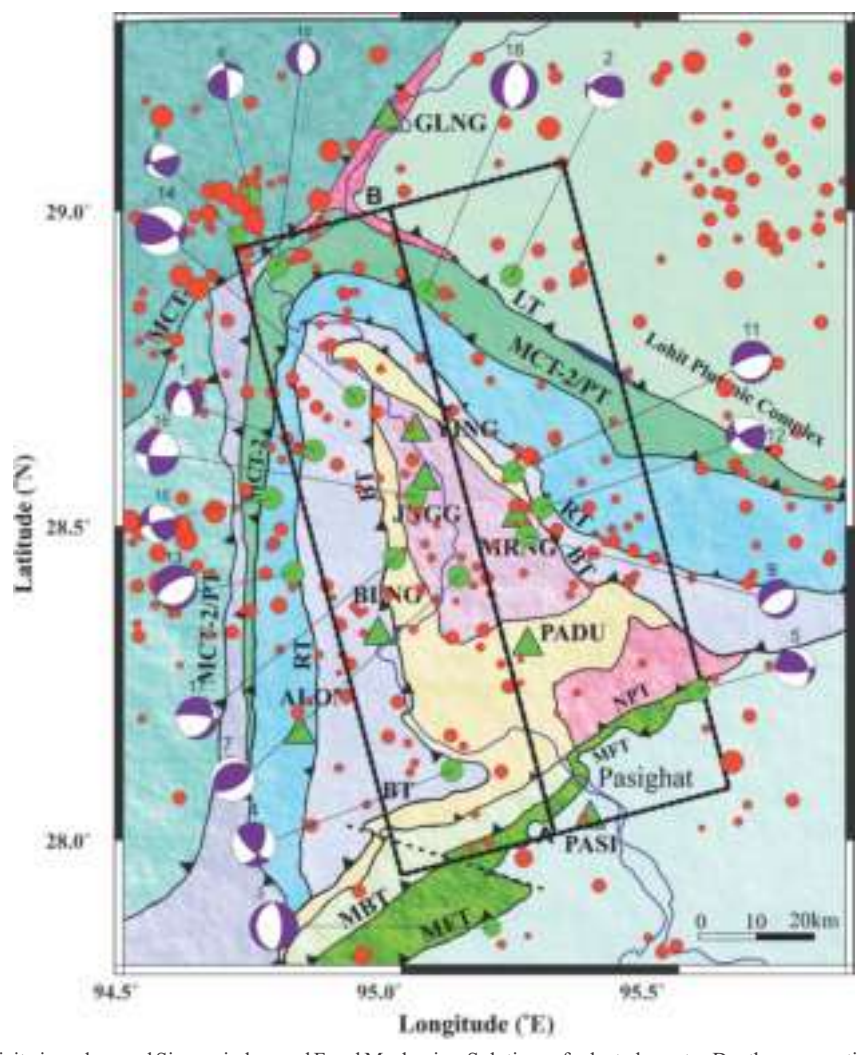


Fig. 2a. Plot depicting seismicity in and around Siang window and Focal Mechanism Solutions of selected events. Depth cross-section along A-B. Green triangles are BBS station. Varying red dots are corresponding size of earthquake events and green dots are earthquake events used for focal mechanism solutions (beach balls). The major tectonic characteristics depicted on the map include the North Pasighat Thrust (NPT), Main Frontal Thrust (MFT), Main Boundry Thrust (MBT), Main Central Thrust (MCT), Bomdo Thrust (BT), Ramgarh Thrust (RT) and Lohit Thrust (LT).

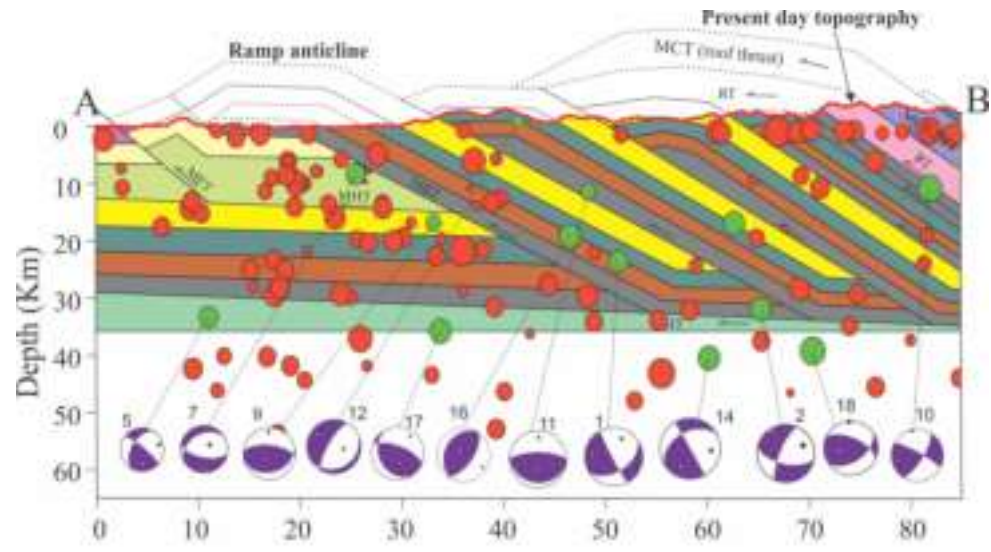


Fig. 2b. Plot (modified after Salvi *et al.* 2021) depicting Depth projected FMSs along section line A-B, highlighting the seismicity with respective depth. Tectonic features are Main Frontal Thrust (MFT), Main Boundry Thrust (MBT), Main Central Thrust (MCT), Ramgarh Thrust (RT).

variation displayed by the initial P-wave arrival across seismic stations positioned in distinct back azimuth relative to an earthquake. Specifically, the first motion can manifest as either compression, indicating movement towards the station, or dilatation, signifying movement away from it. The initial movement could be observed as compression, denoting an approach towards the station, or as dilatation, indicating a departure from it. Subsequently, upon arrival of a P wave at a seismograph station from beneath the Earth, the vertical component of the seismogram records an initial motion that is either rising or falling, representing compression or dilatation, respectively. The data necessary for determining the focal mechanism is gathered by collecting information on the firstarrival polarities and their azimuth from various recording stations. The process of establishing the solution for the focal mechanism using data on the first-arrival polarities needs a back-azimuthally distributed stations. In this study, eighteen events, as showing the data for representative catalogue in table 2, are selected with high-precision location parameters, a clear record of P-wave first motion polarity and a number of seismic stations.

Stress Tensor Inversion

Stress inversions of earthquake events were primarily conducted based on the distribution of FMSs, through which we get two sub-regions. For the stress inversion analysis 46 focal mechanisms, with magnitudes ranging from 3.2 to 8.7 were utilized. The construction of the database commenced with the collection of focal mechanisms derived from waveform modelling and the P-wave first polarity method, as documented in Pal *et al.* (2024b) along with ISC data (http://www.isc.ac.uk/isc-(ISC - EHB) data (ehb/) by Engdahl (1998) for an additional solution in the present study, culminating in the compilation of the earthquake focal mechanism database. Earthquake focal mechanism solutions were evaluated for the events recorded in the vicinity of Siang Antiform. Stress tensor analysis serves as a technique employed to examine the stress state in rocks by utilizing

fault-slip data or earthquake focal mechanisms. This approach facilitates the comprehension of the tectonic evolution and deformation history of a specific area. The methodology for determining stress orientations was conducted following the Vavryčuk (2014) technique (STRESSINVERSE code), which builds upon the works of Michael (1984, 1987). His method is linear and iterative stress inversion and used in MATLAB environment. To deduce the regional stress tensor from earthquake FMSs (strike, dip, and rake) in the area, with the optimal stress tensors determined through stress inversion methodology. The current studies focus on delineating the alignment of the 3 primary stress axes, i.e. σ 1, σ 2, and σ 3, with a hierarchical relationship of $\sigma 1 > \sigma 2 > \sigma 3$. The assessment of stress attributes via focal mechanism inversion is based on the hypothesis of stress homogeneity across the source region, enabling the evaluation of the prevailing stress status within the study region. The methodology involves determining the optimal fit of regional principal stress orientations. The optimal stress tensor alignment can be determined (Gephart & Forsyth 1984) by assuming fault slip occurs along the direction of maximum resolved shear stress at the time of an earthquake (Bott 1959). The shape ratio R is characterized as the relationship between the intermediate stresses considered about the maximum and minimum horizontal stresses, thereby influencing the configuration of the stress ellipsoid. Therefore, we determined the orientations of the three principal stress directions σ 1, σ 2, and σ 3, along with the shape ratio R, which characterizes the configuration of the stress ellipsoid as:

$$\sigma = \frac{\sigma 2 - \sigma 3}{\sigma 1 - \sigma 3}$$

All stress inversions are designed to determine the optimal stress tensor that corresponds to the provided focal mechanisms. This stress tensor is symmetric, which means it consists of only six independent components. The inversion technique introduced by Vavrycuk (2014) incorporates a

Table 2. Computed parameters of focal mechanism solutions for the events used in the present study. NSS: Normal with Strike-Slip Fault, RSS: Reverse with strike-slip Fault, N: Normal Fault, SS: Strike-Slip fault, R: Reverse Fault.

S.	Date	Time	Latitude	Longitude	Depth	Magnitude	Strike	Dip	Rake	P-axi	s (°)	T-axi	is (°)	Type of
No.	(dd/mm/yyyy)	(h:m:s)	(°N)	(°E)	(Km)	(M_L)	(°)	(°)	(°)	Az.	Pl.	Az.	Pl.	fault
1	17/01/2019	04:47.6	28.62	94.84	28.9	3.5	218	52	-37	90.4	50.4	93.4	5.7	NSS
2	15/03/2019	30:20.5	28.9	95.2	30.7	3.5	240	33	42	183.9	19.6	58.7	58.2	RSS
3	02/07/2019	08:35.7	27.85	95.16	40.6	5.4	180	28	-89	267.5	72.9	89.2	17	N
4	14/07/2019	48:20.2	28.11	95.09	108.8	3.7	132	68	36	257.1	6.9	353.1	40.5	RSS
5	10/12/2019	16:51.3	28.23	95.53	32.8	3.6	85	68	55	199.9	15.7	312.2	53.3	RSS
6	02/02/2020	27:06.0	29.02	94.72	10	4.2	354	82	50	114.3	26	228	39.4	RSS
7	26/02/2020	50:17.2	28.42	95.1	9.2	3.7	60	60	90	150	15	330	75	R
8	18/03/2020	20:28.1	28.95	94.7	4.1	3.9	251	82	50	11.4	26	125	39.4	DSS
9	17/04/2020	23:03.5	28.48	95.22	15.2	3.5	240	62	-89	152.4	73	329.2	17	N
10	29/04/2020	41:51.9	28.91	94.77	10	3.8	180	60	-89	92.7	75	269.2	15	N
11	09/09/2020	42:48.0	28.58	95.2	9.8	3.8	252	70	-89	170	85	341.2	5	N
12	04/11/2020	21:57.1	28.53	95.25	3.2	3.5	240	71	30	8	6	102.1	34.3	SS
13	10/12/2020	29:52.5	28.42	94.8	48.6	3.5	240	66	-89	152	69	329.2	21	N
14	06/05/2021	38:42.5	28.7	94.91	42.6	4.6	65	54	37	9.4	4.1	274.6	49.4	SS
15	06/05/2021	10:14:53	28.54	94.76	32.5	4.3	255	80	35	22	16	122.2	31.4	SS
16	14/10/2021	36:27.1	28.54	95.02	21	4.4	96	78	-31	50.5	30.2	147.6	12	NSS
17	31/10/2021	38:07.3	28.44	94.98	36.3	4	276	77	-62	217.1	50.1	344.1	26.6	NSS
18	10/12/2021	03:29.5	28.87	95.04	37.8	4.3	188	52	-89	103.7	83	277.2	7	N

constraint for fault instability to differentiate actual fault slips from the provided data and to assess fault orientations; consequently, it requires multiple iteration steps. Throughout the iterations, the inversion evaluates the given auxiliary nodal planes, and utilizing the Mohr-Coulomb criterion, the identification of the true fault planes is conducted (Michael 1984; Zoback 2010; Vavryčuk 2014). It identifies the most unstable nodal plane as the true fault plane. This method of stress inversion can select the real fault plane based on the constraints of fault instability, thereby defines an optimal stress tensor. Typically, it requires 3 to 4 iterations. Initially, the inversion assesses the orientations of principal stresses and the shape ratio without any predefined fault planes, subsequently identifying the actual fault planes using the Mohr-Coulomb criterion. These processes are reiterated until the outcome aligns with the most accurate solution. The inversion results encompass a stereogram that illustrates P and T axes, a stereogram that depicts primary stress axes along with their precision, a graphical depiction of R values, and a visualization of Mohr circles (Figs. 3, 4 and 5). We investigated the tectonic style further using the stress regime index (R') values. The R' values come from shape ratios depending on which principal axes have the largest plunges. The aim of this investigation was to identify the dominant tectonic regime related with the seismic events in the area and ascertain the direction of the stress field in two specific zones located on the eastern and western limbs of the Siang antiform, where seismic activities are more prevalent in the western sector. Additionally, we combined the dataset from these two regions and identified the overall prevailing stress regime in Siang Valley and surrounding area in the EHS.

RESULTS AND DISCUSSIONS

Focal Mechanism Solutions

Table 2 lists the FMSs, and the plotted beach balls in figure 2a. In the Siang Valley and adjoining region, the FMSs primarily exhibit thrust mechanisms along with a combination of strikeslip mechanisms; the dipping planes oriented in the northeast exhibit similarities with the orientations of the primary tectonic faults and the subduction of the Indian plate. Despite this, the FMS of certain seismic events indicates extensional deformation within a compressional setting, implying a complex subsurface deformation pattern. In the eastern part of the Siang Antiform (Table 2, Fig. 2a), event no. 2 is located near the Lohit thrust, exhibiting a reverse with a strike-slip mechanism. Event no. 5 occurred north of the Pasighat thrust, also showing a reverse with a strike-slip mechanism, while event no. 9 is situated near the Bomdo thrust in the core of the Siang window, this event displays a low dipping normal fault mechanism with a focal depth of 15.2 kilometers. The source zone of the 1950 earthquake indicates a dextral strike-slip

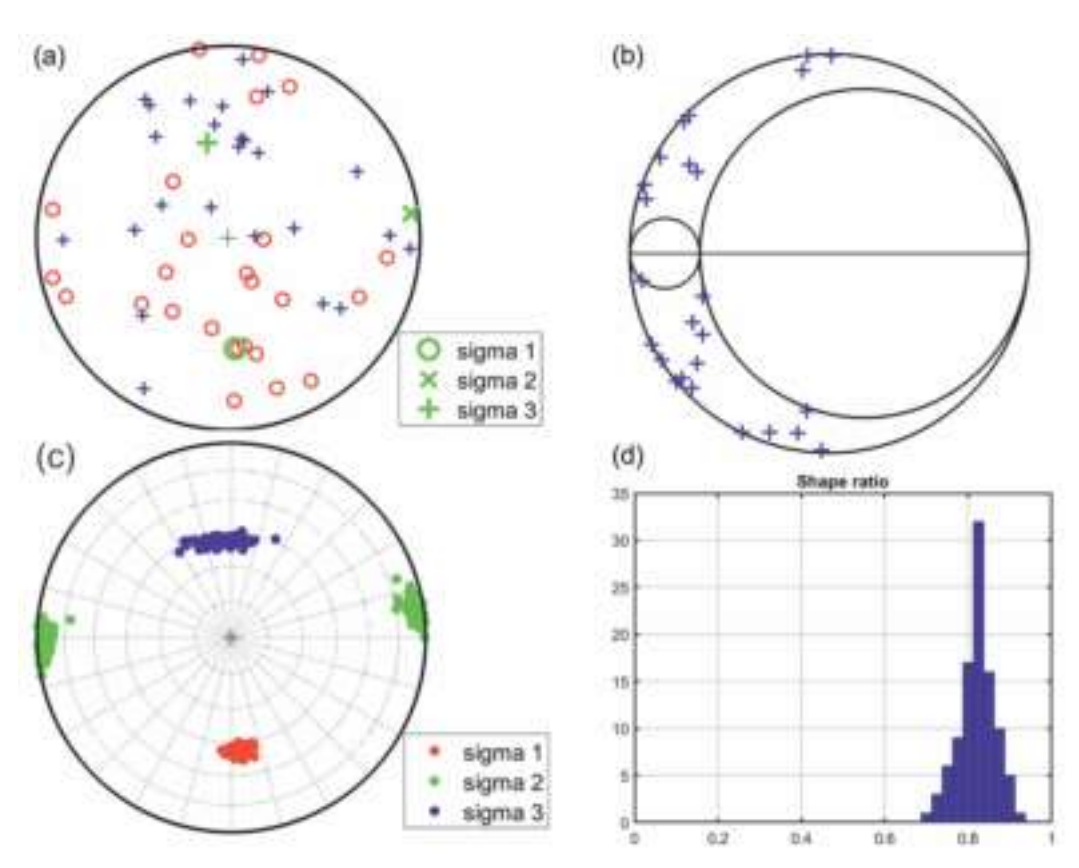


Fig. 3. Plot depicting outcomes of stress analysis performed in the western limb of Siang Window, (a) Plot showing P and T- axes with principal stress axes, the red circles marked the P- axes and T- axes by the blue cross; (b) Mohr's circles with position of fault instability (blue plus signs); (c) red, green, blue circles representing confidence limit of principle stresses sigma 1, 2, 3 direction, respectively; (d) histogram of shape ratio i.e. R.

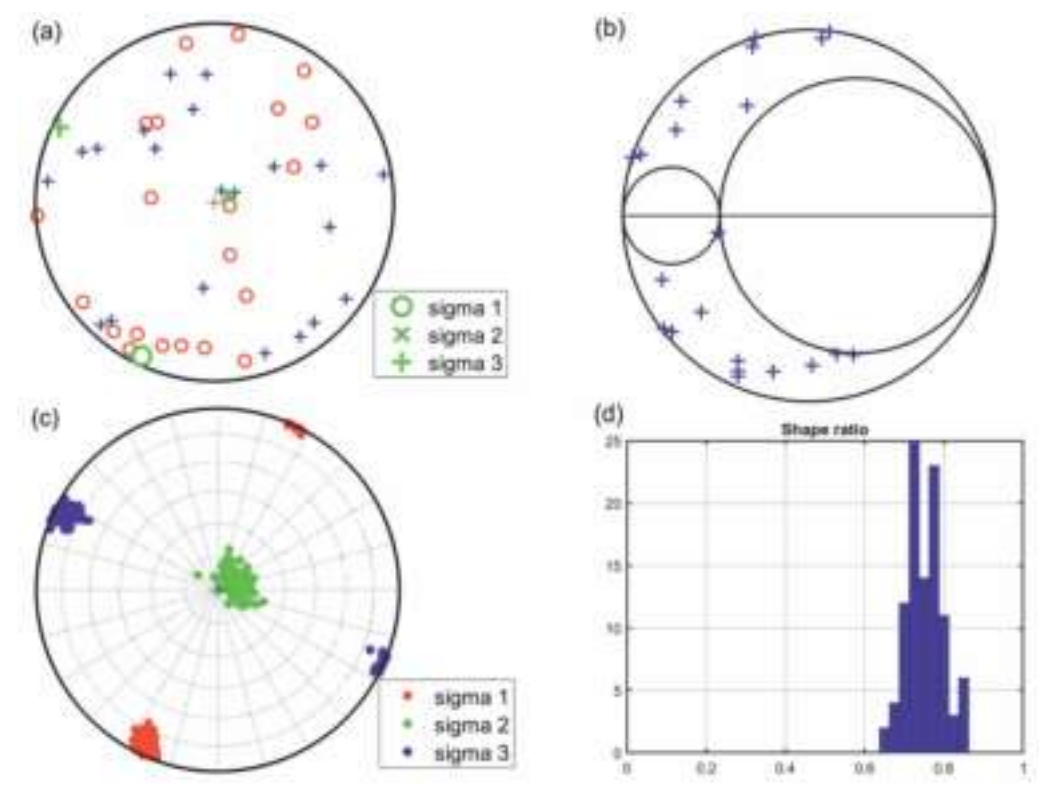


Fig. 4. Plot depicting outcomes of stress analysis performed in eastern limb of Siang Window, (a) Plot showing P and T- axes with principal stress axes, the red circles marked the P- axes and T- axes by the blue cross; (b) Mohr's circles with position of fault instability (blue plus signs); (c) red, green, blue circles representing confidence limit of principle stresses σ1, σ2 and σ3 direction, respectively; (d) histogram of shape ratio i.e. R.

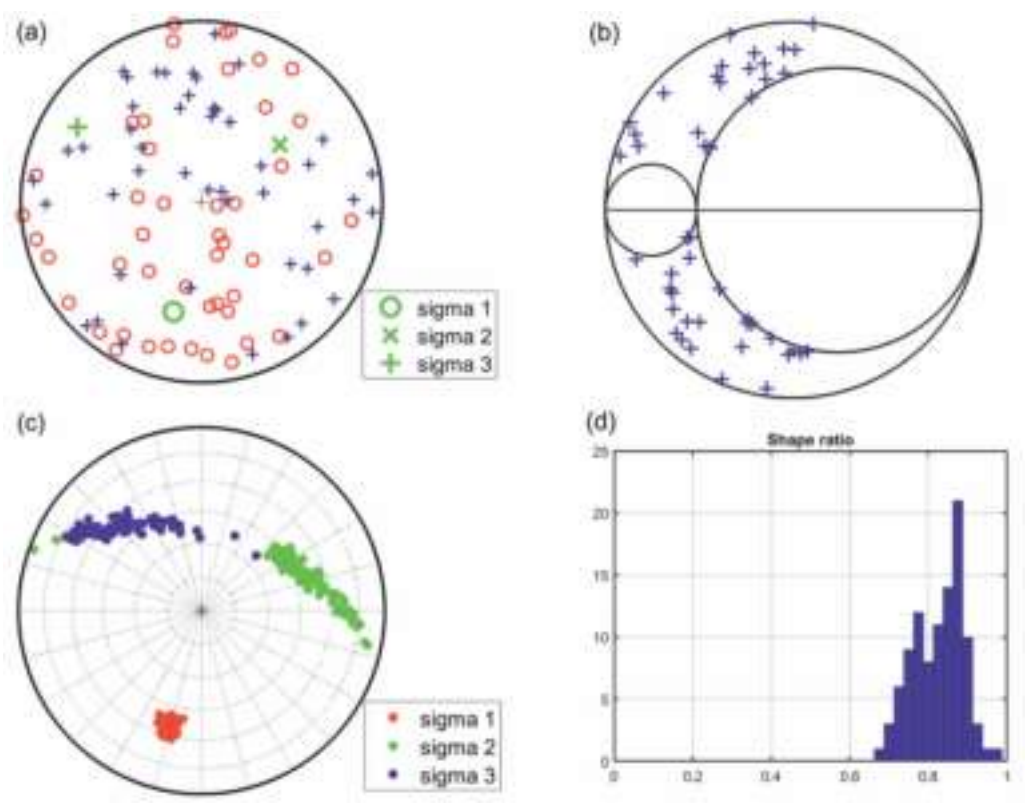


Fig. 5. Plot depicting outcomes of overall stress analysis performed in Siang Window, (a) Plot showing P- and T- axes with principal stress axes, the red circles marked the P- axes and T- axes by the blue cross; (b) Mohr's circles with position of fault instability (blue plus signs); (c) red, green, blue circles representing confidence limit of principle stresses sigma 1, 2, 3 direction, respectively; (d) histogram of shape ratio R.

movement of the plate to the north of the Lohit thrust on the eastern side of the Siang Valley (Ben-Menahem et al. 1974). Events no. 11 and 12 are close to each other and show dipping normal fault and strike-slip with reverse faulting, yet there is a significant difference in focal depth of 15.2 km and 3.2 km, respectively. Event no. 18 is comparatively deeper, showing normal faulting with a 37.8 km focal depth. The epicentre of Event no. 6 and 8 occurred north of the Siang antiform which shows reverse with strike slip mechanism with varying focal depth, while Event no. 10 shows low dipping normal faulting. The western part of the Siang window, which is more seismically active than the eastern part, has more number of earthquakes (events no. 1, 4, 7, 13, 15, 16 and 17, Table 2). Events no. 16 and 7 lie in the core of the Siang antiform, and show normal fault with strike slip and reverse fault mechanism while these epicentres are far away from each other. The deepper event 4 demonstrates a reverse with a strike slip fault mechanism. In contrast event number 17 exhibits a shallow focus normal with strike slip mechanism, both event (4 & 17) located on the Bomdo thrust with varying epicentre positions. Events 1 and 13 are situated along the Ramgarh thrust, displaying normal faulting at different focal depths. Event 15, along the MCT, displays a strike-slip mechanism up to a focal depth of 32.5 kilometers. Event 3, close to the MFT, showcases normal faulting. Chouhan & Srivastava (1975) analyzed the FMSs of seismic events in the northeastern region of India. Utilizing data on first-arrival polarities, they specifically focused on two-years. The findings of the study suggested the presence of strike slip faulting in the northern part and thrust type faulting in the southern part of the Myanmar ranges. According to Panthi et al. (2013), the dominant seismotectonic state in the Eastern Syntaxis regions displays a thrust mechanism, with instances of both normal and strike-slip faulting indicating compressional forces in the vicinity. Additionally, the present study results show that the main mechanism of energy release in the Eastern Himalayan region is mainly linked to thrust faulting, along with a combination of strike-slip mechanisms. The determination of the orientations of the P and T axes is derived from focal mechanism solutions (Table 2), facilitating the understanding of the stress distribution in the Siang Valley. By analyzing FMS, it is possible to ascertain the azimuth and dip angles of both the P- and T- axes.

Depth distribution of seismicity

The Northeastern Himalayan region exhibits a wide occurrence of seismic events ranging from moderate to high magnitude earthquakes within the crust (0-60 km depth). An identifiable grouping of seismic occurrences is specifically observed in the western part of Siang Antiform and Namche Barwa region. A detailed analysis of the depth distribution of earthquake epicentres has been carried out beneath this specific region by employing a north-south-oriented profile A-B (Fig. 2a & b) that divide the Siang Antiform into two sections and traverse through tectonic structures such as the Walong thrust, Lohit thrust, MCT, MBT, Bomdo thrust, Ramgarh Thrust, and the main frontal thrust. The depth distribution of earthquakes along section A-B is graphically represented with depth-projected FMSs along with major

tectonic features and faults (Fig. 2b). The MCT, MBT, and MFT exhibit a dip in the northwest. Seismic activity is predominantly situated between the MFT and MBT within the depth section, while a noticeable cluster of earthquakes is evident in the upper crust extending up to a depth of 40 km. Earthquakes in the Eastern Himalayan region exhibit a high concentration within a specific area delineated by the MFT and MCT, thereby unveiling complex imbricate configuration in the frontal part of the Arunachal Himalaya. The frequency of earthquakes in the lesser Himalayan domain is closely tied to predominantly thrust motions along the MBT and MFT (Gupta et al. 2015). The spatial distribution of hypocenters at various depths aligns with previous research, indicating significant seismic activity in the western and eastern part of Siang Antiform, and Namche Barwa regions, respectively. Seismicity in the western portion of the Siang Valley is more pronounced in comparison to the other parts of the valley (Pal et al. 2024a). In the depth projection view (Fig. 2b), FMS close to the tectonic feature RT (event 10) shows strike-slip fault and near MBT, events 7, 9, 16 and 1 are normal and reverse with a combination of strike-slip mechanisms. Deeper earthquakes (events 5, 17, 14, 2 and 18) show thrust with strike-slip combination.

Stress Tensor Inversions Analysis

Stress Inversion is carried out on both the Western and Eastern sides of the Siang window in the Siang Valley, Arunachal Himalaya. The current stress distribution in this area is determined by utilizing focal mechanism data from these two distinct regions. In the process of inversion insights of significant value regarding the alignment of the primary axes of maximum compression (P), extension (T), and neutral (B) are elucidated through the utilization of inversion parameters. The outcomes derived from the inversion procedure, as depicted in figures 3, 4 & 5, encompass four distinct elements denoted as a, b, c, & d. These components exhibit the focal sphere that showcases the P and T axes, the optimal principal stresses, the Mohr circle, the stereographic projection portraying the principal stresses alongside their associated uncertainties, and a histogram that presents the shape ratios. The Mohr circle diagram's depiction helps to demonstrate the reliability of the results and the results of the stress inversion (Fig. 3b, 4b & 5b). Blue crosses were assigned to the possible orientations of fault slips (one slip direction belongs to each seismic event). If these crosses were located near the largest Mohr circle, that is between $\sigma 1$ and $\sigma 3$, their corresponding direction could be considered unstable and identified as that of the real fault plane. These solutions must be analyzed in relation to the P axes that are perpendicular to the dilatational quadrants. If the orientations of the $\sigma 1$ and P axes align, then S_{hmax} vectors can be identified. Consequently, we can infer the type of tectonic regime that may be associated with the earthquakes.

In the western portion of the Siang Valley region, twenty-five focal mechanism solutions were utilized for the inversion, where three events, including the Mw 5.9 Mechuka Earthquake (Yadav *et al.* 2021), occurred along the MCT resulting in extensive surface ruptures. The primary alignment

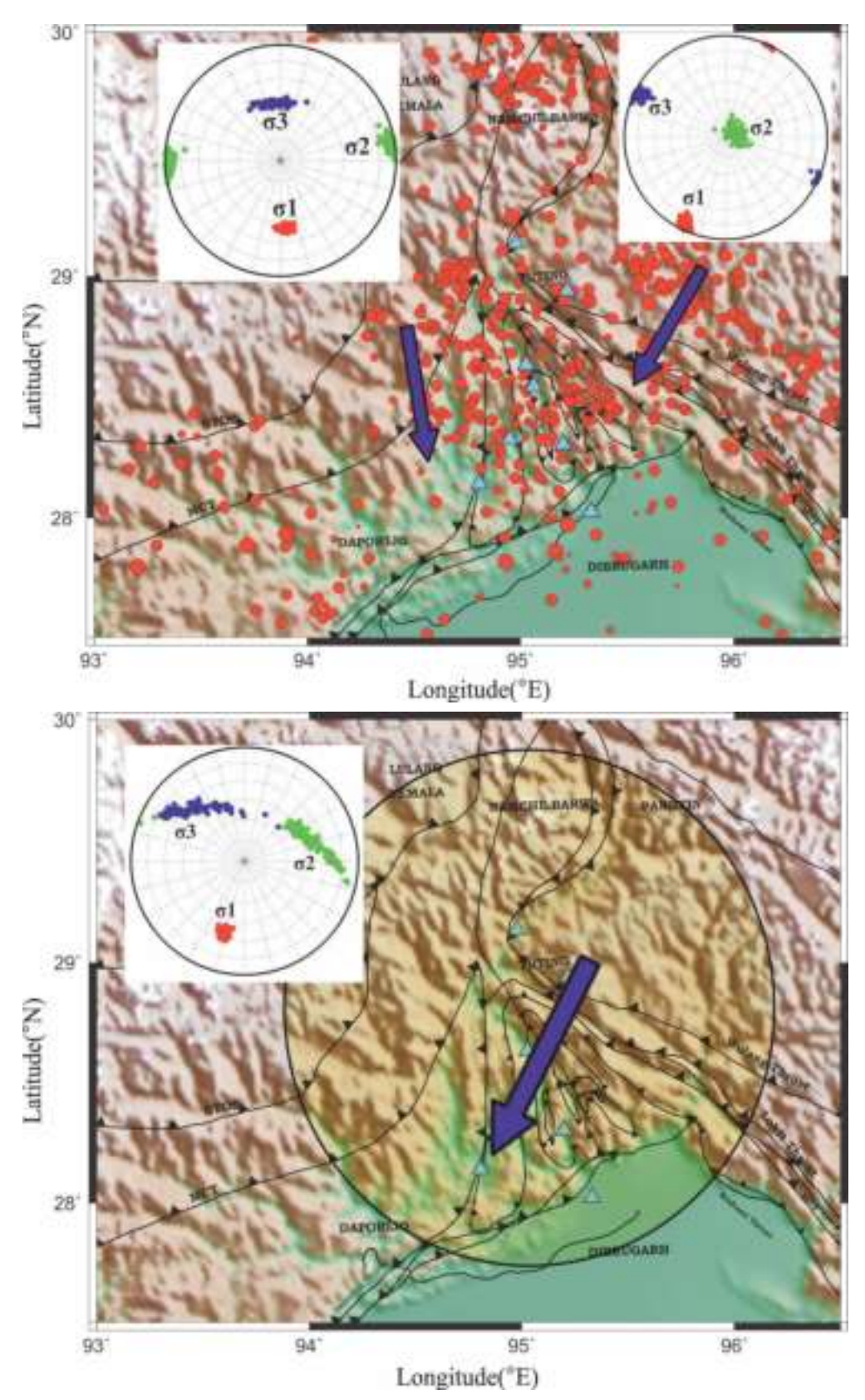


Fig. 6. (a) The plot depicts the FMS results of events used in the stress inversion analysis and the seismicity in and around Siang Valley. Cyan triangles represent the BBS station locations of recorded events. The maximum horizontal stress (Sh_{max}) direction in the western and eastern part of Siang Valley is SSE and SSW, respectively. (b) The direction of Sh_{max} in the Siang Valley of Arunachal Himalaya indicated by a Blue arrow, i.e. SSW.

of the maximum compression (P) axis is oriented towards the SSE direction (represented by red circles), with the azimuth of σ 1 identified as N176.30 (approximately towards the South), illustrated in figure 3a, c. Upon utilizing the obtained inclinations of $\sigma 1$ (red dots), $\sigma 2$ (green dots), and $\sigma 3$ (blue dots), the dominant tectonic regime is established. In the western portion of the Siang Valley region, the plunges of $\sigma 1$, σ2, and σ3 measured approximately 41.6°, 4.5°, and 47.9°, respectively. These values suggest that the $\sigma 1$ axis tends to be oriented nearer to the horizontal plane and the σ^2 axis is horizontal, while the σ 3 axis is near to the vertical, indicating a prevailing compressional stress regime within the area. A histogram depicting shape ratios has been developed based on the realizations (Fig. 3d). The peak observed in this histogram represents the optimal R-value, determined to be 0.82 for the western part of Siang Valley region. Through the assessment of the stress regime index (R'), incorporating the maximum plunge axes and R-value, valuable insights can be gained regarding the primary regional tectonic stress regime currently active in this geographical area (Delvaux et al. 1997; Czirok 2016). Three relations can be provided:

- 1. If $\sigma 1$ is oriented vertically, the resultant R' equals R, demonstrating an extensional tectonic stress regime.
- 2. If σ^2 is oriented vertically, the resultant R' equals 2 R, suggesting a strike-slip or transverse tectonic stress regime.
- 3. If $\sigma 3$ is oriented vertically, the resultant R' equals 2 + R, indicating a compressional tectonic stress regime.

Consequently, the value of R is ascertained with variations falling within the 0-3 range, indicating a radial extension at 0 to radial compression, at 3, tectonic conditions. Thus, R' equals 2.82, signifying the presence of a reverse type of faults and a radial compression tectonic setting. The determination of the predominant horizontal stress S_{hmax} 's orientation is dependent on the azimuth and plunge of the principal stress axes (Zoback 1992). The S_{hmax} azimuth in this area is calculated at 176.30°N (P-axes azimuth). Therefore, we conclude from here that earthquakes in the western part of Siang region are mostly exposed to thrust with strike-slip faulting, and the direction of S_{hmax} is towards almost south (Fig. 6a).

In the eastern part of the Siang Valley region, twenty-one fault plane solutions were used in the inversion process. The focal mechanism of the 1950 earthquake in Assam signifies the presence of a single strike-slip fault system, while subsequent seismic events suggest a combination of oblique motion-thrust faulting alongside a notable strike-slip component. In the eastern region, $\sigma 1$ and $\sigma 3$ exhibit nearly horizontal orientations, as indicated in Fig. 4c, with azimuths of 205.30° and 295.70°, respectively, while $\sigma 2$ is positioned close to vertical. The calculated shape ratio values R (0.73) (Fig. 4d) and R' (1.27) propose the prevailing strike-slip tectonic regime in this area. The azimuth of the maximum horizontal stress, S_{hmax} , in this zone, is N 205.30°, corresponding to a south-southwest orientation (Fig. 6a).

We further amalgamated the moment tensors of the eastern and western sections of the Siang Valley region and

conducted stress inversion analysis on the complete dataset. Our results (Fig. 5, Table 3) indicate that the $\sigma 1$ (37.2°) and $\sigma 3$ (20.8°) axes are oriented close to the horizontal, while the σ 2 (45.4°) axis shows more proximity to the vertical position (with the highest plunge angle), suggesting a prevailing strikeslip regime within the Siang Valley area. The principal stress ratio (R) calculated for the integrated dataset equates to 0.75, whereas the R' value is determined to be 1.25. The combined dataset examination shows that the region is largely characterized by prominent strike-slip movements, with the primary stress direction σ1 pointing towards N194.30° (SSW), almost due south. The direction of S_{hmax} is SSW in this case (Fig. 6b). All the stress inversion parameters for the western, eastern and combined analysis of the study area are listed in Table 3. In contrast to the findings of Kamra et al. (2023), distinct patterns can be observed in the S_{hmax} values across different tectonic regions. Specifically, in the Shillong Plateau, a predominant northerly orientation indicates evident compressional forces. Conversely, the Mikir Hills display a northeast trend, suggesting a transfension regime. Moving to the eastern Himalayan zone, the S_{hmax} orientation shifts to SSW, indicating a prominent strike-slip regime and in the Indo-Burma zone, the $S_{\mbox{\tiny hmax}}$ values align in a northeast direction, highlighting a clear compression regime.

CONCLUSIONS

The studies of FMS and stress inversion in seismically active regions of the Siang Valley within the EHS are conducted. This study was prompted by the occurrence of swarm earthquakes almost annually in the EHS locality. The spatial distribution of seismicity indicates groupings in the eastern and western parts of the Siang valley, as well as in the Namche Barwa vicinity within EHS, reaching depths of up to 60 km. The region of the Eastern Himalayas is primarily distinguished by the prevalence of reverse, strike-slip and a combination of both fault types. In the western sector of the Siang Valley, reverse faulting has a prevalence of with strikeslip characteristics. These faults are characterized by dip angles ranging from low to moderate. The data derived from the FMSs is utilized to gain insights into widespread contemporary tectonic regime in the area. In the NE Himalaya, stress tensor analysis has been applied to various structures, such as the MBT, MCT and Lohit thrust. The region is subdivided into two subareas, and forty-six fault plane solutions were used. It is found that the western side of the Siang Valley region shows radial compression; however, the eastern side shows a clear strike-slip regime. The azimuth of S_{bmax} is N176.3° on the western side and N205.3° on the eastern side. The inversion of the combined data set shows the clear strike-slip with maximum principal stress (σ1) oriented in N194.3°. The stress regime in the region is predominantly transverse, with a sub-horizontal maximum principal stress axis $(\sigma 1)$ oriented to SSW, consistent with the India-Eurasia plate convergence. The elevated seismicity observed in this area is attributed to the northward and eastward displacement of the Indian plate towards the Eurasian and Burmese plates, respectively.

Acknowledgements: The authors express their gratitude to the Director of the WIHG Dehradun for offering the necessary resources and support to carry out the research. We acknowledge Drs. Devajit Hazarika and Naresh Kumar, WIHG, for their assistance with the setup of the BBS stations and conducting fieldwork. The first author expresses gratitude to the University Grants Commission (UGC), New Delhi for providing financial assistance during the entire duration of the research.

Author Contributions: Ashish Pal (AP): Data curation, Data processing, investigation, methodology and writing-original draft. Dilip Kumar Yadav (DKY): conceptualization, validation and supervision. Debonil Baruah (DB): Visualization and editing. Abhishek Kumar Gupta (AKG): review and editing. H.C. Nainwal: supervision. Parakh Sahu (PS): Visualization

Data availability: Wave-form data could be acquired by sending a mail to the Director (director@wihg.res.in) WIHG, Dehradun, India

Statements and Declarations: The authors assert that they do not have any documented conflicting financial benefits or own associations that may have impacted the research detailed in this investigation.

References

- Acharya, S.K., Saha, P. 2013. Age and tectono-magmatic setting of abor volcanics, siang window, eastern himalayan syntaxial area, India. *Journal of Applied Geochemistry*, **15**(2), 170-192.
- Baruah, S., Duarah, R., Yadav, D.K. 1997. Pattern of Seismicity in Shillong-Mikir Plateau and the orientation of compressional axis. *Journal Geological Society of India*, **49**(5), 533-538.
- Ben-Menahem, A., Aboodi, E., Schild, R. 1974. The source of the great Assam earthquake—an interplate wedge motion. *Physics of the Earth and Planetary Interiors*, **9**(4), 265-89.
- Bilham, R., England, P. 2001. Plateau "Pop-Up" in the Great 1897 Assam Earthquake. Nature, 410, 806-809. https://doi.org/10.1038/35071057
- Bilham, R. 2006. Comment on "Interpreting the style of faulting and paleoseismicity associated with the 1897 Shillong, northeast India, earthquake" by C. P. Rajendran et al. *Tectonics*, 25 (2). doi:10.1029/2005tc001893
- Bott, M.H.P. 1959. The Mechanics of Oblique Slip Faulting. *Geological Magazine*, 96, 109-117. https://doi.org/10.1017/S0016756800059987
- Chandra, U. 1978. Seismicity, Earthquake Mechanisms and Tectonics along the Himalayan Mountain Range and Vicinity, *Physics of the Earth and Planetary Interiors*, 16, 109-131. https://doi.org/10.1016/0031-9201(78)90083-3
- Chen, W.P., and Molnar, P. 1990. "Source Parameters of Earthquakes and Intraplate Deformation beneath the Shillong Plateau and the Northern Indo-Burman Range," *Journal of Geophysical Research*, Vol. 95, No. B8, 12527-12552. doi:10.1029/JB095iB08p12527
- Chouhan, R.K.S., Srivastava, V.K.1975. Focal mechanisms in northeastern India and their tectonic implications. *PAGEOPH* 113, 467-482. https://doi.org/10.1007/BF01592932.
- Curray, J.R., Emmel, F.J., Moore, D.G., Raitt, R.W. 1982. Structure, Tectonics, and Geological History of the Northeastern Indian Ocean. In: Nairn, A.E.M., Stehli, F.G. (eds) The Ocean Basins and Margins. Springer, Boston, 399-450. https://doi.org/10.1007/978-1-4615-8038-6-9
- Czirok, L. 2016. Analysis of stress relations using focal mechanism solutions in the Pannonian basin. Geosciences and Engineering: a Publication of the University of Miskolc, 5(8), 65-84.
- Delvaux, D., Moeys, R., Stapel, G., Petit, C., Levi, K., Miroshnichenko, A., Ruzhich, V., San'kov, V. 1997. Paleostress reconstructions and geodynamics of the Baikal region, central Asia, Part 2. Cenozoic rifting. *Tectonophysics*, 282(1-4), 1-38.

- Engdahl, E.R., van der Hilst, R., Buland, R. 1998. Global teleseismic earthquake relocation with improved travel times and procedures for depth determination, *Bulletin of the Seismological Society of America*, 88, 722-743.
- Gephart, J.W., Forsyth, D.W. 1984. An improved method for determining the regional stress tensor using earthquake focal mechanism data: application to the San Fernando earthquake sequence. *Journal of Geophysical Research: Solid Earth*, 89(B11), 9305-9320.
- Gupta, S.D., Nandy, D.R. 1982. Seismicity and Tectonics of Meghalaya Plateau, Northeastern India. VII Symposium on Earthquake Engineering, University of Roorkee, Roorkee, India, Vol.: I, (19-24).
- Gupta, H.K., Singh, S.C., Dutta, T.K. & Saikia, M.M. 1984. Recent investigations of North East India seismicity. *In:* Gongu, G., Xing-Yuan, M. (eds.), Proceedings of the Interna-tional Symposium on Continental Seismicity and Earthquake Prediction, pp. 63-71. Seismological Press, Beijing.
- Gupta, T.D., Riguzzi, F., Dasgupta, S., Mukhopadhyay, B., Roy, S., Sharma, S. 2015. Kinematics and strain rates of the Eastern Himalayan Syntaxis from new GPS campaigns in Northeast India. *Tectonophysics*, 655, 15-26. 10.1016/j.tecto.2015.04.017
- Gururajan, N.S., Choudhuri, B.K. 2003. Geology and tectonic history of the Lohit Valley, Eastern Arunachal Pradesh, India. *Journal of Asian Earth Sciences*, 21(7), 731-741.
- Havskov, J., Ottemoller, L. 1999. SEISAN earthquake analysis software. Seismological Research Letters, 70(5), 532-534.
- Hazarika, D., Kundu, A., Ghosh, P. 2022. Seismotectonic scenario of the indenting northeast corner of the Indian plate in the Tidding-Tuting Suture Zone of the Eastern Himalayan Syntaxis. *Tectonophysics*, 824, 229197. https://doi.org/10.1016/j.tecto.2021.229197
- Kamra, C., Chopra, S., Yadav, R.B.S. 2023. Tectonic stress of northeastern Indian region derived from seismic focal mechanisms and the effect of focal mechanism on stress drop: a comparative analysis with Kachchh intraplate region of India. *Geophysical Journal International*, 234(1), 453-478.
- Kayal, J.R. 1991. Earthquake prediction in Northeast India-a review. Pure and applied Geophysics, 136, 297-313.
- Kayal, J.R. 1998. Seismicity of Northeast India and surrounding-development over the past 100 years. *Journal of Geophysics*, **29**(1), 9-34.
- Kayal, J.R., De, R. 1991. Microseismicity and tectonics in northeast India. Bulletin of the Seismological Society of America, 81(1), 131-138.
- Kayal, J.R., Arefiev, S.S., Barua, S., Hazarika, D., Gogoi, N., Kumar, A., Chowdhury, S.N., Kalita, S. 2006. "Shillong Plateau Earthquakes in Northeast India Region: Complex Tectonic Model. *Current Science*, 19, 109-114.
- Khattri, K.M., Tyagi, A.K. 1983. Seismicity patterns in the Himalayan plate boundary and identification of the areas of high seismic potential. *Tectonophysics*, **96**(3-4), 281-297.
- Le Fort, P. 1975. Himalayas: the collided range. Present knowledge of the continental arc. *American Journal of Science*, **275A**, 1-44.
- Lee, W.H., Lahr, J.C. 1975. HYPO71 (revised; a computer program for determining hypocenter, magnitude, and first motion pattern of local earthquakes. *Open-File Report* Vol. 1975 (75-311) US Geological Survey. doi:10.3133/ofr75311
- Michael, A.J. 1984. Determination of stress from slip data: faults and folds. *Journal of Geophysical Research: Solid Earth*, **89**(B13), 11517-11526.
- Michael, A.J. 1987. Use of focal mechanisms to determine stress: a control study. *Journal of Geophysical Research: Solid Earth*, **92**(B1), 357-368.
- Mitchell, A.H.G. 1981. Phanerozoic plate boundaries in mainland SE Asia, the Himalaya and Tibet. *Journal of Geological Society of London*, 138, 109-122.
- Mitra, S., Priestley, K., Bhattacharyya, A., Gaur, V.K. 2005. Crustal structure and earthquake focal depths beneath northeastern India and southern Tibet. Geophysical Journal International, 160, 227-248.

- Molnar, P., Tapponnier, P. 1975. Cenozoic Tectonics of Asia: Effects of a Continental Collision: Features of recent continental tectonics in Asia can be interpreted as results of the India-Eurasia collision. *Science*, 189(4201), 419-426.
- Nandy, D.R. 2001. Geodynamics of Northeastern India and Adjoining Region. ABC Publ., Kolkata, India, 209p.
- Ni, J., Barazangi, M. 1984. Seismotectonics of the Himalayan collision zone: Geometry of the underthrusting Indian plate beneath the Himalaya. *Journal of Geophysical Research: Solid Earth*, **89**(B2), 1147-1163.
- Pal, A., Yadav, D.K., Kumar, N., Gupta, A.K., Paul, A., Nainwal, H.C. 2024a. Modelling of source parameters of local earthquakes and seismotectonic implications in Siang Valley, NE India. *Journal of Earth System Science*, 133(2), 63. https://doi.org/10.1007/s12040-024-02272-9
- Pal, A., Yadav, D.K., Gupta, A. K., Nainwal, H.C. 2024b. Seismotectonics of Siang Valley and Adjoining Region Inferred from Focal Mechanism Solutions Using Waveform Inversion. *Pure Appl. Geophys.* https://doi.org/10.1007/s00024-024-03518-9
- Panthi, A., Singh, H.N., Shanker, D. 2013. Revisiting state of stress and geodynamic processes in Northeast India Himalaya and its adjoining region. *Geosciences*, 3(5), 143-152.
- Priestley, K., Jackson, J., McKenzie, D. 2008. Lithospheric structure and deep earthquakes beneath India, the Himalaya and southern Tibet. *Geophysical Journal International*, **172**(1), 345-362.
- Poddar, M.C. 1950. The Assam earthquake of 15th August 1950. *Indian Minerals*. **4**, 167-176.
- Raoof, J., Mukhopadhyay, S., Koulakov, I., Kayal, J.R. 2017. 3-D seismic tomography of the lithosphere and its geodynamic implications beneath the northeast India region. *Tectonics*, 36(5), 962-980.
- Rai, A., Mittal, H., Singh, G.P. 2024. Estimation of source and spectral decay parameter for local earthquake in the Siang region of Arunachal Himalya and its Implication to the Tectonic and crustal heterogeneity. Pure and Applied Geophysics, 181, 789-813.
- Rajendran, C.P., Rajendran, K., Duarah, B.P., Baruah, S., Earnest, A. 2004. Interpreting the style of faulting and paleoseismicity associated with the 1897 Shillong, northeast India, Earthquake: implications for regional tectonism. *Tectonics*, 23, TC4009. doi:10.1029/2003TC001605, 2004
- Rastogi, B.K., Singh, J., Verma, R.K. 1973. Earthquake mechanisms and tectonics in the Assam-Burma region. *Tectonophysics*, **18**(3-4), 355-366.
- Salvi, D., Mathew, G., Pande, K., Kohn, B.P. 2021. Phased cooling of the Siang antiform, Eastern Himalaya: Insight from multi-

- thermochronology and thermal studies. *Journal of Earth System Science*, **130**, 1-20.
- Singh, S. 1993. Geology and tectonics of the eastern syntaxial bend, Arunachal Himalaya. *Journal of Himalayan Geology*, **4**, 149-163.
- Snoke, J.A., Munsey, J.W., Teague, A.G., Bollinger, G.A. 1984. A Program for Focal Mechanism Determination by Combined Use of Polarity and SV-PAmplitude Ratio Data. *Earthquake Notes*, 55, 15.
- Snoke, J.A., Lee, W.H.K., Kanamori, H., Jennings, P.C., Kisslinger, C. 2003. FOCMEC: Focal mechanism determinations. *International handbook of earthquake and engineering seismology*, 85, 1629-1630.
- Tapponnier, P., Pelzer, G., Ledain, A.Y., Armijo, R., Cobbold P. 1982. Prop agating extrusion tectonics in Asia: new insights from simple experiments with plasticine. *Geology*, **10**, 611-616.
- Tapponnier, P., Peltzer, G., Armijo, R. 1986. On the mechanics of the collision between India and Asia. Geological Society, London, Special Publications, 19(1), 113-157.
- Thingbaijam, K.K.S., Nath, S.K., Yadav, A., Raj, A., Walling, M.Y., Mohanty, W.K. 2008. Recent seismicity in Northeast India and its adjoining region. *Journal of Seismology*, **12**, 107-123.
- Valdiya, K.S. 1980. The two intracrustal boundary thrusts of the Himalaya. Tectonophysics, 66(4), 323-348.
- Vavryčuk, V. 2014. Iterative joint inversion for stress and fault orientations from focal mechanisms. Geophysical Journal International, 199(1), 69-77.
- Yadav, D.K., Hazarika, D., Kumar, N., Singh, A.K. 2021. Microseismicity study in the Siang Valley of Arunachal Himalaya: tectonic Implications of the 2019 Mw 5.9 Mechuka earthquake. *Himalayan Geology*, 42(2), 290-298.
- Yang, R., Herman, F., Fellin, M.G., Maden, C. 2018. Exhumation and topographic evolution of the Namche Barwa Syntaxis, eastern Himalaya. *Tectonophysics*, 722, 43-52.
- Zhao, W., Nelson, K.D., Che, J., Quo, J., Lu, D., Wu, C., Liu, X. 1993. Deep seismic reflection evidence for continental underthrusting beneath southern Tibet. *Nature*, 366(6455), 557-559.
- Zoback, M.D. 2010. Reservoir Geomechanics. Cambridge university press. https://doi.org/10.1017/CBO9780511586477
- Zoback, M.L. 1992. First-and second-order patterns of stress in the lithosphere: The World Stress Map Project. *Journal of Geophysical Research: Solid Earth*, 97(B8), 11703-11728.

MASW and SPT studies for subsurface soil characterization in Udaipur city area, Tripura state of NE India

AVIK PAUL 1,*, DEEPANKAR CHOUDHURY2, SIMA GHOSH1, SANTANU BARUAH3, G.K. BORUAH4, J.R. KAYAL 1,5

¹Department of Civil Engineering, National Institute of Technology Agartala, India ²Department of Civil Engineering, Indian Institute of Technology, Bombay, India ³Geoscience & Technology Division, CSIR-North East Institute of Science & Technology, Jorhat, Assam, India ⁴Department of Physics, Jorhat Institute of Science & Technology, Jorhat, Assam, India ⁵Formerly Geological Survey of India, Kolkata, India *Email (Corresponding author): aviknit7@gmail.com

Abstract: Tripura state in northeast NE India falls in the high-risk zone V in the seismic zoning map of India. In this study, we select the city Udaipur, Tripura, for seismic hazard analysis. Characterization of soil is much essential for seismic hazard risk studies in any developing urban city like Udaipur. We conducted Multichannel Analysis of Surface Waves (MASW) experiments at 15 selected locations in the city area to estimate shear wave velocity (V_s) of the subsurface soil / weathered layer. The dispersion data of the recorded Rayleigh waves (R-wave) were inverted using a Genetic Algorithm (GA) to obtain shear wave velocity profiles of the investigated sites. In addition, Standard Penetration Test (SPT-N) using, bore logs at these sites, and its proximity, were obtained from the government drilling agencies. These data are used to develop correlation equations by nonlinear regression. The results are then compared with the established correlations for soil characteristics. The V_{s30} ranges from 130-400 m/s in most of the sites except at Bhubeneswari Temple (site no 2) and Kaluadhepa SB School (site no 6), where V_{s30} reaches up to 445 m/s and 425 m/s respectively. A V_{s30} map for the city area is prepared and average dynamic characterization is examined, which reveals susceptibility of site-effects and liquefactions in some parts of the study area. These results are much useful for seismic hazard risk analysis and for seismic design and engineering considerations for urban development in the study area.

Keywords: Site characterization, V_{s30}, MASW, SPT bore log, earthquakes, seismic hazard risk

INTRODUCTION

Dynamic site characterization of subsurface soil profiles is essential for evaluating site response for earthquakes. The characteristics of soil profiles significantly impact the transmitted seismic waves, and consequently, the structures that stand on the soil surface. Site characterization involves studying subsurface soil profiles to understand their dynamic behaviour. Engineers and seismologists estimate how the soil would respond to future triggered earthquakes by evaluating parameters like shear wave velocity, damping characteristics and soil layering. Shear wave velocity is a most significant factor for evaluating dynamic site response. The average shear wave velocity for the top 30 m of soil is referred to as V_{s30}, which is used in seismic site categorization by National Earthquake Hazards Reduction Program (NEHRP). According to the NEHRP guidelines, local site conditions are expressed through average V_{s30} and average Standard Penetration Test-N (SPT-N) values. Based on these parameters, sites are classified.

Shear wave velocity is vital in various aspects of earthquake engineering, including dynamic stability analysis, seismic hazard assessment and ground shaking estimation. One of the critical applications of $V_{\mbox{\tiny s30}}$ is computing shear modulus $(G_{\mbox{\tiny max}})$ in low-strain condition. The $G_{\mbox{\tiny max}}$ represents stiffness of the soil at minor strains. It is a critical input parameter for analysing the dynamic stability of sub structures and super structures. Different soil types and conditions exhibit varying ground motion amplification and attenuation levels. By incorporating the $V_{\mbox{\tiny s30}}$ profiles into hazard computation engineers can estimate PGA at the surface at a particular location and evaluate its potential impact on

structures. Velocity of shear wave (V_s) of soil samples may be measured using different laboratory test methods, like (i) Ultrasonic Pulse test, where an ultrasonic pulses are sent through a soil sample to measure shear wave velocity, (ii) Resonant Column test, where a soil sample is placed in a cylindrical column and subjected to vibrations on increasing frequency, and (iii) Piezoelectric Bending Element test, where piezoelectric sensors are attached to a soil sample to generate and receive shear waves. It is essential to note that the soil samples represent a small volume, and it may not fully capture the site-specific soil behaviour. In-situ measurements overcome these limitations of laboratory tests. In-situ tests are conducted directly in the ground at the site of interest, providing a more precise representation of the soil properties compared to laboratory tests. These are particularly useful for obtaining V_s measurements that reflect actual conditions of the soil in its natural state.

In-situ MASW (Multichannel Analysis of Surface Waves) and SPT (Standard Penetration Test (SPT) are often used for seismic hazard microzonation. These in-situ measurements provide valuable insights into the subsurface V_s distribution, which is crucial for seismic site characterization, foundation design, liquefaction assessment, and other geotechnical and seismic engineering applications. Many researchers used SASW (Spectral Analysis of Surface Waves) technique to generate shear wave velocity profiles (e.g. Nazarian *et al.* 1983, Ganji *et al.* 1997) but it requires experience and judgement for precise V_{s30} estimate (e.g. Wulff 2016). The MASW method, however, has gained popularity in recent years, that provides more precise and reliable shear wave velocity results (e.g. Park & Elrick 1998, Xia *et al.* 1999,

Park et al. 1999, 2002, Zhang et al. 2004 and Xu et al. 2006).

In India, Boominathan computed $V_{\mbox{\tiny s30}}$ for Chennai city area with SPT-N using the relations provided by the Japan Road Association (1980) (Boominathan et al. 2007). MASW experiments was conducted in Bangalore city for developing relationships between $V_{\mbox{\tiny s30}}$ and $N_{\mbox{\tiny 60}}$ (Sitharam & Anbazhagan 2007). In 2008, Hanumantharao & Ramana established relations between SPT-N and V_s for different soils, like sandy and silty sand /sandy silt in Delhi (Hanumantharao & Ramana 2008). For Agartala city a relationship was developed between V_s observed SPT and corrected SPT values for the characterization of the sites (Sil & Sitharam 2013). A nonlinear regression power model was applied to develop a relation between V_s and SPT-N using different bore hole data around Kolkata city (Chatterjee & Choudhury 2013). Microtremor survey was conducted in Amravati city, Andhra Pradesh to develop the relationship between V_s and N (Kumar et al. 2022). Till date no such geophysical investigation has been carried out for the Udaipur city area in Tripura, northeast India. So, an investigation has been carried out to establish a relationship between SPT-N and V_s for this city area and generate V_{s30} map for the study area. The MASW experiments are carried out at 15 selected sites in the city area. The SPT-N data are obtained for the boreholes drilled in to these sites from the Public Works Department (PWD), Government of Tripura. These results are used to develop relationships between Vs and N_{60} , and to prepare a V_{s30} map for the city area. These results are highlighted and discussed in this paper.

GEOLOGY AND SEISMIC ACTIVITY

Udaipur, then (14th to 18th century) capital city of Tripura state, with its rich cultural and historical heritage of temples and landmarks, is situated in the Valley of Gomati River, the largest river in Tripura Fig. (1b). Hills and mountains surround the city and are part of the Tripura Sundari Hill range. The

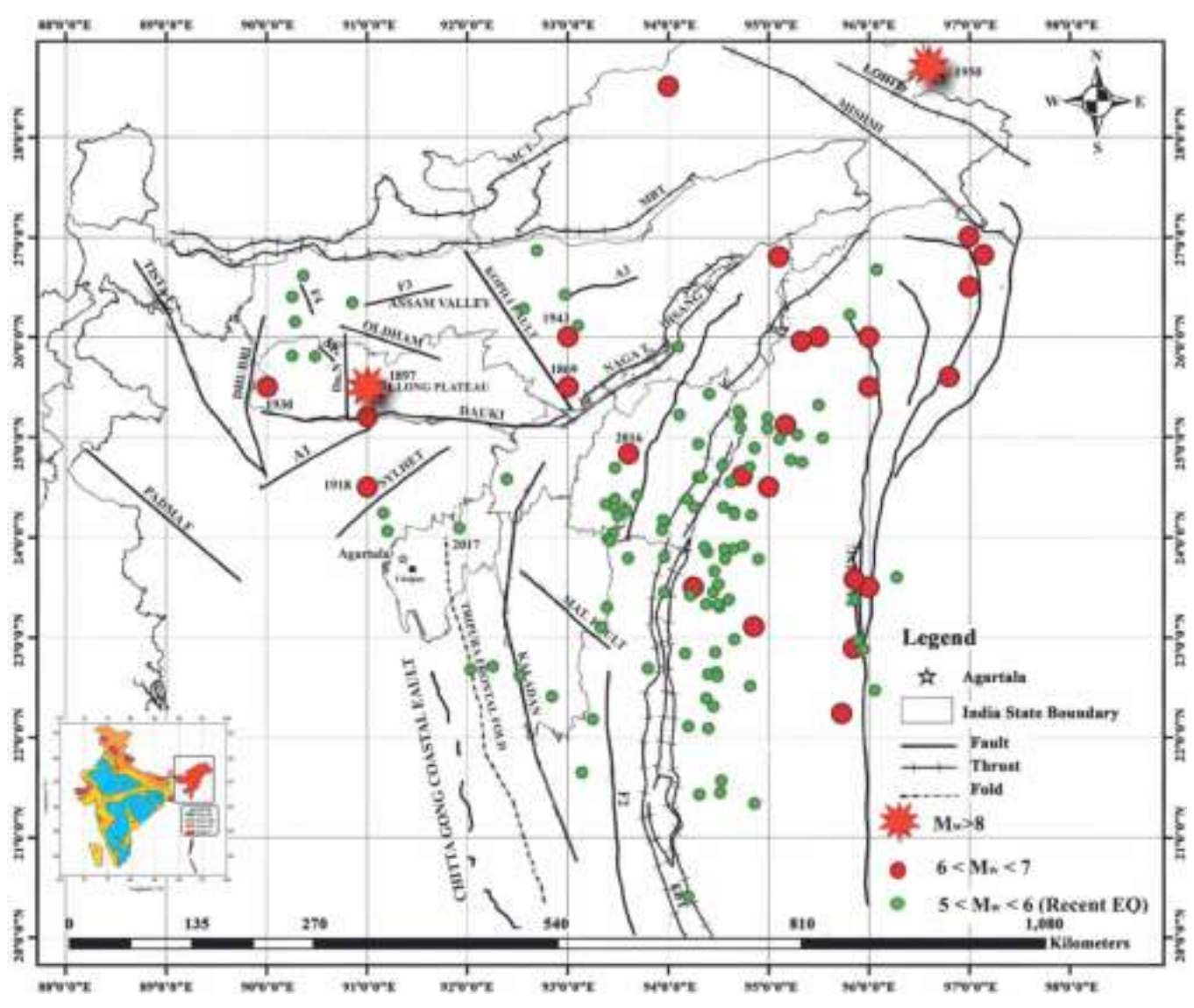


Fig. 1a. Seismotectonic map of NE India showing major tectonic features and large earthquakes (Inset: Seismic zoning map of India).

region around Udaipur primarily comprises rocks of the Surma Group and Tipam Group, which are part of the Bengal Basin sedimentary sequence. These formations consist of sandstone, siltstone, shale and clay deposits, primarily formed during the Cretaceous and Paleogene. The geological and geomorphological features, by the erosive action of the rivers and rains, shaped the region into valleys, floodplains and terraces. The southern part of Tripura, including Udaipur, is characterized by extensive alluvial plains created by the buildup of sediments carried by rivers over thousands of years. These fertile plains support agriculture and are a significant factor in the region's economy. The city of Udaipur is located at an approximate elevation of 18 m above mean sea level. Ground water table is near to the surface (at ~0.5 m -1 m) in the central part of Udaipur city, but it goes deeper (~8 m) farther from the central part.

Seismically Tripura lies in the high-risk zone-V in the seismic zoning map of India, and it experienced severe shaking, damages and liquefactions by several large and great earthquakes in NE India (e.g. Nandy 2001, Kayal 2008). The NE India region is buttressed between the Himalayan collision zone to the north and the Indo-Burma subduction zone to the

east. The Tripura state is affected by several large $M_w \ge 7.0$ and two great earthquakes $(M_w \ge 8.1)$ in the recent past. Chronologically, these are: the 1869 Cachar earthquake (M., 7.4) at the Kopili fault in Assam, the 1897 Shillong great earthquake (M_s 8.6, revised M_w 8.1) in Meghalaya, the 1918 Srimangal (M_s 7.6, revised M_w 7.1) earthquake in Bangladesh (Bengal Basin) and the 1930 Dhubri (M_s 7.1, revised M_w 7.0) earthquake in Assam, 1943 Earthquake around Kapili fault (Mw 7.2) and most recently the 2016 Manipur earthquake (M_w 6.7) on the Kopili fault (Fig. 1a). The 1897 great earthquake (M_w 8.1) with maximum intensity (Modified Mercalli Intensity scale) X-XI and ground acceleration 1g in Shillong produced an east-west trending fissure ~152 m long and 45 m wide in Agartala, Tripura, and ground acceleration in Agartala was equivalent to 0.13g. The 1918 Srimangal earthquake on the Sylhet fault in the Bengal Basin, with maximum intensity X (RF Scale), caused ground subsidence at many places with development of long fissures and sprouting of sand and water causing damage to several masonry structures in Tripura. The 1930 Dhubri earthquake struck in Assam and the shock was severely felt all over the area with movement of objects and damage to buildings in Tripura. The most recent January, 2017

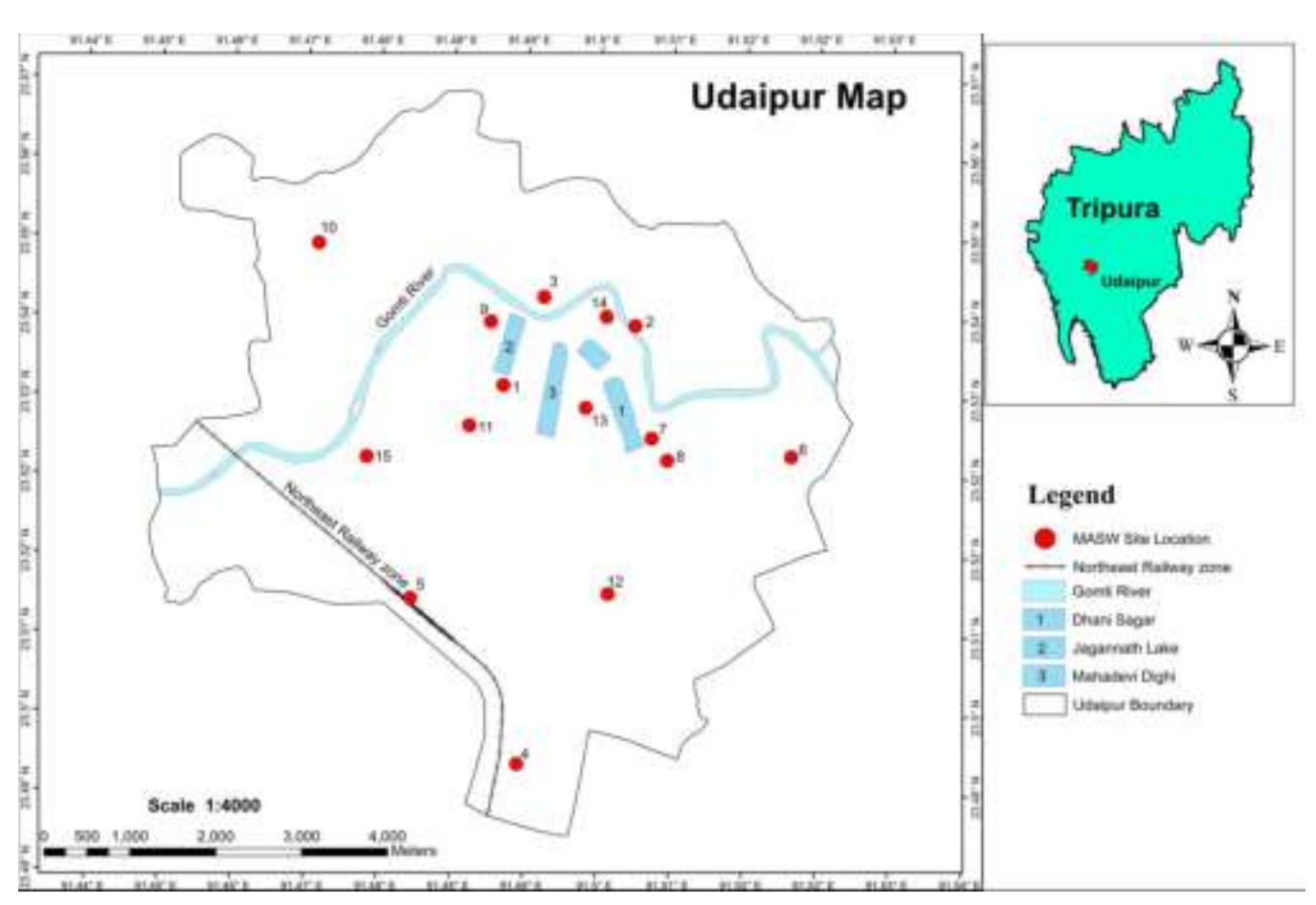


Fig. 1b. Udaipur city area showing selected site locations for MASW survey. Sites: 1) KBI School Ground 2) Bhubeneswari Temple 3) Science City 4) Chandrapur Sports ground 5) Udaipur Railway Station 6) Kaluadhepa SB School 7) Tripura Sundari School 8) East R.K. Pur H.S School 9) Bhagini Nivedita H.S. School 10) Netaji Subhash Mahavidyalaya 11) Ramesh H.S. school 12) Tripura Sundari Temple 13) Veterinary Hospital 14) Hariananda School 15) Khilpara H.S. school.

 $\rm M_{\scriptscriptstyle w}$ 5.7 shallow (depth ~30 km) earthquake in Tripura, about 75 km northeast of the Agartala city, caused damages to the mud-houses, fissures on the ground and liquefaction in the cultivated field (Das *et al.* 2019). Thus, the Tripura area is much close to the past large earthquake source zones like, the Sylhet fault in Bengal Basin (Bangladesh) and the Shillong plateau pop-up tectonics source zone in Meghalaya, ~300 km long Kopili fault zone in Assam and close to the Indo-Burma subduction zone to the east ((Kayal 2008). Also figure 1a shows the recent seismicity of last 10 years around the state Tripura.

FIELD INVESTIGATIONS

Geophysical Investigation (MASW)

MASW is a non-destructive, non-invasive testing method that provides information on the mechanical characteristics of insitu soils and rock formations. It involves analysis the Rayleigh waves (R-wave) on a multichannel system to get the dispersion characteristics. Regardless of its cost and time efficiency, it is a non-invasive procedure fully implemented on the ground surface and covers the subsurface depth in such a manner so that it can continuously provide enhanced coverage similar to Ground Penetrating Radar (GPR) and Resistivity Survey. MASW mainly consists of a collection of multichannel seismic data either in active or passive mode followed by construction of dispersion curve indicating the variation of phase velocities of the different frequency component and production of 1-D and 2-D velocity models.

Methodology: The MASW system used in the current investigation is equipped with 24 geophones of 4.5 Hz capacity. The multichannel technique enables imaging dispersion characteristics of surface waves. This is accomplished using a wave field-transformation approach, such as the Fast Fourier Transform (FFT), which turns the multichannel record into a picture in which specific dispersion patterns may be identified. In case of multimodal dispersion, where more than one phase velocities exist for a single frequency, fundamental modes are the slowest and the ones having faster velocity are called as of higher modes of a different level.

To generate surface waves (R- waves), a 10 kg sledgehammer is used. When the sledgehammer strikes a 30 cm x 30 cm steel plate, it generates surface waves and are recorded by the geophones. To avoid any effects from the far and near field, this test is repeated within different ranges: 3.0m, 6.0m, 12.0m and 24.0m from the 24th geophone. Ten shots are taken at each location to create a mean shot collect file. This averaging helps to minimize uncertainty or errors associated with individual shots. The recording duration of the active survey is kept at 4 s, which may be shortened, if required. The same 48-channel linear array is used for the passive data recording, and the ambient noise for each site. The data acquisition process is conducted using a Vibrascope software which records the multichannel stacked data in Vscope format. These are then exported into SEG2 or SEGY format for dispersion analysis and inversion. MASW field set up and recorded data is shown figures 2a and 2b respectively.



Fig. 2a. MASW field set up.

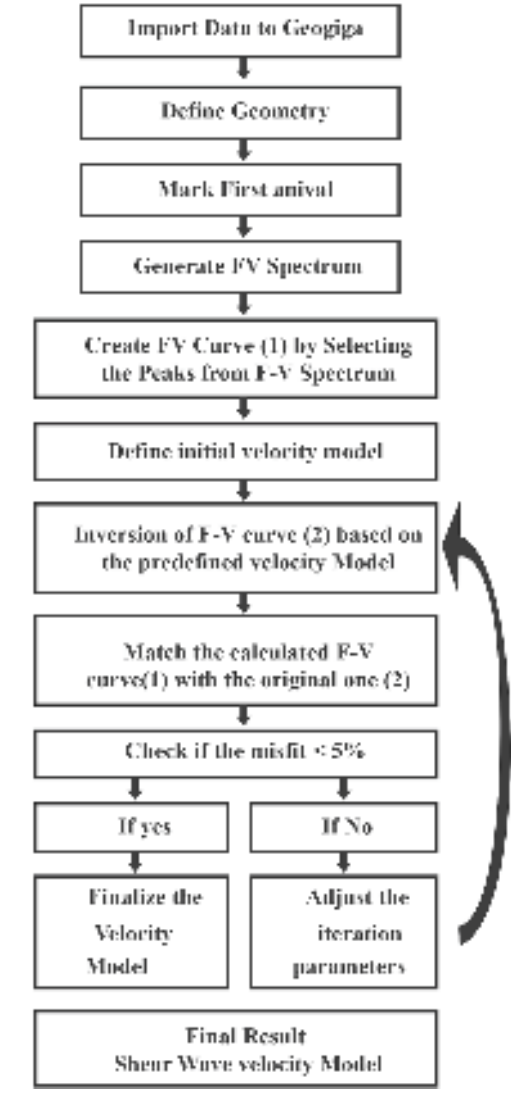
Facergy/Source	Sledgehammer (weight 10 leg)	o o	188	Ti 360	me (ms) 540
Geophone	24 (4.5 Hz Geophone)	46			
No. of stack	24	10			
Geophone distance	2 metres				
Length of spread	46 metres	E 30			
Shot position	46 metres	200	192	k/TAF	
Recording time	4 sec (Enlarged particle of 960 ms is shown in the figure)	Distance (m)			
Sampling	1000 samples per	10			
Filter	Butterworth Low Pass	U			
Delay	None	1 —			, Je 11

Fig. 2b. Recorded MASW data with recording parameter.

Data Processing: The f-k spectrum generated from the MASW data are used to pick up the dispersion curve by selecting different modes of vibration according to their energy accumulation. Analyzing the dispersion patterns, dispersion curves can be obtained that show the relationship between phase velocity and frequency. This curve provides insights into the V_s variations with depth. We analyzed the dispersion curves in the various frequency ranges for different sites. The lowest frequency captures the lower end of the dispersion curve, while the highest frequency provides information about the higher end of the dispersion curve. Derived f-v curves are then inverted using Genetic Algorithm (GA) to develop the Shear Wave velocity profile. Variations of V_s with depth can be derived from the phase velocities and dispersion properties. Such profiling of V_s is crucial for assessing the subsurface conditions, evaluating soil properties, and assessing site response during seismic events. A detail data processing flow chart is presented in figure 3. A typical dispersion (f-v) curve, lithologs, S-wave velocity variation and a 2-D velocity model are illustrated in figures 4a, 4b and 4c respectively.

Geotechnical Investigation

We obtained legitimate and credible geotechnical SPT data from the 15 borehole locations at the investigated sites or near to its proximity (PWD Tripura, 2023, pers. Comm.). The SPT involves driving a split-spoon sampler into the soil using a standard driving weight dropped from a specified height. The sampler is pushed into the ground, and the number of blows needed to move the sample from 15 cm to 45 cm is recorded. This blow counts, known as the N-values, show soil resilience. The SPT-N data are then corrected using several corrections like overburden, size, diameter etc to get N_{60} . Figures 5 and 6 illustrates an example of borehole details along with lateral lithological variation based on borehole for Ramesh H.S. school (site no 11) and khilpara H.S. school (site no 15).



720

900

Fig. 3. MASW Data processing flow chart.

Dispersion Curves

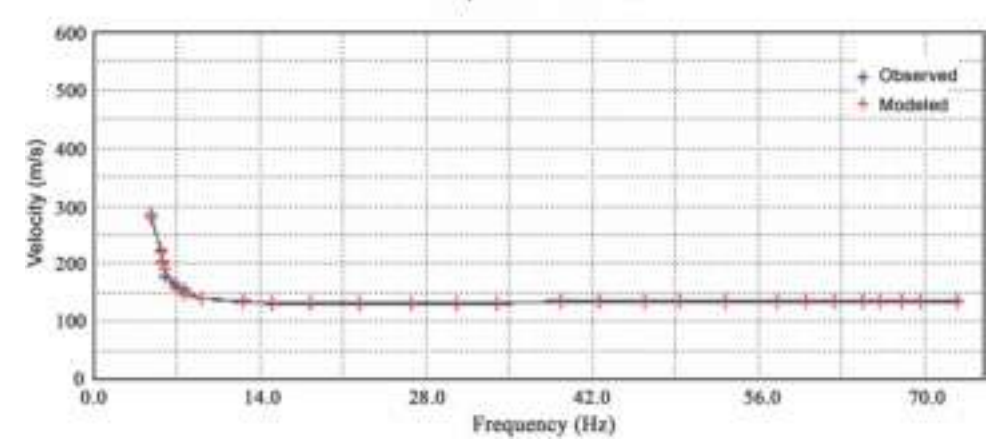


Fig. 4a. dispersion (f-v) curve for site no.11, Ramesh School ground.

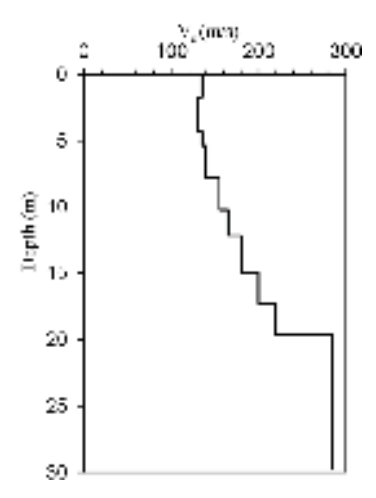


Fig. 4b. S-wave velocity variation with depth for site no.11, Ramesh School ground.

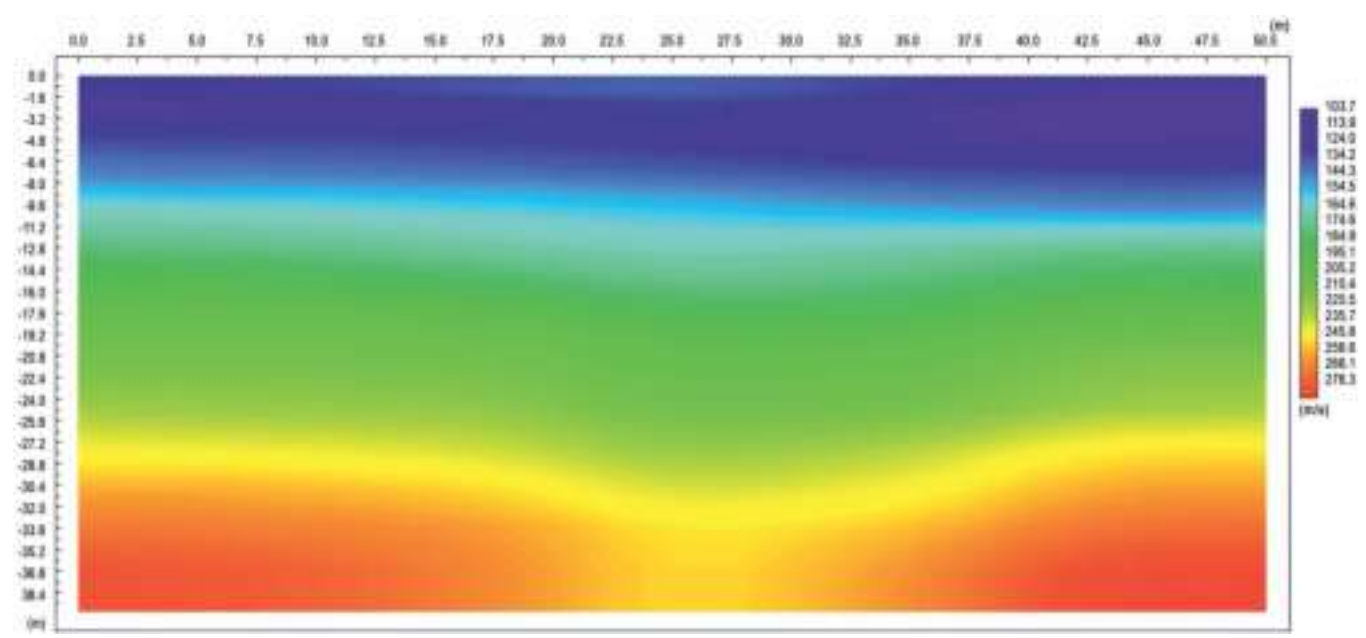


Fig. 4c. 2-D velocity model with depth for site no.11, Ramesh School ground.

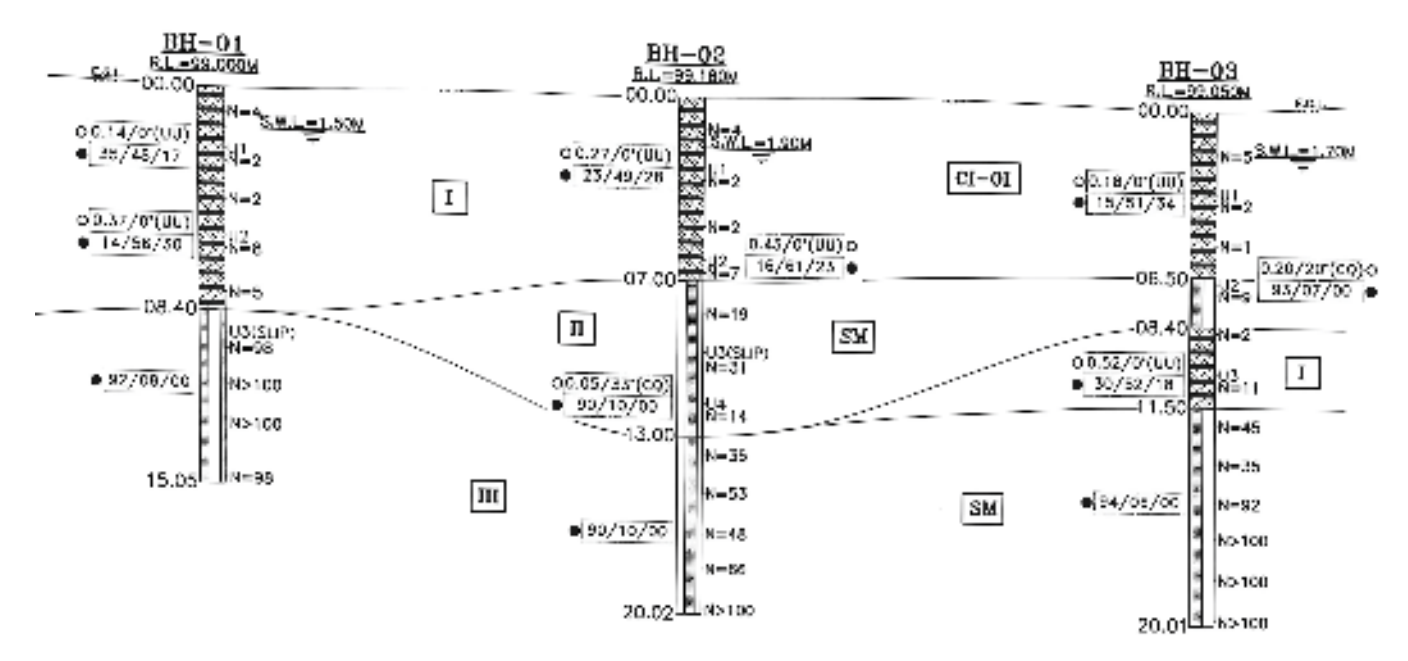


Fig. 5. Shows borehole details along with lateral lithological variation based on borehole for Ramesh H.S. school (site no 11).

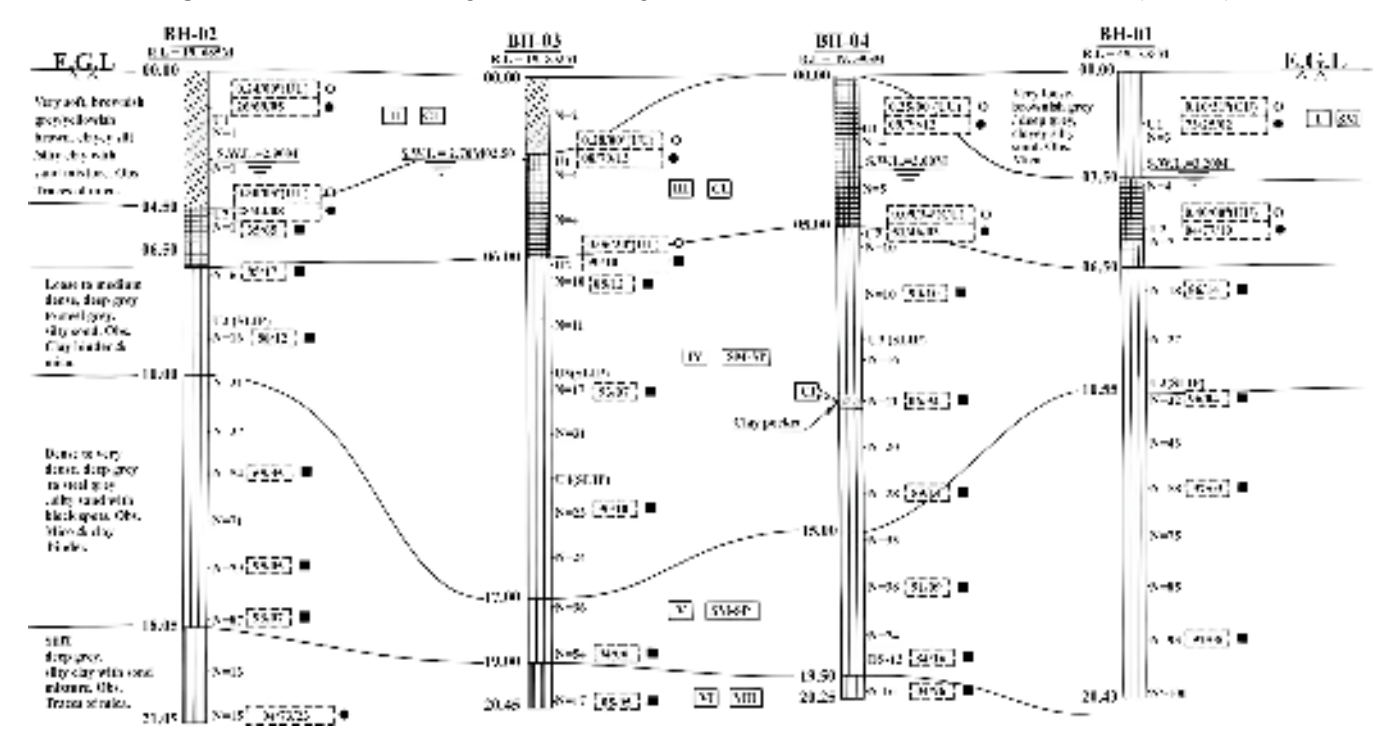


Fig. 6. Shows borehole details along with lateral lithological variation based on borehole for Khilpara H.S. school (site no 15).

ESULTS AND DISCUSSION

A total of 15 locations shown in figure 1b are selected in the study area to determine the shear wave velocity of the soil formations using the MASW survey. We obtained SPT-N data at these specific locations; some are in proximity to the MASW sites. These data are then analysed to understand relationship between the Shear Wave velocity and SPT N value (both Corrected and uncorrected). The correlation

between V_s and N_{60} is illustrated in figure 7. The relationship developed by multiple regression for different types of soils in the study area is presented in table 1.

The results obtained in the present study are compared with previous results (Fig. 8). In this comparison, it is observed that the equations given previous researchers (Imai & Yoshimura (1970), Ohba & Toriumi (1970), Hanumantharao & Ramana (2008), Ohsaki and Iwasaki

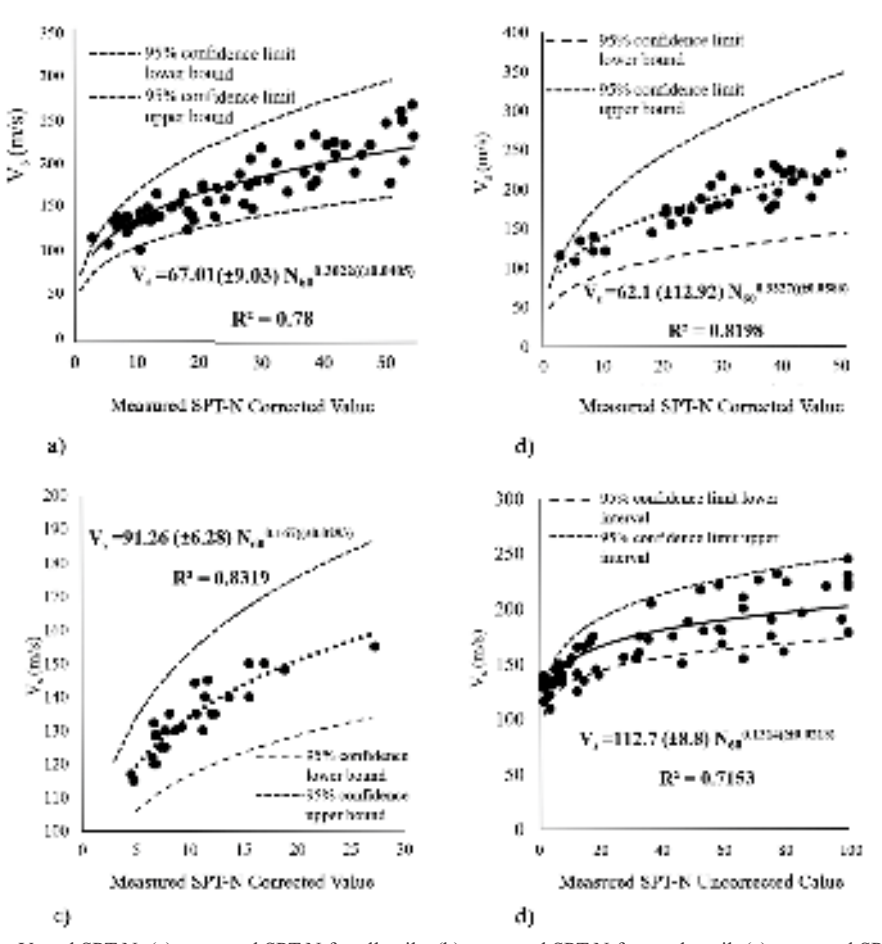


Fig. 7. Correlations between V_s and SPT-N, (a) corrected SPT-N for all soils, (b) corrected SPT-N for sandy soil, (c) corrected SPT-N for clay soils, and (d) uncorrected SPT-N values for all type of soil based on 95 % confidence limit.

Table 1. Correlation between V_{s30} and N_{60} for soil formations, Udaipur city area.

Type of soil	Equation (byax=)	Coefficients (with 95% confidence bounds)	\mathbb{R}^2	RMSE
For all type of Soil	V_s =67.01(±9.03) $N_{60}^{0.3022((\pm 0.0405)}$	a = 67.01(57.98, 76.05) b = 0.3022(0.2617, 0.3426)	0.78	18.5
For sandy type of Soil	V_s =62.1 (±12.92) $N_{60}^{0.3327((\pm0.0586))}$	a =62.1(49.18, 75.02) b = 0.3327 (0.2741, 0.3913)	0.8198	16.94
For clay type of Soil	$V_s = 91.26 \ (\pm 6.28) \ N_{60}^{0.167((\pm 0.0293))}$	a = 91.26 (84.98, 97.53) b = 0.167 (0.1377, 0.1963)	0.8319	4.299
For all type of Soil	V_s =112.7 (±8.8) $N^{0.1314((\pm 0.0213))}$	a =112.7 (103.9, 121.6) b =0.1314 (0.1101, 0.1527)	0.7153	17.3

(1973), Kiku et al. (2001), Imai (1977), Imai & Tonuchi (1982), Seed & Idriss (1981), Sil & Sitharam (2013), Kiku et al. (2001), Hanumantharao & Ramana (2008), Sisman 1995) tend to overestimate the shear wave velocity values compared to Udaipur city area. It may, however, be noted that our correlations show fair agreement with correlation provided by Sil & Sitharam (2013) for the Agartala city area in Tripura, where geologic conditions are much the same. Table 2 presents a comparative analysis of shear wave velocities (V_s) derived from MASW field tests with those estimated using empirical correlations based on SPT N-values. The results show a strong agreement between the measured and calculated V_s values across different soil types and depths at multiple

locations. This validates the reliability of using SPT-based correlations in areas where MASW data may not be available, and supports their integration in site characterization for seismic hazard assessments.

The velocity models are used to project the nature of materials as per the NEHRP classifications, identified by inverting the f-v curves. The lithologs are constructed, which are found to be in compliance with local geology and geomorphology within 800 m of radial distance. In the lithologs, it is observed that in most of the sites the upper top layers consist of softer materials which are highly heterogeneous, and is dominated by the sandy layer of higher strength. While analyzing the dispersion spectra of the event

shots, it is seen that resolution of the spectra is much distinct in the frequency range beyond 15 Hz, which signifies of softer materials with less compact interparticle bonding. The MASW conducted in Udaipur city reveal distinct variations in shear wave velocity across different locations. Hariananda School ground (site no 14) exhibits significant S-wave velocity changes after 10 Hz, reaching up to 450 m/s, with softer layers observed in the top 9 m and stiffer layers below 17 m. At Kaluadhepa School (site no 6), similar characteristics are noted with sandy soil up to 20 m and higher velocities up to 425 m/s at 30 m depth. KBI School Ground (site no 1), near Jagannath Dighi, features very soft soil with low S-wave velocity up to 18 m, transitioning to stiffer sandy layers below. Khilpara School ground (site no 15) shows low S-wave velocity due to saturated loose soil, with soft layers up to 6 m and V_{s30} reaches up to 257 m/s, while Ramesh School Ground (site no 11) also shows the same subsoil characteristics like KBI school ground. Netaji Subhash Mahavidyalaya (site no 10), an excavated football ground, shows higher shear wave velocity in shallow depths due to compacted soil, with significant increases up to 412 m/s at 30 m depth. Science City (site no 3), situated by the Gomati River, has soft soil in shallow layers, with significant shear wave velocity changes after 8 Hz and harder strata below 15 m. Bhagini Nivedita School (site no 9) in central Udaipur exhibits increasing shear wave velocities above 12 Hz, with Vs reaches upto 365 m/s at 30 m. Udaipur Railway Station (site no 5), located in a lowland area, exhibits wide variation in shear wave velocity, with softer layers up to 15 m and stiffer layers below. Tripura Sundari Temple (site no 12) and Tripura Sundari School (site no 7) show similar characteristics with softer elements in shallow depths and stiffer layers below 16 m and 10 m, respectively. Udaipur Veterinary Hospital (site no 13) also shows soft soil conditions in the top layers, with increasing velocities at greater depths. The low $\dot{V}_{\scriptscriptstyle s}$ values attribute to loose clay or fully saturated sandy layers. The velocity models generated for each site have different depth information depending upon the dispersion curves. However, as per the requirement of geotechnical studies, the lithologs are constructed down to a depth of 30 m. V_{s30} is the parameter used for engineering design codes and for describing amplification of seismic waves near the ground surface. Based on the MASW test and velocity models presented, the Shear wave velocity at 30 mt depth (V_{s30}) is estimated (Table 3), and a contour map is presented in figure 9. other geophysical methods, such as Electrical Resistivity Tomography (ERT) and Seismic Refraction, verify MASW and SPT results by identifying layer boundaries, material stiffness, and saturation levels. Techniques like GPR, HVSR, and Downhole Seismic Tests provide detailed velocity profiles, site resonance frequencies, and shallow subsurface features for crosschecking.

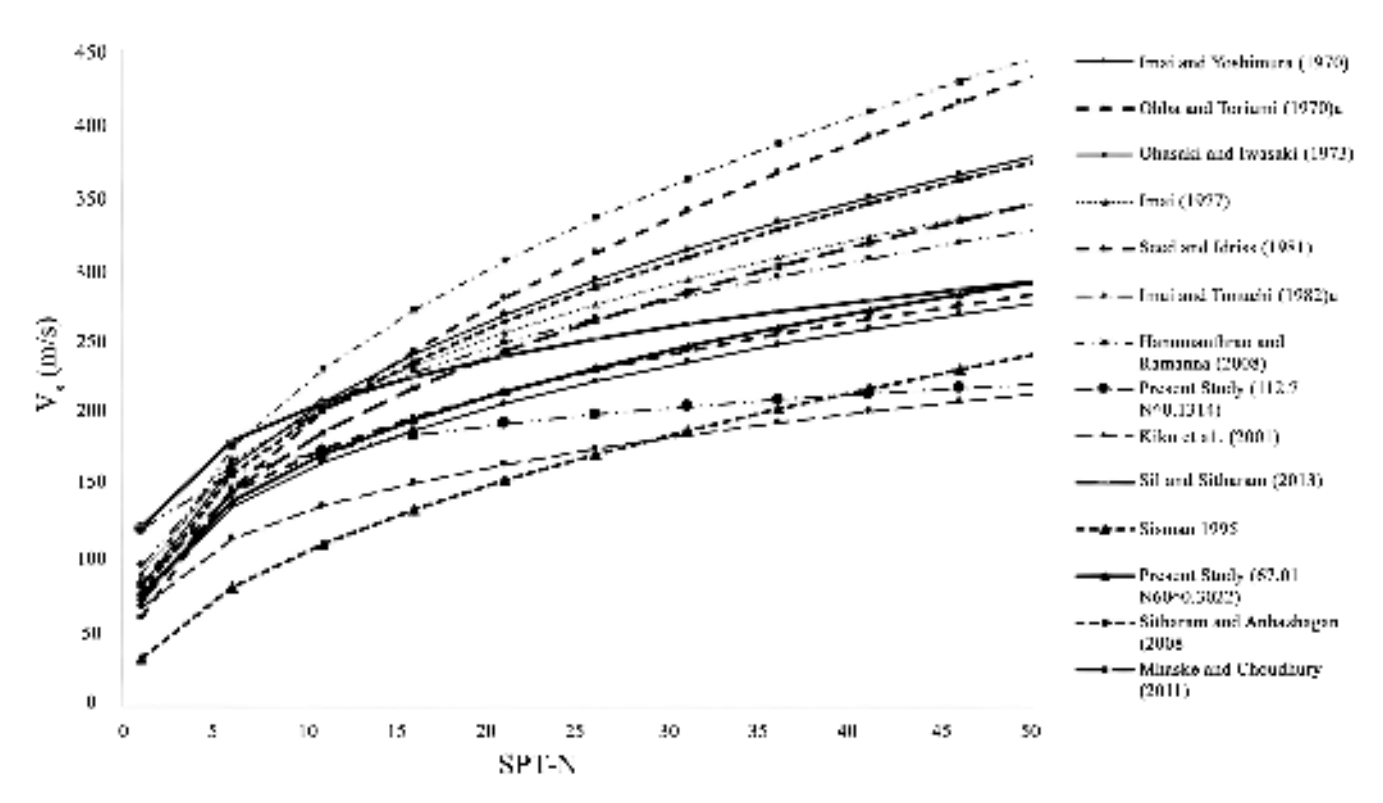


Fig. 8. Comparisons of V_s and SPT-N correlations for all soils in Udaipur city area with known global correlations.

Table 2. Comparative analysis of S-wave velocities derived from MASW data with velocities obtained from SPT $N-V_s$ Corelation.

Site No	Site	Type of Soil	Depth	Vs (in m/s) from MASW Field Test	Vs (in m/s) calculated from SPT N and Vs Corelation		
15	Khilpara H.S. School	Sand	2.175	122	94.90		
15	Khilpara H.S. School	Clay	3.725	131	114.08		
15	Khilpara H.S. School	Clay	5.675	140	122.93		
15	Khilpara H.S. School	Sand	7.225	145	155.52		
15	Khilpara H.S. School	Sand	8.825	156	174.00		
15	Khilpara H.S. School	Sand	10.425	160	187.30		
15	Khilpara H.S. School	Sand	12.225	175	202.58		
15	Khilpara H.S. School	Sand	13.725	182	224.27		
15	Khilpara H.S. School	Sand	15.225	190	240.97		
15	Khilpara H.S. School	Sand	16.825	196	247.86		
15	Khilpara H.S. School	Sand	18.515	220	249.68		
15	Khilpara H.S. School	Sand	20.165	224	252.73		
11	Ramesh School	Clay	0.5	135	125.76		
11	Ramesh School	Clay	1.225	135	135.45		
11	Ramesh School	Clay	3.175	130	128.47		
11	Ramesh School	Clay	4.925	130	128.33		
11	Ramesh School	Clay	6.675	135	138.92		
11	Ramesh School	Clay	8.225	140	153.60		
11	Ramesh School	Clay	10.275	155	158.50		
11	Ramesh School	Clay	12.175	165	140.44		
11	Ramesh School	Sand	13.725	172	176.15		
11	Ramesh School	Sand	15.225	180	191.13		
11	Ramesh School	Sand	16.825	188	184.91		
11	Ramesh School	Sand	18.225	200	197.55		
11	Ramesh School	Sand	19.51	220	217.95		
9	Bhagini Nivedita H.S. School	Sand	2.275	135	114.17		
9	Bhagini Nivedita H.S. School	Sand	3.625	140	126.71		
9	Bhagini Nivedita H.S. School	clay	5.925	145	138.71		
9	Bhagini Nivedita H.S. School	clay	7.325	155	146.50		
9	Bhagini Nivedita H.S. School	clay	9.175	150	137.75		
9	Bhagini Nivedita H.S. School	Sand	10.925	175	188.14		
9	Bhagini Nivedita H.S. School	Sand	12.425	180	209.94		
9	Bhagini Nivedita H.S. School	Sand	13.825	210	215.24		
9	Bhagini Nivedita H.S. School	Sand	15.425	229.9	234.92		
9	Bhagini Nivedita H.S. School	Sand	16.87	247.6	232.36		
1	KBI School Ground	Clay	0.75	128.8	125.89		
1	KBI School Ground	Clay	1.725	128.8	125.89		
1	KBI School Ground	Clay	3.25	128.8	125.41		
1	KBI School Ground	Clay	4.725	144.2	149.10		
1	KBI School Ground	Clay	6.225	161.8	135.22		
1	KBI School Ground	Clay	10.725	180.9	130.20		
1	KBI School Ground	Clay	13.725	195	137.15		
1	KBI School Ground	Sand	15.225	226.7	205.12		
1	KBI School Ground	Sand	16.725	220	211.05		
1	KBI School Ground	Sand	18.225	220	214.89		

Table 3. Distribution of average V_{s3a} for different sites, in the Udaipur city area.

Site No	Place	Lat	Long	VS30 in (m/s)	NEHRP classification
1	KBI School Ground	23.53545	91.48861	300	D
2	Bhubeneswari Temple	23.54006	91.27069	445	C
3	Science City	23.54403	91.49593	307	D
4	Chandrapur Sports ground	23.49462	91.49073	395	C
5	Udaipur Railway Station	23.51038	91.48121	257	D
6	Kaluadhepa SB School	23.52661	91.52203	425	C
7	Tripura Sundari School	23.52889	91.50616	326	D
3	East R.K. Pur H.S School	23.5321	91.50484	325	D
)	Bhagini Nivedita H.S. School	23.54217	91.48871	365	C
10	Netaji Subhash Mahavidyalaya	23.54931	91.46792	412	C
11	Ramesh H.S. school	23.53602	91.48699	285	D
12	Tripura Sundari Temple	23.51122	91.49941	300	D
13	Veterinary Hospital	23.53181	91.49862	300	D
14	Hariananda School	23.5416	91.50096	370	C
15	Khilpara H.S. school	23.52721	91.47353	257	D

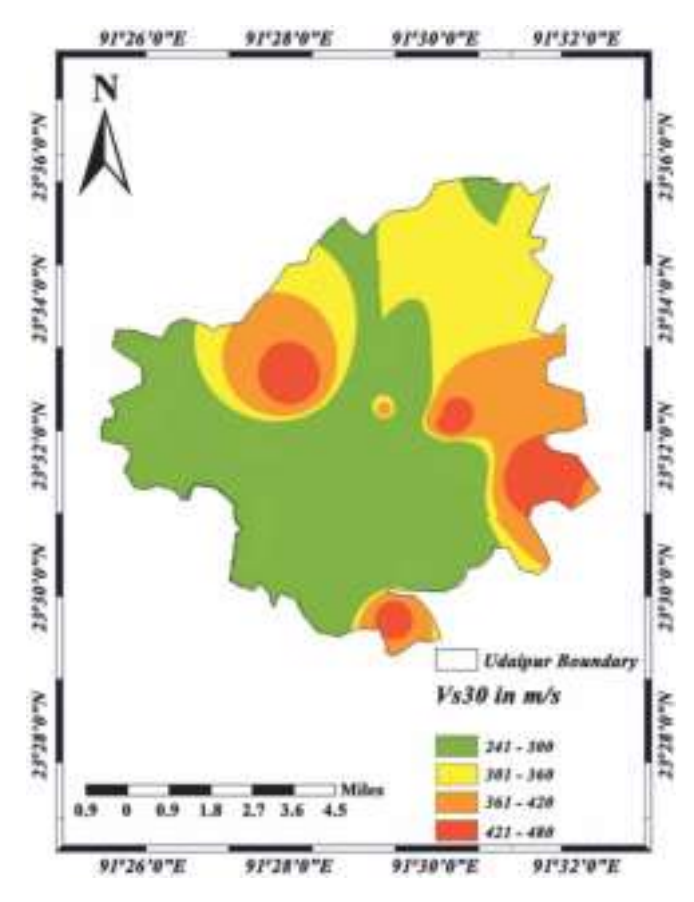


Fig. 9. Map showing distribution of average shear wave velocity (V_{S30}) in m/s for the Udaipur city area.

CONCLUSIONS

The Udaipur city in Tripura state, historically and culturally is an important and rapid developing city in NE India. This city is growing fast for its high potential in tourism. New infrastructure and development projects are flourishing; study of soil characteristics is the need of the hour as the city falls in high seismic risk zone. The estimated shear wave velocity (V_s) by MASW studies at 15 selected sites for different depth in the city area are correlated with the SPT (N₆₀) values. These correlations are useful to determine V_s for the whole city area. Further, shear wave velocity at 30 metre depth (V_{s30}) is the key parameter to assess seismic vulnerability, local site effect, seismic design etc for urban development. The central part of the city is classified as site class D. The sites nos. 2, 4, 6, 9, 10, 14 are classified as class C. The V_{s30} lies between 250-360 m/s, and up to 445 m/s for some of the places. Dispersion curves and reconstructed lithologs show clay soil or loose sandy layer with less V_s down to 10 m depth in the central part of the city, which makes it much vulnerable and susceptible for soil liquefaction. A geospatial map of V_{s30} is generated for the Udaipur city. This $V_{\mbox{\tiny s30}}$ contour map can be used to assess the seismic hazard risk, which will be helpful to the designers and site engineers to construct various infrastructure projects in the city.

Acknowledgement: It is a part of PhD research project of AP under guidance of SG and DC, SB and GB helped with the MASW

instruments and data acquisition, and JRK with discussion and presentation.

Funding Declaration: No funding was received for conducting the study and as well as for the preparation of this manuscript. The authors have no relevant financial or non-financial interests to disclose.

Data Availability Declaration: All data, models, and code generated or used during the study appear in the submitted article.

Competing Interest Declaration: The authors have no competing interests to declare that are relevant to the content of this article.

Declaration by the Authors: All authors have read, understood, and have complied as applicable with the statement on "Ethical responsibilities of Authors" as found in the Instructions for Authors

References

Boominathan, A., Dodagoudar, G.R., Suganthi, A., Uma Maheswari, R. 2007. Seismic hazard assessment considering local site effects for microzonation studies of Chennai city. *Proceedings of microzonation a workshop at Indian Institute of Science, Bangalore*, 94-104.

Chatterjee, K., Choudhury, D. 2013. Variations in shear wave velocity and soil site class in Kolkata city using regression and sensitivity analysis. Natural Hazards, 69, 2057-2082. Doi:10.1007/s11069-013-0795-7

Das, S., Ghosh, S., Kayal, J.R. 2019. Liquefaction potential of agartala city in Northeast India using a GIS platform. Bulletin of Engineering Geology and the Environment, 78, 2919-2931. Doi:10.1007/s10064-018-1287-5

Ganji, V., Gukunski, N., Maher, A. 1997. Detection of underground obstacles by SASW method numerical aspects. *Journal of Geotechnical and Geoenvironmental Engineering*, 123(3), 212-219 ASCE.

- Hanumantharao, C., Ramana, G.V. 2008. Dynamic soil properties for microzonation of Delhi, India. *Journal of Earth System Science*, 117(S2), 719-730.
- Imai, T. 1977. P- and S-wave velocities of the ground in Japan. Proceedings of the IX international conference on soil mechanics and foundation engineering, 2, 127-132.
- Imai, T., Tonouchi, K. 1982. Correlation of N-value with S-wave velocity and shear modulus. Proceedings, 2nd European Symposium on Penetration Testing, Amsterdam, 57-72.
- Imai, T., Yoshimura, Y. 1970. Elastic wave velocity and soil properties in soft soil (in Japanese). *TsuchitoKiso*, 18(1), 17-22.
- Japan Road Association 1980. Specification and interpretation of bridge design for highway—Part V: resilient design.
- Kayal, J.R. 2008. Microearthquake Seismology and Seismotectonics of South Asia. *Springer, Germany*, 503p.
- Kiku, H., Yoshida, N., Yasuda, S., Irisawa, T., Nakazawa, H., Shimizu, Y., Ansal, A., Erkan, A. 2001. In situ penetration tests and soil profiling in Adapazari, Turkey. In: Proceedings of the ICSMGE/TC4 satellite conference on lessons learned from recent strong earthquakes, 259-265.
- Kumar, A., Satyannarayana, R., Rajesh, B.G. 2022. Correlation between SPT-N and shear wave velocity (VS) and seismic site classification for Amaravati city, India. *Journal of Applied Geophysics*, 205, 104757.
- Nandy, D.R. 2001. Geodynamics of North Eastern India and the Adjoining Region. ACB Publications, Kolkata.
- Nazarian, S., Stokoe, II. K. H., Hudson, W. R. 1983. Use of spectral analysis of surface waves method for determination of moduli and thicknesses of pavement systems; *Transportation Research Record*, 930, 38-45.
- Ohba, S., Toriumi, I. 1970. Dynamic response characteristics of Osaka Plain. *Proceedings of the Annual Meeting*. A.I.J (in Japanese)
- Ohsaki, Y., Iwasaki, R., 1973. On dynamic shear moduli and Poisson's ratio of soil deposits; Soils Found, 13(4), 61-73.

- Park, C.B., Miller, R.D., Xia, J. 1999. Multichannel analysis of surface waves (MASW). Geophysics, 64 (3), 800-808.
- Park, C.B., Miller, R.D., Miura, H. 2002. Optimum field parameters of an MASW survey [Exp. Abs.]. *SEG-J*, Tokyo, May, 22-23.
- Park, S., Elrick, S. 1998. Predictions of shear-wave velocities in Southern California using surface geology. *Bulletin of the Seismological Society of America*, 88(3), 677-685.
- Seed, H.B., Idriss, I.M. 1981 Evaluation of liquefaction potential sand deposits based on observation of performance in previous earthquakes. Preprint 81-544, in situ testing to evaluate liquefaction susceptibility. ASCE National Convention, Missouri, 81-54,
- Sil, A., Sitharam, T.G. 2013. Dynamic Site Characterization and Correlation of Shear Wave Velocity with Standard Penetration Test 'N' Values for the City of Agartala, Tripura State, India. *Pure and Applied Geophysics*, 171, 1859-1876. doi:10.1007/s00024-013-0754-y
- Sisman, H. 1995. The relation between seismic wave velocities and SPT, pressure meter tests. *MSc Thesis*, Ankara University (In Turkish).
- Sitharam, T.G., Anbazhagan, P. 2007. Seismic hazard analysis for the Bangalore region. *Natural Hazards*, **40**, 261-278.
- Wulff, Friederike, 2016. Use of Surface Wave Techniques for the Identification of Shallow Rock. *Open Access Master's Theses*, Paper 890. https://digitalcommons.uri.edu/theses/890
- Xia, J., Miller, R.D., Park, C.B. 1999. Estimation of near surface shear-wave velocity by inversion of Rayleigh wave. *Geophysics* **64**(3), 691-700.
- Xu, Y., Xia, J., Miller, R.D. 2006. Quantitative estimation of minimum offset for multichannel surface-wave survey with actively exciting source. *Journal of Applied Geophysics*, **59**(2), 117-125.
- Zhang, S.X., Chan, L.S., Xia, J. 2004. The selection of field acquisition parameters for dispersion images from multichannel surface wave data. *Pure and Applied Geophysics*, **161**, 185-201.

Lower Cretaceous (lower Aptian) radiolarian cherts from the Shyok Suture Zone, Ladakh, Trans-Himalaya, India

RAKESH CHANDRA^{1,*}, IHSAN ULLAH LONE², MEENAL MISHRA², JONATHAN C. AITCHISON³

¹Department of Earth Sciences, University of Kashmir, Hazratbal-190006, J&K, India ²School of Sciences, Indira Gandhi National Open University, New Delhi-110068, India ³School of the Environment, University of Queensland, Brisbane 4072, Australia *Email (Corresponding author): rakeshchandra69@gmail.com

Abstract: An ophiolitic mélange exposed along the Shyok River in the NW part of the Shyok Suture Zone was studied to obtain micropaleontological and geochemical data from blocks of radiolarian chert and to enable a better understanding of age and nature of this mélange. The mélange includes blocks of ultramafic rocks, gabbro, basalts, pillow lavas and radiolarian cherts within both serpentinite and phyllite matrix. Micropaleontological investigation of cherts yielded Lower Cretaceous (lower Aptian) radiolarians. High SiO₂/(SiO₂+Al₂O₃+Fe₂O₃) ratios and the Fe-Al-Mn ternary plot indicate that these biogenic cherts were deposited far from any hydrothermal source. Major and trace element abundances and their relationships suggest an open ocean environment for the studied radiolarites.

Keywords: Radiolaria, Lower Cretaceous, ophiolitic mélange, Shyok suture zone.

INTRODUCTION

The Shyok Suture Zone (SSZ) is a major tectonic zone exposed to the west of the Karakoram Fault (KF) and the E-W trending Indus Suture Zone (ISZ) to the south (Fig. 1a, b). It lies north of the Ladakh Batholith and was first characterized by Gansser (1980). Subsequently numerous other works concerned with the study of this region have been published (e.g., Tahirkheli et al. 1979; Brookfield & Reynolds 1981, 1990; Chandra et al. 1999, 2023; Rai 1982; Thakur & Misra 1984; Srimal 1986; Hanson 1989; Borneman et al. 2015; Pundir et al. 2020; Saktura et al. 2021, 2022, 2023; Lakhan et al. 2022; Gautam et al. 2023; Martin et al. 2023). The SSZ in the NW Himalayan region contains relics of the Tethyan ophiolites and ophiolitic mélange masses that stretch for more than 500 km from west to east (Srimal 1986; Saktura et al. 2021; Lone et al. 2023a). This suture zone extends through the Shyok-Nubra region in Ladakh and into the northern areas of Pakistan (Fig. 1a) where it is known as Northern Suture Zone (NSZ) (Coward et al. 1986; Robertson & Collins 2002). To the east, across the Karakoram Fault it correlates with the Mesotethyan Bangong-Nujiang suture zone in Tibet.

The SSZ comprises two main ophiolitic belts i.e., the Shyok Ophiolites and Saltoro Ophiolites and associated ophiolitic mélanges exposed in the northwestern part of the Nubra-Shyok Valley (Rai 1983: Srimal 1986, Lone et al. 2023a). The Shyok Ophiolites exposed in the NW region are important for understanding the geodynamic evolution of the SSZ. Numerous geochemical and geochronological studies have been carried out by many researchers in last twenty-five years (Chandra et al. 1999, 2023; Rolland et al. 2002; Thanh et al. 2012; Bouihol et al. 2013; Borneman et al. 2015; Saktura et al. 2021; Sivaprabha et al. 2022; Lone et al. 2023b). However, paleontological and geochemical data about the SSZ are less abundant, particularly from the NW part. Radiolarian chert is widely used in stratigraphic, paleontological and geochemical investigations along other Tethyan sutures in the region (Danelian & Robertson 1997; Kojima et al. 2001; Ziabrev et al. 2003, 2004; Rojay et al. 2004; Babazadeh & De Wever 2004; Aitchison & Davis 2004; Göncüoğlu *et al.* 2006; Zyabrev *et al.* 2008 and Tekin *et al.* 2012). Radiolarian age data obtained from cherty rocks are important for constraining the chronology of tectonic events (Baxter *et al.* 2009).

Three blocks of radiolarian chert are exposed in the ophiolitic mélange of the Shyok Ophiolite (Lone et al. 2023a, b). In this paper we present the first report of radiolarian fossils in a chert block associated with this ophiolitic mélange. We discuss the geology, new fossil data, whole-rock chemistry and depositional setting of the radiolarian chert. Available geochronological data from igneous lithologies in the SSZ suggest a Jurassic to Late Cretaceous age or possibly as late as Eocene (Petterson & Windley 1985; Coward et al. 1986, Robertson & Collins 2002; Rolland et al. 2002; Khan et al. 2009; Burg 2011; Thanh et al. 2012; Bouihol et al. 2013; Borneman et al. 2015; Saktura et al. 2021). Thus, any new paleontological data will enable us to constrain the age of Shyok Suture Zone. We compare our results with the published data from elsewhere along the Mesotethyan suture in Tibet where it is referred to as the Bangong-Nujiang suture (Baxter et al. 2009; Wang et al. 2023), the Neotethyan Indus Yarlung Tsangpo Suture Zone (Upadhyay & Sinha 1993; Baxter et al. 2010; Cui et al. 2021a, 2021b; 2023; He et al. 2024) and Naga Ophiolite (Baxter et al. 2011; Ayyamperumal et al. 2021) as well as the Andaman Ophiolite (Jafri et al. 2020), representing the easternmost fringe of the Tethyan belt, extending south of eastern Himalayan syntaxis.

GEOLOGICAL SETTING

The geology of the Trans-Himalaya has been broadly divided into the Neotethyan Indus Yarlung Tsangpo Suture Zone (IYTSZ), the Mesotethyan Shyok and Bangong-Nujiang Suture Zones (SSZ) and the Karakoram/Qiangtang blocks and Trans-Himalaya/Lhasa blocks from south to north (Fig. 1b; Thakur 1981; Thakur & Rawat 1992; Searle *et al.* 1988). The IYTSZ represents a collage of diverse lithologies documenting the closure of the Neo-Tethys Ocean from Late Cretaceous to Early Paleocene time (Frank *et al.* 1977; Honegger *et al.* 1989; Cannat & Mascle 1990; Aitchison *et al.*

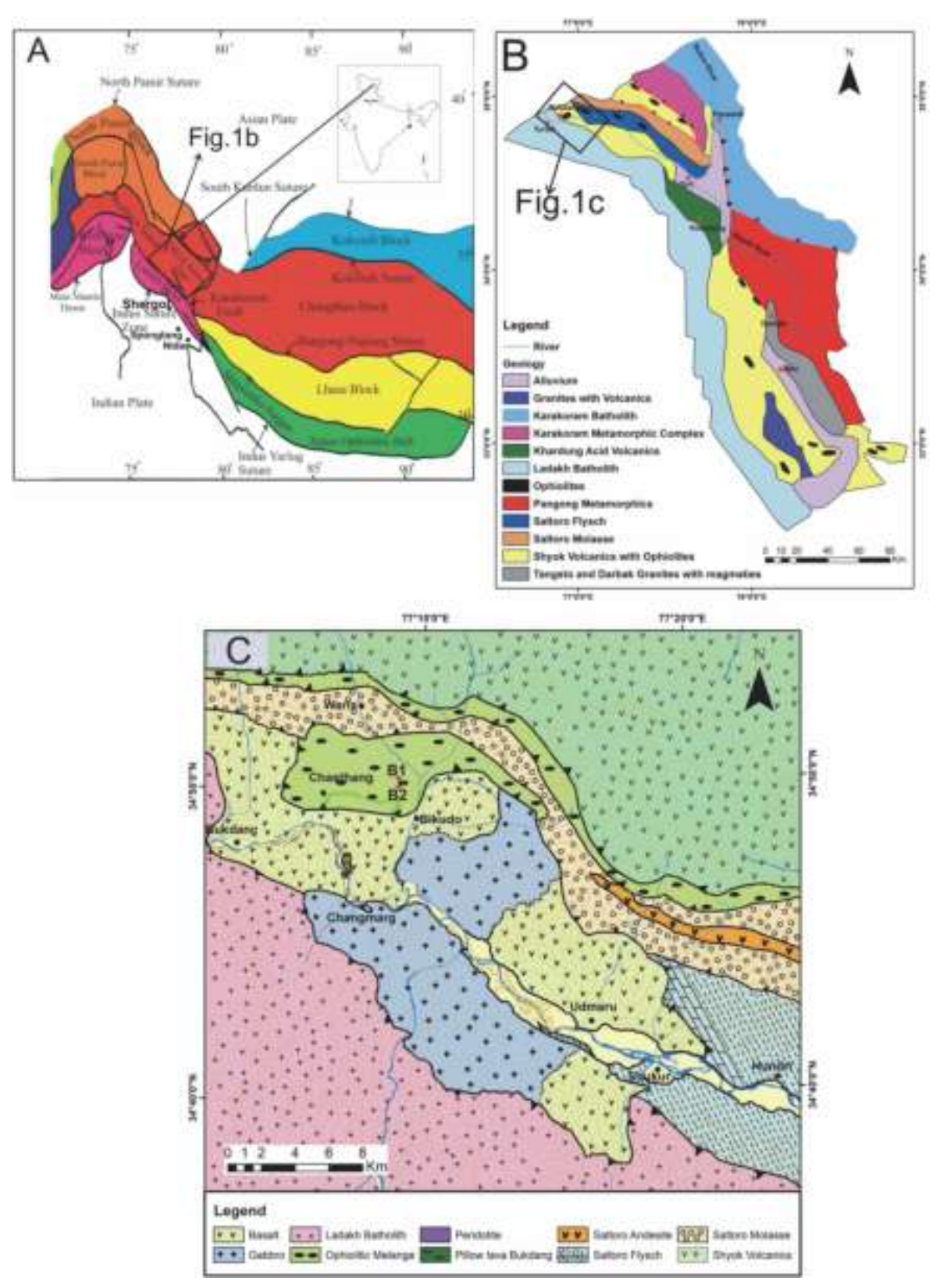


Fig. 1. (a) Regional tectonic map of Pamir-Karakoram, Kohistan and Ladakh showing the Indus and Shyok sutures, modified after Gaetani (1997); (b) Geological map of the Shyok Suture Zone (after Rai 1983), rectangular box shows the study area; (c) Detailed geological map of Bukdang ophiolite showing the distribution of different lithologies (Lone *et al.* 2023a). Star symbols B1 and B2 indicate radiolarian chert sample locations. (GPS locations B1 34°49'43.66"N, 077°06'08.88'E; B2 34°49'45.44"N, 077°06'08.60"E)

2007). The Karakoram block represents the southern margin of the Asian landmass and lies north of the SSZ. (Desio 1979; Gergan & Pant 1983; Sinha et al. 1999; Pundir et al. 2020). The SSZ incorporates a wide spectrum of lithologies the ages of which span from at least Late Jurassic to Eocene. It forms an important Cretaceous-Paleocene suture lying between Ladakh Batholith in the south and Karakoram block to the north. (Fig. 1a, b; Petterson & Windley 1985; Coward et al. 1986; Robertson & Collins 2002; Thanh et al. 2012; Borneman et al. 2015). In Nubra-Shyok Valley, rocks of the SSZ are subdivided into the Shyok Volcanics, Saltoro Flysch (Saltoro Formation), Saltoro Molasse, Shyok Ophiolites and Ophiolitic Mélange (Fig. 1b; Rai 1991; Upadhyay et al. 1999; Chandra et al. 1999; Weinberg et al. 2000; Rolland et al. 2002; Borneman et al. 2015; Lone et al. 2023a, b). Saltoro Flysch mainly consists of phyllites, slates with intercalations of limestones, shales and sandstones. This sedimentary unit contains the Jurassic - Cretaceous bryozoans Eoradiolites gilgitensis, Cyclamina sp., Horiopleura haydeni, Nummulites sp. and Cheilostomata (Rai 1982; Upadhyay 2001, 2014; Juyal 2006). The Cenozoic Saltoro Molasse comprises highly cleaved shales (red and green colored), coarse grained sandstone and conglomerates. It represents erosional detritus shed of mountains formed during collision between the Indian and Eurasian plates along the Shyok Suture. The Shyok Volcanics are composed of calc-alkaline magmas ranging in composition from basalt-basaltic andesite-andesitic-dacitic with continental arc and alkaline arc signatures indicating pre-India - Eurasia collision (Chandra et al. 1999; Saktura et al. 2022; Sivaprabha et al. 2022; Lone et al. 2023b).

The SSZ is marked by the disrupted occurrence of ophiolites and ophiolitic mélange extending from Chang La in the east via Nubra to Bukdang in the west. During the summer of 2018 and 2019 extensive geological field work was carried out in and around Bukdang village, where the maximum width of ophiolites and ophiolitic mélange is exposed hence we refer to these rocks as the Shyok Ophiolite (Fig.1c). They are also referred to as the Changmar Complex (Saktura et al. 2021). They include the majority of lithologies associated with a typical ophiolitic suite i.e, ultramafics, mafics, pillow lavas and pelagic sediments (Fig. 2a). A narrow east-west trending ophiolitic mélange within the Shyok Ophiolite crops out north of Chasthang on the Saltoro Hill (Fig. 2b). The ophiolitic mélange is bounded by the Shyok Ophiolite to the south and the Saltoro Molasse to the north. Overall, it shows typical block-in -matrix fabric. Serpentinite, gabbro, basalt and radiolarian chert, are the main blocks in the mélange, ranging in size from 5-m3 to several meters. These blocks are enveloped in the sedimentary matrix represented by sheared grey to greenish-grey phyllites (Fig. 2c). However, it is challenging to map the radiolarian cherts due to their discontinuous outcrop and limited size (about 3m3). These cherts are best exposed at Chasthang, on the southern slope of the Saltoro hills. Access to the outcrop is restricted as it lies near a military zone. The radiolarian chert is massive and ribboned, reddish-brown color and are highly joined, fractured and sheared (Fig. 2d). They are transected by mmcm scale silica veins.

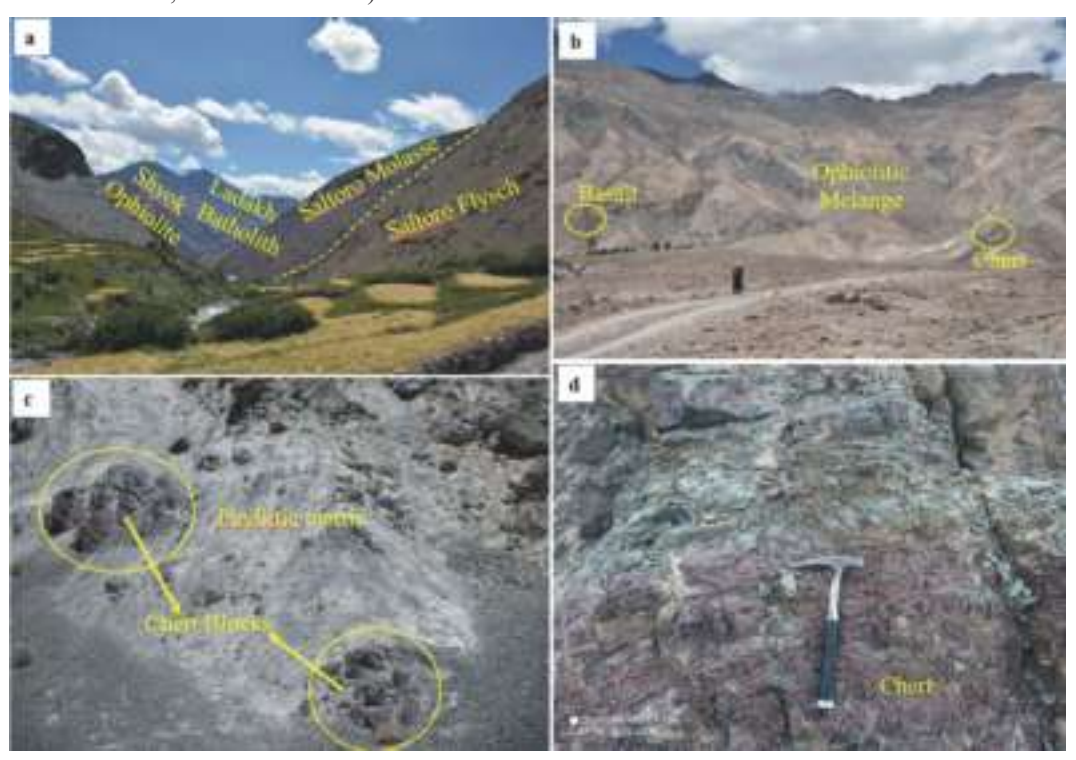


Fig. 2. Field photographs (a) Saltoro Flysch overlain by Saltoro molasse facing south from Waris Village, Shyok Ophiolite and Ladakh batholith are seen in the background; (b) Panoramic view of Shyok ophiolitic mélange facing north from Chastang near Bukdang village; (c) Ophiolitic mélange exhibiting Block-in-Matrix fabric with blocks of chert lying in matrix of phyllite at Chastang; (d) Ribbon-bedded chert at Chastang.

MATERIAL AND METHODS

Two samples of radiolarian bearing chert were collected for micropaleontological investigation from blocks within sediment-matrix mélange that crops out near Bukdang Village (Fig. 1c; B1 34°49'43.66"N, 077°06'08.88'E; B2 34°49'45.44"N, 077°06'08.60"E). The samples were treated in dilute hydrofluoric acid (5%) following the standard methodology of Pessagno & Newport (1972). For taxonomic identification, better preserved specimens were mounted on stubs and photographed using a Scanning Electronic Microscope (SEM, JEOL JSM-6610LV) at the University of Belgrade, Faculty of Mining and Geology. The identification and generic names have been updated according to O'Dogherty et al. (2009, 2017). Radiolarians have been identified by Prof. Nevenka Djerić (Faculty of Mining and Geology, University of Belgrade). All radiolarian specimens reported in this study are deposited in the Faculty of Mining and Geology, University of Belgrade.

The geochemical analysis of the cherts samples was conducted using a Bruker S8 Tiger Model X-ray Fluorescence Spectrophotometer (XRF) at Wadia Institute of Himalayan Geology, Dehradun, India. For XRF analyses, blanks and international standard JCh-1 were added to the sample series

for calibration. The analytical procedure for major and trace elements determination follows Khanna *et al.* 2009. Rare Earth Elements (REE) were determined using a PerkinElmer SCIEX ELAN DRC-e Inductively Coupled Plasma Mass Spectrometer (IC-PMS). The overall accuracy (relative standard deviation) for major oxides is below 5% and for trace elements below 12% with average precision better than 1.5%.

RESULTS

Petrography

In thin section the chert is texturally homogeneous and contains relatively undeformed radiolarian tests that are uniformly distributed in a fine-grained matrix primarily composed of clay minerals or microcrystalline quartz (Fig. 3a, b). Most of the radiolarian tests are intact and primarily filled with microcrystalline quartz, however some are also partially filled with ferruginous material (Fig. 3c). In a few thin sections, the tests are transected by quartz and hematite-rich veinlets (Fig. 3d). Thin section observations show penetrative deformation; as a result, at places microfossils are compressed and aligned along their long axes, giving them an ellipsoidal appearance (Fig. 3d).

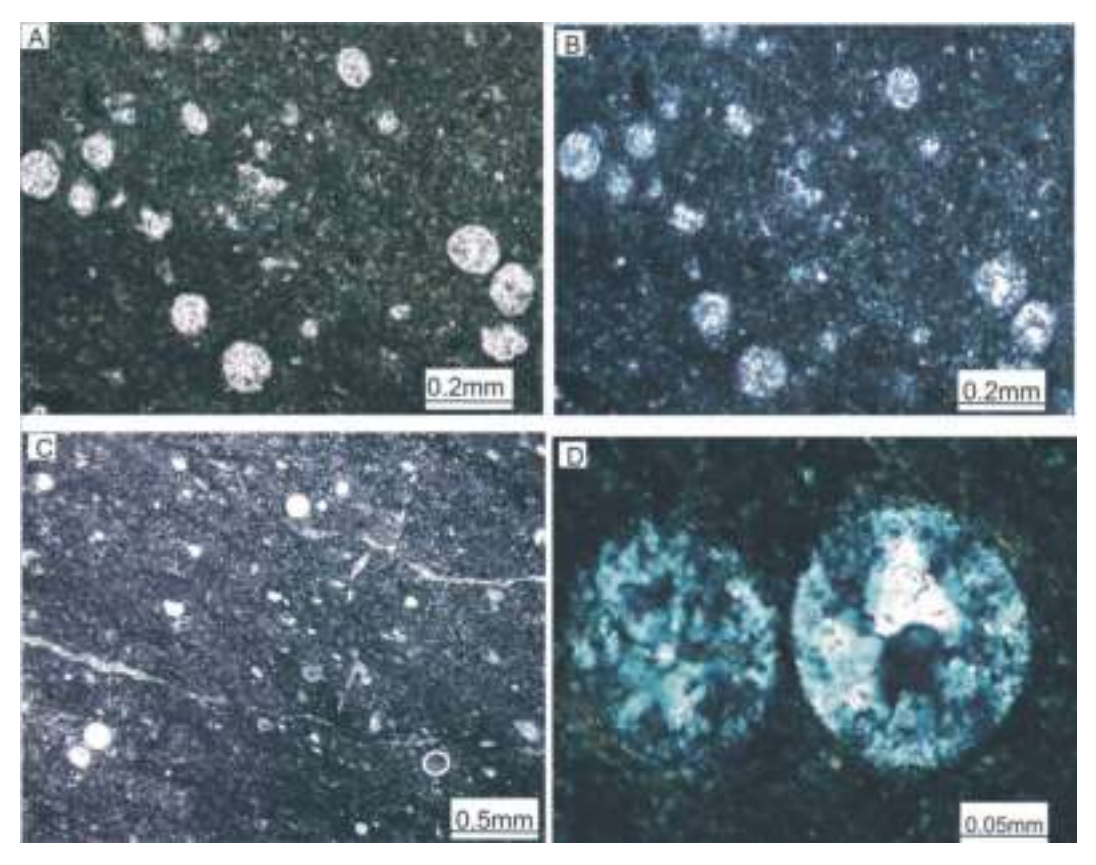


Fig. 3. Photomicrographs showing (a: plain-polarized-light (PPL), b: cross-polarized-light (XPL) cherts showing uniform distribution of radiolarian tests in a dark fine-grained matrix (B1 34°49'43.66"N, 077°06'08.88'E; B2 34°49'45.44"N, 077°06'08.60"E). The intact nature of radiolarian tests is clearly visible; (c) Deformed radiolarian chert with thin veinlets of quartz and hematite (B1 34°49'43.66"N, 077°06'08.88'E). (d) Radiolarian chert showing radiolarian tests filled with secondary silica (B2 34°49'45.44"N, 077°06'08.60"E).

Radiolarian biostratigraphy

Two samples were collected from red chert blocks within the Shyok Ophiolitic Mélange in the vicinity of Bukdang Village in Ladakh Trans-Himalaya. The least deformed sample (B2) was deemed suitable for biostratigraphic analysis. The radiolarians tests are generally poorly preserved and several specimens can be determined only as either Nassellaria or Spumellaria gen. et sp. indet. (Fig. 4). The taxonomic diversity of radiolarian assemblages is low due to selective and poor preservation. Radiolarian identification and age assignment

are mainly based on the well-established Jurassic to Cretaceous biostratigraphic zonations of Tethyan radiolarians of Baumgartner *et al.* 1995, which for the cretaceous part is based on Jud 1994; O'Dogherty 1994. Biostratigraphic data with Unitary Association (UA) zones are correlated to the 2024 IUGS International Chronostratigraphic Chart (Cohen *et al.* 2025). Overlapping age ranges amongst the identifiable taxa indicate assignment to the Aptian (Fig. 5) (O'Dogherty 1994; O'Dogherty *et al.* 2017; Ozsvárt *et al.* 2020).

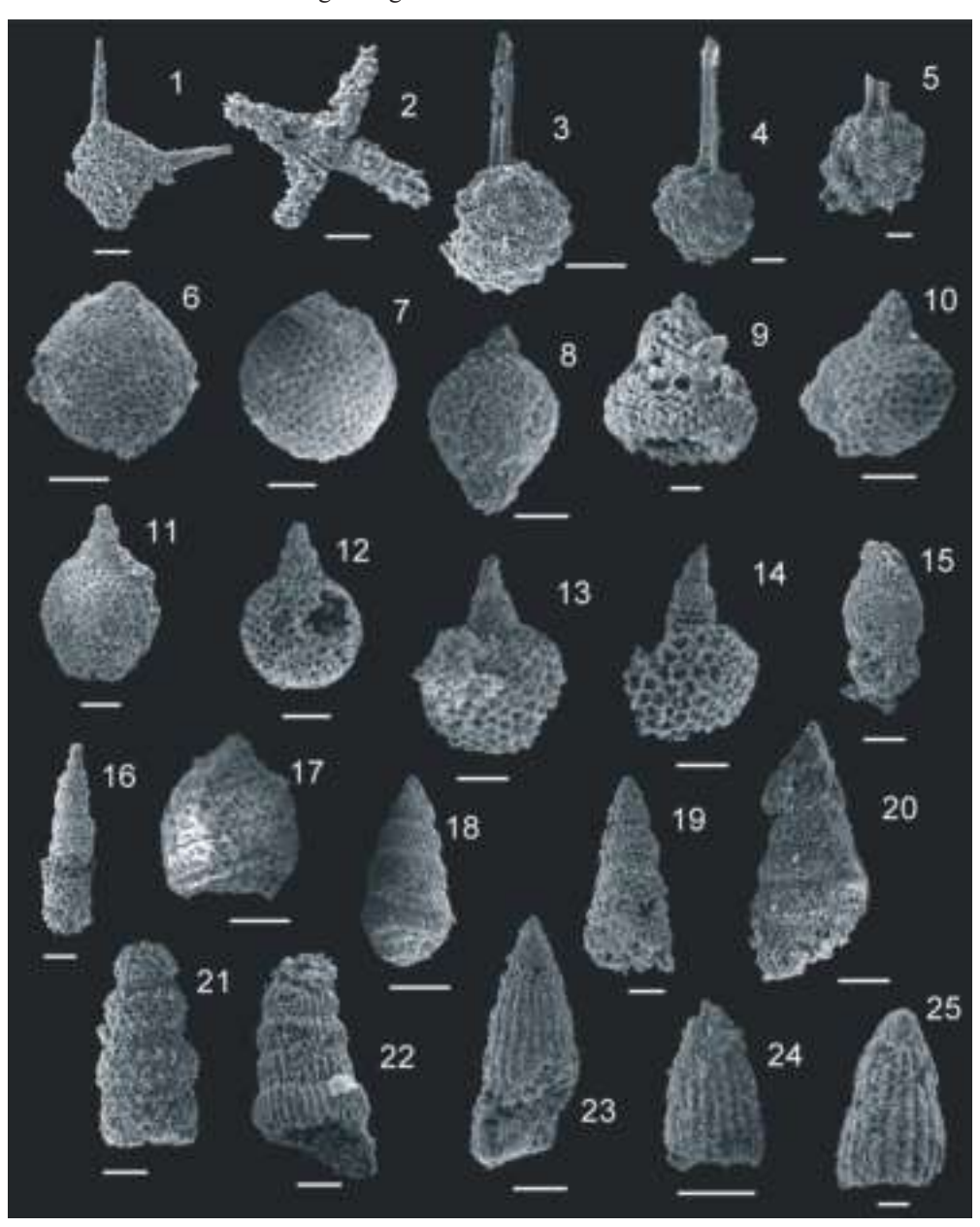


Fig. 4. Lower Cretaceous radiolarians from sample B2 (GPS 34°49'45.44"N, 077°06'08.60"E) the Shyok ophiolitic mélange. Scale bars: = 20 μm (9), = 50 μm (1, 2, 4-8, 10-17, 19-25), = 100 μm (3, 18). (1) ?Tetrapaurinella sp. (2) Crucella sp., (3-5) Acaeniotyle umbilicata (Rüst), (6-7) Holocryptocapsa fallax (Tan), (8) ?Rhopalosyringium fossile (Squinabol) sensu O'Dogherty (1994), (9) Parvimitrella japonica (Nakaseko and Nishimura), (10-14) Crococapsa asseni (Tan), (15-16) Nassellarian gen. et sp. indet., (17) Trimulus parmatus O'Dogherty, (18-19) Parvimitrella communis (Squinabol), (20) Parvimitrella sp., (21) Xitus sp. cf. X. spicularis (Aliev), (22) Pseudodictyomitra lodogaensis Pessagno, (23) Dictyomitra sp. cf. D. communis (Squinabol), (24-25) Archaeodictyomitra mitra Dumitrica

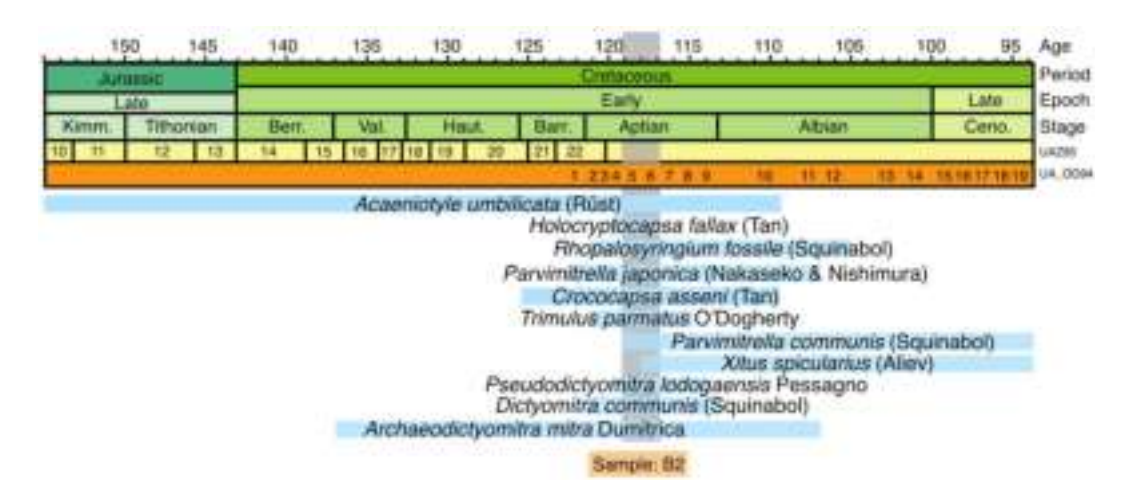


Fig. 5. Chart of stratigraphic ranges of radiolarian species present in sample B2. Age correlations for Lower Cretaceous radiolarian assemblages are based on recent taxonomic studies and biostratigraphic zonations of Mesozoic Tethyan radiolarians (O'Dogherty 1994; O'Dogherty *et al.* 2017). Radiolarian zones are correlated to the 2024 IUGS International Chronostratigraphic Chart (Cohen *et al.* 2025).

Geochemical characteristics

Major and trace elements

Major and trace element data and selected elemental ratios for chert samples from the Shyok Ophiolitic Mélange are presented in table 1. The abundance of silica varies from 75.5-75.6%. The Si/Si+Al+Fe+Ca ratio is commonly used in considerations of the source of the silica in the radiolarian cherts. Aluminium, Potassium and Titanium serve as indicators of terrigenous input into radiolarites. In the SSZ samples the Al₂O₃ content is relatively high and varies from 10.02-10.14 wt.%. This could be due to a contamination of detrital matter. This may be indicated by a high concentration of secondary mica (sericite) visible in thin sections. This is corroborated by high Ba and Sr concentration in comparison to other elements. Ba ranges from 102-106 ppm and shows positive correlation with Sr. The Fe₂O₃ concentration varies from 4.47-4.49 wt.%. The low iron concentration in radiolarian cherts points to a more significant biological contribution during the sedimentation, i.e the depositional area distal from the mid-ocean ridge. This is also supported by the positive correlation Zn (74-75 ppm) and Cu (43-81ppm). The chert samples show low values for MnO, TiO, and P₂O₅ ranging from 0.31-0.34 wt.%, 0.34-0.35 wt.% and 0.05 wt.% respectively. The loss on Ignition (LOI) values for these chert samples vary from 3.05-3.22 wt.%.

DISCUSSION

Radiolarian cherts are exposed as blocks within the phyllitic matrix of an ophiolitic mélange together with mafic and ultramafic rocks (pillow basalts and serpentinite). A relatively poorly preserved radiolarian fauna from a radiolarian chert block from the Shyok Ophiolitic Mélange contains a Lower Cretaceous (lower Aptian) radiolarian assemblage that can be compared to similar better-preserved radiolarian faunas which have been reported from elsewhere in Ladakh, India (Kojima et al. 2001; Baxter et al. 2010), southern Tibet (Ziabrev et al. 2003; Li et al. 2013), Malaysia (Jasin & Tongkul 2012) and Iran (Babazadeh & De Wever 2004; Pirnia et al. 2019;

Table 1. Whole-rock major and trace element data of radiolarian cherts from the Shyok ophiolite.

	- Tautotui tuit ettet is ji ont the shy on ophiotite.								
Sample	B1	B2							
Latitude	34°49'43.66"	34°49'45.44"N							
Longitude	77°6'8.88"E	77° 6'8.60"E							
Major oxides (wt.%)									
SiO ₂	75.70	75.55							
TiO ₂	0.34	0.35							
Al_2O_3	10.02	10.14							
Fe ₂ O ₃	4.47	4.49							
MgO	1.71	1.68							
CaO	1.82	1.51							
Na ₂ O	1.70	1.68							
K ₂ O	1.61	1.62							
MnO	0.34	0.30							
P_2O_5	0.05	0.05							
L.O.I.	3.0	3.0							
Total	100.98	100.36							
Al ₂ O ₃ /100-SiO ₂	0.41	0.41							
Fe ₂ O ₃ /100-SiO ₂	0.18	0.18							
MnO/TiO2	1.00	0.86							
	0.69	0.69							
$Al_2O_3/Al_2O_3+Fe_2O_3$									
Fe ₂ O ₃ /TiO ₂	13.15	12.83							
Si/Al+Fe+Si+Ca	0.01	0.01							
Si/Al+Fe+Si	0.01	0.01							
Al/Al+Fe+Mn	0.03	0.02							
SiO ₂ /SiO ₂ +Al ₂ O ₃ +Fe ₂ O ₃	0.84	0.84							
Trace Elements (ppm)	-	7							
Sc	7	7							
V	34	36							
Ba	219	216							
Cr	111	40							
Co Ni	48	81 40							
Cu	41 29	31							
Zn	74	75							
Ga	5	6							
Pb	26	26							
Th	5.0	5.0							
Rb	83	86							
U	2.7	2.0							
Sr	106	102							
Y	19	19							
Zr	78	80							
Nb	6	6							
U/Th	0.54	0.4							
Sc/Th	1.42	1.46							
Sr/Ba	0.48	0.47							
51/Da	0.40	U. + /							

Ozsvárt *et al.* 2020). These age ranges of the identified radiolarians are younger than and therefore consistent with the SHRIMP U-Pb zircon (151.9 \pm 1.5 Ma) crystallization ages of the Changmarg Complex (plagiogranite, Fig. 6) from the Shyok Ophiolite along the SSZ (Saktura *et al.* 2021).

The formation of radiolarian cherts is not restricted to a single environment and several depositional associations can be recognized (Jones & Murchey 1986). The original setting for radiolarites preserved in mélanges associated with the development of convergent plate margins can be considered by evaluating the behavior of major elements such as Fe₂O₃, Al₂O₃, TiO₂, MnO and their ratios (Adachi et al. 1986; Yamamoto 1987; Aitchison & Flood 1990). Using major element ratio diagrams such as Al₂O₃/100-SiO₂ vs Fe₂O₃/100-SiO₂ (Fig. 7a), Fe₂O₃/TiO₂ vs Al₂O₃/Al₂O₃+ Fe₂O₃ (Fig. 7b), $Al_2O_3/(Al_2O_3 + Fe_2O_3)$ vs La_N/Ce_N (Fig. 7c) and $100*(Al_2O_3/SiO_2)$ vs $100*(Fe_2O_3/SiO_2)$ (Fig. 7d) for the Shyok radiolarites, a pelagic ocean or continental margin affinity is indicated. Several researchers (Hein et al. 1983; Ruiz-Ortiz et 1989) have employed geochemical ratios, such as Si/Si+Al+Fe+Ca = Ia; Si/Si+Al+Fe = Ib; and Al/Al+Fe+Mn = IbIc, to constrain the nature and depositional environment of the radiolarites. Ratio Ia is regarded as a significant indicator of biogenic silica content with respect to aluminosilicates, calcareous and ferruginous minerals. The Ia values of typical biogenic silica-rich cherts = 0.8 to 0.9. The samples examined for this study are chert rich in biogenic silica. According to Adachi et al. (1986), the ratios of Al/(Al+Fe+Mn) range from 0.01 for a hydrothermal origin to 0.60 for a biological source, but the analyzed samples show higher Al/(Al+Fe+Mn) values with an average of 0.68, indicating a significant biological contribution. The Al-Fe-Mn diagram indicates the proximity of the chert samples to the biogenic field (Fig. 8; Adachi et al. 1986; Yamamoto 1987). This is further supported by low Fe₂O₃/TiO₂ ratios (12.97 average) according to Li *et al.* (2013). These data are also in agreement with the biogenic origin of chert, determined using SiO₂/ (SiO₂+Al₂O₃+ Fe₂O₃) ratio with average values of 0.83 (Rangin et al. 1981). The ratio Ic shows the relative input of oceanic versus continental detritus or whether there is a significant submarine exhalative contribution (Bostrom *et al.* 1973). Values (Ic = 0.67) for our samples are comparable to the averages of the chert from the ophiolitic mélange zone (<0.70), which is regarded as the average for biogenic hemipelagic chert (Ruiz-Ortiz et al. 1989). The pelagic nature of chert is further supported by Al-Fe-Mn ternary diagram (Fig. 9; Nohara & Kato 1985). The MnO/TiO, ratio is generally used to assess the origin of the chert as MnO is mostly derived from the deep ocean and TiO, is generally associated with terrigenous input. MnO/TiO, ratio of chert from marginal seas and continental slope deposits is always < 0.5, however for the open ocean environment the ratio is > 0.5 (Adachi et al. 1986) which is comparable to our chert (MnO/TiO₂ = 0.92 average). These geochemical data correlate well with the data reported from Shergol Ophiolite Mélange (Upadhyay & Sinha 1993), Andaman Ophiolites (Jafri et al. 2020), Dajiweng Ophiolite (Cui et al. 2021a) and Zedong Siliceous Mélange (He et al. 2024). The Sr/Ba ratios

of the chert samples (0.5 on average), values below 1 are related to siliceous rocks that evolved in shallow to deep ocean environments (abyssal).

Rare Earth Element data of the studied cherts from the ophiolitic mélange are shown in table 2. The total REE (ΣREE) concentration in the cherts sampled from the ophiolitic mélange varies from 7.18 to 7.64 ppm with an average of 7.41 ppm and show relatively LREE enrichment. The NASC normalized REE Values for the studied samples show a relatively flat distribution curve without significant Eu and Ce anomalies (Fig. 10). The Ce/Ce* and La_N/Ce_N ratios are widely used to determine the depositional environment of cherts. The Ce/Ce* ratio of cherts is lowest (0.29) near an ocean ridge, increasing (0.5-0.76) in ocean basin, and is highest (0.9-1.30) on continental margins (Murray et al. 1994). The studied samples show Ce/Ce* values vary from 0.72-0.77, showing proximity to ocean basin with low input of terrestrial material. The La_N/Ce_N ratios of cherts from continental margins exhibit no apparent fractionation $(La_N/Ce_N=1)$, however an ocean ridge has a high ratio $(La_N/Ce_N=1)$ >3.5) while intermediate values (2-3) are ascribed to oceanic basin (Murray et al. 1994). The La_N/Ce_N ratios of the studied chert samples from the ophiolitic mélange vary from 1.57 to 1.64, consistent with values characteristic of ocean basin environments. Geochemical analyses, including discriminant diagrams and trace element ratios such as La_N/Ce_N, Ce/Ce*,

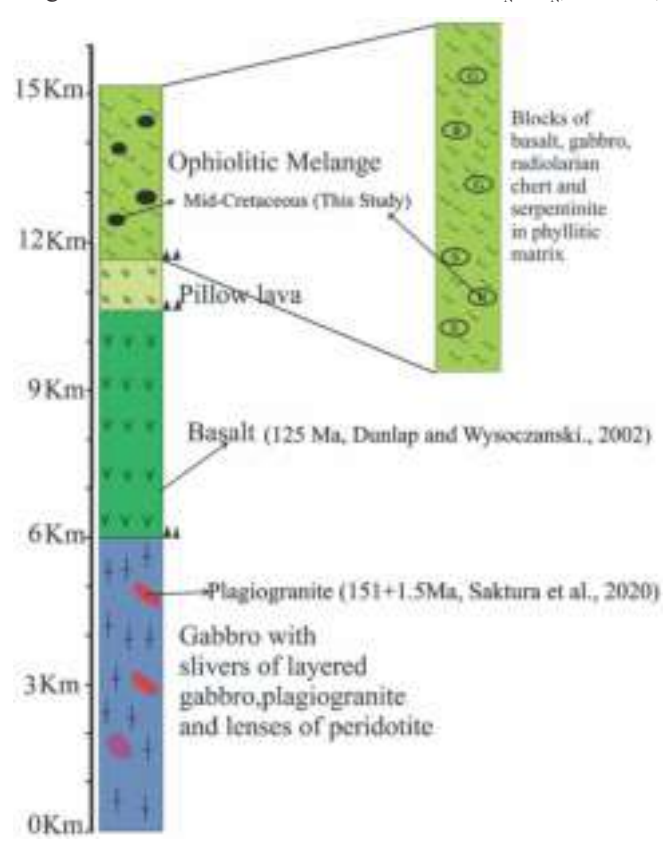


Fig. 6. Tectonostratigraphic column for the Shyok Ophiolite. Geochronological information for the corresponding rock types, where available, is summarized.

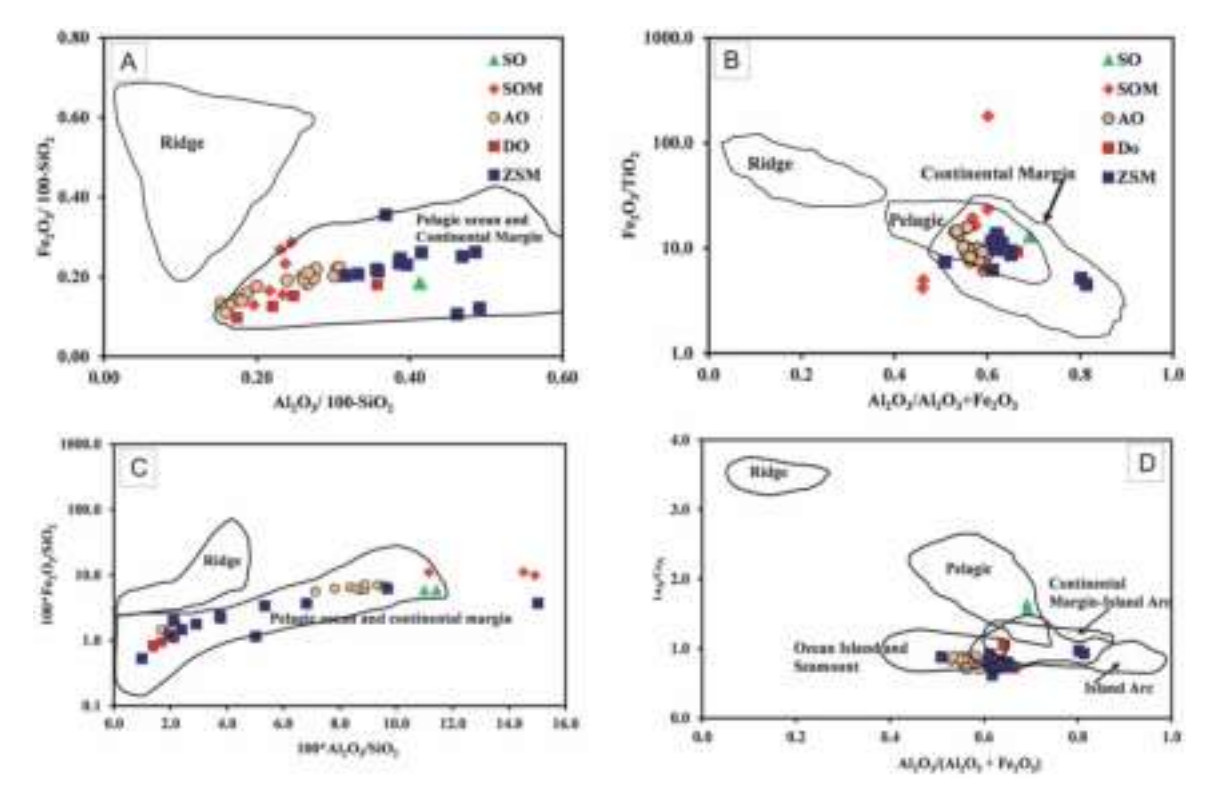


Fig. 7. Tectonic discrimination diagrams: a) Al₂O₃/100–SiO₂ vs. Fe₂O₃/100–SiO₂ diagram (modified from Murray 1994); (b) Al₂O₃/(Al₂O₃ + Fe₂O₃) vs. Fe₂O₃/TiO₂ binary diagrams (after Murray, 1994); (c) Al₂O₃/(Al₂O₃ + Fe₂O₃) vs. La_N/Ce_N diagram; (D) 100*(Al₂O₃/SiO₂) vs 100*(Fe₂O₃/SiO₂) diagram. A, B and C were modified from Murray (1994); D was modified from Girty *et al.* (1996). Prior published data on radiolarian cherts from ISZ (Upadhyay and Sinha, 1993), YTSZ (Cui et al. 2021b and He et al. 2024) and Andaman Ophiolites (Jafri *et al.* 2020) are also shown for comparison. SO-Shyok ophiolite; SOM-Shergol ophiolitic mélange, AO-Andaman ophiolite, DO-Dajiweng ophiolite, ZSM-Zedong siliceous mélange.

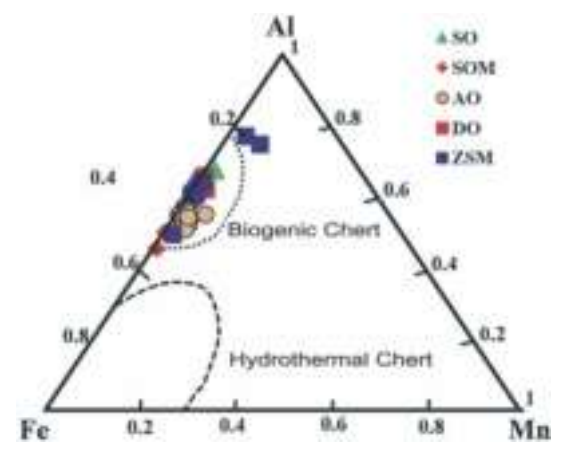


Fig. 8. Al-Fe-Mn diagram (Adachi et al. 1986) of the chert samples from ophiolitic mélange showing their non-hydrothermal character; Prior published data on radiolarian cherts from ISZ (Upadhyay and Sinha, 1993), YTSZ (Cui et al. 2021a and He et al. 2024) and Andaman Ophiolites (Jafri et al. 2020) are also shown for comparison. SOShyok ophiolite; SOM- Shergol ophiolitic mélange, AO-Andaman ophiolite, DO- Dajiweng ophiolite, ZSM-Zedong siliceous mélange.

and Al-Fe-Mn ternary relationships, collectively indicate that these radiolarian cherts were deposited in a deep ocean basin setting.

The integration of well-established biostratigraphic and lithostratigraphic data plays a pivotal role in advancing our understanding of paleoceanography and paleogeography. Various studies have proposed different timings for the

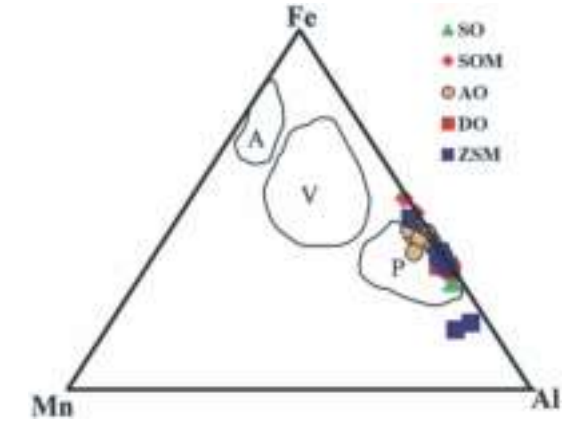


Fig. 9. Al-Fe-Mn relation in the chert samples from ophiolitic mélange. Present study infers normal pelagic sediments. A: high heat flow oceanic ridge sediments or volcanic sediments, V: Low heat flow oceanic ridge sediments or volcanic sediments, P; Normal Pelagic sediments (after Nohara and Kato, 1985). Prior published data on radiolarian cherts from ISZ (Upadhyay & Sinha 1993), YTSZ (Cui et al. 2021b and He et al. 2024) and Andaman Ophiolites (Jafri et al. 2020) are also shown for comparison. SO-Shyok ophiolite; SOM-Shergol ophiolitic mélange, AO-Andaman ophiolite, DO- Dajiweng ophiolite, ZSM-Zedong siliceous mélange.

opening of the Mesotethyan Ocean (MTO), ranging from the Late Paleozoic to Mesozoic (Metcalfe 1996; Fan *et al.* 2017; Zhang *et al.* 2007, 2012; Wang *et al.* 2008). Closure of the Mesotethyan Ocean in Tibet resulted in collision of the Lhasa terrane with the Qiangtang terrane along the Bangong Suture.

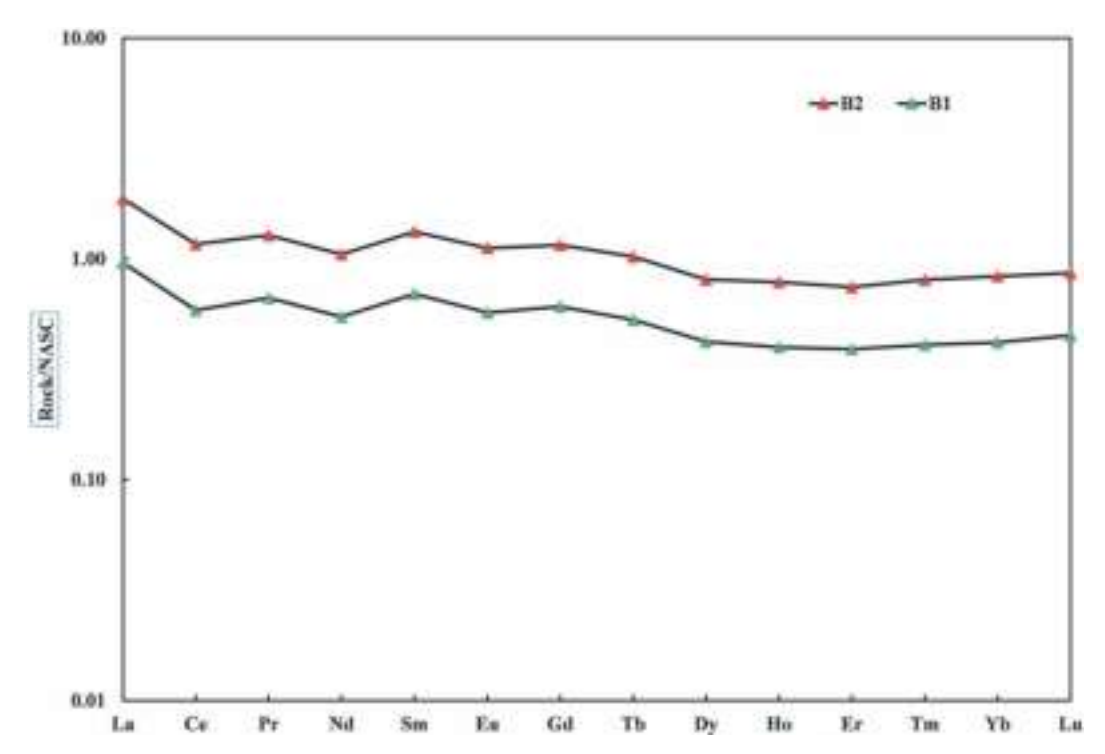


Fig. 10. NASC-normalized REE patterns of chert samples from ophiolite mélange. NASC data from McLennan (1989).

Table 2. Rare earth element data of radiolarian cherts from the Shyok ophiolite.

B1	B2
30.74	29.14
42.71	42.29
5.26	4.85
18.04	16.57
3.95	3.61
0.71	0.68
3.16	2.84
0.45	0.42
2.44	2.23
0.41	0.40
1.33	1.21
0.20	0.20
1.30	1.29
0.22	0.20
110.92	105.93
1.64	1.57
0.72	0.77
	30.74 42.71 5.26 18.04 3.95 0.71 3.16 0.45 2.44 0.41 1.33 0.20 1.30 0.22 110.92

Similarly, in Ladakh and Kohistan, the closure of the Mesotethys resulted collision of the Shyok ophiolite and the Kohistan Island Arc with the Karakoram block along the Shyok Suture (Clift *et al.* 2002, Borneman *et al.* 2015, Saktura *et al.* 2021). The finding of our Lower-Cretaceous (early Aptian) radiolarians within the ophiolitic mélange associated with the Shyok Ophiolite provides crucial insights on the closing history of the MTO. The Shyok Ophiolite represents dismembered thrust slices of diverse lithologies lacking lateral continuity and are exposed along the SSZ. The Shyok Ophiolite sequence consists of ultramafics, gabbros, pillow basalt, radiolarites and clastic turbidites. The radiometric ages of the Shyok Ophiolite range from Late Jurassic to mid-Cretaceous (Saktura *et al.* 2021; Borneman *et al.* 2015; Thann *et al.* 2012; Fig. 6). The formation of oceanic

crust began in the Late Jurassic to Early Cretaceous and was followed by the late Early Cretaceous deposition of radiolarites atop/over the pillow basalt. The age of the overlying Saltoro Molasse comprising of shales and sandstones is not known but as it contains chert clasts it is obviously younger than the radiolarites. These Lower Cretaceous (lower Aptian) radiolarian assemblages together with the occurrence of Aptian—Albian rudists and orbitolinids from the Saltoro Flysch (Upadhyay, 2014) along the SSZ indicate that the Mesotethyan ocean basin in this area had not yet fully closed in the Aptian (Fig. 11).

CONCLUSION

Detailed fieldwork in and around the Shyok Ophiolite in the northwestern part of the SSZ, resulted in identification of an ophiolitic mélange with blocks of serpentinite, basalt, gabbro and radiolarite. The radiolarian assemblage from a chert block encapsulated in the Shyok Ophiolitic mélange has an early Aptian affinity. Geochemical analysis of chert samples from the study area indicates that they are of biogenic origin and were deposited far away from any hydrothermal source such as an active spreading ridge, as shown by the high SiO₂/(SiO₂+Al₂O₂+Fe₂O₃) ratios and the Fe-Al-Mn ternary diagram. Further comparison of geochemical characteristics, including discriminant graphs, trace element ratios, and their relationships to other lithologies (e.g., basalt, Saltoro Flysch, and Molasse), indicates that the Lower Cretaceous radiolarite block is derived from the sedimentary succession that developed upon Mesotethyan oceanic crust. The presence of Lower Cretaceous (lower Aptian) radiolarian assemblages along the SSZ indicate that the final closure of MTO likely occurred no earlier than the Lower-Cretaceous.

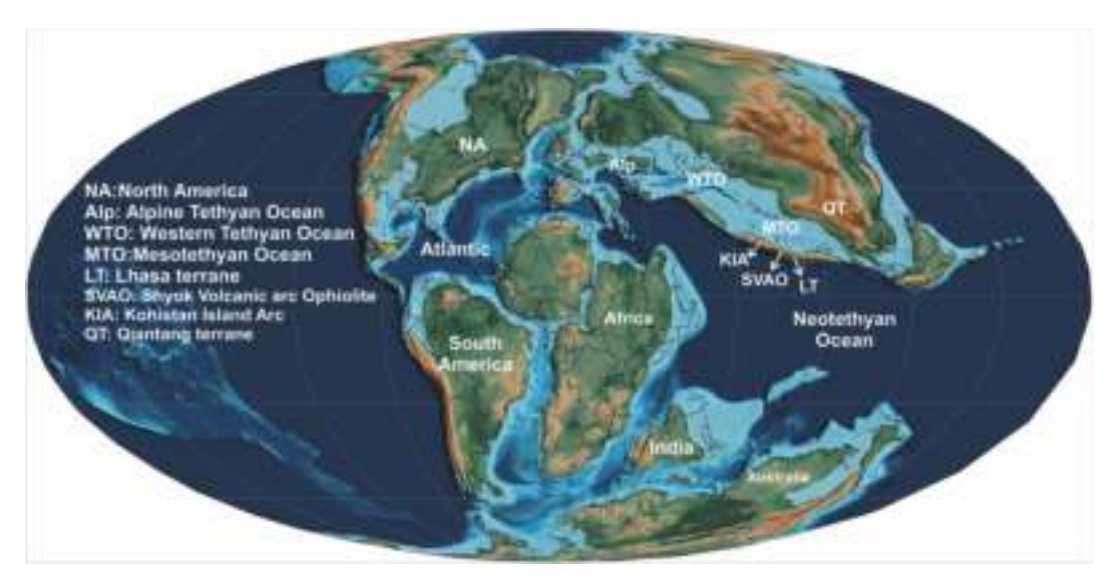


Fig. 11. Paleogeographic map showing the Mesotethyan Ocean during the mid- Cretaceous (Aptian). Brown, mountains; green, lowlands; light blue, flooded continents; deep blue, deep ocean (modified after Scotese 2021).

Declaration of Competing Interest: The authors declare that they have no known competing financial interests or personal relationships that could have appeared to influence the work reported in this paper.

Credit authorship contribution statement: Ihsan Ullah Lone: Conceptualization, Methodology, Writing- original draft, Investigation, Visualization. Meenal Mishra: Supervision, Investigation, Writing-review and editing. Rakesh Chandra: Conceptualization, Investigation, Writing-review and editing. Jonathan C. Aitchison: Writing-review and editing, Investigation.

Acknowledgements: We would like to express our thanks to the Director School of Sciences, IGNOU and HoD, Department of Earth Sciences, University of Kashmir, J&K for allowing us to carry out this work. We extend our thanks to Prof. R. Jayangonda Permual., Wadia Institute of Himalayan Geology, for generating geochemical data. We thank Prof. Nevenka Djerić (Faculty of Mining and Geology, University of Belgrade) for SEM analysis and radiolarian identifications. We extend our sincere gratitude to the Editors and reviewers Tim Cifer and Duje Kukoč for their insightful comments and suggestions that helped to improve the manuscript.

References

- Adachi, M., Yamamoto, K., Sugisaki, R. 1986. Hydrothermal chert and associated siliceous rocks from the northern Pacific their geological significance as indication of ocean ridge activity. Sedimentary Geology, 47, 125-148.
- Aitchison, J.C., Davis, A.M. 2004. Evidence for the multiphase nature of the India–Asia collision from the Yarlung Tsangpo suture zone, Tibet. In: Malpas, J.G., Fletcher, C.J.N., Ali, J.R., Aitchison, J.C. (eds), Aspects of the Tectonic Evolution of China. Geological Society, London, Special Publication, 226, 217-233.
- Aitchison, J.C., Flood, P.G. 1990. Geochemical constraints on the depositional setting of Paleozoic cherts from the New England Orogen, NSW, eastern Australia. *Marine Geology*, **94**, 79-95.
- Aitchison, J.C., Ali, J.R., Davis, A.M. 2007. When and where did India and Asia collide? *Journal of Geophysical Research: Solid Earth*, **112**, B05423, doi.org/10.1029/2006JB004706
- Ayyamperumal., R., Sooriamuthu, R., Gopalakrishnan, G., Biswa, G., Perumal., R., Gahlaut, P., Antony, J. K. 2021. Micropalaeontological and Geochemical Evidence of the Late Jurassic Radiolarians Cherts of Naga Ophiolite Hill, Nagaland, Northeast-India. *Open Journal of Geology*, 11, 356-372.

- Babazadeh, S.A., De Wever, P. 2004. Early Cretaceous radiolarian assemblages from radiolarites in the Sistan Suture (eastern Iran). *Geodiversitas*, **26**, 185-206.
- Baumgartner, P.O., Bartolini, A., Carter, E.S., Conti, M., Cortese, G., Danelian, T., De Wever, P., Dumitrica, P., Dumitrica-Jud, R., Gorican, S., Guex, J., Hull, D.M., Kito, N., Marcucci, M., Matsuoka, A., Murchey, B., O'Dogherty, L., Savary, J., Vishnevskaya, V., Widz, D., Yao, A., 1995. Middle Jurassic to Early Cretaceous radiolarian biochronology of Tethys based on Unitary Associations. *In:* Baumgartner, P.O., O'Dogherty, L., Gorican, S., Urquhart, E., Pillevuit, A., De Wever, P. (eds), *Mémoires de Géologie (Lausanne)*, 23, 1013-1048
- Baxter, A., Aitchison, J.C., Zyabrev, S.V. 2009. Radiolarian age constraints on Mesotethyan ocean evolution, and their implications for development of the Bangong-Nujiang suture Tibet. *Journal of the Geological Society, London*, 166, 689-694.
- Baxter, A., Aitchison, J.C., Ali, J.R., Zyabrev, S.V. 2010. Lower Cretaceous radiolarians from the Spongtang massif, Ladakh, NW India: implications for Neo-Tethyan evolution. *Journal of the Geological Society, London*, 167, 511-517.
- Baxter, A.T., Aitchison, J.C., Zyabrev, S.V., Ali, J.R. 2011. Upper Jurassic radiolarians from the Naga Ophiolite, Nagaland, northeast India. *Gondwana Research*, 20, 638-644.
- Borneman, N.L., Hodges, K.V., van Soest, M.C., Bohon, W., Wartho, J.A., Cronk, S.S., Ahmad, T. 2015. Age and structure of the Shyok suture in the Ladakh region of northwestern India: implications for slip on the Karakoram fault system. *Tectonics*, **34**, 2011-2033.
- Bostrom, K., Kraaemer, T., Gartner, S. 1973. Provenance and accumulation rates of opaline silica, Al, Ti, Fe, Mn, Cu, Ni, and Co in Pacific pelagic sediments. *Chemical Geology*, **11**, 132-148.
- Bouihol, P., Jagoutz, O., Dudas, F.O., Hanchar, J.M. 2013. Dating the India-Asia collision through arc magmatic records. *Earth and Planetary Science Letters*, **366**, 163-175.
- Brookfield, M.E., Reynolds, P.H. 1981. Late Cretaceous emplacement of the Indus suture zone ophiolitic melanges and an Eocene-Oligocene magmatic arc on the northern edge of the Indian plate. *Earth and Planetary Science Letters*, **55**, 157-162.
- Brookfield, M.E., Reynolds, P.H. 1990. Miocene ⁴⁰Ar/³⁹Ar ages from the Karakorum Batholith and Shyok Mélange, northern Pakistan, indicate late Tertiary uplift and southward displacement. *Tectonophysics*, **172**, 155-167.
- Burg, J.P. 2011. The Asia–Kohistan–India Collision: Review and Discussion. In: Brown, D., Ryan, P.D. (eds), Arc-Continent Collision. Springer-Verlag, Berlin, Heidelberg, 279-309.

- Cannat, M., Mascle, G. 1990. Reunion extraordinaire de la Societe Geologique de France en Himalaya du Ladakh (6 aout-1er septembre 1987). Bulletin de la Société Géologique de France, 6, 553-582.
- Chandra, R., Upadhyay, R., Sinha, A.K. 1999. Subduction and collision related magmatism in the Shyok Suture and eastern Karakoram. *Paleobotanist*, 48, 183-209.
- Chandra, R., Kowser, N., Brookfield, M.E., Satyanarayanan, M., Stöckli, D. 2023. Nature of the Shyok (Northern) Suture Zone between India and Asia: petrology, geochemistry and origin of the Tirit granitoids and associated dykes (Nubra Valley Ladakh Himalaya, NW India). Geological Magazine, 160, 1020-1039.
- Clift, P. D., Hannigan, R., Blusztajn, J., Draut, A. E. 2002. Geochemical evolution of the Dras–Kohistan Arc during collision with Eurasia: evidence from the Ladakh Himalaya, India. *Island Arc*, 11, 255-273.
- Cohen, K., Harper, D., Gibbard, P., Car, N. 2025. The ICS international chronostratigraphic chart this decade. *Episodes Journal of International Geoscience*, 48(1), 05-115.
- Coward, M.P., Rex, D.C., Khan, M.A., Windley, B.F., Broughton, R.D., Luff, I.W., Petterson, M.G., Pudsey, C.J. 1986. Collision tectonics in the NW Himalayas. *Geological Society, London, Special Publications*, 19, 203-219. doi.org/10.1144/GSL.SP.1986.019.01.11
- Cui, X.H., Luo, H., Aitchison, J.C., Li, X.C. 2021a. Middle Jurassic radiolarians and chert geochemistry, Dajiweng ophiolite, SW Tibet: implications for Neotethyan Ocean evolution. *Journal of Asian Earth Sciences*, 221, doi.org/10.1016/j.jseaes.2021.104947.
- Cui, X.H., Luo, H., Aitchison, J.C., Li, X.C., Feng, P.Y. 2021b. Early Cretaceous radiolarians and chert geochemistry from western Yarlung-Tsangpo suture zone in Jianyema section, Purang county, SW Tibet. Cretaceous Research, 125, doi.org/10.1016/j.cretres.2021.104840.
- Cui, X.H., Li, X.C., Aitchison, J.C., Luo, H. 2023. Early Cretaceous monsoonal upwelling along the northern margin of the Gondwana continent: evidence from radiolarian cherts *Marine Micropaleontology*, 181, doi.org/10.1016/j.marmicro.2023.102247.
- Danelian, T., Robertson, A.H. 1997. Radiolarian evidence for the stratigraphy and palaeo-oceanography of the deep-water passive margin of the Indian Plate (Karamba Formation, Indus suture zone, Ladakh Himalaya). *Marine Micropaleontology*, **30**, 171-195.
- Desio, A. 1979. Geologic evolution of the Karakorum. *In:* Farah, A., De Jong, K.A. (eds), *Geodynamics of Pakistan. Quetta*. Geological Survey of Pakistan, pp. 111-124.
- Fan, S., Ding, L., Murphy, M.A., Yao, W., Yin, A. 2017. Late Paleozoic and Mesozoic evolution of the Lhasa Terrane in the Xainza area of southern Tibet. *Tectonophysics*, 721, 415-434.
- Frank, W., Gansser, A., Trommsdorff, V. 1977. Geological observations in the Ladakh area (Himalayas), a preliminary report. *Schweizer Mineralogische und Petrographische Mitteilungen*, **57**, 89-113.
- Gaetani, M. 1997. The Karakorum Block in Central Asia, from Ordovician to Cretaceous. Sedimentary Geology, 109, 339-359.
- Gansser, A. 1980. The significance of the Himalayan suture zone. *Tectonophysics*, **62**, 37-52.
- Gautam, S., Awatar, R., Sharma, A. 2023. Evidence of an early Permian palynomorphs in Ophiolitic Mélange of the Shyok Suture Zone, Eastern Karakoram, Ladakh, India. *Journal of Palaeosciences*, **72**, 29-41.
- Gergan, J.T., Pant, P.C. 1983. Geology and stratigraphy of eastern Karakoram, Ladakh. In Geology of Indus Suture zone of Ladakh. V.C. Thakur and K.K. Sharma (eds). Wadia Institute of Himalayan Geology, Dehradun, 99-106.
- Girty, G.H., Ridge, D.L., Knaack, C., Johnson, D., Alriyami, R.K. 1996. Provenance and depositional setting of Paleozoic chert and argillite of Sierra Nevada, California. *Journal of Sedimentary Research*, 66, 107-118
- Göncüoglu, M.C., Yalınız, M.K., Tekin, U.K. 2006. Geochemistry, tectonomagmatic discrimination and radiolarian ages of basic extrusives within the Izmir-Ankara Suture Belt (NW Turkey): time constraints for the Neotethyan evolution. *Ofioliti*, 31, 25-38.
- Hanson, C. R. 1989. The northern suture in the Shigar valley, Baltistan, northern Pakistan. Geological Society of America, Special Paper 232, 203-215.

- He, Z., Li, X., Li, Y., Matsuoka, A., Luo, H., Cui, X., Cheng, J. 2024. Evolution of the Neo- Tethys traced by Late Triassic to Early Cretaceous marine remnants in the eastern segment of the Yarlung-Tsangpo suture zone, southern Tibet. *Journal of Asian Earth Sciences*, 265, 106090 doi.org/10.1016/j.jseaes.2024.106090.
- Hein, J.R., Kuijpers, E.P., Denyer, P., Sliney, R.E. 1983. Petrology and geochemistry of Cretaceous and Paleogene cherts from western Costa Rica. *Developments in Sedimentology*, 36, 143-174. Elsevier.
- Honegger, K., Le Fort, P., Mascle, G., Zimmermann, J.L. 1989. The blueschists along the Indus suture zone in Ladakh, NW Himalaya. *Journal of Metamorphic Geology*, 7, 57-72.
- Jafri, S.H., Sarma, D.S., Khan, T., Singh, D.K. 2020. Geochemical characteristics of the Late Cretaceous radiolarian cherts from North Andaman Island, Bay of Bengal., India. *Journal of Earth System Science*, 129, 1-10.
- Jasin B., Tongkul, F. 2012. Cretaceous radiolarians from Baliojong ophiolite sequence, Sabah, Malaysia. *Journal of Asian Earth Sciences*, 76, 58-265.
- Jones, D., Murchey, B. 1986. Geologic significance of Paleozoic and Mesozoic radiolarian chert. Annual Review of Earth and Planetary Sciences 14, 455-492.
- Jud, R. 1994. Biochronology and systematics of Early Cretaceous Radiolaria of the western Tethys. Mémoires de Géologie (Lausanne), 19, 1-147.
- Juyal., K.P. 2006. Foraminiferal biostratigraphy of the Early Cretaceous Hundiri Formation, lower Shyok area, eastern Karakoram, India. Current Science, 1096-1101.
- Khan, S.D., Walker, D.J., Hall, S.A., Burke, K.C., Shah M.T., Stockli, L. 2009. Did the Kohistan-Ladakh Island arc collide first with India? Geological Society of America Bulletin, 121, 366-384.
- Khanna, P.P., Saini, N.K., Mukherjee, P.K., Purohit, K.K. 2009. An appraisal of ICP-MS technique for determination of REEs: long term QC assessment of silicate rock analysis. *Himalayan Geology*, 30, 95-99.
- Kojima, S., Ahmad, T., Tanaka, T., Bagati, N.T., Mishra, M., Kumar, R., Islam, R., Khanna, P. 2001. Early Cretaceous radiolarians from the Indus suture zone, Ladakh, northern India. News of Osaka Micropaleontologists, 12, 257-270.
- Lakhan, N., Singh, A.K., Akhtar, S., Singh, B.P. 2022. Geochemical characteristics and petrogenesis of magmatic rocks of the Shyok suture zone, NW Ladakh Himalaya, India. *Arabian Journal of Geosciences*, 15(3), 223, doi.org/10.1007/s12517-021-09361-9.
- Li, H., Zhai, M., Zhang, L., Zhou, Y., Yang, Z., He, J., Liang, J., Zhou, L. 2013. The distribution and composition characteristics of siliceous rocks from Qinzhou Bay Hangzhou Bay Joint Belt, South China: constraint on the tectonic evolution of plates in South China. *The Scientific World Journal*, 2013(1), 949603. doi.org/10.1155/2013/949603
- Lone, I.U., Mishra, M., Tiwary, S.K., Chandra, R. 2023a. Recognition of Shyok Ophiolites of NW Ladakh Trans-Himalaya as a Geoheritage: Importance to Himalayan Orogeny and Remnant of Tethyan Oceanic Lithosphere. *Geoheritage*, 15, 3.
- Lone, I. U., Mishra, M., Chandra, R. 2023b. Petrological studies of Bukdang Ophiolite, Shyok Suture Zone, Trans-Himalaya. *Himalayan Geology*, 44, 130-146.
- Martin, C.R., Jagoutz, O., Upadhyay, R., van Tongeren, J.A., Mueller, P.A., Weiss, B.P. 2023. Paleomagnetic Constraint on the Age of the Shyok Suture Zone. *Journal of Geophysical Research: Solid Earth* 128(10): e2022JB026137.
- McLennan, S.M. 1989. Rare Earth Elements in Sedimentary Rocks: Influence of Provenance and Sedimentary Processes. *In:* Lipin, B.R., McKay, G.A., (eds), *Geochemistry and Mineralogy of Rare Earth Elements*. De Gruyter, Berlin, pp. 169-200. https://doi.org/10.1515/9781501509032-010
- Metcalfe, I. 1996. Pre-Cretaceous evolution of SE Asian terranes. *Geological Society, London, Special Publications*, **106**(1), 97-122.
- Murray, R.W. 1994. Chemical criteria to identify the depositional environment of chert: general principles and applications. *Sedimentary Geology*, **90** (3-4), 213-232.
- Nohara, M., Kato, K. 1985. Chemical compositions of pelagic deep-sea sediments its relation to the formation of authigenic mineral phase under the chemical control of sea water. *In:* Nasu, N.et al. (eds), Formation of Active Ocean Ridges. Terra Pub, Tokyo, pp. 893-912.

- O'Dogherty, L. 1994. Biochronology and Paleontology of mid-Cretaceous radiolarians from northern Apennines (Italy) and Betic Cordillera (Spain). *Mémoires de Géologie (Lausanne)*, **21**, 1-415.
- O'Dogherty, L., Carter, E.S., Dumitrica, P., Goričan, Š., De Wever, P., Bandini, A.N., Baumgartner, P.O., Matsuoka, A. 2009. Catalogue of Mesozoic radiolarian genera. Part 2: Jurassic-Cretaceous. *Geodiversitas*, **31**, 271-356.
- O'Dogherty, L., Goričan, Š., Gawlick, H.J. 2017. Middle and late Jurassic radiolarians from the Neotethys suture in the eastern Alps. *Journal of Paleontology*, 91, 25-72.
- Ozsvárt, P., Bahramnejad, E., Bagheri, S., Sharifi, M. 2020. New Albian (Cretaceous) radiolarian age constraints for the Dumak ophiolitic mélange from the Shuru area, Eastern Iran. *Cretaceous Research*, **111** /doi.org/10.1016/j.cretres.2020.104451.
- Pessagno, E.A., Newport, R.L. 1972. A technique for extracting Radiolaria from radiolarian chert. *Micropaleontology*, **18**, 231-234.
- Petterson, M.G., Windley, B.F. 1985. Rb/Sr dating of the Kohistan arc batholith in the Trans-Himalaya of north Pakistan, and tectonic implications. *Earth and Planetary Science Letters*, **74**, 45-57.
- Pirnia, T., Saccani, E., Torabi, G., Chiari, M., Goričan, Š., Barbero, E. 2019. Cretaceous tectonic evolution of the Neo-Tethys in Central Iran: Evidence from petrology and age of the Nain-Ashin ophiolitic basalts. Geoscience Frontiers, 11, 57-81.
- Pundir, S., Adlakha, V., Kumar, S., Singhal, S. 2020. Closure of India—Asia collision margin along the Shyok suture zone in the eastern Karakoram: New geochemical and zircon U–Pb geochronological observations. *Geological Magazine*, 157, 1451-1472.
- Rai, H. 1982. Geological evidence against the Shyok Palaeo-suture, Ladakh Himalaya. Nature, 297, 142-144.
- Rai, H. 1983. Geology of the Nubra valley and its significance on the evolution of the Ladakh Himalaya. *In:* Thakur, V.C., Sharma, K.K. (eds), *Geology of Indus Suture Zone of Ladakh*. Wadia Institute of Himalayan Geology, Dehradun, pp. 79-97.
- Rai, H. 1991. The Shyok valley (Northern Ladakh, India): An entrapped and compressed marginal oceanic basin. *Journal of Himalayan Geology*, 2, 1-5.
- Rangin, C., Steinberg, M., Bonnot-Courtois, C. 1981. Geochemistry of the Mesozoic bedded cherts of Central Baja California (Vizcaino-Cedros-San Benito): implications for paleogeographic reconstruction of an old oceanic basin. *Earth and Planetary Science Letters*, 54, 313-322.
- Robertson, A.H.F., Collins, A.S. 2002. Shyok Suture Zone, N. Pakistan: Late Mesozoic Tertiary evolution of a critical suture separating the oceanic Ladakh Arc from the: continental margin. *Journal of Asian Earth Sciences*, 20, 309-351.
- Rolland, Y., Picard, C., Pecher, A., Lapierre, H., Bosch, D., Keller, F. 2002. The cretaceous Ladakh arc of NW Himalaya—slab melting and melt–mantle interaction during fast northward drift of Indian Plate. *Chemical Geology*, 182, 139-178.
- Rojay, B., Altıner, D., Altıner, S.Ö., Pırıl Önen, A., James, S., Thirlwall, M.F. 2004. Geodynamic significance of the Cretaceous pillow basalts from North Anatolian Ophiolitic Mélange Belt (Central Anatolia, Turkey): geochemical and paleontological constraints. *Geodinamica Acta*, 17, 349-361.
- Ruiz-Ortiz, P.A., Bustillo, M.A., Molina, J.M. 1989. Radiolarite sequences of the Subbetic, Betic Cordillera, Southern Spain. *In:* Hein, J.R. and Obradovic, J. (eds), *Siliceous deposits of the Tethys and Pacific regions*. Springer, New York. pp. 107-127.
- Saktura, W.M., Buckman, S., Nutman, A.P., Bennett, V.C. 2021. Late Jurassic Changmar complex from the Shyok ophiolite, NW Himalaya: a prelude to the Ladakh Arc. *Geological Magazine*, **158**, 239-260.
- Saktura, W.M., Buckman, S., Nutman, A.P., Zhou, R. 2022. Jurassic-Cretaceous arc magmatism along the Shyok-Bangong Suture of NW Himalaya: formation of the peri-Gondwana basement to the Ladakh Arc. *Journal of the Geological Society, London*, 179. doi.org/10.1144/jgs2021-035
- Saktura, W.M., Buckman, S., Nutman, A.P., Walsh, J., Murray, G. 2023. Magmatic records from the Karakoram terrane: U-Pb zircon ages from granites and modern sediments in the Nubra Valley, NW Himalaya.

- Journal of Asian Earth Sciences, doi.org/10.1016/j.jseaes.2023.105771.
- Scotese, C.R. 2021. An atlas of Phanerozoic paleogeographic maps: the seas come in and the seas go out. *Annual Review of Earth and Planetary Sciences*, **49**, 679-728.
- Searle, MP., Cooper, D.J.W., Rex, A.J. 1988. Collision tectonics of the Ladakh-Zanskar Himalaya. Philosophical Transactions of the Royal Society of London Series A, Mathematical and Physical Sciences, 326, 117-150.
- Sinha A.K., Rai H., Upadhyay R., Chandra, R. 1999. Contribution to the geology of the eastern Karakoram, India. Geological Society of America, Special Paper 328, 33-46.
- Sivaprabha, S., Bhat, I.M., Ahmad, T., Tanaka, T., Balakrishnan, S., Asahara, Y., Mukhopadhyay, D. 2022. Geochemical analysis of magmatic rocks from Shyok Suture Zone (SSZ) Trans-Himalaya, NW India: Insights for geodynamic evolution of the terrane. *Lithos*, **410**, doi.org/10.1016/j.lithos.2022.106594.
- Srimal., N. 1986. India- Asia collision: implications from the geology of eastern Karakoram. Geology, 14, 523-527.
- Tahirkheli, R.K. 1979. The India-Eurasia suture zone in northern Pakistan: Synthesis and interpretation of recent data at plate scale. *Geodynamics of Pakistan*, 125-130.
- Tekin, U. K., Göncüoğlu, M. C., Pandolfi, L., Marroni, M. 2012. Middle-Late Triassic radiolarian cherts from the Arkotdağ mélange in northern Turkey: implications for the life span of the northern Neotethyan branch. *Geodinamica Acta*, 25, 305-319.
- Thakur, V.C. 1981. Regional framework and Geodynamic evolution of the Indus Tsangpo Suture Zone in Ladakh Himalayas. *Transactions of the Royal Society of Edinburgh: Earth Sciences*, **72**, 89-97.
- Thakur, V.C., Misra, D.K. 1984. Tectonic framework of Indus and Shyok suture zones in eastern Ladakh, NW Himalaya. *Tectonophysics*, 101, 207-220.
- Thakur, V.C., Rawat, B.S. 1992. *Geologic map of Western Himalaya*. Wadia Institute of Himalayan Geology, Dehradun: scale, 1:1,000,000.
- Thanh, N.X., Rajesh, V.J., Itaya, T., Windley, B., Kwon, S., Park, C.S. 2012. A Cretaceous forearc ophiolite in the Shyok suture zone, Ladakh, NW India: implications for the tectonic evolution of the Northwest Himalaya. *Lithos*, 155, 81-93.
- Upadhyay, R., Sinha, A.K. 1993. Siliceous deposits of ophiolitic mélange zone. Indus Suture, Ladakh Himalaya, India. *Journal of Himalayan Geology*, 4, 121-129.
- Upadhyay, R. 2014. Palaeogeographic significance of 'Yasin-type' rudist and orbitolinid fauna of the Shyok Suture Zone, Saltoro Hills, northern Ladakh, India. Current Science, 106, 223-228.
- Upadhyay, R. 2001. Middle Cretaceous carbonate build-ups and volcanic seamount in the Shyok Suture, northern Ladakh, India. *Current Science*, **81**, 695-698.
- Upadhyay, R., Sinha, A.K., Chandra, R., Rai, H. 1999. Tectonic and magmatic evolution of the eastern Karakoram, India. *Geodinamica Acta* 12, 341-358.
- Wang, W.L., Aitchison, J.C., Lo, C.H., Zeng, Q.G. 2008. Geochemistry and geochronology of the amphibolite blocks in ophiolitic melanges along Bangong- Nujiang suture, central Tibet. *Journal of Asian Earth Sciences*, 33, 122-138.
- Wang, T., Li, G., Aitchison, J.C., Sheng, J., Ma, X. 2023. Lower Cretaceous deep marine deposits in western Tibet: implications for paleoceanographic evolution of the Mesotethyan Ocean. Cretaceous Research, 148: doi.org/10.1016/j.cretres.2023.105527.
- Weinberg, R.F., Dunlap, W.J., Whitehouse, M. 2000. New field, structural and geochronological data from the Shyok and Nubra valleys, northern Ladakh; linking Kohistan to Tibet. *In:* Khan, A., Treloar, P.J., Searle M.P., Jan, Q. (eds). *Tectonics of the Nanga Parbat syntaxis and the western Himalaya*. Geological Society, London, Special Publication, 170, 253-275.
- Yamamoto, K. 1987. Geochemical characteristics and depositional environments of cherts and associated rocks in the Franciscan and Shimanto Terranes. Sedimentary Geology, 52, 65-108.

- Zhang, K.J., Zhang, Y.X., Li, B., Zhong, L.F. 2007. Nd isotopes of siliciclastic rocks from Tibet, western China: constraints on provenance and pre-Cenozoic tectonic evolution. *Earth and Planetary Science Letters*, 256, 604-616.
- Zhang, K.J., Zhang, Y.X., Tang, X.C., Xia, B. 2012. Late Mesozoic tectonic evolution and growth of the Tibetan plateau prior to the Indo-Asian collision. *Earth-Science Reviews*, **114**, 236-249.
- Ziabrev, S., Aitchison, J.C., Abrajevitch, A., Badengzhu, Davis, A., Luo, H. 2003. Precise radiolarian age constraints on the timing of ophiolite generation and sedimentation in the Dazhuqu terrane, Yarlung Tsangpo suture zone, Tibet. *Journal of the Geological Society, London*, 160, 591-599.
- Ziabrev, S.V., Aitchison, J.C., Abrajevitch, A.V., Badengzhu, Davis, A.M., Luo, H. 2004. Bainang Terrane, Yarlung-Tsangpo suture, southern Tibet (Xizang, China): a record of intra-Neotethyan subduction accretion processes preserved on the roof of the world. *Journal of the Geological Society, London*, 161, 523-539.
- Zyabrev, S.V., Kojima, S., Ahmad, T. 2008. Radiolarian biostratigraphic constraints on the generation of the Nidar ophiolite and the onset of Dras arc volcanism: Tracing the evolution of the closing Tethys along the Indus–Yarlung–Tsangpo suture. *Stratigraphy*, 5, 99-112.

Fluid Evolution of the Asian Continental Crust: Implication for Exhumation Tectonics of Trans Himalaya

ADITYA KHARYA^{1,2,*}, HIMANSHU K. SACHAN^{1,2}, SAMEER K. TIWARI^{1,2}, SHASHI RANJAN RAI³, DEEPASHU JOSHI^{1,2}, VAIBHAV DUBEY^{1,2}

¹Wadia Institute of Himalayan Geology, Dehradun-248001, India ²Academy of Scientific and Innovative Research (AcSIR), Ghaziabad, India ³Department of Geology, Lucknow University, Lucknow, India *Email (Corresponding author): adityakharya@gmail.com / aditya@wihg.res.in

Abstract: The Trans-Himalaya represents the South Tibetan Thickened Crust. This thickened crust is the product of the collision between the Indian and Eurasian plates. The trans-Himalaya ranges from the Hindukush mountain to the Tibetan plateau. It comprised of Karakorum batholith, metamorphosed rocks, migmatite, and mylonites. The main emphasis of our review is to reveal the role of the fluid in the evolution of the Asian continent crust. This review emphasizes the fluid flux and its evaluation history (exhumation, metamorphism, and magmatic process).

The Trans-Himalayan rocks are comprised of carbonic, carbonic-aqueous, and aqueous-rich fluids. The aqueous-rich carbonic fluids, having 70-45% water, were initially entrapped in the Karakoram terrane. This aqueous phase was drained out from the aqueous-carbonic inclusions during the deformation and partial melting. Henceforth, the monophase pure carbonic (CO_2) fluid was predominantly present in the Trans-Himalayan rocks. The carbonic fluid derived from prograde decarbonization of the marl carbonate-rich rocks during metamorphism is associated with the subduction–collision tectonics.

The Karakorum rocks were unearthed from the deepest part of the crust (i.e., 1020 MPa at 670 °C) as well as speedily exhumed along the isothermal cooling path at 4.5 °C/km rate from 34 Km to 11 Km (i.e., 1020 MPa to 330 MPa) by losing 105 °C (670 to 565 °C) temperature following crustal thickening of the Asian continent (or South Tibetan Crust) between 18 and 15 Ma. The metamorphic rocks are syn-tectonically placed along with leucogranites along the Karakorum. This further implies that the Karakorum fault acted as a conduit for fluids. Thus, it can be suggested that the CO_2 throughout metamorphism might have been tracked from a deep-seated reservoir through the Karakorum fault.

Keywords: Fluid Inclusion, CO₂, Trans Himalaya, Exhumation

INTRODUCTION

The Indian and Asian plates collided during the Eocene period. This collision resulted in crustal thickening along the northern Indian plate margin and the southern Asian plate margin (forming the Hindu Kush, Karakoram Range) Zhao *et al.* (2010). The Himalaya were formed at the northern Indian margin, whereas Trans Himalaya (including the Hindu Kush mountain Range and the Karakoram mountain Range) was formed at the southern Asian margin (Fig. 1).

Fluids play a crucial role in nearly all crustal processes, facilitating the transport of heat and chemical components through their movement and circulation (Yardley & Shmulovich 1995). The water and pore fluid pressure influenced deformed crustal rocks (Gottardi & Hughes 2022). The mechanical processes for controlling rock deformation in the subduction zone are affected by pore fluid pressure (Vrolijk & Myers 1990; Jamtveit *et al.* 2019; Wang *et al.* 2020). Quite a few fluid sources, possibly, include internal fluids produced by metamorphic reactions and partial melting of the lower crust (Touret & Huizenga 2012). The tectonic origin of fluids has substantial roles in faulting, magma generation, hydrocarbon migration, minerals transport, and metamorphism (Oliver 1986; Miller 2013).

The Trans Himalayan terrane is well-conserved in the north of the Ladakh batholith (Fig. 1) (Thakur & Misra 1984; Thakur & Rawat 1992; Rolland 2002; Kharya 2015; Kharya et al. 2016; Sachan et al. 2016; Singh et al. 2020; Kumar et al. 2022). The Trans Himalayan rocks are mainly comprised of

Karakorum batholith, Karakorum metamorphic complex, and sediments. The calc-alkaline signature of the batholith is linked to the Tethyan subduction (ages ranging from 120±80 Ma, Searle et al. 1989). The Shyok Suture Zone (SSZ) lies north of the Ladakh batholith and indicates the subduction phase of the Neo-Tethyan oceanic crust beneath the Asian Paleozoic-Mesozoic platform (Srimal 1986; Rolland et al. 2000) (Fig. 1). The ophiolitic melanges in the Shyok suture zone consist of serpentinites, shales, limestones, and basic volcanic (Rolland et al. 2000). Continental sedimentation in the Shyok suture is characterized by Saltoro molasses, which comprises shales, sandstones, and conglomerates (Thanh et al. 2012). The southernmost margin of the Asian Plate is put adjacent to the Shyok Suture zone along the Karakorum shear zone, which mylonitises the Karakorum batholith (Jain & Singh 2008).

Here, we present a comprehensive synthesis of fluid flux in the Trans-Himalaya. This is the first-ever review for the role of fluids in the Trans-Himalaya in terms of metamorphic exhumation history and tectonics from our work, as well as previously published datasets. The current understanding of the Trans-Himalaya is assimilated into a reliable fluid progression that interpretations for the exhumation and tectonic history, in turn, bringing restraints on the Trans-Himalayan geodynamics.

GEOLOGICAL SETTING

The NW-SE trending Karakoram Range of the Trans-Himalaya extends ~700 km in length and 100-150 km in width, forming an arcuate belt between the Afghanistan–Pakistan border in the west and Tibet in the east (Fig. 1). It is bounded to the north by the Paleo-Tethyan Rushan–Pshart Suture Zone (RPSZ) and to the south by the Shyok Suture Zone (SSZ), which has been reactivated as a major Late Tertiary backthrust—the Main Karakoram Thrust (MKT) (Searle *et al.* 1987). Regional strain is accommodated through trans-tensional deformation along this zone (Searle *et al.* 1998; Valli *et al.* 2007). The western SSZ is marked by sinistral strike-slip faults, while its eastern boundary extends toward Afghanistan and Tajikistan (Buchroithner 1980; Tapponnier *et al.* 1981). The dextral Karakoram Fault defines the northeastern margin of the terrane.

The crustal thickness of 55 to 70 km combine to form a single coherent segment (e.g. crustal thickness vaies from 55 Km beneath Karakorum to 70 Km comparable to the Tibetan Plateau (Chen & Molnar 1983; Hirn *et al.* 1984; Krestnikov *et al.* 1984; Molnar 1984)). Further, Brandon & Romanowicz (1986); and Agius & Lebedev (2013) suggest the hot, Tibetan mantle lithosphere and asthenosphere. Caporali (2000) reported negative gravity anomalies († 500 mGal) and high heat flow from the Karakoram terrane, which indicate the deep roots of the Karakoram region.

The Karakoram terrane is divided into four units (south to north): 1) Karakoram Fault Zone (KFZ) characterized by diorite (hornblende-biotite), granite, and granodiorite; 2)

Karakoram Batholith (KB)/ Karakoram Plutonic Complex (KPC) containing monzogranite, two-mica granite (Baltoro/Hazan granite); 3) Karakoram Migmatites; 4) Karakoram Metamorphic Complex (KMC), comprised of garnet-staurolite schist, amphibolites, and marbles; (Sharma & Kumar 1978; Thakur & Virdi 1979; Rai 1995; Searle *et al.* 1998; Jain & Singh 2008; Mukherjee *et al.* 2012) (Fig. 1).

The northern margin of the Karakoram Range is the Karakoram Batholith, and the southern end is the Shyok Suture Zone (SSZ) or Main Karakoram Thrust (MKT), which is jointly known as Karakoram Metamorphic Complex (KMC). Metamorphic rocks are well-exposed in the Shyok, Pangong, and Tangse valleys (India), Baltoro (central Pakistan), and Hunza Valley (western Pakistan) (Zeitler 1985; Searle *et al.* 2010; Baig *et al.* 2022). The range consists predominantly of metapelites, metabasites, calc-silicates, orthogneisses, migmatites, granodiorites, and leucogranites (Desio 1964; Searle *et al.* 1989; Rolland *et al.* 2006a).

South-East Karkaoram Unit

The southeastern Karakoram plutonic complex is comprised of I- and S-type granodiorites (Reichardt *et al.* 2010). It is characterized by quartz monzonite-bearing granodiorites and garnet-bearing two-mica granite. To the east of this plutonic complex, KMC is exposed and consists of slate, schist, calc-silicate, amphibolite and greenschist facies, mylonite, augen gneisses, orthogneisses, migmatite, metapelites, metabasites,

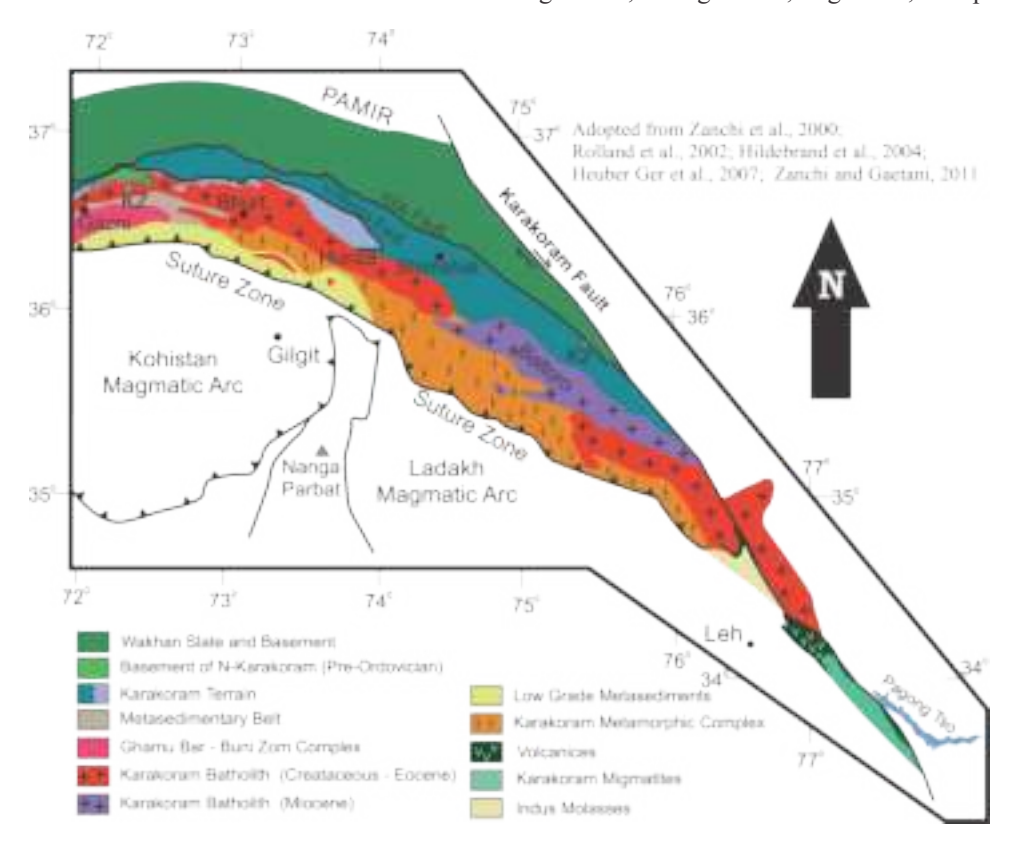


Fig. 1. Geological Map of the Trans Himalaya adopted from Adopted from Zanchi et al. (2000); Rolland (2002); Heuberger et al. (2007); Zanchi & Gaetani (2011).

and leucogranites and granodiorites (Phillips & Searle 2007). The U-Pb dating of the zircon from the metamorphic complex of this region suggested the maximum age of 131 Ma for the deposition of the sedimentary protolith and also reported the metamorphism age of 114 Ma, which is similar to the adjoining metapelites (Singh et al. 2020). This stage of metamorphosis corresponds to the well-known Cretaceous period of high pressure and heat within the active continental boundary of South Asia (Singh et al. 2020). Further, Schärer et al. (1990) advocate that the Karakoram leucogranites have two plutonism pulses at 25.5 + 0.3 - 0.8 and 21.4 + 0.3 - 0.6 Ma based on the U-Pb dating of zircon and monazite, and also suggest the Precambrian material in the magma source for the formation of the batholith. It was also suggested that the leucogranites cooled from 750-650°C at 25-21 Ma to 250-350°C at 6 Ma. After granite emplacement, their cooling through the Ar blocking temperature in mica and K-feldspar occurred from 15 to 20 Ma. The metamorphic grade in this region increases from biotite to sillimanite zone (Chaudhry 1983; Searle et al. 1998). The Karakoram fault is divided into two branches, namely 1) Tangtse strand (south-western) and 2) Pagong strand (north-eastern). The orthogneisses and amphibolites were intruded with extensive dike-sill networks in this region (Searle et al. 1998; Weinberg & Searle M 1998; Phillips et al. 2004; Weinberg & Mark 2008). A 10 Km wide Pagong Metamorphic Complex (PMC) has a sequence of Staurolite-bearing schists, meta-pelites, meta-psammites, meta-carbonates, and amphibolites. This metamorphic complex rapidly exhumed from ~31 km depth (8.5-9.5 Kbar) and 630-655 °C to 18 km depth (5.5-5.7 Kbar) and 620-630 °C (Singh et al. 2020). Whereas the migmatite rocks are well exposed in the Tangtse Gorge area. Which shows alternate leucocratic, mesocratic, and melanocratic layers. The newsome or leucocratic containing amphibole. The newcosome layers are melt-enriched components, whereas the paleosomes melt-depleted, residual components (Sawyer 2008). The Metatexite shows banding and newsomes diffused in the paleosomes (mafic layers), which folded as isoclinal folds. Whereas, metatextite represents parallels shear layering trimmed by leucogranite dyke. The migmatite was also rapidly exhumed from 33 km depth (8.5-10.2 Kbar) and 640-670 °C to 18 km (5.9-5.5 kbar) and 550-670 °C in a similar fashion to the metamorphic rocks of this area (Kumar et al. 2022).

Central Karkaoram Unit

The Baltoro Valley represents the central Karakoram (in northern Pakistan) which is mainly comprised of metabasites, orthogneisses, and amphibolite, intruded by leucogranitic dyke/veins. The zircon U-Pb age of orthogneiss from this region is 115-120 Ma (Searle $et\ al.$ 1990). Further, Ar-Ar hornblende analysis suggests a plateau age of 90.6 ± 1.8 Ma, indicating a mid-Cretaceous magmatism phase (Searle $et\ al.$ 1990). The Baltoro Karakoram Batholith is comprised of I-type granodiorites and monzogranites. It crystallized from 120 to 80 Ma (Rb–Sr whole rock; Debon $et\ al.$ 1987; Crawford & Searle 1992). The Baltoro Plutonic Unit (BPU) of the central Karakoram region is comprised of biotite-monzogranite and

garnet two-mica leucogranite, which crystallized at 25 -13 Ma (U–Pb zircon and monazite dating, Parrish, 1989; Schärer, 1990; Searle, 2010). The recent metamorphism episode and the crustal melting were observed in the Baltro region (the Bullah and Dassu gneiss domes), which is composed of sillimanite and K-feldspar- grade migmatites (Rolland *et al.* 2001; Rolland *et al.* 2006a; 2006b). U-Pb monazite age of this migmatite suggested the formation age 5.4 ± 0.2 to 6.7 ± 0.5 Ma (Smith 1993; Fraser *et al.* 2001), which exhumed from the maximum depth of about 25 km (4–7.5 kbar; Villa *et al.* 1996). These metamorphic rocks were extended from the MKT (south) to the BPU of the Karakoram Batholith (to the north), which shows the increase in metamorphic grade from the chlorite- to sillimanite-grade

U-Pb zircon, and K-Ar hornblend age of the Karakoram Batholith (Hushe gneisses) suggest the formation age between 200 and 145 Ma (Searle *et al.* 1989). Andalusite- and garnetbearing metapelites are associated with the gneisses of this region and formed by contact metamorphism with subduction of the Tethys Ocean (Searle *et al.* 1989; Searle & Tirrul 1991; Crawford & Searle 1992). The two main episodes of metamorphism were recorded in the metapelitic of this unit, which is very common throughout the complex. This Baltoro metamorphic complex (BMC) shows amphibolite facies Barrovian-type metamorphic, similar to the south-eastern Karakoram (from PMC). It suggests the peak P-T condition of 6-10 kbar and 650-700 C (Bertrand *et al.* 1988; Allen & Chamberlain 1991; Villa *et al.* 1996; Rolland *et al.* 2001) between 28-22±0.5 Ma (Fraser *et al.* 2001; Searle *et al.* 2010).

North-West Karkaoram Unit

The Hunza Valley represents the north-west Karakoram range, which juxtaposes various tectonic units. The metamorphic grade in this region increases northwards with age. The metamorphic complex is bound by the subduction-related Hunza Plutonic complex (HPC) to the north of the batholith. This plutonic complex is comprised of granodiorites and quartz diorites, which crystallized between 195 \pm 0.6 and 105.7 ± 0.6 Ma (U-Pb zircon age, U-Pb zircon age, Le Fort et al. 1983; Fraser et al. 2001). The monzogranite and leucogranite dykes were intruded at 52-50 Ma (Fraser et al. 2001). The plutonic complex and dyke were together deformed during the southward movement along the Hunza thrust, which associates with India-Asia continental collision. The 35 Ma dyke was undeformed and younger. It cut the plutonic and Hunza metamorphic complexes (HMC) to the south and indicates this region's minimum thrusting time. The sillimanite zone metamorphism has been reported from the norther part of the Hunza Valley, which divided into two sections: 1) upper sillimanite zone (consisting high-grade Kfeldspar bearing migmatitic) and 2) lower sillimanite zone (muscovite-bearing lower grade).

The upper sillimanite zone (USZ) juxtaposed against the lower sillimanite zone (LSZ) along the E–W trending thrust. U-Pb age of the palaeosome monazite from USZ is in the range of 82.9 ± 6.1 to 63.3 ± 0.4 Ma at 550 C, corresponding with the closure of the Shyok Suture (Fraser *et al.* 2001; Foster

et al. 2004). Whereas newsome monazite suggests the U-Pb age between 56.3 ± 0.3 and 53.4 ± 0.3 Ma from the Hunza Valley migmatites (Fraser et al. 2001; Foster et al. 2004). Whereas LSZ rocks metamorphosed at a younger time of 44.0 \pm 2.0 Ma (U-Pb monazite dating, Fraser et al. 2001) than the USZ metamorphism in this section. The kyanite-grade metamorphic rocks were also reported from this region (Palin et al. 2012). Younger staurolite-grade rocks that occurred on the Valley's southern side were metamorphosed at 16.0 ± 1.0 Ma (Fraser et al. 2001). The Sumayar granite intruded at about 9.3 ± 0.1 Ma (U-Pb uraninite, U-Pb uraninite, Fraser et al. 2001). This granite is associated with kyanite grade, which over-thrusting onto the staurolite grade (Crawford & Searle 1993).

RESULTS AND DISCUSSION

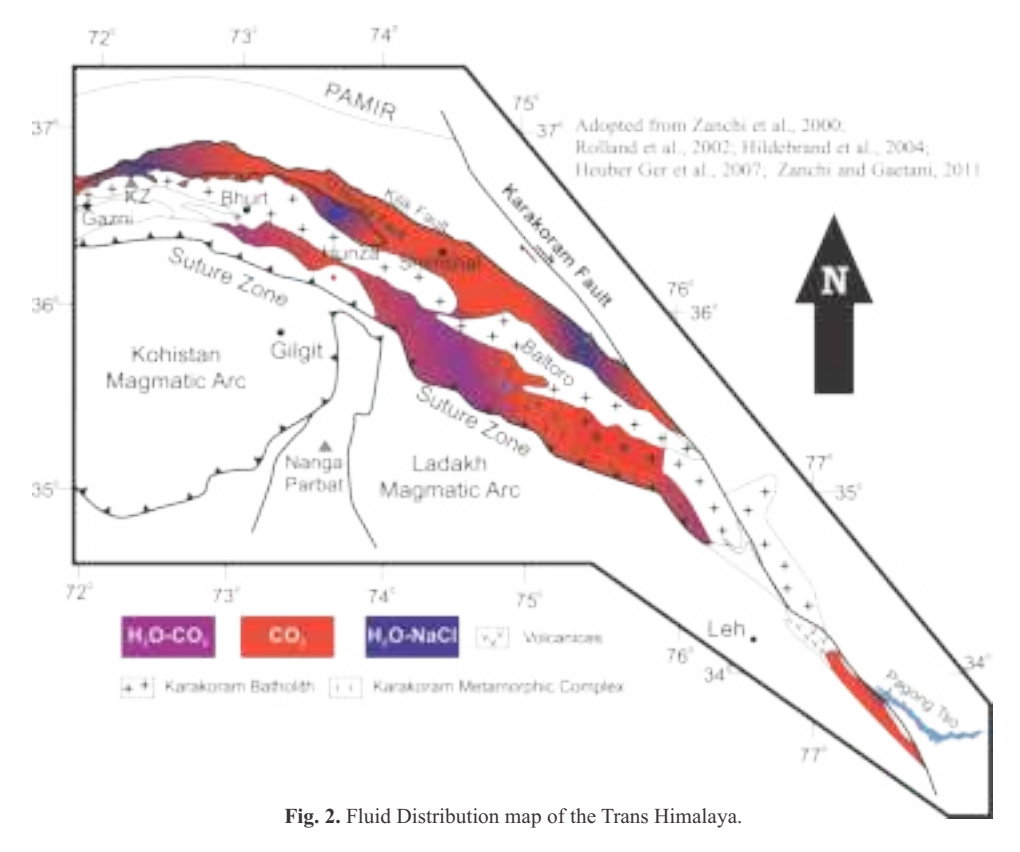
Fluids in Trans Himalaya

The fluid inclusion isochores for the various types of rocks have been recalculated for the entire Karakoram region using multiple programs. The isochore for two-phase aqueous (H₂O-NaCl) fluid inclusions is calculated using the Package FLUID 5: 'AqSo_NaCl' fluid program of Bakker (2019), and the modified Haar *et al.* (1984) equation of state (EoS) used for the calculation of isochores given by Bakker (2018). The two-phase aqueous-carbonic (H₂O-CO₂) inclusion isochores are drawn using the 'FLUID 1: Bulk and Isoc' program of Bakker (2003) and EoS used suggested by Duan *et al.* (1992, 1996). The isochores of monophase carbonic (CO₂) fluid inclusion are calculated using the 'Loner SpW' program and the EoS of Span and Span & Wagner (1996). The fluid inclusion data (i.e.,

eutectic temperature (Te); final ice melting temperature (Tm.ice); homogenization temperature (Th)) for the calculation of the isochores have been adopted from previous works done in Tangse, Pagong, Shyok, Baltoro, and Hunza Valley. The density in g/cm³) and molar volume (Vm in cm³/mol) have been calculated from the homogenization temperature (Th) of various fluid inclusions. Salinity for aqueous inclusions is calculated from the final ice melting temperature (Tm.ice) using the freezing point depression equation of H₂O-NaCl is given by Bodnar (1993). The aqueous and (or) aqueous-carbonic fluids, along with the pure carbonic fluid inclusions, are omnipresent throughout the trans-Himalaya. The fluid distrubation in karakoram range is shown in figure 2. The Fluid inclusion microthermometry data are summarized in table 1, bar diagram for the data set given in figure 3, and discussed below.

Role of Fluid for Crustal Deformation

Fluids of various concentrations and compositions are present throughout the lithosphere (Touret 2001). Fluids preserve the signature of the rock deformation through mechanical or chemical (rock-fluid interactions) processes. The tectonically induced fluid formed by dehydration, melting and degassing may be transported through fractures/fault zones from deeper sources. The syn-metamorphic rocks recorded high fluid flow due to increased porosity and permeability. The high fluid flow enhances hydrolytic fracture, weakening the mineral grain boundary and localized strain due to kinetic reactions in semi-brittle and ductile shear zones (Carter *et al.* 1990; Sibson 1994).



224

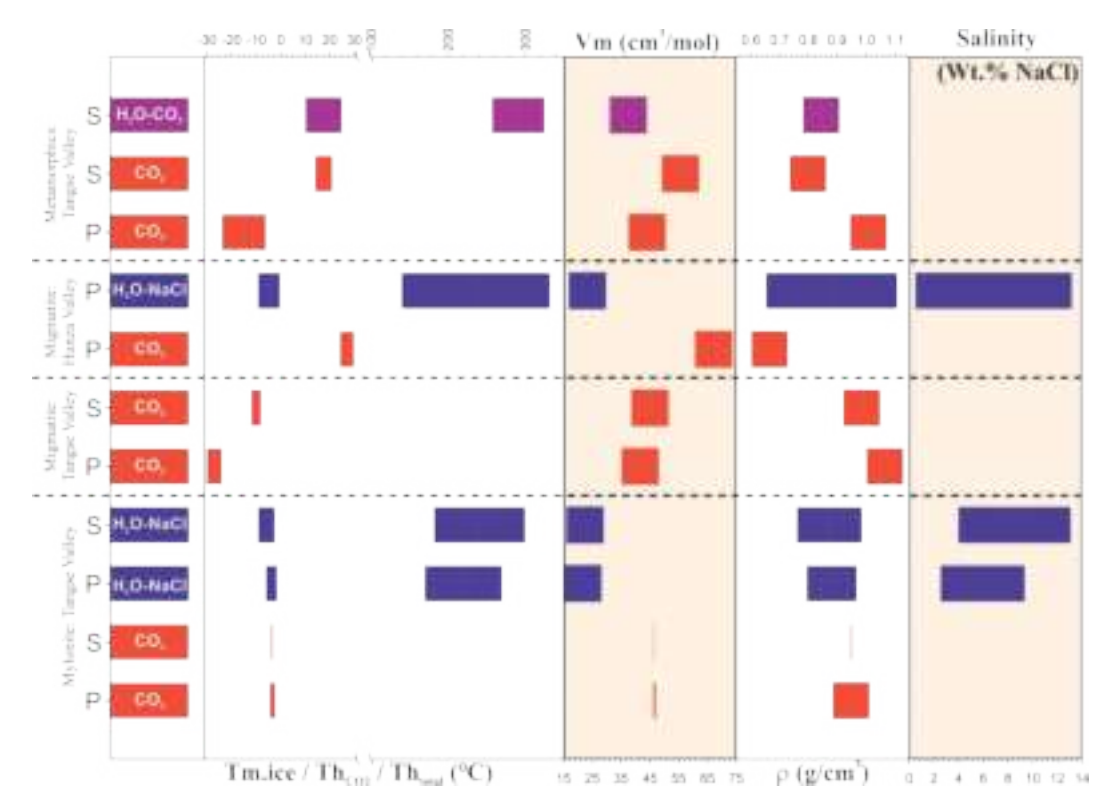


Fig. 3. Bar Diagram showing the micro-thermometry data [i.e. First ice melting temperature (Tm.ice), CO₂ homogenization temperature for aqueous-carbonic fluid (Th_{cox}), and Total homogenization temperature (Th_{total})] along with the molar volume (Vm), density (ρ), and Salinity.

The Mylonites are present in the Tangtse Valley of southeast Karakoram region in the Trans Himalava, Mylonite is strongly foliated and sheared hornblende-and mica-bearing granitoid, having well-developed NW-SE trending and steeply dipping ductile S-C shear fabric (Roy et al. 2010). These mylonites are quartzofeldspathic in nature. The presence of biotite, white mica, and chlorite are also noticed. It represents the crustal deformation in the Karakoram. Mukherjee et al. (2012) reported the occurrence of monophase and two-phase fluid inclusions in the Mylonites of this region. These monophase and two-phase inclusions are primary and secondary. The secondary fluid inclusions were formed due to the deformation of the host rock and were trapped in the fracture planes. The microthermometry measurement of these mylonites was carried out by Mukherjee et al. (2012) and suggests the eutectic temperature of the primary and secondary monophase inclusions -56.5 ± 0.5 °C (indicating CO, fluid; Goldstein 1994). Where, two-phase inclusion shows the eutectic temperature for both primary and secondary fluids was -21.6 ± 0.8 °C, suggesting H₂O-NaCl \pm KCl (see Fig. 2).

The primary monophase carbonic (CO₂) inclusions homogenized between -4.5 and -2.0 °C, and secondary monophase carbonic (CO₂) inclusions homogenized from -4 to -3.2 °C. The molar volume (Vm) of carbonic (CO₂) inclusions ranges from 46.9 to 46.2 cm³/mol and 46.5 to 46.3 cm³/mol of primary and secondary fluids, respectively. The primary and secondary carbonic (CO₂) fluid densities are in

ranges of 0.939 to 0.953 g/cm³ and 0.946 to 0.951 g/cm³, respectively (see Table 1, and Fig. 3).

The two-phase inclusions show the final ice melting temperature (Tm.ice) of the primary fluid between -6.1 and -1.5 °C, corresponding to the fluid's salinity between 9.34 and 2.57 Wt. % NaCl. The homogenization temperature (Th) ranges from 170 to 270 °C, corresponding to the molar volume (Vm) of 19.9 to 23.1 cm³/mol and density of 0.968 to 0.794 g/cm³. The secondary two-phase inclusions show Tm.ice between -9.2 and -2.4 °C, having 13.07 to 4.03 Wt. % NaCl salinity. These secondary two-phase inclusions were homogenized between 182 and 300 °C with a molar volume (Vm) of 20.1 to 24.4 cm³/mol and 0.985 to 0.760 g/cm³ density (see Table 1, and Fig. 3).

The primary monophase carbonic (CO₂) fluids were entrapped at the maximum depth of ~14 km in mylonites at 610 °C and 436 MPa. The two-phase aqueous (H₂O-NaCl) fluids were entrapped at 335 °C and 300 MPa (~10 Km depth). This study of secondary fluid inclusions suggests that the rocks in the Karakoram region of the trans-Himalaya were deformed and mylonitized a maximum depth of 8 Km at 323 °C and 246 MPa (Fig. 4A). These mylonites were exhumed gradually to the surface from the maximum depth of ~14 km (i.e., 436 MPa) following the isochoric cooling path. The fluids in Karakoram mylonites started entrapped in the amphibolite phase and continued up to the greenschist phase (see Fig. 4A).

Table 1. Fluid Inclusion Micro-thermometry results along with re-calculated data set to draw the isochores for this study.

tion		Fluid Type		stem		THCOZ C C C Olume :m³/mol wity wity %NaCl	Maximum Fluid Entrapment Condition			Mineral P-T Condition		logical ference								
Location	Litho Unit	Mode of occurr	Fl Comp	uid oosition	Tm.ice / *Th _{C02}	Th in °C	Molar Volume (Vm) in cm³/mol	Density (p) in g/cm ³	Salinity in Wt. %NaCl	Pressu re (Kbar	Temp.	Depth (Km)	Fluid Inclusion Data Reference	Pressu re (Kbar	Temp.	Minerological data reference				
Tangse Valley		Primary	Carbonic	CO,	N/A	-3.3 ±1.2	46.6 ±0.4	0.946 ±0.007	N/A	4.4	610	14.0								
	se	Secondary	Carbonic	<i>C0</i> 2	N/A	-3.6 ±0.4	46.4 ±0.1	0.949 ±0.003	N/A	2.5	323	8.0	ıl. (2012)							
	Mylonites	Primary	Aqueous	H ₂ O-NaCl H ₂ O-NaCl	-3.8 ±2.3	220 ±50	21.5 ±1.6	0.881 ±0.087	5.96 ±3.39	3.0	335	10.0	Mukherjee et al. (2012)	lukherjee et a	-	-	1			
		Secondary	Aqueous	H2O-NaCl	-5.8 ±3.4	241 ±59	22.3 ±2.2	0.873 ±0.113	8.55 ±4.53	2.5	323	8.0								
		Presumed Primary	Aqueous- Carbonic	H20-CO2	-30	-	-	-	-	10.2	670	34.0				122)				
Tangse Valley	Migmatite	Primary	Carbonic	CO ₂	N/A	-27 ±3	41.4 ±0.5	1.063 ± 0.013	N/A	5.9	640	19.5	Kumar et al. (2022)	8.5 to 10.2	640 to 670	Kumar et al. (2022)				
T		Secondary	Carbonic	<i>CO</i> ²	N/A	-10 ±2	44.8 ±0.5	0.983 ± 0.010	N/A	-	-	-	Kumar et			Kun				
		Presumed Primary	Aqueous- Carbonic	H20-CO2	27	-	-	-	-	8.0	670	26.5		7.4 to		12)				
Hunza Valley	Migmatite	Primary	Carbonic	CO,	N/A	27 ±2.9	67 ±6.2	0.663 ±0.061	N/A	2.1	545	6.5	(2022)		640 to 660	Palin et al. (2012)				
4		Primary	Aqueous	H ₂ O- NaCl	-4.8 ±4.5	236 ±96	23.1 ±4.6	0.881 ± 0.228	6.85 ±6.32	2.1	545	6.5	Baig et al. (2022)			Pal				
		Presumed Primary	Aqueous- Carbonic	H,0-CO,	-15	-	-	-	-	9.5	655	31.5			630 to 655	Searle et al., 2010; al., 2009				
Tangse Valley	Complex	Primary	Carbonic	CO,	N/A	-15 ±9	43.8 ±1.9	1.006 ± 0.044	N/A	6.0	650	20.0	. (2020)	8.5 to 630		achan et al., 2016; '				
	Metamorphic Complex	Secondary	Carbonic	<i>C0</i> ,	N/A	17.5 ±3.5	55.4 ± 2.4	0.796 ± 0.034	N/A	2.4	455	8.0	Sachan et al. (2016) and Singh et al. (2020)	9.5		Fraser et al., 2001; Palin et al., 2012; Sachan et al., 2016; Searle et Searle et al., 1989; Singh et al., 2020; Streule et al., 2009				
		Secondary	Aqueous- Carbonic	H ₂ O-CO ₂	17.5 ±7.5	291 ±34	37.3 ±1.8	0.842 ±0.057	N/A	2.4	455	8.0	Sachan et al. (20					Fraser et al., 2001; Searle et		
*Th _{CO2} : Only for the aqueous-carbonic fluid																				

Role of Fluid in Partial Melting of crust

The crustal anatexis plays a significant role during the continental—continental collision tectonics, influencing the orogenic crust rheology (Brown 2001; Foster *et al.* 2001; Whitney *et al.* 2003; Vanderhaeghe 2009). Various geophysical studies carried out by Nelson *et al.* (1996), Unsworth *et al.* (2005), and Caldwell *et al.* (2009) advocate that melt was present in the intermediate part of the crust in the Tibetan Plateau. The crust was weakening due to the melts at and around the grain boundary, and melts may have increased the deformation processes (Sawyer 1999; Rey *et al.* 2001; Vanderhaeghe & Teyssier 2001a; b; Rosenberg & Handy 2005). This melt can be increased due to fluid flux melting by the external source of water (Weinberg & Hasalová 2015).

The partial melting is widely known in the Higher Himalaya and Trans Himalaya (Karakoram Region) in the Himalayan mountain chain from India and Pakistan which is marked by the presence of migmatites in the Himalayan terrane and is reported from the trans-Himalaya by several workers (Searle *et al.* 1989; Searle *et al.* 1998; Weinberg & Searle M 1998; Weinberg *et al.* 2000; Palin *et al.* 2012; Sen *et al.* 2018; Baig *et al.* 2022; Kumar *et al.* 2022).

In this study, we focused on the trans-Himalaya and examined the Tangse Valley migmatite (India) from south-east Karakoram and the Hunza Valley migmatite (Pakistan) from north-west Karakoram. Fluid inclusion research on the migmatites of the Tangse and the Hunza Valley was conducted by Kumar *et al.* (2022) and Baig *et al.* (2022), respectively. Kumar *et al.* (2022) documented the occurrence of both primary and secondary monophase carbonic inclusions exclusively from the Tangse region. In contrast, Baig *et al.* (2022) noticed the presence of primary monophase carbonic (CO₂) and two-phase aqueous (H₂O-NaCl) inclusions in migmatites from the Hunza Valley.

The Tangse and Hunza Valley monophase carbonic fluid shows a eutectic temperature of -56.6 \pm 0.4 °C, suggesting pure CO₂ (Mukherjee et al. 2012; Sachan et al. 2016; Singh et al. 2020; Baig et al. 2022; Kumar et al. 2022). Furthermore, primary monophase carbonic fluid of Tangse Valley were homogenized between -30 and -24 °C, having a molar volume (Vm) of 41.4 ± 0.5 cm³/mol and 1.063 ± 0.013 g/cm³ density. Whereas, the Hunza Valley primary monophase carbonic fluid was homogenized between 29.8 and 24.1 °C, which shows very high molar volume (73.1 to 60.8 cm³/mol) and very low density (0.602 to 0.724 g/cm³) related to the Tangse Valley migmatites (see Table 1, and Fig. 3). The secondary monophase carbonic fluid from the migmatites of the Karakoram region was reported by Kumar et al. (2022), which homogenized at -10 \pm 2 °C with 44.8 \pm 0.5 cm³/mol molar volume and 0.983 ± 0.010 g/cm³ density. The two-phase primary aqueous inclusions were also noticed by Baig et al. (2022) from the Hunza Valley migmatite of the Karakoram region, which shows that the final ice melting temperature between -9.3 and -0.3 °C corresponds to the salinity between 28.98 and 0.53 Wt. % NaCl. These two-phase inclusions show the homogenization temperature between 140 and 332 °C, having a molar volume of $23.1 \pm 4.6 \text{ cm}^3/\text{mol}$ and $0.881 \pm 0.228 \text{ g/cm}^3$ density (see Table 1, and Fig. 3). The thermodynamic modeling of the Karakoram migmatites was carried out by Kumar *et al.* (2022) from the south-east Karakoram (Tangse Valley, India) and Palin *et al.* (2012) from north-west Karakoram (Hunza Valley, Pakistan) suggested peak *P-T* conditions of 670-640 °C at 850-1020 MPa and 660-640 °C at 740-800 MPa, respectively (Fig. 4B).

The fluid inclusion isochores of south-east Karakoram (Tangse Valley, India) shown in figure 4B, which could not intersect the peak P-T field given by Kumar et al. (2022) and lies at a lower P-T space. Further, it was presumed by Kumar et al. (2022) that the two-phase aqueous-carbonic (H₂O-CO₂) fluid was initially present in the system at the time of entrapment, which contains about 45% water. These twophase aqueous-carbonic fluids intersect the peak P-T condition. However, the two-phase aqueous-carbonic fluid is not present in the system due to the preferential leaching of the aqueous phase from the system and goes into the melt during anatexis. Henceforth pure carbonic (CO₂) inclusions remained in the system. The combined thermodynamic modeling and fluid inclusion study of the south-east Karakoram (Tangse Valley, India) suggests that the migmatites of this region were exhumed from ~ 34 Km to 17 Km depth (i.e., 1020-500 MPa) rapidly following an initial isothermal cooling path (with a drop of 50 °C). Further, it gradually exhumed to the surface from 17 Km depth (i.e. 500 MPa and 610 °C) following an isochoric cooling path.

The fluid inclusion isochore of north-west Karakoram migmatites from Humza Valley is shown in figure 4C. It preserves two-phase aqueous and low-density monophase carbonic fluid inclusions, intersecting aqueous fluid between 550 and 186 °C at 206 – 50 MPa. The aqueous and/or carbonic isochores are not cross-cut the peak *P-T* condition of the Hunza Valley of 660-640 °C at 740-800 MPa (Palin *et al.* 2012). Palin *et al.* (2012) suggested that these migmatites were melted due to the excess H₂O present in the system. Therefore, we presumed that aqueous-carbonic (H₂O-CO₂) inclusions were initially present in the host rock. These two-phase aqueous-carbonic inclusions were rich in the aqueous phase (~70 %) (figure 4C).

The aqueous phase was segregated from the inclusions and subsequently released into the melt, resulting in the absence of aqueous-carbonic inclusions in the Hunza Valley migmatite. Palin *et al.* (2012) reported the presence of excess H₂O in melt and considered it in the thermodynamic modeling of this area. This excess H₂O was derived, which originated from the internal sources of the fluid inclusions. Additionally, these migmatites exhibit an initial isothermal decompression-driven cooling path ~26 Km to ~6.5 Km, followed by an isochoric cooling path from ~6.5 Km to the surface. This P–T evolution closely parallels that documented in the southeastern Karakoram migmatites of the Tangtse Valley, India

Migmatites from both the southeastern (Tangtse Valley, India) and northwestern (Hunza Valley, Pakistan) regions of

the Karakoram terrane show evidence of exhumation along an isothermal cooling path. This is indicated by the presence of various re-equilibrated fluid inclusion microtextures, such as 'C' shape, and 'hooked' shape inclusions (Baig et al. 2022; Kumar et al. 2022). Thermodynamic modeling suggests that migmatization temperatures ranged between 640 and 670 °C (Palin et al. 2012; Kumar et al. 2022). The host rocks of these migmatites contain aqueous-carbonic fluid inclusions, comprising 45-70% aqueous phase by volume (Fig. 4). During the process of anatexis, the aqueous component was selectively removed, facilitating partial melting and resulting in an excess of H₂O in the melt. As a result, both migmatite suites exhibit elevated H₂O content. Their exhumation occurred rapidly, with a temperature decrease of approximately 70 °C and H₂O loss from a maximum depth of around 34 km (~1020 MPa, 670 °C) to about 10 km (~300 MPa 600 °C), followed by continued decompression to the surface (Figs. 4 B&C).

Role of Fluid in Metamorphic Complex

Metamorphic rocks are prominently exposed throughout the entire northwest-southeast-trending Karakoram Range, which extends from Tangtse in the southeast to Hunza in the northwest, aligning with the magmatic arc. These rocks have undergone upper amphibolite facies conditions, as evidenced by the presence of key index minerals such as kyanite and sillimanite (Searle et al. 1989; Fraser et al. 2001; Streule et al. 2009; Searle et al. 2010; Palin et al. 2012; Sachan et al. 2016; Singh et al. 2020). The peak metamorphic conditions reached approximately 950-850 MPa at temperatures ranging from 630 to 655 °C, with retrograde paths indicating conditions of 570-550 MPa at 630-620 °C (Singh et al. 2020). The metapelites in this region is relatively low, 800-show lower pressure-temperature ranges: 800-300 MPa at 650-565 °C (Sachan et al. 2016) and 725-605 MPa at 605-585 °C (Streule et al. 2009). These metamorphic assemblages, particularly amphibolites and metapelites, constitute the Karakoram Metamorphic Complex (KMC).

Fluid inclusion studies in the Karakoram Metamorphic Complex (KMC), particularly in the southeastern region encompassing the Pangong-Tso and Tangtse Valley in India, have been explored by Sachan *et al.* (2016) and Singh *et al.* (2020). These studies have identified both primary and secondary monophase carbonic inclusions within amphibolites and metapelites, characterized by eutectic temperatures ranging from –56.9 to –56.6 °C, indicative of pure CO₂ compositions. Additionally, amphibolites are found to contain secondary two-phase aqueous—carbonic inclusions that exhibit similar eutectic temperatures, suggesting the presence of H₂O–CO₂ fluid mixtures (Singh *et al.* 2020).

Primary carbonic inclusions demonstrate homogenization temperatures between -24 and -6 °C, with molar volumes of 43.8 ± 1.9 cm³/mol and densities of 1.006 ± 0.044 g/cm³ (Table 1, and Fig. 3). In contrast, secondary carbonic inclusions have lower densities and homogenize at temperatures ranging from 14 to 21 °C, exhibiting molar volumes of 55.4 ± 2.3 cm³/mol and densities of 0.796 ± 0.034

g/cm³ (refer, Table 1, and Fig. 3). Secondary aqueous-carbonic inclusions show carbonic-phase homogenization (ThCO $_2$) between 10 and 25 °C, with overall homogenization temperatures (Th) ranging from 257 to 325 °C (Table 1, and Fig. 3). The similarity in Th CO $_2$ values between monophase and two-phase inclusions indicates their coeval development during metamorphism.

The notable absence of primary two-phase aqueous-carbonic inclusions is interpreted as a result of selective H₂O loss during deformation, with the fluid components likely incorporated into hydrous minerals within the amphibolites. Singh *et al.* (2020) suggested that a primary H₂O–CO₂ fluid was initially trapped, undergoing subsequent modifications during the processes of deformation and metamorphism.

P-T estimates indicate that the KMC experienced exhumation along an isothermal decompression-driven cooling path from approximately 31.5 km depth (950 MPa, 655 °C) to around 11 km (330 MPa, 565 °C), corresponding to a rapid exhumation rate of about 4.4 °C/km-significantly steeper than the average geothermal gradients recorded in the Himalayas (Fig. 4D). This exhumation was followed by an isochoric cooling path to the surface, underscoring a complex exhumation history intertwined with fluid evolution related to deformation and partial melting processes.

Role of Fluid for the Exhumation of the Tibetan Plateau

The ~700 km-long Karakoram terrane is characterized by a complex variety of lithological units, including batholiths, migmatites, mylonites, metapelites, and high-grade metamorphic rocks. These units have undergone amphibolite facies metamorphism, as extensively documented by various previous studies (Streule *et al.* 2009; Mukherjee *et al.* 2012; Palin *et al.* 2012; Reichardt & Weinberg 2012; Sachan *et al.* 2016; Singh *et al.* 2020; Kumar *et al.* 2022).

Migmatites demonstrate the most significant evidence of deep exhumation, with peak conditions approximately 1020 MPa and 670 °C, indicative of lower crustal environments (Figs. 2B–C). In contrast, other metamorphic rocks show exhumation occurring from about 950 MPa at 630 °C (Fig. 4D), while mylonites indicate shallower crustal exhumation at roughly 436 MPa and 610 °C (Fig. 4A).

Fluid inclusion results throughout the Karakoram terrane reveal that the initial metamorphic fluids were primarily aqueous—carbonic (H_2O - CO_2) in composition, with H_2O constituting 45-70% of the fluid volume, while CO_2 accounted for the remainder (Fig. 4). These fluids were initially trapped as two-phase H_2O - CO_2 inclusions within the host lithologies. However, during deformation and anatexis, there was a progressive loss of the H_2O phase, resulting in a predominance of monophase carbonic inclusions (CO_2 -rich) throughout the terrane.

In the migmatites, the H₂O phase was incorporated into the melt during the anatexis process, promoting enhanced partial melting. In contrast, in other metamorphic units, aqueous (H₂O) components became integrated into hydrous

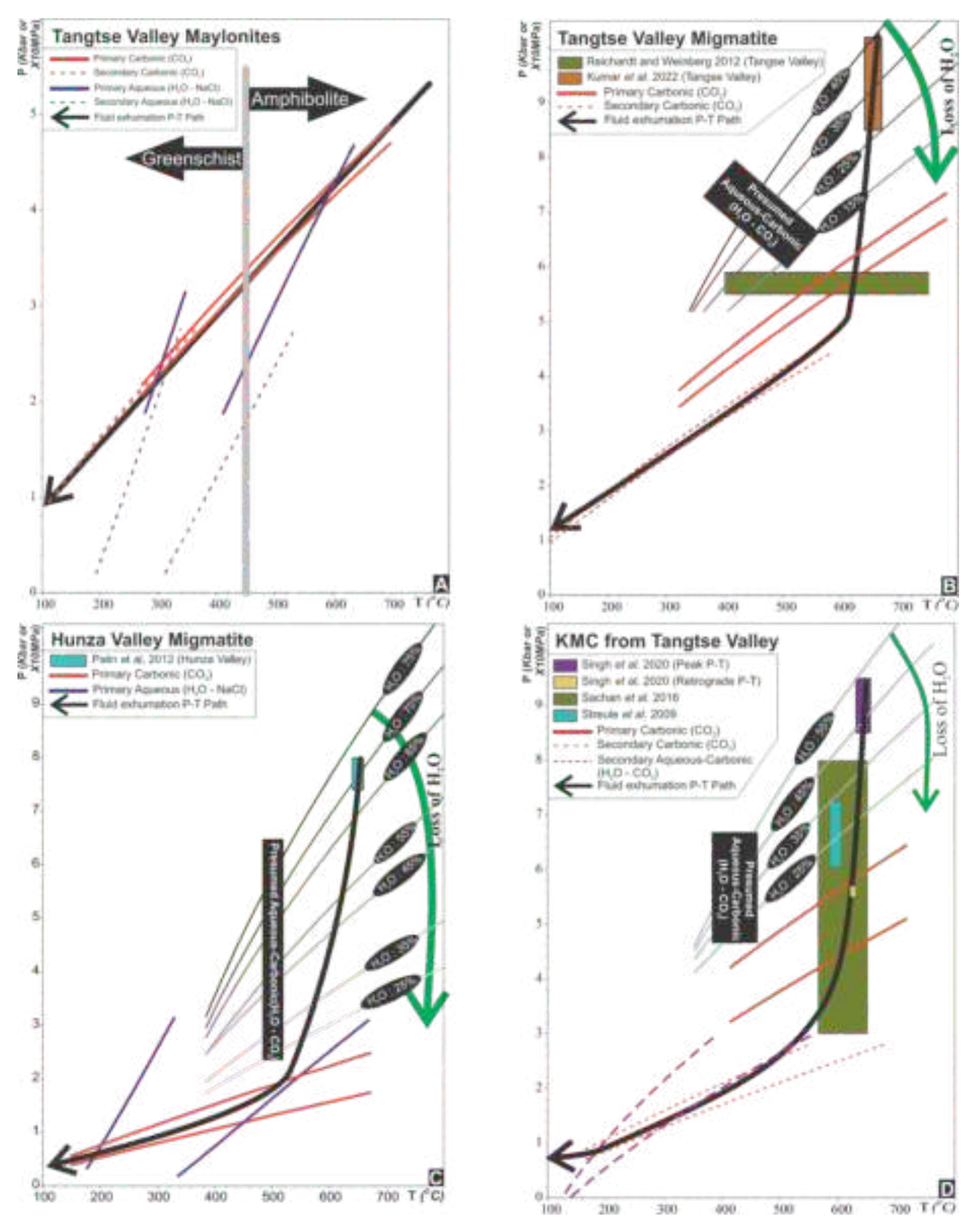


Fig. 4. Recalculated Fluid Inclusion (FI) isochores of the various fluid present in the Trans-Himalaya along with the mineral PT dataset; SLV: Solid-Liquide-Vapor line of the Aqueous fluid; T: Temperature in deg Celcius (°C); P: Pressure in Kilo Bar (Kbar) and Mega Pascal (MPa). (A) FI isochores of the fluid present in the Trans-Himalayan Maylonites. (B) FI isochore of the fluid present in the Eastern Karakoram (Tangtse Valley, India) Migmatite of Trans-Himalaya. (C) FI isochore of the fluid present in the Western Karakoram (Hunza Valley, Pakistan) Migmatite of Trans-Himalaya. (D) FI isochore of the fluid in the Karakoram Metamorohic Complex or Trans-Himalayan metamorphic rocks.

mineral phases during ductile deformation, particularly within amphibolites and metapelites (Figs. 4B–C).

The Karakoram terrane underwent rapid exhumation along an isothermal decompression-driven cooling path, with a calculated cooling rate of approximately 4.5 °C/km based on fluid inclusion data (Table 1, Figs. 3, 4). This exhumation path spans depths from ~34 km (1020 MPa, 670 °C) to ~11 km (330 MPa, 565 °C), corresponding to a temperature reduction of about 105 °C (Figs. 4B–D). Following this, exhumation continued along an isochoric cooling trajectory to the surface (Figs. 4A–D). Notably, this initial cooling rate is significantly steeper than the average Himalayan geothermal gradient, estimated at ~90 °C/km (Chandrasekharam 2000), highlighting the tectonothermal uniqueness of the Karakoram exhumation regime.

CONCLUSION

The first detailed review, recalculation and reinterpretation of fluid-inclusion data of igneous, metamorphic and mylonitized rocks from Trans-Himalaya. The following are the inferences drawn from this study.

- The Karakoram Migmatites and metamorphic rocks were initially formed with two-phase aqueous-rich carbonic fluid.
- The rocks of eastern Karakoram consist of about 45-55% water in the aqueous-carbonic fluid. Concomitantly, the western Karakoram rocks comprised ~70% water in an aqueous-carbonic fluid.
- These aqueous phases were preferentially drained out from aqueous-carbonic fluid inclusions during anatexis and metamorphism. This aqueous phase went to the hydrous minerals from the aqueous-carbonic fluid inclusion due to preferentially drained out the aqueous phase after marl carbonate-rich rocks.
- The pure carbonic (CO₂) fluid largely occurs in the Trans Himalaya, which may be derivative from prograde decarbonization of the marl carbonate-rich rocks.
- The Trans-Himalaya were rapidly exhumed from the innermost part of the crust along the isothermal cooling path from the maximum depth of 34 Km (i.e. 1020 MPa) resulting in the thickening of the South Tibetan Crust between 18 and 15 Ma.
- Karakorum fault acted as a carbon conduit in the form of carbonic (CO₂-rich) fluid throughout the metamorphic process.

Acknowledgements: The authors are thankful to the Director, Wadia Institute of Himalayan Geology, Dehra Dun, for providing lab facilities and encouragement to carry out this work. The authors are also thankful to Prof. Talat Ahmad for providing necessary inputs to improve the Manuscript. AK and HKS gratefully acknowledge financial support from the SERB (Grant # CRG/2022/000341 and CRG/2020/000022) for this work.

References

- Agius, M.R., Lebedev, S. 2013. Tibetan and Indian lithospheres in the upper mantle beneath Tibet: Evidence from broadband surface-wave dispersion. *Geochemistry, Geophysics, Geosystems*, **14**(10), 4260-4281. doi: 10.1002/ggge.20274
- Allen, T., Chamberlain, C.P. 1991. Metamorphic evidence for an inverted crustal section, with constraints on the Main Karakorum Thrust, Baltistan, northern Pakistan. *Journal of Metamorphic Geology*, **9**(4), 403-418. doi: 10.1111/j.1525-1314.1991.tb00535.x
- Baig, S.S., Xue, C., Akhter Qureshi, J., Hussain, A., Alam, M., Khan, G., Hussain, S.A. 2022. Fluid Inclusion Study Of Karakoram Metamorphic Complex Hunza Valley, Pakistan. *Bahria University Research Journal* of Earth Sciences, 6, 40-45. doi:
- Bakker, R.J. 2003. Package FLUIDS 1. Computer programs for analysis of fluid inclusion data and for modelling bulk fluid properties. *Chemical Geology*, **194**(1), 3-23. doi: 10.1016/S0009-2541(02)00268-1
- Bakker, R.J. 2018. AqSo_NaCl: Computer program to calculate p-T-V-x properties in the H2O-NaCl fluid system applied to fluid inclusion research and pore fluid calculation. *Computers & Geosciences*, 115, 122-133. doi: 10.1016/j.cageo.2018.03.003
- Bertrand, J.-M., Kienast, J.-R., Pinardon, J.-L. 1988. Structure and metamorphism of the Karakorum gneisses in the Braldu-Baltoro Valley (North Pakistan). *Geodinamica Acta*, **2**(3), 135-150. doi: 10.1080/09853111.1988.11105162
- Bodnar, R.J. 1993. Revised equation and table for determining the freezing point depression of H2O-Nacl solutions. *Geochimica et Cosmochimica Acta*, **57**(3), 683-684. doi: 10.1016/0016-7037(93)90378-A
- Brandon, C., Romanowicz, B. 1986. A "no-lid" zone in the central Chang-Thang platform of Tibet: Evidence from pure path phase velocity measurements of long period Rayleigh waves. *Journal of Geophysical Research: Solid Earth*, 91(B6), 6547-6564. doi: 10.1029/JB091iB06p06547
- Brown, M. 2001. Orogeny, migmatites and leucogranites: A review. *Journal of Earth System Science*, **110**(4), 313-336. doi: 10.1007/BF02702898
- Buchroithner, M.F. 1980. An outline of the geology of the Afghan Pamirs. *Tectonophysics*, **62**(1), 13-35. doi: 10.1016/0040-1951(80)90072-4
- Caldwell, W.B., Klemperer, S.L., Rai, S.S., Lawrence, J.F. 2009. Partial melt in the upper-middle crust of the northwest Himalaya revealed by Rayleigh wave dispersion. *Tectonophysics*, 477(1), 58-65. doi: 10.1016/j.tecto.2009.01.013
- Caporali, A. 2000. The gravity field of the Karakoram Mountain Range and surrounding areas. *Geological Society, London, Special Publications*, 170(1), 7-23. doi: 10.1144/GSL.SP.2000.170.01.02
- Carter, N.L., Kronenberg, A.K., Ross, J.V., Wiltschko, D.V. 1990. Control of fluids on deformation of rocks. *Geological Society, London, Special Publications*, 54(1), 1-13. doi: 10.1144/GSL.SP.1990.054.01.01
- Chandrasekharam, D. 2000. Geothermal energy resources of India: country update.
- Chen, W.-P., Molnar, P. 1983. Focal depths of intracontinental and intraplate earthquakes and their implications for the thermal and mechanical properties of the lithosphere. *Journal of Geophysical Research: Solid Earth*, **88**(B5), 4183-4214. doi: 10.1029/JB088iB05p04183
- Crawford, M.B., Searle, M.P. 1992. Field relationships and geochemistry of pre-collisional (India-Asia) granitoid magmatism in the central Karakoram, northern Pakistan. *Tectonophysics*, 206(1), 171-192. doi: 10.1016/0040-1951(92)90375-G
- Crawford, M.B., Searle, M.P. 1993. Collision-related granitoid magmatism and crustal structure of the Hunza Karakoram, North Pakistan. *Geological Society, London, Special Publications*, **74**(1), 53-68. doi: 10.1144/GSL.SP.1993.074.01.05
- Debon, F., Le Fort, P., Dautel, D., Sonet, J., Zimmermann, J.L. 1987. Granites of western Karakorum and northern Kohistan (Pakistan): A composite mid-cretaceous to upper cenozoic magmatism. *Lithos*, 20(1), 19-40. doi:10.1016/0024-4937(87)90022-3
- Desio, A. 1964. On the geological ages of some granites of the Karakoram-Hindukush and Badakhashan (Central Asia), 22nd International Geological Congress, New Delhi, pp. 479-496.

- Duan, Z., Møller, N., Greenberg, J., Weare, J.H. 1992. The prediction of methane solubility in natural waters to high ionic strength from 0 to 250°C and from 0 to 1600 bar. Geochimica et Cosmochimica Acta, 56(4), 1451-1460. doi: 10.1016/0016-7037(92)90215-5
- Duan, Z., Møller, N., Weare, J.H. 1996. A general equation of state for supercritical fluid mixtures and molecular dynamics simulation of mixture PVTX properties. *Geochimica et Cosmochimica Acta*, 60(7), 1209-1216. doi: 10.1016/0016-7037(96)00004-X
- Foster, D.A., Schafer, C., Fanning, C.M., Hyndman, D.W. 2001. Relationships between crustal partial melting, plutonism, orogeny, and exhumation: Idaho–Bitterroot batholith. *Tectonophysics*, **342**(3), 313-350. doi: 10.1016/S0040-1951(01)00169-X
- Foster, G., Parrish, R.R., Horstwood, M.S.A., Chenery, S., Pyle, J., Gibson, H.D. 2004. The generation of prograde P-T-t points and paths; a textural, compositional, and chronological study of metamorphic monazite. *Earth and Planetary Science Letters*, 228(1), 125-142. doi: 10.1016/j.epsl.2004.09.024
- Fraser, J.E., Searle, M.P., Parrish, R.R., Noble, S.R. 2001. Chronology of deformation, metamorphism, and magmatism in the southern Karakoram Mountains. *GSA Bulletin*, **113**(11), 1443-1455. doi: 10.1130/0016-7606(2001)113<1443:CODMAM>2.0.CO;2
- Goldstein, H.R. 1994. Systematics of fluid inclusions in diagenetic minerals. SEPM Short Course, 31, 199. doi:
- Gottardi, R., Hughes, B. 2022. Role of fluids on deformation in mid-crustal shear zones, Raft River Mountains, Utah. *Geological Magazine*, **159**(11-12), 2206-2218. doi: 10.1017/S0016756822000231
- Haar, L., Gallagher, J.S., and Kell, G.S. 1984. NBS/NRC steam tables. Hemisphere Publishing Corporation, Washington, Washington.
- Heuberger, S., Schaltegger, U., Burg, J.-P., Villa, I.M., Frank, M., Dawood, H., Hussain, S., Zanchi, A. 2007. Age and isotopic constraints on magmatism along the Karakoram-Kohistan Suture Zone, NW Pakistan: evidence for subduction and continued convergence after India-Asia collision. Swiss Journal of Geosciences, 100(1), 85-107. doi: 10.1007/s00015-007-1203-7
- Hirn, A., Lepine, J.-C., Jobert, G., Sapin, M., Wittlinger, G., Zhong Xin, X., En Yuan, G., Xiang Jing, W., Ji Wen, T., Shao Bai, X., Pandey, M.R., Tater, J.M. 1984. Crustal structure and variability of the Himalayan border of Tibet. *Nature*, 307(5946), 23-25. doi:10.1038/307023a0
- Jain, A.K., Singh, S. 2008. Tectonics of the southern Asian Plate margin along the Karakoram Shear Zone: Constraints from field observations and U-Pb SHRIMP ages. *Tectonophysics*, 451(1), 186-205. doi: 10.1016/j.tecto.2007.11.048
- Jamtveit, B., Petley-Ragan, A., Incel, S., Dunkel, K.G., Aupart, C., Austrheim, H., Corfu, F., Menegon, L., Renard, F. 2019. The Effects of Earthquakes and Fluids on the Metamorphism of the Lower Continental Crust. *Journal of Geophysical Research: Solid Earth*, 124(8), 7725-7755. doi: 10.1029/2018JB016461
- Kharya, A. 2015. Isotopic and Geochemical Studies of the Ladakh Accretionary Prism North West Himalaya. Ph.D. Thesis, University of Petroleum and Energy Studies, Dehra Dun (India), 295 pp. http://hdl.handle.net/10603/183097
- Kharya, A., Sachan, H.K., Tiwari, S.K., Singhal, S., Singh, P.C., Rai, S., Kumar, S., Mehta, M., Gautam, P.K.R. 2016. New occurrence of albitite from Nubra valley, Ladakh: characterization from mineralogy and whole rock geochemistry. *Current Science*, 111(9), 1531-1535. doi: 10.18520/cs/v111/i9/1531-1535
- Krestnikov, V.N., Nersesov, I.L., Stange, D.V. 1984. The relationship between the deep structure and quaternary tectonics of the pamir and Tien-Shan. *Tectonophysics*, **104**(1), 67-83. doi: 10.1016/0040-1951(84)90102-1
- Kumar, V., Honsberger, I.W., Kharya, A., Sachan, H.K., Rai, S.R., Kumar, M. 2022. Mineralogical and fluid inclusion constraints on the formation of the Karakorum Migmatite: implications for H2O-fluxed melting and exhumation of the South Tibetan Crust. Contributions to Mineralogy and Petrology, 177(6), 60. doi: 10.1007/s00410-022-01927-4
- Le Fort, P., Michard, A., Sonet, J., Zimmermann, J.L. 1983. Petrography, geochemistry and geochronology of some samples from the Karakorum Axial Batholith (northern Pakistan), *Granites of Himalayas Karakorum and Hindu Kush*, pp. 377-387.

- Miller, S.A. 2013. Chapter 1 The Role of Fluids in Tectonic and Earthquake Processes. In: R. Dmowska (Editor), Advances in Geophysics. Elsevier, pp. 1-46.
- Molnar, P. 1984. Structure and Tectonics of the Himalaya: Constraints and Implications of Geophysical Data. Annual Review of Earth and Planetary Sciences, 12(1), 489-516. doi: 10.1146/ annurev.ea. 12.050184.002421
- Mukherjee, B.K., Sen, K., Sachan, H.K., Paul, S.K. 2012. Exhumation history of the Karakoram fault zone mylonites: New constraints from microstructures, fluid inclusions, and 40Ar-39Ar analyses. *Lithosphere*, 4(3), 230-241. doi: 10.1130/l163.1
- Nelson, K.D., Zhao, W., Brown, L.D., Kuo, J., Che, J., Liu, X., Klemperer, S.L., Makovsky, Y., Meissner, R., Mechie, J., Kind, R., Wenzel, F., Ni, J., Nabelek, J., Leshou, C., Tan, H., Wei, W., Jones, A.G., Booker, J., Unsworth, M., Kidd, W.S.F., Hauck, M., Alsdorf, D., Ross, A., Cogan, M., Wu, C., Sandvol, E., Edwards, M. 1996. Partially Molten Middle Crust Beneath Southern Tibet: Synthesis of Project INDEPTH Results. Science, 274(5293), 1684-1688. doi: 10.1126/science.274.5293.1684
- Oliver, J. 1986. Fluids expelled tectonically from orogenic belts: Their role in hydrocarbon migration and other geologic phenomena. *Geology*, **14**(2), 99-102. doi: 10.1130/0091-7613(1986)14<99:FETFOB>2.0.CO;2
- Palin, R.M., Searle, M.P., Waters, D.J., Horstwood, M.S.A., Parrish, R.R. 2012. Combined thermobarometry and geochronology of peraluminous metapelites from the Karakoram metamorphic complex, North Pakistan; New insight into the tectonothermal evolution of the Baltoro and Hunza Valley regions. *Journal of Metamorphic Geology*, 30(8), 793-820. doi: 10.1111/j.1525-1314.2012.00999.x
- Phillips, R.J., Parrish, R.R., Searle, M.P. 2004. Age constraints on ductile deformation and long-term slip rates along the Karakoram fault zone, Ladakh. Earth and Planetary Science Letters, 226(3), 305-319. doi: 10.1016/j.epsl.2004.07.037
- Phillips, R.J., Searle, M.P. 2007. Macrostructural and microstructural architecture of the Karakoram fault: Relationship between magmatism and strike-slip faulting. *Tectonics*, **26**(3). doi: https://doi.org/10.1029/2006TC001946
- Rai, H. 1995. Geology of Eastern Karakoram, Ladakh District, India. *Journal of Nepal Geological Society*, 10(0), 11–20. doi: 10.3126/jngs.v10i0.32134
- Reichardt, H., Weinberg, R.F., Andersson, U.B., Fanning, C.M. 2010. Hybridization of granitic magmas in the source: The origin of the Karakoram Batholith, Ladakh, NW India. *Lithos*, **116**(3), 249-272. doi: 10.1016/j.lithos.2009.11.013
- Reichardt, H., Weinberg, R.F. 2012. Hornblende Chemistry in Meta- and Diatexites and its Retention in the Source of Leucogranites: an Example from the Karakoram Shear Zone, NW India. *Journal of Petrology*, 53(6), 1287-1318. doi: 10.1093/petrology/egs017
- Rey, P., Vanderhaeghe, O., Teyssier, C. 2001. Gravitational collapse of the continental crust: definition, regimes and modes. *Tectonophysics*, 342(3), 435-449. doi: 10.1016/S0040-1951(01)00174-3
- Rolland, Y. 2002. From intra-oceanic convergence to post-collisional evolution: example of the India-Asia convergence in NW Himalaya, from Cretaceous to present. *Journal of the Virtual Explorer*, 8, 185-208. doi:10.3809/jvirtex.2002.00052
- Rolland, Y., Pêcher, A., Picard, C. 2000. Middle Cretaceous back-arc formation and arc evolution along the Asian margin: the Shyok Suture Zone in northern Ladakh (NW Himalaya). *Tectonophysics*, 325(1), 145-173. doi: 10.1016/S0040-1951(00)00135-9
- Rolland, Y., Mahéo, G., Guillot, S., Pecher, A. 2001. Tectono-metamorphic evolution of the Karakorum Metamorphic complex (Dassu–Askole area, NE Pakistan): exhumation of mid-crustal HT–MP gneisses in a convergent context. *Journal of Metamorphic Geology*, **19**(6), 717-737. doi: 10.1046/j.0263-4929.2001.00342.x
- Rolland, Y., Carrio-Schaffhauser, E., Sheppard, S.M.F., Pêcher, A., Esclauze, L. 2006a. Metamorphic zoning and geodynamic evolution of an inverted crustal section (Karakorum margin, N Pakistan), evidence for two metamorphic events. *International Journal of Earth Sciences*, 95(2), 288-305. doi: 10.1007/s00531-005-0026-x
- Rolland, Y., Villa, I.M., Guillot, S., Mahéo, G., Pêcher, A. 2006b. Evidence for pre-Cretaceous history and partial Neogene (19–9Ma) reequilibration in

- the Karakorum (NW Himalayan Syntaxis) from 40Ar–39Ar amphibole dating. *Journal of Asian Earth Sciences*, **27**(4), 371-391. doi: 10.1016/j.jseaes.2005.04.008
- Rosenberg, C.L., Handy, M.R. 2005. Experimental deformation of partially melted granite revisited: implications for the continental crust. *Journal of Metamorphic Geology*, **23**(1), 19-28. doi: 10.1111/j.1525-1314.2005.00555.x
- Roy, P., Jain, A.K., Singh, S. 2010. Microstructures of mylonites along the Karakoram Shear Zone, Tangste Valley, Pangong Mountains, Karakoram. *Journal of the Geological Society of India*, 75(5), 679-694. doi:10.1007/s12594-010-0065-1
- Sachan, H.K., Santosh, M., Prakash, D., Kharya, A., Singh, P.C., Rai, S.K. 2016. Metamorphic P-T conditions and CO2 influx history of mediumgrade metapelites from Karakorum, Trans-Himalaya, India. *Journal of Asian Earth Sciences*, 124, 126-138. doi: 10.1016/j.jseaes.2016.04.019
- Sawyer, E.W. 1999. Criteria for the recognition of partial melting. *Physics and Chemistry of the Earth, Part A: Solid Earth and Geodesy*, **24**(3), 269-279. doi: 10.1016/S1464-1895(99)00029-0
- Sawyer, E.W. 2008. Atlas of Migmatites. Canadian Science Publishing.
- Schärer, U., Copeland, P., Harrison, T.M., Searle, M.P. 1990. Age, Cooling History, and Origin of Post-Collisional Leucogranites in the Karakoram Batholith; A Multi-System Isotope Study. *The Journal of Geology*, 98(2), 233-251. doi: 10.1086/629395
- Searle, M.P., Windley, B.F., Coward, M.P., Cooper, D.J.W., Rex, A.J., Rex, D., Tingdong, L.I., Xuchang, X., Jan, M.Q., Thakur, V.C., Kumar, S. 1987. The closing of Tethys and the tectonics of the Himalaya. GSA Bulletin, 98(6),678-701.doi:10.1130/0016-7606(1987)98<678:TCOTAT>2.0.CO;2
- Searle, M.P., Rex, A.J., Tirrul, R., Rex, D.C., Barnicoat, A., Windley, B.F. 1989. Metamorphic, magmatic, and tectonic evolution of the central Karakoram in the Biafo-Baltoro-Hushe regions of northern Pakistan. In: Malinconico, L.L., Lillie, Jr., R.J. (Eds)., Tectonics of the western Himalayas. Geological Society of America Special Papers. Geological Society of America, pp. 47-74.
- Searle, M.P., Parrish, R.R., Tirrul, R., Rex, D.C. 1990. Age of crystallization and cooling of the K2 gneiss in the Baltoro Karakoram. *Journal of the Geological Society*, **147**(4), 603-606. doi: 10.1144/gsjgs.147.4.0603
- Searle, M.P., Tirrul, R. 1991. Structural and thermal evolution of the Karakoram crust. *Journal of the Geological Society*, **148**(1), 65-82. doi: 10.1144/gsjgs.148.1.0065
- Searle, M.P., Weinberg, R.F., Dunlap, W.J. 1998. Transpressional tectonics along the Karakoram fault zone, northern Ladakh: constraints on Tibetan extrusion. *Geological Society, London, Special Publications*, 135(1), 307-326. doi: 10.1144/GSL.SP.1998.135.01.20
- Searle, M.P., Parrish, R.R., Thow, A.V., Noble, S.R., Phillips, R.J., Waters, D.J. 2010. Anatomy, age and evolution of a collisional mountain belt: the Baltoro granite batholith and Karakoram Metamorphic Complex, Pakistani Karakoram. *Journal of the Geological Society*, 167(1), 183-202. doi: 10.1144/0016-76492009-043
- Sen, K., Adlakha, V., Singhal, S., Chaudhury, R. 2018. Migmatization and intrusion of "S-type" granites in the trans-Himalayan Ladakh Magmatic Arc of north India and their bearing on Indo-Eurasian collisional tectonics. *Geological Journal*, 53(4), 1543-1556. doi: 10.1002/gj.2973
- Sharma, K.K., Kumar, S. 1978. Contribution to the geology of Ladakh. Himalayan Geology, 8, 252-287. doi:
- Sibson, R.H. 1994. Crustal stress, faulting and fluid flow. *Geological Society*, London, Special Publications, **78**(1), 69-84. doi: 10.1144/GSL.SP.1994.078.01.07
- Singh, P.C., Sachan, H.K., Kharya, A., Rolfo, F., Groppo, C., Singhal, S., Tiwari, S.K., Rai, S.R. 2020. Tectono-metamorphic evolution of the Karakoram Terrane: Constrained from P-T-t-fluid history of garnetbearing amphibolites from trans Himalaya, Ladakh, India. *Journal of Asian Earth Sciences*, 196, 104293. doi: 10.1016/j.jseaes.2020.104293
- Smith, H.A. 1993. Characterization and timing of metamorphism within the Indo-Asian suture zone, Himalayas, northern Pakistan. Ph.D. Thesis, Dartmouth College, United States -- New Hampshire, 304 pp. https://www.proquest.com/dissertations-theses/characterizationtiming-metamorphism-within-indo/docview/304041019/se-2?accountid=30156

- Span, R., Wagner, W. 1996. A New Equation of State for Carbon Dioxide Covering the Fluid Region from the Triple-Point Temperature to 1100 K at Pressures up to 800 MPa. *Journal of Physical and Chemical Reference Data*, 25(6), 1509-1596. doi: 10.1063/1.555991
- Srimal, N. 1986. India-Asia collision: Implications from the geology of the eastern Karakoram. *Geology*, 14(6), 523-527. doi: 10.1130/0091-7613(1986)14<523:ICIFTG>2.0.CO:2
- Streule, M.J., Phillips, R.J., Searle, M.P., Waters, D.J., Horstwood, M.S.A. 2009. Evolution and chronology of the Pangong Metamorphic Complex adjacent to the Karakoram Fault, Ladakh: constraints from thermobarometry, metamorphic modelling and U–Pb geochronology. *Journal of the Geological Society*, 166(5), 919-932. doi: 10.1144/0016-76492008-117
- Tapponnier, P., Mattauer, M., Proust, F., Cassaigneau, C. 1981. Mesozoic ophiolites, sutures, and arge-scale tectonic movements in Afghanistan. *Earth and Planetary Science Letters*, **52**(2), 355-371. doi: 10.1016/0012-821X(81)90189-8
- Thakur, V.C., Virdi, N.S. 1979. Lithostratigraphy, Structural frame work, deformation and metamorphism of the south east region of Ladakh, Kashmir Himalaya, India. *Himalayan Geology*, **9**, 63-78. doi:
- Thakur, V.C., Misra, D.K. 1984. Tectonic framework of the Indus and Shyok suture zones in Eastern Ladakh, Northwest Himalaya. *Tectonophysics*, **101**(3), 207-220. doi: 10.1016/0040-1951(84)90114-8
- Thakur, V.C., Rawat, B. 1992. Geological map of the Western Himalaya. Wadia Institute of Himalayan Geology.
- Thanh, N.X., Rajesh, V.J., Itaya, T., Windley, B., Kwon, S., Park, C.-S. 2012.
 A Cretaceous forearc ophiolite in the Shyok suture zone, Ladakh, NW India: Implications for the tectonic evolution of the Northwest Himalaya. *Lithos*, 155, 81-93. doi: 10.1016/j.lithos.2012.08.016
- Touret, J.L.R. 2001. Fluids in metamorphic rocks. *Lithos*, **55**(1), 1-25. doi: 10.1016/S0024-4937(00)00036-0
- Touret, J.L.R., Huizenga, J.M. 2012. Fluid-assisted granulite metamorphism: A continental journey. *Gondwana Research*, **21**(1), 224-235. doi: 10.1016/j.gr.2011.07.022
- Unsworth, M.J., Jones, A.G., Wei, W., Marquis, G., Gokarn, S.G., Spratt, J.E., Bedrosian, P., Booker, J., Leshou, C., Clarke, G., Shenghui, L., Chanhong, L., Ming, D., Sheng, J., Solon, K., Handong, T., Ledo, J., Roberts, B., The, I.-M.T.T. 2005. Crustal rheology of the Himalaya and Southern Tibet inferred from magnetotelluric data. *Nature*, **438**(7064), 78-81. doi: 10.1038/nature04154
- Valli, F., Arnaud, N., Leloup, P.H., Sobel, E.R., Mahéo, G., Lacassin, R., Guillot, S., Li, H., Tapponnier, P., Xu, Z. 2007. Twenty million years of continuous deformation along the Karakorum fault, western Tibet: A thermochronological analysis. *Tectonics*, 26(4). doi: 10.1029/2005TC001913
- Vanderhaeghe, O., Teyssier, C. 2001a. Crustal-scale rheological transitions during late-orogenic collapse. *Tectonophysics*, **335**(1), 211-228. doi: 10.1016/S0040-1951(01)00053-1
- Vanderhaeghe, O., Teyssier, C. 2001b. Partial melting and flow of orogens. *Tectonophysics*, **342**(3), 451-472. doi: 10.1016/S0040-1951(01)00175-5
- Vanderhaeghe, O. 2009. Migmatites, granites and orogeny: Flow modes of partially-molten rocks and magmas associated with melt/solid segregation in orogenic belts. *Tectonophysics*, 477(3), 119-134. doi: 10.1016/j.tecto.2009.06.021
- Villa, I.M., Lemennicier, Y., Le Fort, P. 1996. Late Miocene to Early Pliocene tectonometamorphism and cooling in south-central Karakorum and Indus-Tsangpo suture, Chogo Lungma area (NE Pakistan). *Tectonophysics*, **260**(1), 201-214. doi: 10.1016/0040-1951(96)00086-8
- Vrolijk, P., Myers, G. 1990. Fluid pressure history in subduction zones: evidence from fluid inclusions in the Kodiak Accretionary Complex, Alaska, *The Role of Fluids in Crustal Processes*, pp. 148-157.
- Wang, L., Kwiatek, G., Rybacki, E., Bonnelye, A., Bohnhoff, M., Dresen, G. 2020. Laboratory Study on Fluid-Induced Fault Slip Behavior: The Role of Fluid Pressurization Rate. *Geophysical Research Letters*, 47(6), e2019GL086627. doi: 10.1029/2019GL086627
- Weinberg, R.F., Searle M, P. 1998. The Pangong Injection Complex, Indian Karakoram: a case of pervasive granite flowthrough hot viscous crust. *Journal of the Geological Society*, **155**(5), 883-891. doi: 10.1144/gsjgs.155.5.0883

- Weinberg, R.F., Dunlap, W.J., Whitehouse, M. 2000. New field, structural and geochronological data from the Shyok and Nubra valleys, northern Ladakh: linking Kohistan to Tibet. *Geological Society, London, Special Publications*, **170**(1), 253-275. doi: 10.1144/GSL.SP.2000.170.01.14
- Weinberg, R.F., Mark, G. 2008. Magma migration, folding, and disaggregation of migmatites in the Karakoram Shear Zone, Ladakh, NW India. GSA Bulletin, 120(7-8), 994-1009. doi:10.1130/B26227.1
- Weinberg, R.F., Hasalová, P. 2015. Water-fluxed melting of the continental crust: A review. Lithos, 212-215, 158-188. doi: 10.1016 /j.lithos.2014.08.021
- Whitney, D.L., Teyssier, C., Fayon, A.K., Hamilton, M.A., Heizler, M. 2003. Tectonic controls on metamorphism, partial melting, and intrusion: timing and duration of regional metamorphism and magmatism in the Niğde Massif, Turkey. *Tectonophysics*, **376**(1), 37-60. doi: 10.1016/j.tecto.2003.08.009
- Yardley, B.W.D., Shmulovich, K.I. 1995. An introduction to crustal fluids. *In: K.I. Shmulovich, B.W.D. Yardley, G.G. Gonchar (Editors), Fluids in the Crust: Equilibrium and transport properties. Springer Netherlands, Dordrecht*, pp. 1-12.

- Zanchi, A., Poli, S., Fumagalli, P., Gaetani, M. 2000. Mantle exhumation along the Tirich Mir Fault Zone, NW Pakistan: pre-mid-Cretaceous accretion of the Karakoram terrane to the Asian margin. *Geological Society, London, Special Publications*, 170(1), 237-252. doi: 10.1144/GSL.SP.2000.170.01.13
- Zanchi, A., Gaetani, M. 2011. The geology of the Karakoram range, Pakistan: the new 1:100,000 geological map of Central-Western Karakoram. *Italian Journal of Geosciences*, **130**(2), 161-262. doi: 10.3301/IJG.2011.09
- Zeitler, P.K. 1985. Cooling history of the NW Himalaya, Pakistan. *Tectonics*, 4(1), 127-151. doi: 10.1029/TC004i001p00127
- Zhao, J., Yuan, X., Liu, H., Kumar, P., Pei, S., Kind, R., Zhang, Z., Teng, J., Ding, L., Gao, X., Xu, Q., Wang, W. 2010. The boundary between the Indian and Asian tectonic plates below Tibet. *Proceedings of the National Academy of Sciences*, 107(25), 11229-11233. doi: 10.1073/pnas.1001921107

Rockfall dynamics and mitigation strategies for a vulnerable location along a National Highway (NH-7) near Shivpuri in the Tehri Garhwal district of Uttarakhand, India

NEERAJ DAHIYA^{1,2,*}, KOUSHIK PANDIT^{1,2}, ANINDYA PAIN^{1,2}, SHANTANU SARKAR³

¹Academy of Scientific and Innovative Research (AcSIR), Ghaziabad 201 001, India

²CSIR – Central Building Research Institute (CBRI), Roorkee 247 667, India

³Uttarakhand Landslide Mitigation & Management Center (ULMMC), Dehradun 246001, India

*Email (Corresponding author): neerajdahiya413@gmail.com

Abstract: In mountainous regions, rockfall stands out as a prevalent natural process where rock fragments detach and move downhill through actions such as sliding, toppling, and falling. These incidents usually impact the surrounding infrastructure, such as roads, bridges, buildings, trains, and other essential facilities. The rockfall hazards are intensified by recurrent freezing and thawing cycles, heavy precipitation, and seismic activity. In the present research, a vulnerable roadcut slope with rockfall potential, located along a National Highway (NH-7) near Shivpuri in the Tehri Garhwal district of Uttarakhand, India has been studied. A kinematic analysis was carried out to determine the potential failure mode in the slope (Planar/Wedge/Toppling). The studied slope was found to have potential for a wedge mode of failure. The slope mass rating (SMR) rock mass classification has been used for slope stability assessment. The studied slope has been found to be under the completely unstable category of stability grade with SMR value 13. The trajectory path of rockfall has been traced using rockfall simulation. The various parameters, including run-out distance, total kinetic energy, translational velocity, and maximum bounce height, were evaluated by rockfall simulation followed by design and comparison of two mitigation strategies, i.e., rock traps or ditches and rockfall catching nets or rockfall barriers. The rockfall simulation result shows that the maximum bounce height, run-out distance, translational velocity, and total kinetic energy of the falling block are 3.1 m, 39.7 m, 16.6 m/s and 137.3 kJ, respectively. All the falling blocks have the potential to reach the road level and accumulate, thus posing a significant risk to vehicular traffic in the future. Therefore, proper mitigation measures are required to minimize the risk. For this, the effectiveness of a ditch, designed by utilizing the ditch design chart for rock fall catchment, has been analysed. Furthermore, the potential barrier capacity for the studied site was calculated as 130 KJ for 914 Kg of falling block and we checked its net barrier against rockfall events. Notably, the rockfall net barrier demonstrated superior efficiency, considering space constraints and mitigating associated risks.

Keywords: Rockfall simulation, kinematic analysis, rock slide, slope mass rating, mitigation measures, Garhwal Himalayas

INTRODUCTION

A rockfall is a fragment of rock (a block) detached by sliding, toppling or falling that falls along a vertical or sub-vertical cliff, proceeds down the slope by bouncing and flying along ballistic trajectories or by rolling on talus or debris slopes. It is a recurring phenomenon along the hill roads, especially in the Indian Himalaya, where it is predominantly triggered by the presence of steep slopes, weathered and highly fractured rocks, unfavourable geological structures, intense rainfall, tectonic and anthropogenic activities (Bhambri et al. 2017; Kumar et al. 2017; Ozmen 2023). Most of the slopes in the Himalayan belt consist of deformed rocks and joints with the unfavourable alignment of discontinuities in the rock mass, making them particularly vulnerable to rockfall. Different rock types have different compositions and structures, which contribute to the material's strength (Ray et al. 2021). The main natural factors responsible for rockfall activity are an increase in extreme rainfall, especially during the monsoon season (Gupta et al. 2017; Kumar et al. 2017). The construction of hill roads without appropriate geotechnical and geological investigation will likely increase slope failures (Sarkar et al. 2012). Rockfall events in the hilly areas create major obstructions to any infrastructure developments that may eventually cause the destruction of property and loss of lives. Therefore, to minimize the effect of rockfalls, the stability assessment and mitigation measures of rockfallprone slopes need to be pre-analysed for any road widening activity.

Over the years, the Garhwal Himalayas have witnessed several rockfall incidents resulting in significant damage and fatalities. Notably, the National Highway, NH-7 experienced a major rockfall incident on May 19, 2017 in Vishnuprayag, Chamoli district of Uttarakhand, devastating damage to a nearly 150-meter length of the road and approximately 15,000 tourists being stuck on either side of the landslide (Sarkar et al. 2018). This slide may have been activated by water seeping through rock mass fractures. Another rockfall incident occurred close to Byasi, Tehri Garhwal, Uttarakhand in 2021 in which two people were injured when a large boulder fell on a car (Amar Ujala 2021). This incident was probably caused due to dislodging of the area's highly jointed rock mass. Furthermore, a significant tragedy occurred at the Rishi Ganga River in Chamoli, where a glacial lake outburst created an avalanche of dense snow, followed by a rockslide which killed about 72 people (Shah 2021). This fatal incident may be attributed to the global warming and melting of thick snow.

Till date, various qualitative and quantitative methods have been employed for rockfall hazard assessment, such as quantitative risk assessment (QRA) (Corominas *et al.* 2005; Ferlisi *et al.* 2012) and Rockfall Hazard Rating System (RHRS) (Ansari *et al.* 2012; Pellicani *et al.* 2015). These methods consider geological characteristics, slope geometry,

vehicle risk, failure magnitude, roadway width, rockfall history, frequency, and climate. Numerical modelling is also used to simulate rock block trajectories and assess the probability of different paths (Guzzetti *et al.* 2002; De Almeida & Kullberg 2011). Although there are a large number of places where rockfall studies have been conducted, the input parameters, rockfall mechanism, and energy distribution system vary greatly; therefore, results obtained at one site may not apply to another for the same set of inputs. This is mainly due to the different environmental and climatic conditions of different countries; the proposed methodology result for a particular area may vary at different locations for the same set of input parameters.

In India, the research on rockfall is still under development, with limited research conducted by a few researchers. Past studies have explored factors like bounce height and translational kinetic energy with respect to the mass of the falling block. For example, Ansari et al. (2012) found that bounce height decreases as the mass of the falling block increases, whereas translational kinetic energy increases with the mass of the falling block. Ahmad et al. (2013) simulation study concluded that the geometry of slope (height and angle) has a more effective role in rockfall than the block's mass. Numerous hazard assessments have been carried out along different roads and locations in India, highlighting the diversity in input parameters, rockfall processes, and energy distribution systems. A few significant examples are: (i) Singh et al. (2013) assessed the road cut cliff stability and risk of rockfall along SH-121, Maharashtra. This study shows that the impact on the toe of the slope is very crucial and is enough to cause causality. The climatic conditions and vibrations produced due to daily high-density traffic, the slope can undergo recurrent failures; (ii) Vishal et al. (2017) conducted numerical simulation study along NH-58 in Uttarakhand Himalaya. This study reveals that an increasing slope angle could significantly increase the kinetic energy of the rock blocks. However, an increase in the ditch angle and the ditch width reduces the energy of moving blocks; (iii) Sharma et al. (2020) conducted a study along Mumbai-Pune expressway, Maharashtra, this study suggests the appropriate preventive measures for this site to minimise the frequent slope failure and rockfall; (iv) Verma et al. (2019) conducted a study along NH-44A, Lengpui Airport (Aizwal City), this study shows that the high kinetic energies were associated with the large size of falling rock blocks, which is quite enough to break down any structure or vehicle or can cause fatalities; (v) Ansari et al. (2014) conducted a study at the world heritage site of Ajanta cave, this rockfall study indicates that certain locations at Ajanta caves are at alarming situation and needs proper protection for the prevention of the possible rockfall hazard., and Bagde (2021), in this study the rock slope surface and dislocated boulders vulnerability to failure risk is carried out with the Rockfall Hazard Rating System (RHRS); (vi) Singh et al. (2016) conducted a study along the transportation corridor, Luhri (Kullu) this study estimated loss of energy due to the impact of falling blocks on the slope face and subsequently on the road through rockfall simulation, etc.

In recent years, semi-empirical equations were developed using multivariate linear regression to obtain important parameters used to estimate the trajectory of the block, such as bounce height, velocity and kinetic energy (Sardana *et al.* 2022). Roul *et al.* (2023) explored the rotational effect of a rock block or boulder on the trajectory by using RocFall trajectory simulation, assuming from a completely spherical shape to a hexa-contagon shape. The rigid body 3D stochastic analysis has been carried out to understand the rockfall mechanism and mitigation in the Batseri Zone, Kinnaur district in Himachal Pradesh, India (Pandey *et al.* 2025).

In the present study, a vulnerable road-cut slope having rockfall potential, located along the NH-7 near Shivpuri in Tehri Garhwal district of Uttarakhand, India, has been selected. The kinematic analysis has been used to find potential failure modes, and Slope Mass Rating (SMR), an engineering rock mass classification system, has been utilized for the evaluation of slope stability. Rockfall simulation has been used to observe the trajectory path and identify the exact location where the falling block will hit. The maximum bounce height, run-out distance, translational velocity and total kinetic energy have been evaluated using rockfall simulation. Finally, the design and comparison of two different mitigation measures, namely rock traps, also known as ditches, and rockfall catching nets or rockfall barriers, were also executed.

STUDY AREA AND GEOLOGY

The rockfall site is located near Shivpuri in the Garhwal Himalaya along a National Highway (NH-7). The NH-7 links Rishikesh with the well-known shrines of Badrinath and Kedarnath on the Char Dham Yatra that attracts thousands of visitors yearly. This highway is important from both the tourism and defence point of view. This area was selected because of damage of infrastructure and human life caused due to landslides every year. Rockfall is a very common phenomenon in this region, particularly in the rainy season. The location map of the study area is shown in figure 1.

Geologically, the present study area falls under a part of Garhwal Lesser Himalaya, which lies between the Greater Himalaya and Siwalik Range and is bounded by Main Central Thrust (MCT) and Main Boundary Thrust (MBT), respectively (Heim and Gansser 1939). The Lesser Himalayan belt is one of the most structurally complex litho-tectonic units of Himalaya. The studied slope comprises of quartzarenite sandstone of Tal Formation.

The climatic conditions in the Lesser Himalayas is also very diverse and extreme in terms of the amount of rainfall and fall in temperature during winter. The rainy season follows the monsoon cycle, which begins in this region from June to August. The winter season is very cold, particularly from December to March. Throughout the year, the temperature varies from -3° C to 30° C and the maximum rainfall is about 250 cm (Lawrence 1977).

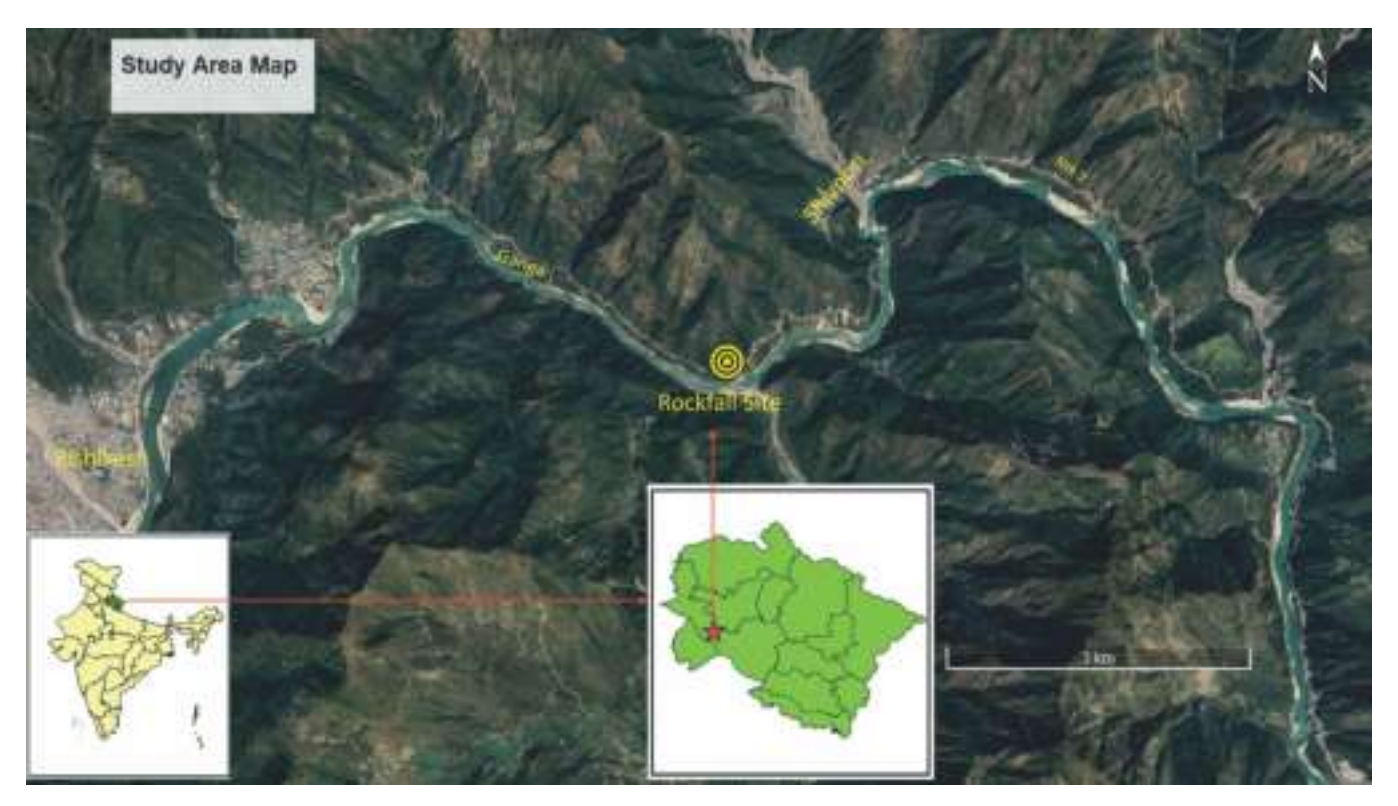


Fig. 1. Location Map of Studied Rockfall Site.

FIELD AND LABORATORY INVESTIGATION

All relevant geometrical, geological, and geotechnical data, such as the type of rock, joint spacing, joint condition (roughness, weathering, infilling), joint set numbers, joint orientation, joint alteration, hydrological conditions and rock mass structure were collected from the site to evaluate stability. Representative lumped shape rock samples were taken from the toe portion of the selected slope for laboratory tests. The rock block dimension has been measured to determine the mass of the falling block, as it is one of the important input parameters for rockfall simulation. Due to unavailability of rock core sample, the Point Load Strength Index test has been carried out to determine the Uniaxial Compressive Strength (as per IS 8764). According to Palmstrom's 2005, the value of the Rock Quality Designation (RQD) was determined by using its empirical relationship with the volumetric joint count (Jv), i.e.,

$$RQD = 110 - 2.5J_{v}$$
 (1)

The Uniaxial Compressive Strength of rock (UCS) and Rock Quality Designation (RQD) value has been used to calculate RMR_{basic}. The description of studied site with

orientation and surface condition of joints is given in table 1. The Rockfall source zone (seeder location) is the area from where chances of detachment of rock block. The 33m height of studied slope, 13.4-m roadway width including unpaved shoulder and two seeder location has been identified based on field observation are shown in figure 2.

METHODOLOGY

Kinematic Analysis

Kinematic analysis is the geometrical assessment of slope to identify potential failure modes, such as planar, wedge, or toppling failures, which may be caused by unfavourably oriented discontinuities with respect to slope orientation in the rock mass. Markland's test (1972) is used to evaluate the possibility of slope failures due to discontinuity orientation (Hoek & Bray 1981). These different modes of slope failure are one of the important parameters to obtain the value of adjustment factor (F_1 , F_2 & F_3) for determining Slope Mass Rating (SMR) values as given in table 2.

According to Markland's test, a planar failure occurs when the discontinuity's dip angle is greater than the friction

Table 1. Description of orientation and surface nature of the joints at the rock fall site.

Joint Set	Joint orientation dip/dip direction	Average Spacing (cm)	Roughness	Weathering	Infilling
J1	75°/N65°	30	Smooth	Slightly Weathered	Nil
J2	60°/N135°	60	Slightly Rough	Slightly Weathered	Nil
J3	75°/N340°	47	Slightly Rough	Slightly Weathered	Nil



Fig. 2. Field photograph of the studied slope near Shivpuri.

Table 2. Values for adjustment factor for different joint orientation (Romana, 1985).

Case of Slope Failure		Failure Very Favourable		Fair	Unfavourable	Very Unfavourable	
P	$ \alpha_i - \alpha_s $						
T	$ \alpha_i - \alpha_s - 180 $	>30	30 - 20	20 - 10	10 - 5	>5	
W	$ \alpha_i - \alpha_s $						
P/W/T	F1	0.15	0.40	0.70	0.85	1.00	
P	β	<20	20 - 30	30 - 35	35 - 40	>45	
W	$\dot{\beta}_{i}$						
P/W	F2	0.15	0.40	0.70	0.85	1.00	
T	F2	1.0	1.0	1.0	1.0	1.0	
P	$\beta_i - \beta_s$	>10	10 - 0	0	0 - (10)	< -10	
W	$\beta_{\rm i} - \beta_{\rm s}$						
T	$\beta_{\rm i} - \beta_{\rm s}$	<110	110 - 120	>120			
P/W/T	F3	0	-6	-25	-50	-60	

angle but less than the slope angle, and the discontinuity's dip direction is parallel to the slope face (within 20°) (Hoek & Bray 1981) and a wedge failure is probable to occur When the slope face and the line of intersection of the two discontinuity planes that create the wedge-shaped block fall in the same direction and the plunge angle should be greater than the friction angle but less than the slope angle. A toppling failure is indicated by the vertical to sub-vertical discontinuity plane dipping inside the slope and parallel to the slope face. (Yoon *et al.* 2002).

Slope Stability Assessment

In the present study, the Slope Mass Rating (SMR) classification has been used for qualitative slope stability assessments. The Romana (1985) rock slope stability classification system is a tool used in geotechnical engineering to evaluate and categorise the stability of the rock slopes. The equation 2 demonstrates the way to calculate SMR by adding adjustment factors related to joint and slope orientation and an

additional factor based on the excavation method to RMR $_{\text{basic}}$. (Romana *et al.* 2003).

$$SMR = RMR_{basic} + (F_1, F_2, F_3) + F_4$$
 (2)

The adjustment factor F_1 is dependent on parallelism between the joint plane and the slope face, F_2 is dependent on the joint plane's dip angle or plunge angle of the line of intersection between two joint planes and F_3 is dependent on the relationship between the slope and the joint plane's dip angle or plunge in case of wedge failure. F_4 is an adjustment correction factor for the excavation method, ranging from +15 (natural slope) to 8 (deficient blasting).

Rockfall Simulation

Rockfall simulations play a crucial role in assessing and mitigating the risks associated with natural hazards, providing valuable insights for land-use planning, engineering design, and public safety efforts in areas prone to rockfalls. Simulations consider the interactions between falling rocks

and the terrain. This involves assessing how rocks bounce, roll, or slide upon impact with the ground or other obstacles. The results of the simulation are then used to assess the potential risk to infrastructure, people, or the environment. This information is crucial for designing protective measures or establishing safety guidelines. Simulations are often validated by comparing the results with real-world observations or experiments. It helps to ensure the precision and reliability of the simulation model. Rockfall simulation can be done by using RocFall software (Version 8.0265) that was developed by Stevens (Steven 1998). The software employs various equations and algorithms to model and predict the trajectory and impact of falling rocks on slopes or cliffs. The equations used in rockfall analysis often involve principles of physics, including projectile motion and energy conservation.

The RocFall program consists of three envelopes: the bounce-height envelope, the velocity envelope, and the kinetic energy envelope. The maximum value (such as the maximum velocity) at several horizontal locations spaced evenly along the slope profile defines each envelope. The maximum kinetic energy that a rock could possibly have while passing through each horizontal position is measured by the kinetic energy envelope. The velocity envelope measures the highest velocity that any rock attained while passing each horizontal location. The bounce height graph calculates the highest point any rock could have reached at each horizontal location, deducting the slope height (i.e. the maximum height above the slope). These envelopes are frequently used to determine where remedial measures should be placed, therefore, it is crucial that they function properly.

It is significant to observe that the vertical velocity is zero at the top of the parabola, which represents the peak of the rock's trajectory path. Since the rock's horizontal velocity remains constant while it is in the air. The velocity that the rock possesses at the peak of the trajectory is the only initial horizontal velocity. Consequently, the velocity at the peak of each parabolic path (the troughs of the kinetic energy and velocity envelopes) is equal to the post-impact velocity (V_{x_A}) of the previous impact.

The projectile algorithm is used to calculate the rock's movement as it travels through the air and bounces upon different locations on the slope. The rock is assumed to have some velocity by the projectile algorithm, which will allow it to travel through the air from its current location to a new one (which can be further along the same object). Due to gravity, the rock will follow a parabolic path as it travels through the air.

The primary objective of the projectile algorithm is to locate the point of intersection between a line segment (a barrier or a slope segment) and a parabola, which represents the rock's path. The impact is computed using the coefficients of restitution once the intersection site has been identified. If, the rock is still moving quickly enough after the impact, the process restarts again with the search for the next intersection point.

All equations given below have been taken from published literature (Steven 1998).

The parametric equations for the velocity of the rock particle at any point along the parabolic path, before impact:

$$V_{xB} = V_{x0}$$
 (3)
 $V_{yB} = V_{y0} + gt$ (4)

$$V_{yB} = V_{y0} + gt \tag{4}$$

where, V_{XB} , V_{YB} is the velocity of the rock at any point along the parabolic path, before impact, V_{x0} , V_{y0} is the initial velocity of the rock, g is the acceleration due to gravity (sign is negative), t is the time.

$$t = \frac{-b \pm \sqrt{b^2 - 4ac}}{2a} \tag{5}$$

where:

$$\begin{aligned} a &= \frac{1}{2} g \\ b &= V_{y_0} \text{-} q V_{x_0} \\ c &= Y_0 \text{-} Y_1 \text{+} q (X_1 \text{-} X_0) \\ q &= \frac{Y_2 \text{-} Y_1}{X_1 \text{-} X_0} \end{aligned}$$

where, Q is the slope of the line segment, X_0 , Y_0 is the initial position of the rock, X_1 , Y_1 is the first endpoint of the line, X_2 , Y₂ is the second endpoint of the line.

The parametric equations for the velocity of the rock particle at any point along the parabolic path, after impact:

$$V_{XA} = (V_{NA}) \sin(\theta) + (V_{TA}) \cos(\theta)$$
 (6)

$$V_{YA} = (V_{TA}) \sin(\theta) + (V_{NA}) \cos(\theta)$$
 (7)

where, V_{XA} , V_{YA} are the velocity components of the rock. after impact in the horizontal and vertical directions respectively, V_{NA} , V_{TA} are the velocity components of the rock, after impact, in the normal and tangential directions, respectively, θ is the slope of the line segment.

The impact is calculated using the coefficients of restitution (CoR), according to:

$$V_{XA} = (V_{NA}) \tag{8}$$

$$V_{TA} = R_T V_{TB} \tag{9}$$

here, V_{NB} , V_{TB} are the velocity components of the rock. before impact in the normal and tangential directions respectively, R_N is the coefficient of normal restitution, R_T is the coefficient of tangential restitution.

The coefficient of restitution (CoR) is the ratio of the velocities before and after the impact of rock block on the slope's surface. The rockfall trajectories are significantly impacted by the values of CoR, particularly Rn. When predicting rockfall, the values of R_n and R_n are utilized to measure the energy dissipation during an impact (Buzzi et al. 2011).

The values of the coefficient of restitution vary between 0 and 1. In the context of rockfall analyses, the typical range of values for the coefficient of normal restitution (RN) is 0.3-0.5. For tangential restitution (RT), typical values are between 0.8 and 0.95. The top of the road is asphalt, the uphill side of the road is fractured sandstone and the downhill slope below road is sandstone bedrock The talus covers also exist between asphalt and uphill fractured sandstone as shown in figure 4. Minute variations in the coefficients of restitution have a significant impact on the rockfall simulation. In comparison to the same slope segment with RN = 0.5, a slope section with RN = 0.4 will, for instance, behave considerably differently.

Now, the velocities are transformed into components normal and tangential to the slope according to:

$$V_{NB} = (V_{YB}) \cos(\theta) - (V_{XB}) \sin(\theta)$$
 (10)

$$V_{TR} = (V_{VR}) \sin(\theta) - (V_{XR}) \cos(\theta)$$
 (11)

The velocity and kinetic energy just before the impact are calculated as:

$$V_{B} = \sqrt{V_{YB}^{2} + V_{YB}^{2}} \tag{12}$$

$$KE_{B} = \frac{1}{2} (m) V_{B}^{2}$$
 (13)

The velocity and kinetic energy just after the impact are calculated as:

$$V_{A} = \sqrt{V_{XA}^2 + V_{YA}^2} \tag{14}$$

$$KE_{A} = \frac{1}{2} \text{ (m) } V_{A}^{2}$$
 (15)

The velocity and kinetic energy at the next peak of the rock trajectory are calculated as:

$$V_{PEAK} = V_{XA} \tag{16}$$

$$KE_{PEAK} = \frac{1}{2} (m) V_{PBAK}^2$$
 (17)

The bounce-height at the slope vertex is calculated as:

$$t = \frac{x_2 + x_1}{V_y} \tag{18}$$

$$y = Y_0 + V_y t + 0.5 gt^2$$
 (19)

$$\Delta h = y - H_s \tag{20}$$

where, Δh is the bounce height, H_s is the slope height, y is the height of rock block from the base of slope.

RESULTS AND DISCUSSION

The "Char Dham" typically refers to the four sacred pilgrimage sites, namely Yamunotri, Gangotri, Kedarnath, and Badrinath, all located in the Indian state of Uttarakhand. These sites attract a significant number of pilgrims and tourists each year, making these roads the most important risk element from landslide point of view. Road conditions and associated risks can vary depending on factors such as weather,

maintenance, and local infrastructure. The one of the Char Dham road has been selected for the present study and a vulnerable site has been selected that is prone to rockfall. The kinematic analysis and stability assessment using Slope Mass Rating (SMR) has been done to find potential failure modes and for evaluation stability condition. For the studied slope, the failure mechanisms through kinematic analysis can be clearly demonstrated by plotting the slope face and all the discontinuity planes in Stereonet as shown in figure 3. The kinematic analysis results show that the studied slope has wedge mode of failure. The rating of each input parameters, SMR values along with stability grade of studied slope are given in table 3. The results depict that the obtained SMR values of studied slope has been found to be under the completely unstable category of stability grade. The rockfall trajectory path of the selected slope has been observed through rockfall simulation by using RocFall2 V 8.024 software and the falling block's impact location has also been identified. The maximum bounce height, total kinetic energy, run-out distance, translational velocity, and design of mitigation measures were all assessed using a rockfall simulation. The slope's geometry has been created to present the actual scenario of the studied slope in order to provide best possible approximation (Fig. 4). Based on field survey, the studied slope's model has been divided into 3 materials. The top of the road is asphalt, the uphill side of the road is fractured quartzarenite sandstone and the downhill slope below road is quartzarenite sandstone bedrock. The talus covers also exist between asphalt and uphill fractured quartzarenite sandstone. The Rocscience COR table (Hoek, Evert) was used to determine the normal and tangential COR values for the asphalt and talus. The values of normal and tangential COR for the bedrock quartzarenite sandstone and fractured quartzarenite sandstone have been taken from different literature (Verma et al. 2019; Sardana et al. 2021). The friction angle of different type of materials (Sandstone, Talus cover, Asphalt) for rockfall simulation have been taken from literature (Vishal et al. 2017). In the field, the rock block that is most vulnerable to detach has been identified as source locations and kinematic analysis result shows that the slope is potential for wedge failure, due to this characteristics, probability of number of falling block is maximum and the total number of falling block i.e., 200 has been considered. The input parameters of rockfall simulation are given in table 4. Rockfall simulation results show that all the considered (200) falling blocks can reach the road level. It moves toward the valley side with approximate maximum bounce height, runout distance, translational velocity and total kinetic energy of 3.1 m, 39.7 m, 16.6 m/s and 137.3 kJ respectively. The obtained value of all these output parameters of rockfall simulation has been verified by hand calculation. The graphical representation of all the obtained parameters from the rockfall analysis is shown in figure 5. This result leads to the conclusion that in case of a rockfall event in the future, the falling rock block poses a risk to vehicular traffic on this road. Proper mitigation measures need to be designed for this site to minimize the risk. To mitigate the effects of rockfall, engineers can implement a variety of techniques such as constructing benches, shotcrete, possible barriers, catch nets, wire and mesh, catch ditches, and anchors. There are standard codes and special reports related to rockfall protection measures such as IRC SP: 106-2015, IRC SP:48-2023.

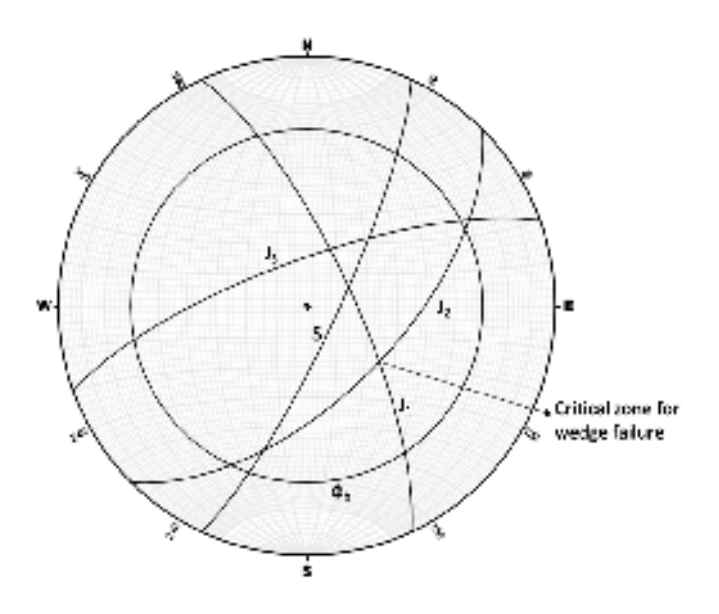


Fig. 3. Kinematic analysis of the studied slope showing the possibility of wedge failure.

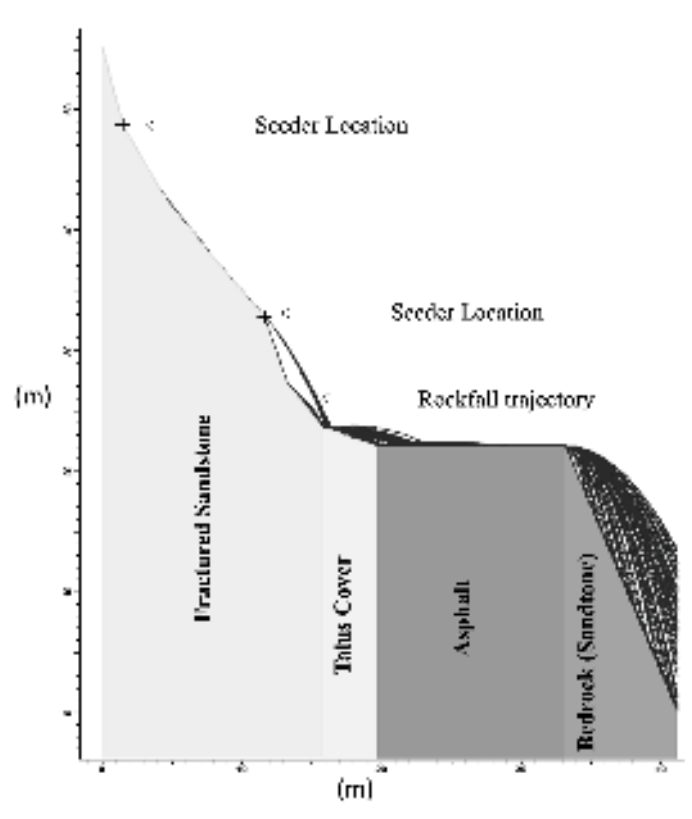


Fig. 4. A two-dimensional slope profile showing rockfall initiation zones (seeder location), slope material and probable simulated rockfall trajectory.

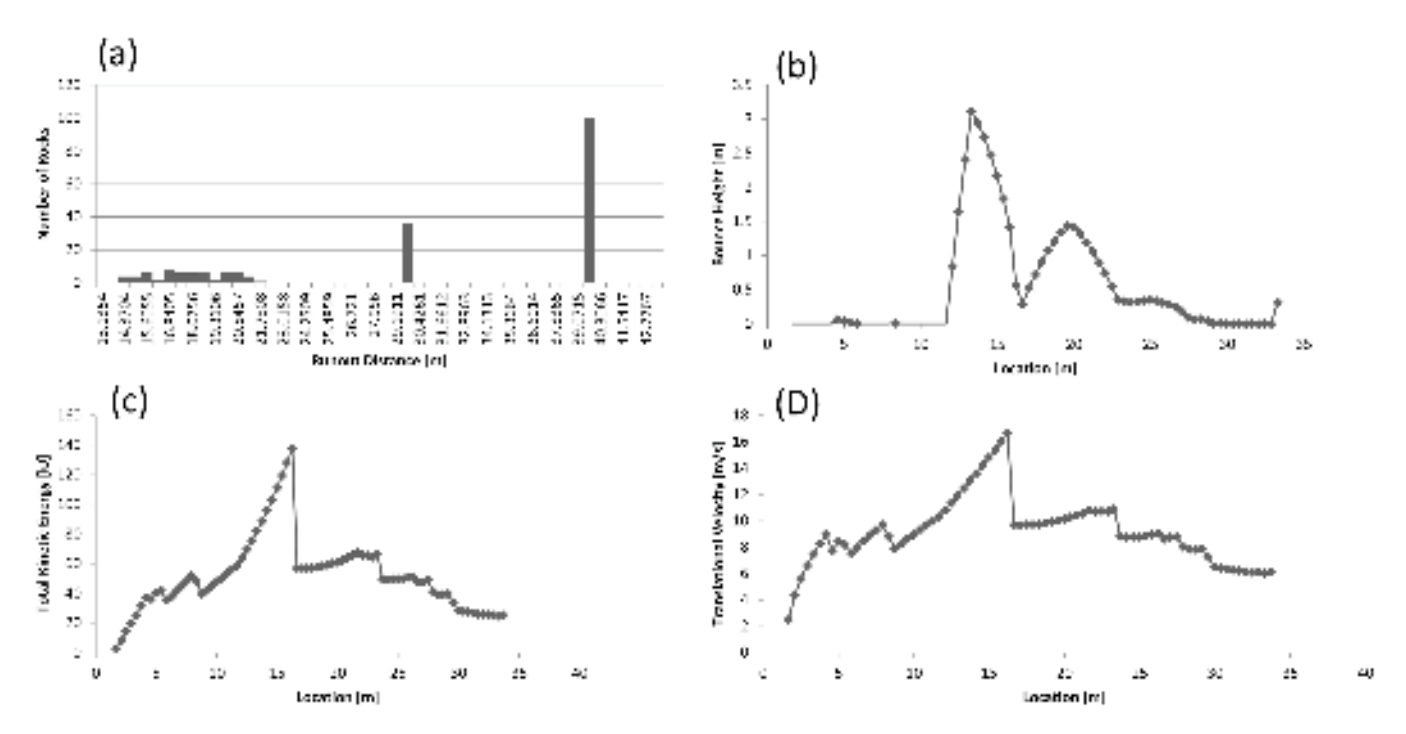


Fig. 5. a) Run-out distance of falling rock blocks; b) Bounce height envelope on the slope and the roadway at varying locations; c) Total kinetic energy envelope on the slope and the roadway at different locations; d) Translational velocity envelope at different locations.

Table 3. Slope mass rating result of rockfall site.

RMR _{basic}	$\mathbf{F}_{\scriptscriptstyle 1}$	\mathbb{F}_2	\mathbf{F}_3	\mathbb{F}_4	SMR	Stability Grade
73	1	1	-60	0	13	Completely Unstable

Table 4. Input parameters of rockfall simulation.

a) Seeder/Falling block properties

Seeder Location	Rock Type	Mass(kg)	Density (kg/m³)	Number of Rocks	Horizontal Velocity (m/s)	Vertical Velocity (m/s)	Rotational Velocity (*/s)
Seeder 1 & 2	Sandstone	914	2463	200	0.005	0	0

b) Slope material properties

Material Name	Normal Restitution	Tangential Restitution	Friction Angle (degree)
Fractured Sandstone	0.45	0.85	30
Talus Cover	0.32	0.82	12.38
Asphalt	0.4	0.9	6.34
Bedrock (Sandstone)	0.35	0.85	36

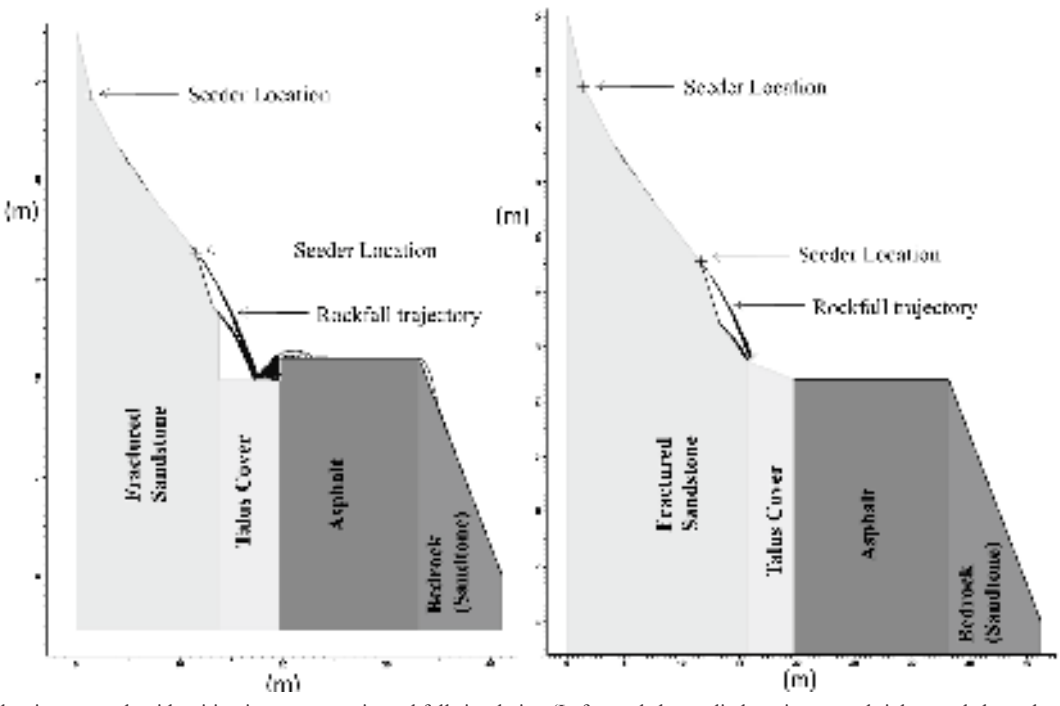


Fig. 6. Rockfall trajectory path with mitigation measures in rockfall simulation (Left panel shows ditch on its toe and right panel shows barrier technique).

For the present studied location, the effectiveness of two different mitigation measures has been analysed. Firstly, the effectiveness of a ditch was analysed by creating a ditch of 2.13 depth and 6.1m width using a ditch design chart for a rock fall catchment (Ritchie 1963). This ditch would create a 96% reduction in risk. Only eight rock blocks out of 200 rock blocks reach the road. So, it has been observed that the ditch is an effective mitigation measure. However, the selected site is a road-cut slope. Along the roadside in a hilly area, due to the unavailability of land, there may be some chances for destabilization of the hill, and the ditch can also become a threat to the moving vehicles. Creating a ditch of 6.1m wide was found to be non-feasible for the selected site. This technique is only effective for a large rockfall site where the

risk element is far from the rockfall source zone. So, for this site, the potential barrier capacity has been calculated for providing mitigation measures, i.e., 130 KJ for 914 Kg mass of rock block. By designing this barrier in the model, it has been observed that it arrested all falling rock blocks and the risk on the road is 0%. The rockfall trajectory path with both mitigation measures in the rockfall simulation has been shown in figure 6. It has been found that the potential barrier mitigation measures are more effective at the place where risk element is near to rockfall source zone.

CONCLUSIONS

In the present study, the kinematic analysis results shows that the studied slope has potential for a wedge mode of failure. The obtained SMR values of studied slope are under the completely unstable category of stability grade with SMR value 13.

The rockfall simulation result illustrates that:

- The value of maximum bounce height, run-out distance, translational velocity and total kinetic energy of falling block are 3.1 m, 39.7 m, 16.6 m/s and 137.3 kJ respectively.
- Rockfall simulations suggest falling blocks may reach the road level and move toward the valley side.
- It is concluded that any future rockfall occurrence could pose a serious risk to the safety of the vehicles on this road.

To reduce the risk, suitable mitigation measures are required. The design & effectiveness of two mitigation measures: rock trap or ditches and rockfall catching nets or rockfall barriers has been carried out.

- Firstly, the effectiveness of a ditch was analysed and it has been observed that the ditch would create a 96% reduction in risk, so that the ditch is an effective mitigation measure. However, the selected site is a road-cut slope, due to the unavailability of land, there may be some chances for destabilization of the hill, and the ditch can also become a threat to the moving vehicles.
- The potential barrier capacity has also been calculated for providing mitigation measures, i.e., 130 KJ for 914 Kg mass of rock block. By designing this barrier in the model, it has been observed that it arrested all falling rock blocks and the risk on the road is 0%.
- It has been found that the potential barrier mitigation measures are more effective at the place where risk element is near to rockfall source zone. However, creating a ditch is an effective mitigation measure for a large rockfall site where the risk element is far from the rockfall source zone.
- The methodology presented in the current study may be used for preliminary assessment of the rockfall site and the elementary design of the support system to minimize the risk.

Acknowledgements: The authors would like to thank the Director, CSIR-Central Building Research Institute, Roorkee for giving his kind permission to communicate this research work for publication. The first author acknowledges AcSIR (Ghaziabad, India) for providing the opportunity to carry out this doctoral research. The authors are immensely grateful to the Associate Editor, Dr. R. Jayangondaperumal for his generous review and anonymous reviewers for their useful suggestions to enhance the quality of the manuscript.

References

- Ahmad, M., Umrao, R.K., Ansari, M.K., Singh, R., Singh, T.N. 2013. Assessment of rockfall hazard along the road cut slopes of State Highway-72, Maharashtra, India. *Geomaterials*, 3, 1523.
- Amar Ujala 2021. https://www.amarujala.com/dehradun/uttarakhand-news-boulder-fell-on-car-on-rishikesh-badrinath-highway-two-passengers-injured (Last access on 01/08/2024)

- Ansari, M.K., Ahmad, M., Singh, R., Singh, T.N. 2012. Rockfall assessment near Saptashrungi Gad temple Nashik, Maharashtra, India. *International Journal of Disaster Risk Reduction*, 2, 77–83. doi: 10.1016/j.ijdrr.2012.09.002
- Ansari, M.K., Ahmad, M., Singh, T.N. 2014. Rockfall risk assessment for pilgrims along the circumambulatory pathway, Saptashrungi Gad Temple, Vani, Nashik Maharashtra, India. *Geomatics, Natural Hazards* and Risk, 5(1), 81-92
- Bagde, M.N. 2021. Assessment of rockfall hazard and stabilization of rock slope surface at the world heritage Ajanta Cave. *Geotechnical and Geological Engineering*, **39**(4), 3101–3114.
- Bhambri, R., Mehta, M., Singh, S., Jayangondaperumal, R., Gupta, A.K., Srivastava, P. 2017. Landslide inventory and damage assessment in the Bhagirathi valley, Uttarakhand, during June 2013 flood. *Himalayan Geology*, 38, 193–205.
- Buzzi, O., Giacomini, A., Spadari, M.; Fityus, S. 2011. Numerical modeling of a rock fall mesh perforation upon impact. *In: IACMAG* 2011 Melbourne, Australia, 9–11 May 2011.
- Corominas, J., Copons, R., Moya, J., Vilaplana, J.M., Altimir, J., Amigo, J. 2005. Quantitative assessment of the residual risk in a rockfall protected area. *Landslides*, 2, 343–357.
- De Almeida, J.A., Kullberg, J.C. 2011. Rockfall hazard and risk analysis for Monte da Lua, Sintra, Portugal. *Natural Hazards*, **58**(1), 289–310. DOI: 10.1007/s11069-010-9668-5
- Ferlisi, S., Cascini, L., Corominas, J., Matano, F. 2012. Rockfall risk assessment to persons travelling in vehicles along a road: the case study of the Amalfi coastal road (southern Italy). *Natural Hazards*, 62(2), 691–721. DOI: 10.1007/s11069-012-0102-z
- Guzzetti, F., Crosta, G., Detti, R.; Agliardi, F. 2002. STONE: a computer program for the three-dimensional simulation of rockfalls. *Computational Geosciences*, **28**(9), 1079–1093.
- Gupta V., Jamir, I., Kumar, V., Devi, M. 2017. Geomechanical characterisation of slopes for assessing rockfall hazards in the Upper Yamuna Valley, Northwest Higher Himalaya India. *Himalayan Geology*, 38, 156–170.
- Heim, A. A., Gansser, A. 1939. Central Himalaya: geological observations of the Swiss Expedition 1936, India, Hindustan Publishing, Delhi.
- Hoek, Evert. "Unpublished notes" NSERC Industrial Research Professor of Rock Engineering, Department of Civil Engineering, University of Toronto, St George Street, Toronto, Ontario, Canada M5S 1A4.
- Hoek, E., Bray, J. 1981. Rock slope engineering. Stephen Austin and Sons Limited Publishers, Hertford.
- IS 8764: 1998. Method of determination of point load strength index of rocks (First Revision). Published by Bureau of Indian Standards, 9 Bahadur Shah Zafar Marg, New Delhi 110002.
- Kumar, A., Asthana, A.L., Priyanka, R.S., Jayangondaperumal, R., Gupta, A.K., Bhakuni, S.S. 2017. Assessment of landslide hazards induced by extreme rainfall event in Jammu and Kashmir Himalaya, northwest India. *Geomorphology*, 284, 72–87.
- Lawrence, F.J. 1977. Geology of the area around Uttarkashi, Garhwal Himalaya, Uttar Pradesh. MTech Thesis, IIT Roorkee.
- Ozmen, M. 2023. Evaluating earthquake vulnerability of 2023 Kayseri, Tu¨rkiye via BWM-ABAC method. *Sadhana*, **48**: 179. https://doi.org/10.1007/s12046-023-02216-x
- Palmstrom, A. 2005. Measurements of and correlations between block size and rock quality designation (RQD). *Tunnelling and Underground Space Technology*, 20, 362–377. https://doi.org/10.1016/j.tust.2005.01.005.
- Pellicani, R., Spilotro, G.; Van Westen, C.J. 2015. Rockfall trajectory modeling combined with heuristic analysis for assessing the rockfall hazard along the Maratea SS18 coastal road (Basilicata, Southern Italy). *Landslides*, **13**, 985–1003. doi: 10.1007/s10346-015-0665-3
- Pandey, V.H.R., Kainthola, A., Yadav, V. et al. 2025. 3D Stochastic Simulation of Rockfall Mechanism and Mitigation in the Batseri Zone.

- Geotechnical and Geological Engineering, 43: 34. https://doi.org/10.1007/s10706-024-03035-5
- Ray, A., Bharati, A.K., Rai, R., Singh, T.N. 2021. Landslide occurrences in Himalayan residual soil: a review. *Himalayan Geology*, 42 (1), 189–204.
- Ritchie, A.M. 1963. The evaluation of rockfall and its control. *Highway record*, 17, 13-28.
- Romana, M. 1985. New adjustment ratings for application of Bieniawski classification to slopes. *International symposium on the role of rock mechanics ISRM, Zacatecas*, pp. 49–53.
- Romana, M., Seron, J.B., Montalar, E. 2003. SMR Geomechanics classification: Application, experience and validation. 10th ISRMtechnology roadmap for rock mechanics, South African Institute of Mining and Metallurgy.
- Roul, A.R., Pradhan, S.P., Tulsawadekar, K., Vishal, V. 2023. A Python based optimization method to define the trajectory of rockfalls: a case study of Malshej Ghat, India. Bulletin of Engineering Geology and the Environment 82: 421.
- Sardana, S., Sharma, P., Verma, A.K., Singh, T.N. 2021. A case study on the rockfall assessment and stability analysis along Lengpui-Aizawl highway, Mizoram India. *Arabian Journal of Geosciences*, https://doi.org/10.1007/s12517-020-06196-8.
- Sardana, S., Sinha, R.K., Verma, A.K., Jaswal, M., Singh, T.N. 2022. A Semiempirical approach for rockfall prediction along the Lengpui-Aizawl highway Mizoram, India. *Geotechnical and Geological Engineering*, 40, 5507–5525. https://doi.org/10.1007/s10706-022-02229-z
- Sarkar, S., Kanungo, D.P., Kumar, S. 2012. Rock mass classification and slope stability assessment of road cut slope in Garhwal Himalaya, India. *Geotechnical and Geological Engineering*, **30**, 827–840. https://doi.org/10.1007/s10706-012-9501-x

- Sarkar, S., Pandit, K., Sharma, M., Pippal, A. 2018. Risk assessment and stability analysis of a recent landslide at Vishnuprayag on the Rishikesh-Badrinath highway Uttarakhand, India. Current Science, https://doi.org/10.18520/cs/v114/i07/1527-1533.
- Shah, A. 2021. The Chamoli Disaster of 2021 merits our attention. https://www.mapmyops.com/the-2021-chamoli-disaster-merits-our-attention.
- Sharma, L.K., Umrao, R.K., Singh, R.; Singh, T.N. 2020. Assessment of rockfall hazard of hill slope along Mumbai-Pune expressway, Maharashtra, India. Acta Geodynamica et Geomaterialia, 17(3), 285–296. https://doi.org/10.13168/AGG.2020.0021
- Singh, P.K., Wasnik, A.B., Kainthola, A., Sazid, M., Singh, T.N. 2013. The stability of road cut cliff face along SH-121: a case study. *Natural Hazards*, 68: 497507.
- Singh, P.K., Kainthola, A., Singh, T.N. 2016. Rock mass assessment along the right bank of river Sutlej, Luhri, Himachal Pradesh, India. *Geomatics, Natural Hazards and Risk*, 6(3), 212-223.
- Stevens, W.D. 1998. RocFall: a tool for probabilistic analysis, design of remedial measures and prediction of rockfalls. Dissertation, University of Toronto, Toronto.
- Verma, A.K., Sardana, S., Sharma, P., Dinpuia, L.; Singh, T.N. 2019. Investigation of rockfall-prone road cut slope near Lengpui Airport, Mizoram, India. *Journal of Rock Mechanics and Geotechnical Engineering*, 11(1), 146–158. https://doi.org/10.1016/j.jmge.2018.07.007
- Vishal, V., Siddique, T., Purohit, R., Phophliya, M.K. and Pradhan, S.P. 2017. Hazard assessment in rockfall-prone Himalayan slopes along National Highway-58, India: rating and simulation. *Natural Hazards*, **85**, 487–503. doi 10.1007/s11069-016-2563-y
- Yoon, W.S., Jeong, U.J., Kim, J.H. 2002. Kinematic analysis for sliding failure of multifaced rock slopes. *Engineering Geology*, 67, 51–61. https://doi.org/10.1016/S0013-7952(02)00144-8

Himalaya and its Bearings – Progress and Sustainability: A synoptic view

The Himalaya possesses a plethora of resources: snow and glaciers; springs and river systems; precious minerals and orebodies; abundant renewable energy resources geothermal, wind and solar; hydrocarbons in thrust-fold belts; medicinal plants and herbs; scenic beauty and astonishing landscapes; sediments and water transmit; forests with timbers for wood-works, and assortments of leaves for handicrafts; grassland and shrubs for livestock; fodders; beautiful meadows and flower-gardens; striking lakes and wetlands; harmonious ecosystem and biodiversity with a variety of fauna and flora; tourists and pilgrims attractions, etc. All these can be harnessed in scientific manners for socioeconomic growth, agricultural advancement, strategic development, climate change (CC) mitigation by tapping renewable energy resources, building green environment with smart towns/villages, and preserving Himalayan ecosystem. Glaciers, snow and mighty rivers are lifeline to hundreds of millions of people for irrigation, drinking water, hydro-power, domestic usages and industrial requirements. Thus, the Himalaya provides great opportunities for the investment, progress and prosperity in terms of construction of roads, bridges, tunnels, ropeways; building hydro-power projects and geothermal or hybrid energy plants; evolution of agriculture and livestock farms; construction of geoparks or geoheritage sites for gaining knowledge about the Himalaya and green ecotourism; expansion of micro-scale industries using local resources. The tall-standing Himalaya also influences the monsoon rains, snow precipitations, weather patterns or climate variability from humid and subtropical to cold and dry desert due to orographic barriers and high albedo.

However, the Himalaya is stressed by subsurface processes like plate convergence; exhumation, deformation and reworking of rocks; crustal shortening; complex tectonics and neo-tectonics leading to earthquakes; and surface processes such as weathering and erosion leading to land degradation etc. The stresses are aggravated by extremities like excessive rainfall leading to landslides, flash floods, debris flows; and snow precipitation leading to avalanches or flash floods. Besides, there are several other climate-induced hazards such as glacier-lakes outburst floods (GLOFs). landslide-lakes' outburst floods (LLOFs), fluvial extremes, risks due to river incisions, forest fires, etc. The stresses are being added further by unplanned civil constructions and several other types of anthropogenic loads that are being exerted unscientifically. Hence, the Himalaya is home to different kinds of disasters with variable intensities, which retard the progress of the Himalayan states and impede wellbeing of the people living therein, especially under the influence of present climate change consequences.

Therefore, the biggest challenge in the Himalayan states is how to maintain an equilibrium between the utilization of available resources for socio-economic development at one hand, and safeguarding the ecology or Himalayan environment and building disaster-resilient and climate-

adaptable future on the other hand. Definite answer is the scientific comprehension of the site-specific issues with regard to natural processes, climatic influences, anthropogenic stresses, environmental degradation; establishment of science-society link; understanding the technological barriers and development of innovative approaches for optimal utilisation of resources and preservation of ecological balance; advancement of strategies for disaster risk reduction; and providing guidelines for effective implementation of policies towards sustainable development. It must be mentioned that the entire Himalayan regions may not be vulnerable or susceptible to geological hazards and hence do not pose threat or risks everywhere, Therefore, assessment and identification of hotspots, and providing their plausible remediation are need of the hours.

Geosciences play a pivotal role for resilience and strong emergence of economy in areas of (i) Water security – spring rejuvenation, river regeneration, water storage as subsurface reservoirs, and assessment/monitoring of big surface reservoirs or lakes, even rivers; (ii) Energy security conversion of geothermal energy into green electricity; utilisation of hydro, solar and wind powers and development of hybrid technology for synergising energy production; (iii) Industrial expansion – exploration of precious minerals and orebodies that are formed in specific P-T regime of the Himalaya; (iv) In-depth understanding of the impact of climate change to almost all sectors: energy, water, food/agriculture, environment, health, ecology and biodiversity, and building schemes for sustainable growth and to live with the disasters; (v) Identification of the most vulnerable zones based on satellite and land-based data (wherever possible); (vi) Assessment of geological risks, and their monitoring, management and mitigation; (vii) Development of Early Warning and Alert Systems (EWAS) of geo-hazards; (viii) Sensitization or Education through mock drills for effective implementation and sensible response to EWAS; (ix) Establishment of link between subsurface features with surface observations through geophysical and geological studies in ensuring site-selection, and warranting safety and durability of any project like tunnel or hydropower or other developmental activities; and (x) Way forward for conservation of Himalayan ecosystem and environment etc. It is the Earth and Environmental Sciences that provide crucial information in understanding the processes associated with the climatic phenomena, natural processes, load bearing capacity or anthropogenic impact, and land degradation or changes of landscapes/geomorphology. Integrated study involving all these will provide basic input that can control the damage patterns during a catastrophe.

The 2500-km long stretch of the Himalayan arc including the western and eastern syntaxes constitutes a large part of India covering eleven states: Uttarakhand, Himachal Pradesh, Arunachal Pradesh, Manipur, Meghalaya, Mizoram, Nagaland, Sikkim, Tripura, part of Assam and Northern West Bengal and two Union Territories: Jammu & Kashmir and Ladakh. Different kinds of people living in the hard-hitting Himalaya have limited exposure to education and training, inadequate infrastructural support for their way to progress, and scanty means of livelihoods. They often experience disasters with variable intensities and lose their lives. livestock, properties, other belongings. These are some of the issues that have compelled people to migrate away from the Himalayan terrains with a view to have quality education, jobs, and disaster-free future. There are certain efforts of education on environment and traditional knowledge base: research on socio-cultural, ecological, economic and physical systems; training and collaboration; and advanced research on mountain-building processes and improved understanding of the geodynamics, climate-tectonics, geo-hazards and georesources by both private and central/state government organizations. However, the basic education on the Himalayan Sciences are beyond the mandate of research institutes or organizations or universities, and thus the scopes for the Education and Research on Himalayan Sciences in a comprehensive manner are inadequate.

The students are unable to orient themselves towards the Himalayan-centric courses such as Geology, Tectonics and Neo-tectonics, River Sciences, Fluvial Extremes, Glaciology, Climate-Tectonics, Paleoclimates, Seismology, Earthquake Engineering, Climate Change, Glacial Dynamics, Hydrology, Landslides, Early Warnings and Alert Systems, Ecology, Geomorphology, Himalayan Resources, Civil Constructions, Green Energy, Carbon Sequestration, Green Environment, Clean Water, Traditional Knowledge, Flash Floods, Debris Flow, Rocks, Fossils, Soils & Landforms, Disaster Management: readiness, remediation, response, restoration, rescue, and rehabilitation, Biodiversity and Ecosystem, Anthropogenic Load, Weathering and Erosion, and many other topics. In this context, there must be a devoted Centre of Himalayan Science Education and Research (CHSER) with a view to building trained manpower and developing institutional capabilities in comprehending Himalayan Sciences and furthering researches for resilient and sustainable growth. Such a Centre would provide a platform where fundamentals of Himalayan Sciences would be taught to the Master students; mountainous site-specific knowledge can be accrued through researches; science-society linkages can be established; gained knowledge can be translated into products and processes with industry partners that can meet the aspirations of people living into the Himalayan states; opportunities for technological advancement and development of innovative approaches; and Environment Impact Assessment (EIA) can be substantiated by advancing researches. This model would pave the way for a positive impact on rapidly evolving scenarios in the Himalaya, especially under the impact of the present climate change scenario towards the socio-economic and strategic development; understanding the geo-hazards and their remediation; development of green environment with clean water and green energy; and preservation of Himalayan ecosystems, natural habitats through all-embracing learning, training, research and invention. In fact, the Himalaya is an

excellent natural laboratory to study the impact of climate change as well as quantification of arresting carbon footprints through its forests and large water bodies. The Himalayacentric education and research can also provide an opportunity of embryonic strategies for sustainable growth, providing input in formulating policy/decision for invigorating the economic stability, green revolution as a part of fulfilling the Sustainable Development Goals (SDGs) for the people living in the Himalaya and adjoining regions.

Here are some steps that can serve as guidelines for the protection, prevention, and preparedness against any disaster; evolving strategies for minimisation of damage due to a catastrophe; developing disaster-resilient and climate-adaptable future; and building confidence for secured living, which can lead to economic stability.

- Identification of the most susceptible or vulnerable or risk zones through geoscientific investigation
- Monitoring risk-prone areas by deploying specific stateof-the-art web-based sensors
- Development of ML-enabled Early Warning and Alerting Systems (EWAS)
- Inculcating fundamental Education on Himalayan Sciences, particularly the causes and consequences of disasters, and their plausible alleviation at Schools/Colleges
- Building trained manpower on Himalayan Sciences and Disaster Management - preparedness, remediation, response, restoration, rescue, and rehabilitation
- Comprehension of mountain-specific local challenges and alleviation of technological barriers for sustainable growth in the Himalaya
- Drawing attention of stakeholders to scopes and opportunities for mitigation of challenges and development of innovative approaches
- Inspiration of young minds in pursuing Himalayan Sciences and building institute-industry partnership for translation researches
- Implementation of hill-specific town planning and building codes, and strict execution of penalty against violation or unauthorised civil construction
- Optimal utilization of nature-based solutions and traditional knowledge base in conjunction with the modern practices for exploitation of natural resources, execution of any project, and conservation of the Himalayan environment
- To define "people's role on do's and don'ts" and dissemination of scientific knowledge and other information to all levels - local people, city planners, administrators, investors, policy makers, political leaders, intellectuals, builders, environmentalists, scientists/ engineers, and all others who matter for taking holistic decisions.

Here are some other information and knowledge that can be quickly spread to the people for sustainable growth:

- Importance of tree-roots that protect hilly region from slope failure
- Proper drainage system that prevents percolation of household water, which otherwise can develop underground planes of weakness and trigger surficial mass movement or land subsidence (as we have observed at Joshimath in the UK state)
- Construction of retaining walls and usage of wire-mesh or other structural measures for preventing impact of rock falls or mass movement
- Development of satellite towns with limited storey buildings, instead of having congregation of multi-storey structures at one business town. This will distribute the overburden stresses
- Slope stability assessment before construction of any project in hilly-area as well as during toe-cutting for the construction of roads or tunnels or ropeways
- Immediate disposal of muck after rock cutting, which otherwise can form temporary dam(s) at downstream river channel and lead to flash floods by sudden breaching
- Non-exposure of heavy structures and anthropogenic activities to or near highly vulnerable zones
- Usage of light-weight construction materials for buildings or infrastructures

- Adaptation of disaster-resilient engineered structures and retrofitting of old buildings
- A hybrid of Traditional and Modern Practices for building Disaster-resilient society
- Periodic assessment of load bearing capacity at multiple scales
- Practice through mock-drill and observation of a 'calamity day' that can remind to following up the codes for safeguarding from disasters
- Habit of using green energy for climate change mitigation and
- Say 'No to Plastics' for protection of the Himalayan environment

This is an outcome from the deliberations at several meetings during my tenure as the Director of the Wadia Institute of Himalayan Geology, Dehradun. I express my deep sense of gratitude to His Excellency Lt. Gen. (Retd.) Gurmit Singh Ji, Honourable Governor of Uttarakhand State for his special interests and inspirational words to write on this topic. I owe my indebtedness to Prof. Harsh K. Gupta who has enthused and nourished me at different stages of my professional career and personal development. I would also like to thank and acknowledge Prof. Shailesh Nayak, Prof. Ashutosh Sharma, Prof. Ashok Sahni and Prof. Talat Ahmad for their valuable guidance and continual motivation.

Kalachand Sain
J.C. Bose National Fellow
CSIR-National Geophysical Research Institute, Hyderabad
Advisor, DST Center of Excellence on Climate Information, IIT-Delhi
Former Director, Wadia Institute of Himalayan Geology, Dehradun

National Training Programme on "Policy for Science and Science for Policies"

A week course on the theme "Policy for Science and Science for Policies" was organised at National Institute of Advanced Studies (NIAS), Bengaluru, supported by Department of Science and Technology (DST), Govt. of India from December 16-20, 2024 for the Directors, Divisional Heads, Chief Scientists and Senior Scientists. The prime objective of the programme was to acquaint and update the participants with the latest developments in science, technology and public policy, and the overarching scientific, social and policy dimensions and their inter-relations. The programme commenced with a welcome address and an introductory speech by Prof. Sangeetha Menon, Course Co-ordinator and Dean, School of Humanities, NIAS Bengaluru followed by inaugural lecture delivered by Prof. V.S. Ramamurthy, Former Secretary, DST, Govt. of India.

A total of 26 participants from across India represented various Institutions, Ministries and Departments such as Department of Science & Technology (DST), Ministry of Science and Technology; Ministry of Commerce and Industry; Department of Atomic Energy; Ministry of Earth Sciences; Ministry of Defence; Indian Council of Medical Research; Ministry of Health and Family Welfare; Ministry of Electronics & Information Technology; Ministry of Food Processing Industries; Department of Atomic Energy; Survey

of India (SoI); Ministry of Defence; Department of Space; Ministry of Power; Ministry of Environment, Forest and Climate Change. To achieve the objectives of the course, 16 distinguished resource persons from various ministries, institutions and organizations of repute in the country shared their works on how it impacts the society and the nation at large followed by highly educative and thought-provoking interactive sessions after every lecture. Another important component of the course was the Group Session where all the participants made a presentation on their respective domains sharing insights, views and experiences on their achievements, challenges and responses, and the societal and national impact of their work. A valedictory lecture was delivered by Prof. Annapurni Subramaniam, Director, Indian Institute of Astrophysics, Bengaluru. The event concluded successfully with a certificate distribution ceremony graced by Dr. Shailesh Navak, Director of NIAS, Former Secretary of the Ministry of Earth Sciences (MoES) Govt. of India, and the then Chairman, Research Advisory Committee (RAC) as well as the incumbent Chairman, Governing Body (GB) of the Wadia Institute of Himalayan Geology (WIHG), Dehradun marking a meaningful closure of the programme with an enriched and interdisciplinary learning experience.



Photograph of the organisers and participants at the National Institute of Advanced Studies (NIAS), Bengaluru

Sitting: Suchitha Maddhikunta, K. Arul Selvi, Sangeetha Menon, Rakesh Godhwani, Shailesh Nayak, V.S. Ramamurthy,

M.R. Bhuvaneswari, Saritha Nair, Archana Joshi Saha, P. Srinivasa Aithal

Standing 1st Row: R. Paramasivan, Hasibur Rahaman, Partha Ghosal, L.K. Sahoo, Devendra Kumar Sakhare, Neeraj, C.S. Tomar,

D.B. Sathe, P. Arumugam, R. Vidyalakshmi

Standing 2nd Row: K. Vijesh Sreedhar, Ashish Kaushal, Basanta Kumar Jena, Sanjeev Kumar Gupta, Rahul Sharma, K. Gopkumar,

Partha Sarathy Uppala, Kapesa Lokho, R. Jayasree, Samir Kumar Nath

Standing 3rd Row: P. Nagaraja, V.A. Ramesh, J. Chandra Babu, Srikumar M. Menon, Arul Anand

Kapesa Lokho Wadia Institute of Himalayan Geology, Dehradun Email: kapesa@wihg.res.in



वाडिया हिमालय भूविज्ञान संस्थान WADIA INSTITUTE OF HIMALAYAN GEOLOGY

सदस्यता/Membership No.
_TSS

हिमालयन जियोलॉजी **HIMALAYAN GEOLOGY**

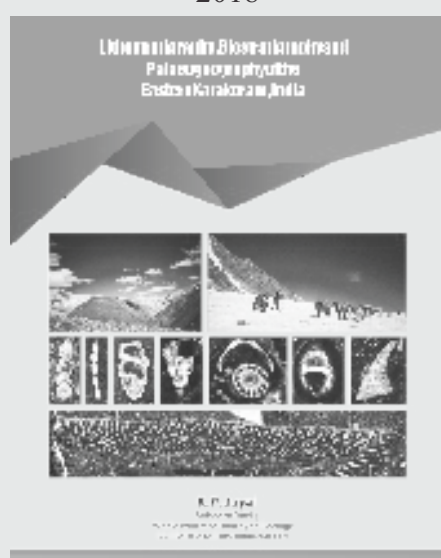
आजीवन ग्राहक सदस्यता हेतु पंजीकरण प्रपत्र Registration form for Life Time Subscriber membership

	केवल व्यक्तिगत उपयोग हेत/for individuals use only
1.	में "हिमालयन जियोलॉजी" का आजीवन ग्राहक बनना चाहता हूँ। I would like to become a Life Time Subscriber for "Himalayan Geology".
2.	आजीवन सब्सक्रिप्शन शुल्क की राशि निदेशक, वाडिया हिमालय भूविज्ञान संस्थान के पक्ष में ऑनलाइन भुगतान विवरण/ड्राफ्ट/चैक के साथ निम्नलिखित के लिए संलग्न है। The Life Time subscription fee with online payment details/Draft/Cheque in favour of Director, Wadia Institute of Himalayan Geology is enclosed herewith for the following:
	Type of subscription (Tick [✓] which is applicable): ☐ Print copy ☐ Soft copy by online access/email
	☐ Fee for Print copy: Rs. 7500.00 (India) US\$ 750.00 (Foreign) ☐ Fee for Soft copy: Rs. 4000.00 (India) US\$ 250.00 (Foreign)
	नाम/Name:
	पता/Address:
	ईमेल/Email:
	मोबाइल/Mobile:
	में प्रमाणित करता हूँ कि यह सदस्यता केवल मेरे निजी प्रयोग के लिए है तथा यह प्रिंट/साफ्ट-सदस्य प्रति, प्रकाशन होने से कम से कम दो वर्ष अवधि तक किसी पुस्तकालय या वाचनालय को उपलब्ध नहीं करवाई जाएगी। I certify that the subscription is for my personal use only and that print/soft subscriptions will not be released ibraries or reading rooms for at least 2 years after publication.
	हस्ताक्षर / Signature
आफॅ	र (सीमित अवधि के लिए): नये पंजीकृत आजीवन ग्राहकों को "हिमालयन जियोलॉजी" के पुराने प्रिंट वोल्यूमों का एक मुफ्त सैट (1971 से 2012 तक, उपलब्धता के आधार पर) उपलब्ध कराया
Offe	जाएगा (डाक शुल्क ग्राहक द्वारा वहन किया जाएगा)। r (for a limited period): A free set of old print volumes (1971 to 2012, subject to availability) of "Himalayan Geology" will be provided to the newly registered Life Time Subscribers (Postage to be borne by the Subscriber).
का	र्यालय उपयोग हेतु /For office use
रर्स	ोद सं./Receipt No.:दिनांक/Dated:राशि/Amt. Rs
जा	री मौजूदा वोल्यूम /Issue Current Vol. No.:

WADIA INSTITUTE OF HIMALAYAN GEOLOGY, DEHRADUN

Latest Publications

2018 2015



Rs.600/- (India), US\$ 50/- (Abroad)

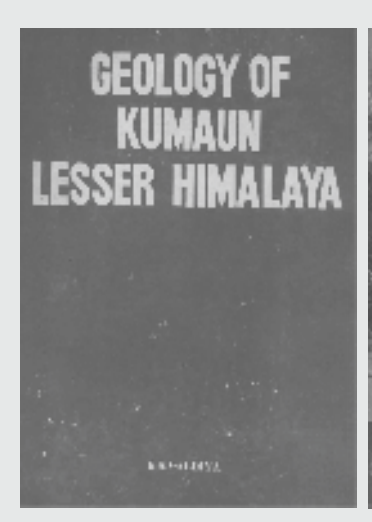


Rs.1200/- (India), US\$ 100/- (Abroad)



Price: Rs. 500/- (India), US\$ 50/- (Abroad)

Previous Publications



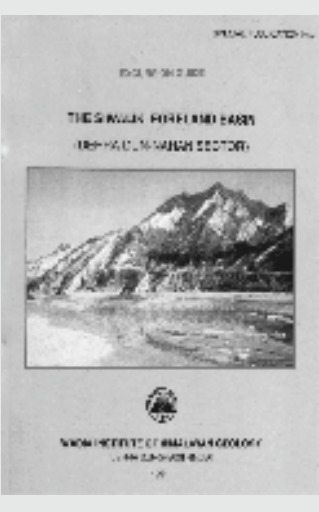
Rs.180/- (India), US\$ 50/- (Abroad)



Rs.205/- (India), US\$ 40/- (Abroad)



Rs.180/- (India), US\$ 15/- (Abroad)



Rs.45/- (India), US\$ 8/- (Abroad)



Rs.200/- (India), US\$ 15/- (Abroad)

Procurement details:

Corresponding address:

The Director

Wadia Institute of Himalayan Geology, 33, GMS Road, Dehradun 248001, India

or

Publication Division

Wadia Institute of Himalayan Geology, 33, GMS Road, Dehradun 248001, India Phone: +91-0135-2525430, Fax: 0135-2625212 Email: himgeol@wihg.res.in, himgeology.com@gmail.com Web: http://www.himgeology.com

Online payment/Cheque/Bank Draft:

Should be in favour of the 'Director, Wadia Institute of Himalayan Geology'

GUIDELINES FOR AUTHORS

General Information: 'Himalayan Geology' is a biannual (January and July) flagship scholarly journal of the Wadia Institute of Himalayan Geology, Dehradun. It publishes original research contributions on several aspects of geology, geophysics, sedimentology, paleontology, stratigraphy, magmatism, metamorphism, collisional tectonics, seismicity, seismogenesis, geomorphology, geological map, glaciology, hydrology, environment, climate change, natural hazards, geotechnical studies, remote sensing, natural resources about the Himalaya and other regions. Himalayan Geology also publishes scholarly invited state-of-theart review articles presenting significant advances on any of the abovementioned themes to facilitate communication among scientists from a broad range of disciplines and interests to an international readership. The Journal encourages scholarly articles based on extensive field-based studies, experimental results, geophysical investigations, theoretical analysis, numerical simulation, and novel ideas; to propagate science in understanding some fundamental issues related to the following Key- or Index-words: geodynamics, magmatism & metamorphism, palaeontology & paleobiology, structural geology & tectonics, petrology & geochemistry, geomorphology, sedimentology & sequence stratigraphy, geophysical technique, seismology, geophysical exploration & processing, cryosphere, climate record, geodesy, biodiversity, remote sensing and GIS, soils, geo-archaeology, artificial intelligence for geoscience, natural hazards, and natural

The average length of a paper including figures and tables should not exceed 20 printed pages. Short communications including Discussion, Comments and Replies on papers, which have appeared in a recent issue of *Himalayan Geology*, are welcome. They should normally not exceed two printed pages. All contributions are subject to the normal review procedure. Authors may provide names and email addresses of three reviewers to aid the editors in their selection. Acceptance of a manuscript is decided after the receipt of its final version along with tables and good quality figures. The scientific content of the papers will be the sole responsibility of the authors.

Submission of an article to *Himalayan Geology* is understood to imply that it has not been published on paper or electronically, that it has not been simultaneously submitted for publication elsewhere, and that the author agrees to transfer the copyright to Wadia Institute of Himalayan Geology.

Manuscripts and all related correspondence should be addressed to:

Editorial Office, "Himalayan Geology" Phone (off): (91) 135-2525430; Fax: 0135-2625212

Wadia Institute of Himalayan Geology Email : himgeol@wihg.res.in; himgeology.com@gmail.com

33-G.M.S. Road, Dehradun 248 001, India Website : www.himgeology.com

Manuscripts preparation: Electronic copy of manuscripts (in journal format) should be submitted on A4 size (297 x 210 mm) in 'MSWORD'. Manuscripts are to be written in English in a simple style. Care should be taken to avoid long and complicated sentences and unnecessary jargon. The text is to be organized as Abstract, Introduction, Methodology, Main body including Data, Results and Interpretations, Discussion, Summary and or Conclusions, Acknowledgments and References. The length of the abstract should be limited to 250 words. It should summarize the results rather than contents of the paper and should include all new taxonomic names. Citation of literature in the abstract is discouraged. The headings and subheadings should be numbered hierarchically (such as 1/1.1/1.1.1 etc.). This numbering serves as an aid in editorial process and is deleted in the final layout. The text should be in one and half-spaced with 30 mm margin on each side. Only names of genera and species are to be set in italics. Foot notes are not allowed.

Literature citations in the text should be formatted as follows: Author (1990: 525) or (Author 1990: 525). Two author are linked by "&": Author & Author (1990: fig. 2). Three or more authors are abbreviated by "et al." after the first author: Author et al. (1990). References are separated by a semi colon ";" and year by a coma ",": Author 1990; Author 1995, 1996). Citations of figures, plates and tables are written in small letters: (Author 1990: 56, pl. 4, fig. 5) or (Author 1990: 56, text-fig. 4, tab.4). Note that there is no coma between authors name and year of publication.

All pages of scripts, including references and explanations of illustrations, should be numbered consecutively. Papers on palaeontology must strictly follow the most recent issues of the International Codes of Zoological Nomenclature (ICZN) and Botanical Nomenclature (ICBN). In making any stratigraphical changes or erecting new stratigraphic terms the International Stratigraphic guidelines should be followed. As per the recommendations of ICZN and ICBN, all illustrated and described fossils must be registered and deposited in an appropriate permanent institution. The register number and the name of the repository must be quoted.

Illustrations: Illustrations must be submitted camera-ready for copying and they should be numbered in the same sequence that they appear in the text. When designing figures, tables and plates it is important to keep the maximum size of the printed illustration in mind (full page format: 230 mm high and 180 mm wide in two columns, single column format: 230 mm high and 85 mm wide). So potential reduction of illustrations is to be kept in mind especially with regard to lettering. After reduction to column or page size, the smallest letters should be at least 8 pt). All figures, tables and plates are referred to in the text with capitalized abbreviations like Fig. 1, Table 2 or Plate 3. A scale bar should accompany line drawings as well as photographs of specimen; its length is to be indicated in the figure-caption. Fold-out tables are not acceptable. If a table of larger than page size is essential, it should be arranged for two facing pages. Fold-out maps, and colour plates may be considered for inclusion only if essential - for both a contribution towards the extra cost involved will be expected from the author.

The author should retain original illustrations until the manuscript is accepted. Review copies must include high-quality photographs of halftone illustrations; photocopies are acceptable only for line drawings. Digital versions of line drawings are encouraged (in cdr/tiff) but they should be accompanied with high quality laser printouts. Each plate and photographic figure should be protected by an overlay attached along the upper edge.

References: The authors are organized in alphabetical and chronological order, every author separated by coma ",". References by the same author, published in the same year should be distinguished by the use of suffixes: 1999a, 1999b, 1999c. All author names are set in small letters. Publication/journal name are given in full title/name. Volume numbers are printed in bold and issue numbers are given in parenthesis followed by a coma and page numbers. Examples:

Author, A. 1998. Title of paper. Full name of journal, 11 (2) 205-221.

 $Author, B., Author, C., Author, D.\ 1999.\ Title\ of\ paper.\ \textit{Full name of journal,}\ \textbf{32}, 295\text{-}300.$

Author, A. 1999. Title of book. Name of Publisher, place of publication, 280p.

Author, A. 1999. Title of contribution. In: Editor, A. (ed.), Title of book. Name of Publisher, place of publication, 150p.

Author, A., Author, B. 2000. Title of contribution. In: Editor, A., Editor, B. (eds.), Title of book. Name of Publisher, place of publication, 150p.

Electronic version of manuscript: After the acceptance of a paper the authors are required to submit an electronic version of their manuscript in MS-Word for Windows. The electronic text may be formatted as follows: use 10 pt Times New Roman font, justify margins only, do not hyphenate words, set generic and specific names of taxa in *italics*. Number headings and subheadings hierarchically (such as 1/1.1/1.1.1 etc.) and do not underline them or set in bold/italic. All author names in text as well as list of references are set in small letters.

Cover Photographs: High quality photograph (TIFF file on min 400 resolution) related to the submitted manuscript is welcome for use on the cover page.

Publication time: Currently the time between initial submission and publication of regular articles is about 1 year. Articles accepted for publication are generally published in order of submission. Exceptions can be made for papers of high scientific significance.

Reprints: PDF file of published article will be provided free of cost to authors.

HIMALAYAN GEOLOGY

Vol. 46, No. 2, 2025 CONTENTS

	Pages
ZHU XIMING, JIA JINLONG, ZHANG LONGGANG, MA ZHENG, QIN ZHENGYUAN, ZHANG HANQUAN, LIU ZILONG: Study on the numerical simulation model for quantitative evaluation on effect factors of multi-branch pinnate borehole gas extraction in high-gas thick coal seams	125-135
MALLIKA K. JONNALAGADDA, NITIN. R. KARMALKAR, RAYMOND A. DURAISWAMI: Partial transformation of coesite to quartz in eclogitic garnets of the Tso Morari complex, Ladakh, NW Himalayas: Insights from Raman mapping	136-144
PARV KASANA, VIMAL SINGH, TANYA: Comparative analysis of Himalayan rivers and Central Indian Forebulge rivers: Insights from contrasting tectonic regimes	145-159
HIMANTA BORGOHAIN, SOWRAV SAIKIA, SUMER CHOPRA, RAJIB BISWAS, SANTANU BARUAH, VICKEY SHARMA, BIBHUTI GOGOI: Mapping intensity distribution of Mw~6.1 Dhekiajuli earthquake in the context of tectonic settings	160-169
DEEPA ARYA, GUNJAN ARYA: Petrogenesis of Granite and Granite gneiss of Lansdowne Klippe, Garhwal Lesser Himalaya, Uttarakhand, India	170-183
ASHISH PAL, DILIP KUMAR YADAV, DEBONIL BARUAH, ABHISHEK KUMAR GUPTA, H.C. NAINWAL, PARAKH SAHU: Stress pattern analysis and its tectonic implications in the Eastern Himalayan Syntaxis: A special emphasis to the Siang Valley, Arunachal Pradesh, Northeast India	184-195
AVIK PAUL, DEEPANKAR CHOUDHURY, SIMA GHOSH, SANTANU BARUAH, G.K. BORUAH, J.R. KAYAL: MASW and SPT studies for subsurface soil characterization in Udaipur city area, Tripura state of NE India	196-207
RAKESH CHANDRA, IHSAN ULLAH LONE, MEENAL MISHRA, JONATHAN C. AITCHISON: Lower Cretaceous (lower Aptian) radiolarian cherts from the Shyok Suture Zone, Ladakh, Trans-Himalaya, India	208-220
ADITYA KHARYA, HIMANSHU K. SACHAN, SAMEER K. TIWARI, SHASHI RANJAN RAI, DEEPASHU JOSHI, VAIBHAV DUBEY: Fluid Evolution of the Asian Continental Crust: Implication for Exhumation Tectonics of Trans Himalaya	221-233
NEERAJ DAHIYA, KOUSHIK PANDIT, ANINDYA PAIN, SHANTANU SARKAR: Rockfall dynamics and mitigation strategies for a vulnerable location along a National Highway (NH-7) near Shivpuri in the Tehri Garhwal district of Uttarakhand, India	234-243
KALACHAND SAIN: Himalaya and its Bearings – Progress and Sustainability: A synoptic view	244-246